MODELLING

WARP AND DIMENSIONAL STABILITY

IN

SOFTWOOD

A thesis

submitted in partial fulfillment

of the requirements for the degree

of

Doctor of Philosophy in Mechanical Engineering

in the
University of Canterbury

by
N. Navaranjan

University of Canterbury

2002

Abstract

Seasoned softwood board exposed to in-service moisture variations is subject to dimensional changes and distortions. In-service dimensional instability of a board is a critical issue since it causes serious problems in buildings and other engineering structures.

This thesis presents research involving the development of numerical models to describe the in-service changes in dimension, at a board scale, for small variations in the moisture content. The models used input data defining the properties of the microstructural components that make up the cellular structure of the wood resulting in the cells having heterogeneous anisotropic properties. The application of full cyclic constraint to the boundaries of the elements that made up the representative volume element was investigated and used to determine the equivalent homogenised properties. A cellular model was developed to describe the behaviour of the wood as a function of density, microfibril angle, spiral grain angle and moisture content. The resultant finite element board models used a database generated from the cellular model to describe the dimensional changes associated with small in-service changes in moisture content.

In conjunction with the development of this model the candidate carried out an experimental programme using a specific supplied *pinus radiata* log. The determination of the cellular shrinkage/swelling coefficients, using an experimental technique developed for this research, verified the accuracy of the homogenization method and its subsequent application to the cellular model. The results from the sawn boards were compared with the results from the finite element board models.

Acknowledgment

The research reported in this thesis was initially supervised by Professor Jeremy Astley and latterly by Dr John Smaill. In submitting this thesis, I wish to express my sincere gratitude and thanks to these supervisors for their invaluable advice, constructive guidance and constant encouragement.

I wish to express my sincere thanks to Professor Kenneth Entwistle (Manchester Materials Science Centre, University of Manchester) for his invaluable advice and constant encouragement.

Thanks are extended to technical, workshop, computer and administrative staff especially Paul Southward, Adam Latham, Mike Flaws, Kevin Stobbs, Eric Cox, Ken Brown, Scott Amies, Elizabeth Sands and Jill Porter for their assistance and co-operation.

Thanks are due to Professor John Walker (School of Forestry) for his encouragement and Paul Fuller (School of Forestry) for his valuable assistance for specimen preparation.

Thanks are also due to the Department of Civil Engineering for the permission to use the environmental chamber and the Department of Chemical Engineering for the permission to use the tunnel kiln.

Last but not least I would like to thank my wife Nanthini, son Prashad and daughter Nalini for their patience, cheerful encouragement and support.

Nomenclature

Notations are explained in the text when they first occur. In addition, a list of the main notations is given below. Matrices are represented by boldface uppercase letters when they are not vectors. Vectors are represented by uppercase or lowercase boldface.

General notations

$[\,]^T$	transpose of a matrix
$[\,]^{-1}$	inverse of a matrix
∇	differential operator
$\int(\,)dS$	integration over a surface
$\int(\,)dV$	integration over a volume
Δw, ΔT, Δl_i	change of moisture, temperature, length
$\Sigma(\,)$	sum of ( )
MFA	microfibril angle
SGA	spiral grain angle
pro	value of a property

Times New Roman uppercase letters

$\mathbf{A}$	transformation matrix
A_w	area of the cell wall
A_c	area of the cross-section of cell
$\mathbf{B}^e$	element strain displacement matrix
$\mathbf{C}$	compliance matrix in the global coordinate system
$\mathbf{C}'$	equivalent compliance matrix in the global coordinate system
$\mathbf{C}^*$	compliance matrix in the local coordinate system
$\mathbf{D}$	stiffness matrix in the global coordinate system
$\mathbf{D}'$	equivalent stiffness matrix in the global coordinate system
$\mathbf{D}^*$	stiffness matrix in the local coordinate system
D_a, D_g, D_o	air-dry, green, oven-dry dimension
D_{sa}, D_{so}	air-dry, oven-dry dimensional shrinkage

E_T, E_R, E_L	elastic moduli in the T, R and L directions
E_x, E_y, E_z	elastic moduli in the global directions
E_{11}, E_{22}, E_{33}	elastic moduli in the local axes 1, 2 and 3 directions
$\mathbf{F}$	external force vector
G_{TR}, G_{TL}, G_{RL}	shear moduli in the orthotropic planes T-R, T-L and R-L
G_{xy}, G_{xz}, G_{yz}	shear moduli in the orthotropic planes x-y, x-z and y-z
G_{12}, G_{13}, G_{23}	shear moduli in the orthotropic planes 1-2, 1-3 and 2-3
$\mathbf{H}$	transformation matrix for stresses, strains and constitutive matrices between local and global coordinate systems
$\mathbf{K}^e$	element stiffness matrix
$\mathbf{K}$	stiffness matrix
$\mathbf{M}$, $\mathbf{M}_1$, $\mathbf{M}_2$, $\mathbf{M}_3$	transformation matrices between local and global coordinates
$\mathbf{N}^e$	element interpolation matrices
S	boundary surface
U^e	element strain energy
V	volume
V^e	element potential energy
V_n	vertices of the representative volume element

Times New Roman lowercase letters

$\mathbf{b}$	body force
b_x, b_y, b_z	body forces in the global x, y and z directions
d_i	density of cell wall layer
d_w	density of cell wall material
d_c	density of cell
$\mathbf{d}^e$	column matrix of element nodal displacements
$\mathbf{d}$	column matrix of nodal displacements
$\mathbf{f}$	column matrix of loads
$\mathbf{f}_T^e$	column matrix of element thermal loads
$\mathbf{f}_g^e$	column matrix of element body forces
$\mathbf{f}_T$	column matrix of thermal loads
$\mathbf{f}_g$	column matrix of body forces
$\mathbf{f}_t$	column matrix of nodal forces by surface tractions

$\mathbf{g}$	vector of body force components
$\mathbf{l}$	unit vector in the local L direction
l_i	length in the i direction
$\mathbf{n}$	matrix of unit vector components normal to a surface
n_x, n_y, n_z	unit vector components in the x, y and z directions of a unit vector normal to a surface
r_c	radius of corewood
$\mathbf{r}$	unit vector in the local direction R
$\mathbf{t}$	unit vector in the local direction T
$\hat{\mathbf{t}}$	traction
$\mathbf{u}$	displacement vector
u	displacement component in the x direction
v_i	volume fraction of cell wall layer
v	displacement component in the y direction
v_a, v_g, v_o	air-dry, green, oven-dry volume
w	displacement component in the z direction
$\mathbf{x}$	unit vector in the x direction
$\mathbf{y}$	unit vector in the y direction
$\mathbf{z}$	unit vector in the z direction

Greek letters

χ^e	total energy of element
χ	total energy
$\boldsymbol{\alpha}_T$	column matrix of thermal expansion coefficients
$\boldsymbol{\alpha}_s$	column matrix of thermal shrinkage coefficients
α_T, α_R, α_L	shrinkage coefficients in the orthotropic directions T, R, and L
α_{11}, α_{22}, α_{33}	shrinkage coefficients in the orthotropic directions 1, 2, and 3
α_x, α_y, α_z	shrinkage coefficients in the global directions x, y, and z
γ_{TR}, γ_{TL}, γ_{RL}	shear strains in the orthotropic planes T-R, T-L and R-L
γ_{xy}, γ_{xz}, γ_{yz}	shear strains in the global planes x-y, x-z and y-z
$\boldsymbol{\varepsilon}$	column matrix of total strains in the global coordinate system
$\boldsymbol{\varepsilon}_T$	column matrix of total thermal strains in the global coordinate system

ε_s	column matrix of total shrinkage strains in the global coordinate system
ε'	column matrix of equivalent strains in the global coordinate system
ε^*	column matrix of total strains in the local coordinate system L, T and R
σ	column matrix of stresses in the global coordinate system
σ'	column matrix of equivalent stresses in the global coordinate system
σ^*	column matrix of stresses in the local coordinate system L, T and R
σ_{TT}, σ_{RR}, σ_{LL}	normal stresses in the orthotropic directions T, R and L
σ_{xx}, σ_{yy}, σ_{zz}	normal stresses in the global directions x, y and z
τ_{TR}, τ_{TL}, τ_{RL}	shear stresses in the orthotropic planes T-R, T-L and R-L
τ_{xy}, τ_{xz}, τ_{yz}	shear stresses in the global planes x-y, x-z and y-z
ρ_a, ρ_b, ρ_g	air-dry, basic, green density
δ, δ_x, δ_y, δ_z	column matrices of global displacements
ν_{TR}, ν_{TL}, ν_{RL}	Poisson's ratios relating stresses to strains in the orthotropic directions
ν_{12}, ν_{13}, ν_{23}	Poisson's ratios relating stresses to strains in the orthotropic directions
ν_{xy}, ν_{xz}, ν_{yz}	Poisson's ratios relating stresses to strains in the global directions
ϕ	conical angle
φ	spiral grain angle
ψ	microfibril angle
ω	orientation of a cell wall with local axis
Π	boundary of the global region
η	dimensional ratio of the global region to representative volume element

Contents

1. Introduction 1

1.1 Background 1

1.2 Outline 2

1.3 Aim and Scope 3

2. Characteristics and Properties of Softwood 6

2.1 Introduction 6

2.2 Macrostructure 7

2.3 Microstructure 8

2.4 Ultrastructure and Molecular Structure 10

2.4.1 Chemical Constituents 10

2.4.1.1 Cellulose 11

2.4.1.2 Hemicelluloses 11

2.4.1.3 Lignin 12

2.4.1.4 Extractives 12

2.4.2 Microfibril 12

2.4.3 Orientation of Microfibrils and Cell Wall Layers 14

2.5 Density 16

2.6 Variation in Structure 18

2.7 Hygroscopic Properties 19

2.7.1 Moisture Content 20

2.7.2 Moisture in Wood 20

2.7.3 Adsorption and Desorption 21

2.7.4 Wood in Service 22

2.7.5 Shrinkage and Swelling 23

2.7.6 Anisotropic Shrinkage and Swelling 24

2.7.7 Significance of Shrinkage and Swelling 26

2.8 Stiffness Properties 27

2.8.1 Factors Affecting Stiffness Parameters 28

3. Mechanics of Continuum and Finite Element Theory 30
3.1 Introduction 30
3.2 Continuum Mechanics 30
3.2.1 Continuum Equations 30
3.2.2 Orthotropic Heterogeneous Material 32
3.2.3 Transformation of Constitutive Properties 34
3.3 Finite Element Method 37
3.3.1 Element Formulation 38
3.3.2 Total Energy 39
3.3.3 Minimisation of System Energy 40
3.3.4 Boundary Conditions 41

4. Homogenization of Elastic Composite Continuum 42
4.1 Introduction 42
4.2 Homogenization Principles 43
4.2.1 Composite Continuum 43
4.2.2 Representative Volume Element 44
4.2.3 Full Cyclic Constraint 46
4.3 Implementation of Full Cyclic Constraint by the Finite Element Method 50
4.3.1 Energy Concept 50
4.3.2 Applying Constraint Equations 53
4.4 Determining the Equivalent Properties 57
4.4.1 Six Elementary Stress Cases 57
4.4.2 Thermal Load Case 58
4.5 Test Models 58
4.5.1 First Test Model 59
4.5.1.1 Homogenization Analysis 60
4.5.1.2 Analytical Method 61
4.5.2 Second Test Models 63
4.6 Discussion 65

5. Modelling Wood Behaviour at Micro Level 67
5.1 Introduction 67
5.1.1 Microfibril Model 67
5.1.2 Existing Cell Models 70
5.2 Cell Model 71
5.2.1 Periodic Nature of Wood at Micro Level 71
5.2.2 Homogenization of Cell Model 73
5.3 Measuring Transverse Shrinkage Coefficients at Cellular Level 78
5.3.1 Specimen Preparation and Measurement 79
5.4 Comparison of Results and Discussion 84
5.4.1 Shrinkage/Swelling Coefficients 84
5.4.2 Stiffness Properties 88

6. Modelling Moisture-Induced Behaviour of Board 92
6.1 Introduction 92
6.1.1 A Brief Review of Existing Model 92
6.1.2 Present Model 92
6.2 Properties for Board Models 93
6.2.1 Generating Input Properties from Experiment 93
6.2.2 Property Variation in Log 97
6.2.3 Interpolation of Properties 99
6.2.3.1 Interpolations for First Model 99
6.2.3.2 Interpolations for Second Model 101
6.2.4 Transformation of Properties 102
6.2.4.1 Transformation in First Model 102
6.2.4.2 Transformation in Second Model 104
6.3 Implementation of Board Model 107
6.3.1 First Model 107
6.3.2 Second Model 108
6.4 Results 109
6.5.1 Results from the Board Models 109
6.5.2 Results from the Experiments 116
6.5 Comparisons, Verification and Discussion 116
6.5.1 Results from the First and Second Models 116

6.5.1.1 Longitudinal Shrinkage/Swelling Coefficients..... 116
6.5.1.2 Transverse Shrinkage/Swelling Coefficients..... 117
6.5.1.3 Warping Properties..... 118
6.5.2 Experimental Results and Verification..... 120
6.5.2.1 Longitudinal Shrinkage..... 130
6.5.2.2 Transverse Shrinkage..... 130
6.5.2.3 Warping Properties..... 130
6.6 Validation..... 131
6.7 Limitation..... 131

7. Conclusion..... 133
7.1 Conclusion..... 133
7.2 Limitation of Models and Future Work..... 134

8. References..... 137

Appendices

A. Computing new system stiffness matrix..... 145
B. Applying constraint equations at element level..... 147
C. Predicted stiffness and shrinkage properties from the cell model as the function of density and microfibril angle..... 152
D. Deformed cell meshes for seven load cases..... 160
E. Measurement of the cell wall geometry..... 164
F. Density vs. radial distance graphs of sixteen specimens..... 165
G. Microfibril angle (MFA) vs. radial distance graphs of sixteen specimens..... 173
H. Spiral grain angle (SGA) vs. radial distance graphs of sixteen specimens..... 181
I. Deformed and undeformed FE meshes of twenty boards..... 189
J. Contour plots of board B1..... 199
K. Measurement of dimensions for shrinkage/swelling and warp deformations..... 204
L. Graphs of shrinkage/swelling and warping behaviours from experimental results..... 205

List of Tables

5.1 Volume fractions of chemical constituents of the cell wall layers used in the microfibril model..... 68

5.2. Stiffness and shrinkage coefficients of the chemical constituents..... 69

5.3. Equivalent stiffness and hygroexpansion coefficients for the five layers of cell wall from the microfibril model..... 70

5.4. Volume fractions and densities of cell wall layers of early- and latewood..... 74

5.5 Measured transverse shrinkage coefficients..... 84

6.1 Board deformation in (m) from the first model..... 112

6.2 Board deformation in (m) from the second model..... 113

6.3 Shrinkage/Swelling coefficients in longitude, width and thickness of boards from the first model..... 114

6.4 Shrinkage/Swelling coefficients in longitude, width and thickness of boards from the second model..... 115

6.5 Shrinkage/Swelling coefficients along the longitude, width and thickness of twenty boards from the first (1ST) and second (2ND), and experiment (EXP)..... 121

6.6 Bow, crook, cup and twist of twenty boards from the first (1ST) and second (2ND), and experiment (EXP)..... 122

C. Predicted stiffness and shrinkage properties from the cell model as the function of density and microfibril angle..... 152

List of Figures

1.1 Board distortion..... 1

1.2 Change of shape of various cross sections and warping due to differential radial and tangential shrinkage..... 2

1.3 Modelling sequences..... 5

2.1 Structure of softwood at macro, micro, and ultra and Molecular levels..... 6

2.2 Cross-section of stem..... 7

2.3 Growth characteristics..... 8

2.4 Microstructure of *pinus radiata*..... 9

2.5 Simplified structure of cell wall..... 9

2.6 Pits in the tracheids of *pinus radiata*..... 10

2.7 Distribution of the principle cell wall constituents within the wall of a softwood tracheid..... 11

2.8 Structural formula of a cellulose molecule..... 11

2.9 Models of the cross section of a microfibril..... 13

2.10 The cellulose unit cell..... 14

2.11 Structure of the cell wall of a tracheid and the orientation of microfibrils within each wall layers..... 15

2.12 Variation of average MFA from pith in radial direction..... 15

2.13 Density variation within growth ring in radial direction..... 17

2.14 Average density variation from pith to bark in radial direction..... 18

2.15 RTL is the coordinate system of the stem..... 18

2.16 Variation of SGA in a *pinus radiata* log..... 19

2.17 Natural drying of board..... 21

2.18 Adsorption and desorption of water by radiata pine sapwood at 15°C..... 22

2.19 Hygroscopic expansion in the *i* direction..... 23

2.20 Variation of longitudinal and transverse shrinkage with MFA..... 25

3.1 Elastic body with volume V and boundary S..... 30

3.2 Three principle rotations..... 35

3.3 Transformation of local directions to global directions..... 36

4.1 An elastic composite continuum with infinitely extended periodic stricture..... 44

4.2 Undeformed and deformed periodic cells..... 45

4.3 An orthogonal RVE..... 46

4.4 Deformed RVE..... 47

4.5 An RVE is represented in a selected global region of the continuum..... 50

4.6 Heterogeneous RVE and equivalent homogeneous RVE are under same stress and strain field..... 57

4.7 x-z face of a composite with strips..... 59

4.8 RVE2 referred to t, r, l axes..... 61

4.9 x-z face of composite with sphere particles..... 64

4.10 Variation of equivalent MOE with mesh number..... 65

5.1 Distribution of cell length and orientation..... 72

5.2 Simplified model of periodic cells in *pinus radiata* softwood..... 72

5.3 Cross-section of cell model with five cell wall layers..... 73

5.4 Cell mesh..... 76

5.5 Orientation of microfibril in a cell wall layer..... 77

5.6 Sections of log used for specimen preparation..... 80

5.7 Cell image at fibre saturation..... 81

5.8 Simplified environmental chamber..... 81

5.9 Cell image after drying..... 82

5.10 Points for measurements in the field of view..... 82

5.11 A – E: Comparisons of transverse shrinkage/swelling coefficients vs. microfibril angle from the model and experiments..... 85

5.12 Predicted longitudinal shrinkage coefficient vs. MFA for earlywood with density 450 kg/m^3..... 87

5.13 A – D: predicted stiffness coefficients vs. MFA for earlywood with density of 450 kg/m^3..... 88

5.14 A – D: predicted stiffness coefficients vs. density for wood with MFA of S_2 layer is 25°..... 90

6.1 Sections of *pinus radiata* log used for experimental studies..... 94

6.2 Specimens obtained at 45° from the discs..... 95

6.3 Average density from butt disc B..... 95

6.4 Average microfibril angle from butt disc B..... 96

6.5 Average spiral grain angle from butt disc B..... 96

6.6 Average density from top disc D..... 96

6.7 Average microfibril angle from top disc D..... 97

6.8 Average spiral grain angle from top disc D..... 97

6.9 Variation of average MFA, SGA and density in the radial direction, and input log properties..... 98

6.10 Material point in a conical log with pith as the centre line..... 100

6.11 Material point in the log considered for interpolation..... 101

6.12 Coordinate transformations of a material point in a log..... 103

6.13 Pith orientation and transformation due to spiral grail, conical angle and pith orientation..... 105

6.14 Transformation due to conical angle, pith orientation..... 106

6.15 Dimensions of board and boundary conditions..... 108

6.16 Nodal displacements to determine bow, crook, cup and twist..... 110

6.17 Board numbers and locations with respect to global axes are indicated in the butt of the one half of the log..... 111

6.18 Board numbers and location with respect to global axes are indicated in the butt of the other half of the log..... 112

6.19 Comparison of shrinkage/swelling coefficients in the longitudinal direction of twenty boards from the first (1ST) and second (2ND) models, and experiments (EXP)..... 123

6.20 Comparison of shrinkage/swelling coefficients along the width of twenty boards from the first (1ST) and second (2ND) models, and experiments (EXP)..... 124

6.21 Comparison of shrinkage/swelling coefficients along the thickness of twenty boards from the first (1ST) and second (2ND) models, and experiments (EXP)..... 125

6.22 Comparison of bows of twenty boards from the first (1ST) and second (2ND) models, and experiments (EXP)..... 126

6.23 Comparison of crooks of twenty boards from the first (1ST) and second (2ND) models, and experiments (EXP)..... 127

6.24 Comparison of cups of twenty boards from the first (1ST) and second (2ND) models, and experiments (EXP)..... 128

6.25 Comparison of twists of twenty boards from the first (1ST) and second (2ND) models, and experiments (EXP)..... 129

Chapter 1

Introduction

1.1 Background

New Zealand has a total land area of 27.05 million hectares, of which an estimated 1.39 million hectares is planted in production forests. As stated by Lane (1995) *radiata pine* is the dominant species, constituting 90% of the planted area whereas other softwoods species cover only 3% of this area. In 1994 New Zealand used approximately 6.7 million cubic metres of wood products (Sutton (1995)). Sutton also stated that over 60% of the forestry products produced in New Zealand was exported in 1993. Gorman (1995) predicted that the global annual demand would increase from 3.43 to 5.07 billion cubic metres between 1991 and 2010, and thus New Zealand wood exports would increase by 75% in 2010. As stated in the latest available Forestry Handbook the New Zealand sawmill industries utilized 6.0 million cubic metres of logs and produced 2.7 million cubic metres of sawn board in 1994 (Ministry of Forestry (1995)).

Dimensional instability is one of the major impediments in the processing and use of wood for many applications as explained by Walker (1993c). Three aspects of dimensional instability are *shrinkage on drying*, *movement in service* and *responsiveness of wood* to a fluctuating environment. When a softwood board is seasoned, it shrinks as the moisture content decreases below the *fibre saturation point.* If a seasoned board is subjected to a change in the moisture content due to service conditions, it will shrink further if dried or expand on taking up moisture from the environment. The board exposed to moisture variations may also distort in the form of bow, cup, crook and twist as shown in Figure 1.1.

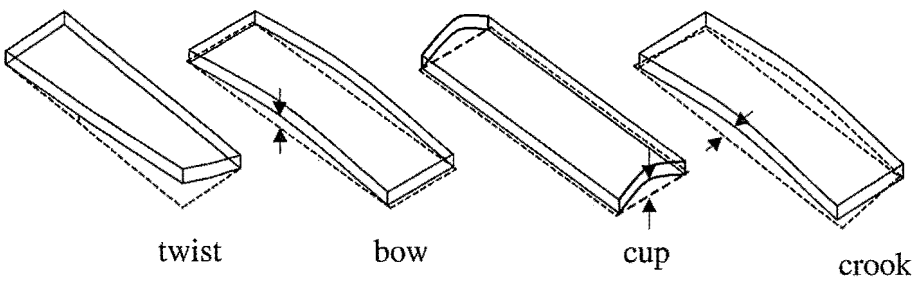

Figure 1.1 Board distortions

The magnitude of these dimensional changes varies with wood species and the location and orientation of the board in a log. Since the orientation of the board in relation to the log is an influencing factor, the shape stability in service is also dependent on the sawn pattern as illustrated in Figure 1.2.

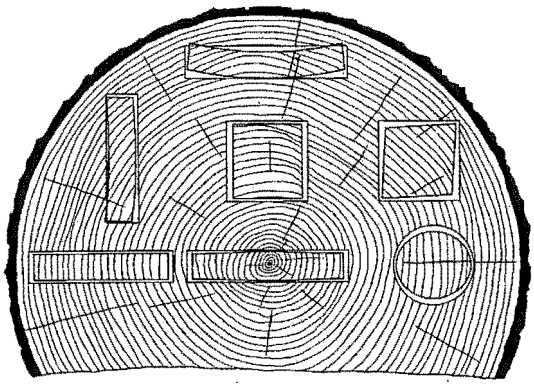

Figure 1.2. Change of shape of various x-sections and warping due to differential radial and tangential shrinkage – source: Tsoumis (1991)

The stiffness of wood is also a function of the moisture content when it is below the fibre saturation point with an increase in moisture content decreasing the stiffness and *vice versa* (Dinwoodie (1981)). The main factors, which determine the stiffness and dimensional stability of wood, are the microfibril angle, density and the spiral grain angle while other contributing factors are the orientation of the pith and the growth ring pattern.

1.2 Outline

During the seasoning process, unfavorable deformation of wood can be minimized by modern kiln drying techniques. The in-service dimensional instability of board is the major critical issue addressed in this research since it causes serious problems mainly in buildings and other engineering structures (Jackson and Ravindara (1996)). The shrinkage or swelling causes opening or tightening of joints, changes of cross-section and cracks in paint coatings. The warp deformations cause instability in building and engineering structures. When dimensional stability is critical as in these applications, it is necessary to understand the moisture dependent behaviour of the wood and predict the deformations from the available constitutive properties. These deformations can then be related to all the commonly used movement classifications.

The relationship between the microstructure of wood and the mechanical properties is complex and hence it is necessary to use computer simulations. The computer model can also be used to improve and optimize the sawing pattern in sawmills.

1.3 Aims and Scope

In this research the aim was to develop a suite of computer programmes to predict deformations due to small variations of moisture content for boards with no external load based upon the numerical modelling of the complex relationship that exists between the structure, and stiffness and shrinkage properties of wood. The outline of the numerical modelling can be seen in Figure 1.3. The results from the numerical simulation were subsequently validated experimentally using specimens prepared from a log obtained from a selected 20 years old *pinus radiata* tree in the Bottle Lake plantation forest.

An overview of the macro/ microstructure of wood and the factors affecting dimensional stability and stiffness in a softwood are presented in chapter two. This addresses the role of microfibril angle, density, spiral grain angle, growth ring pattern as well as pith orientation on the elastic properties and the distortion of the wood.

The fundamentals of continuum mechanics and finite element analysis used in the development of the subsequent models are presented in chapter three.

Chapter four describes the development of the initial numerical models used to define a composite behaviour by the implementation of the full cyclic constraint boundary condition in the development of the representative volume element to evaluate the overall equivalent homogenous modulus and compliance tensors based upon the assumption of an heterogeneous material with periodic microstructure. The model is validated by comparison with an analytical method and the variations in convergence for two test models.

The development of the cellular model used to generate the database that defines the moisture dependent behaviour in the board as a function of local density, microfibril angle and spiral grain angle is presented in chapter five. The resultant database was derived using constituent stiffness and shrinkage properties from numerical models

that were developed by others i.e. Harrington *et al* (1998) and Persson (2000) to data for each layer of the cell wall.

The development of an experimental method to determine the transverse shrinkage coefficients using direct measurement of changes in surface microstructure for small colonies of wood cells in specimens in which there are differing moisture contents is described in this chapter. The advantage of the method is that measurement is made for the differing moisture contents without any surface treatments or use of replicas. The resultant experimentally measured transverse shrinkage coefficients are compared with the predicted values.

The development of an initial board model based upon work carried out by Astley(1999) is reported in chapter six and the predicted results are compared with experimental results. In this model major assumptions were that: (a) the pith is a straight line and taken as the longitudinal axis, (b) the log is perfectly conical, (c) the properties vary linearly from pith to bark as well as from bottom to top. The experimental results were obtained from specimens prepared from a log of a selected 20 years old *pinus radiata* tree in the Bottle Lake plantation forest. The microfibril angle (MFA), spiral grain angle (SGA) and density of the specimens were measured by the SilviScan method at CSIRO, Australia. Larger scale measurements were made on boards of 50x100x1000 mm. The board dimensions were measured as the boards were dried slowly in the initial stage, and further measurements were subsequently made as their moisture content was increased. This was done with no load applied to the boards in a controlled environment. The changes of dimensions and weights of the boards with time were recorded. In a modified model, actual pith orientation and growth ring pattern were used to interpolate the properties for the analysis. Predicted board distortions from the both models methods are compared with the experimentally obtained results and the conclusions, limitation and further suggested work based upon the numerical modelling is presented in chapter seven in this thesis.

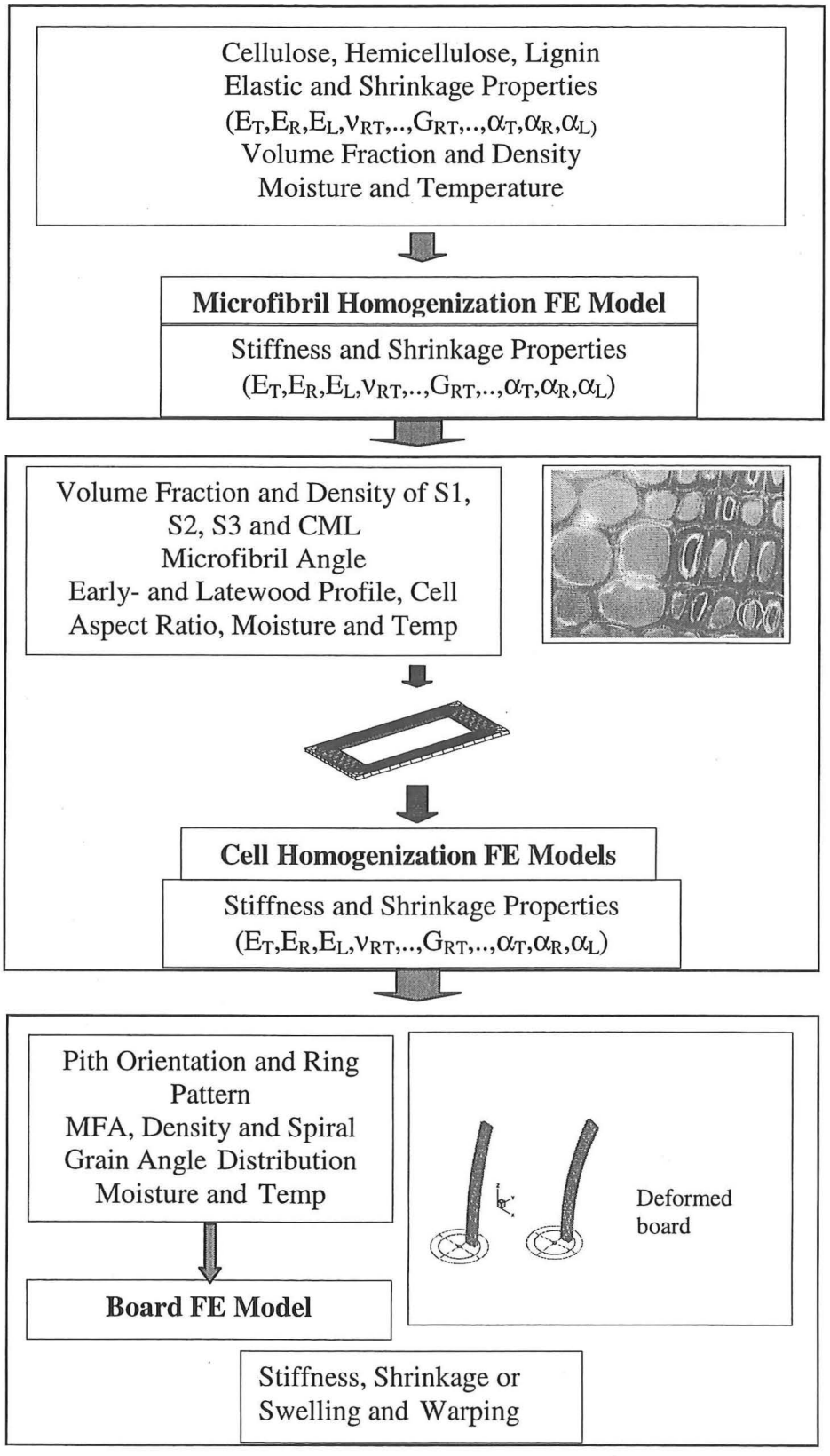

Figure 1.3 Modelling sequences

Chapter 2

Characteristics and Properties of Softwood

2.1 Introduction

To model the shrinkage and warping behaviours of softwood it is necessary to understand its structure and properties. Structural features of softwood can be recognized at three different levels: macroscopic, microscopic, and ultrastructural. The Figure 2.1 shows brief illustrations of the structures at the three different levels.

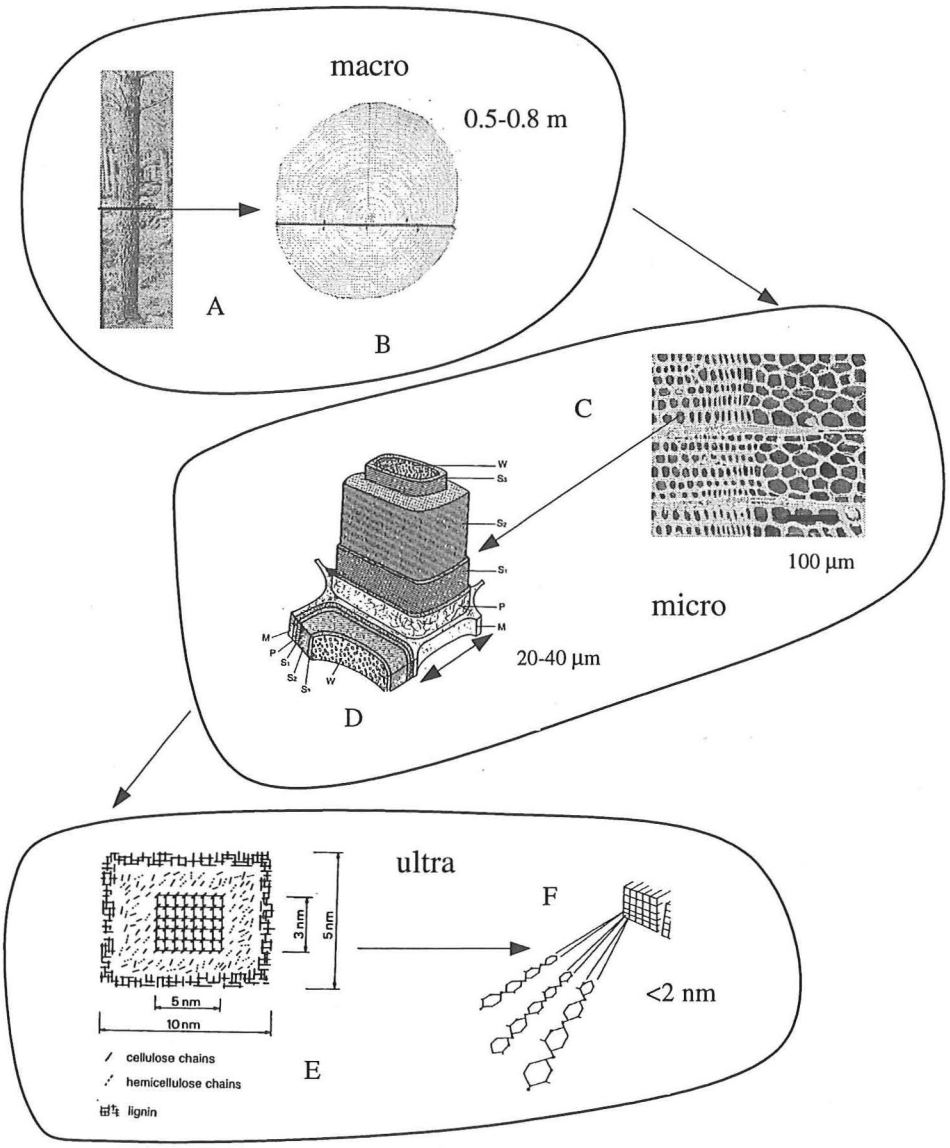

Figure 2.1 Structure of softwood at macro, micro, and ultra and molecular levels: (A) Photograph of *Pinus radiata* tree (source: Kininmonth and Whitehouse (1991)), (B) Cross section of stem, (C) Early- and latewood, (D) Cell wall layers (source: Tsoumis (1991)), (E) Microfibril (source: Dinwoodie (1981)) and (F) Cellulose molecules (source: Walker (1993a)).

Properties of wood vary not only from one tree to another of the same species but also within the same tree. Variation of properties can significantly influence dimensional stability. In this chapter, the structure and properties, and their relationship and variation are discussed.

2.2 Macrostructure

The part of the tree which is above ground level that supports the branches and leaves is called *stem* or *trunk*. The stem provides commercially viable sawn timbers. The stem has an outer covering called bark. Between the bark and the wood, a thin delicate tissue, known as the *cambium* produces wood cells on the inside and the bark cells on the outside. The enlargement in girth of the stem is brought about by the production of wood and bark tissues which in turn depend on the growth of the cambium.

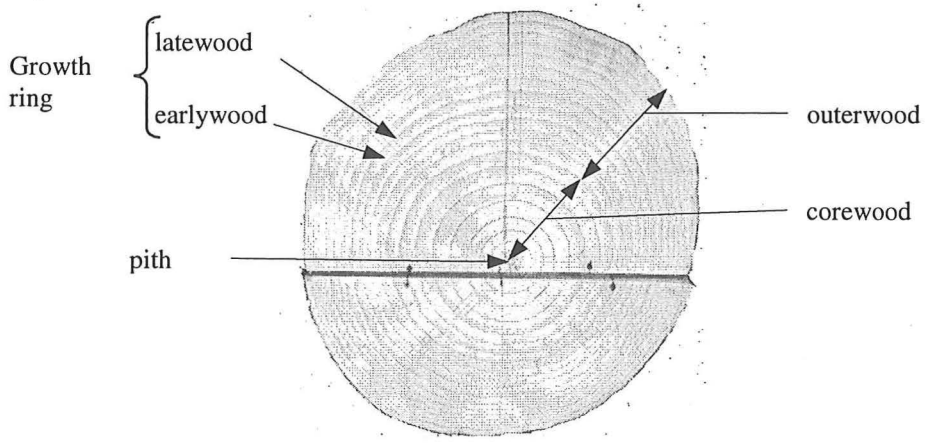

Figure 2.2 Cross-section of stem

The center part of the stem is known as *pith*. The area around the pith consists of *corewood* which is generally formed during the first few years along the entire length of a tree (Figure 2.2). The proportion of corewood increases from the butt to the top of the tree as explained by Walker and Butterfield (1995). The *outerwood* has properties that result in a greater commercial value than the corewood. The property variation in the corewood and outerwood will be discussed in the latter part of this chapter. The cross section of the stem (Figure 2.3) comprises two regions: the inner region, which has older cells that no longer participate in the biological processes of the tree is the *heartwood* while the outer region that has living cells is known as the *sapwood*. In softwood, the heartwood is generally darker than the sapwood. However, some

species exhibit no macroscopically apparent difference between heartwood and sapwood. The heartwood usually begins to form in species like *Pinus radiata* after approximately 15 years as described by Kininmonth and Whitehouse (1991).

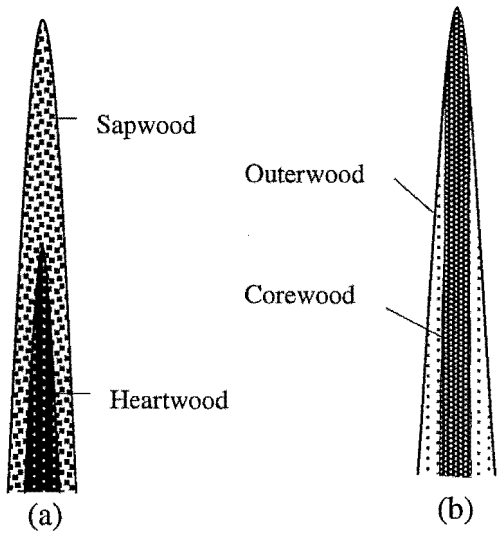

Figure 2.3 Growth characteristics

The other important characteristic of the cross-section of a stem is the *growth rings*. Each growth ring consists of two parts known as *earlywood* and *latewood*. The transition phase between the early- and latewood is sometimes known as *transitionwood*. The earlywood is formed during the spring and early summer and the latewood is formed during the summer. The latewood appears dark whereas the earlywood is light and thus the growth ring is visible.

2.3 Microstructure

Softwoods are mainly composed of long and narrow tube-like cells, with closed and pointed or blunt ends, called *tracheids* (see Figure 2.4). The tracheids are also known as *fibres* or *grains* and their main functions in the trunk are providing mechanical support and transporting fluids. The longitudinal axes of tracheids are generally parallel to the pith of the tree. A tracheid can be divided into three parts: *lumen*, *cell wall* and *middle lamella* (ML). The lumen is the cavity of the tracheid. The middle lamella is the bonding medium that bonds the cells to each other in the wood. The tracheids which are in earlywood, have large *lumens* (apertures) and thin walls to allow better conduction of fluids since they are formed during spring, whereas in latewood they have small lumens and thick walls as shown in Figure 2.4.

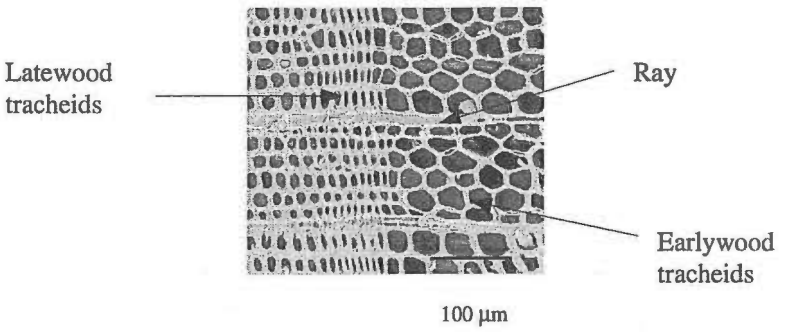

Figure 2.4 Microstructure of *pinus radiata*

The cell wall consists of the *secondary wall* and *primary wall* (PW) (see Figure 2.5). The secondary wall contains three major layers called the outer layer (S_1), the middle layer (S_2) and the inner layer (S_3). The volume fraction and the density of cell wall layers are the prime factors determining the strength and shrinkage properties of wood.

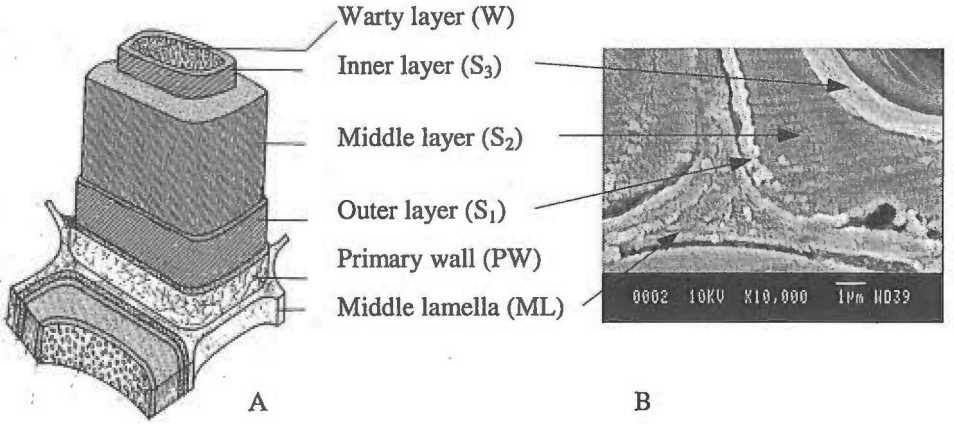

Figure 2.5 (A) Simplified structure of cell wall. (source: Tsoumis (1991)) (B) Cell wall layers of *pinus radiata* tracheid.

Softwoods possess *rays* that, in cross section, appear as very fine lines extending in the direction from pith to bark. Not all rays start from pith, some of them start within a growth ring, but once they have started, all of them continue toward the bark. Among the tracheids are a few small brick-like structures known as *parenchyma* cells that are mostly located in the wood rays and are responsible for the storage of nutrients for the wood. Other micro level features that can be found in the walls of tracheids and parenchyma cells are the *pits*. Figure 2.6 shows pits in the tracheids of *pinus radiata* which are generally found in radial walls of the earlywood tracheids. The function of pits is to permit the passage of mineral solutions and nutrients in both

longitudinal and horizontal planes. The existence of the pits reduces the strength of the tracheids.

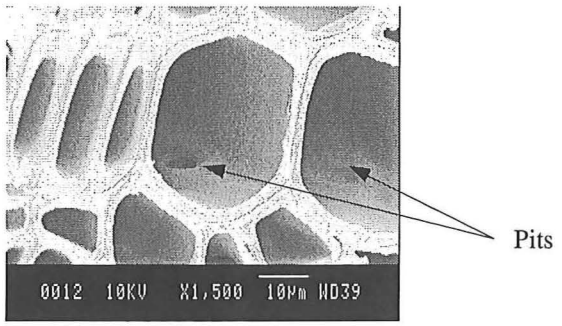

Figure 2.6. Pits in the tracheids of *pinus radiata*

Another distinctive feature of the transverse section of the wood is the appearance of *resin canals*. These consist of a central tube surrounded by the parenchyma cells. In a living tree the parenchyma cells secrete resin into these canals.

2.4 Ultrastructure and Molecular Structure

2.4.1 Chemical Constituents

Wood consists of organic chemical substances originally produced in living cells of a tree near its cambium. However the major portion of trees contains no living cells at the time of felling. The composition of wood substance by weight, given by Bodig *et al* (1982), is approximately 50% carbon, 6% hydrogen, 44% oxygen, and a nitrogen value of 0.1% or less. In addition to the above, 0.2-0.3% (by weight) of mineral elements such as calcium, potassium and magnesium are found in wood.

Carbon, hydrogen and oxygen combine to form the principal organic components of cell wall substances such as *cellulose*, *hemicelluloses* and *lignin*, and extraneous substances called *extractives*. The proportions of cellulose, hemicelluloses, lignin and extractives in softwoods are approximately 40-50%, 20-25%, 25-30% and 0-10% by weight respectively as given by Dinwoodie (1981), and their contents in the three layers are illustrated in Figure 2.7.

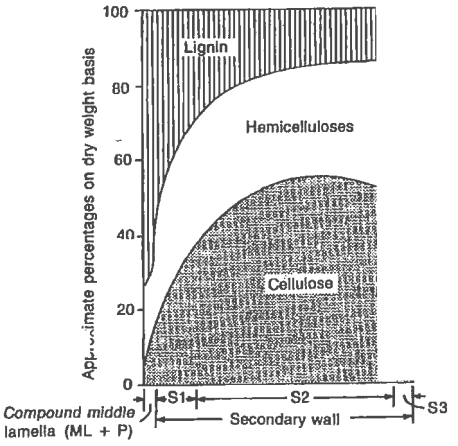

Figure 2.7 Distribution of the principal cell wall constituents within the wall of a softwood tracheid (source:Walker (1993a) after Panshin *et al*).

2.4.1.1 Cellulose

Cellulose is a linear polymer $(C_6H_{10}O_5)_n$ and formed by polymerization of glucose units ($C_6H_{10}O_6$). The number of glucose monomers in a cellulose molecule ranges from a few to as many as 15,000 (Bodig *et al* (1982)), depending on its location within the cell wall.

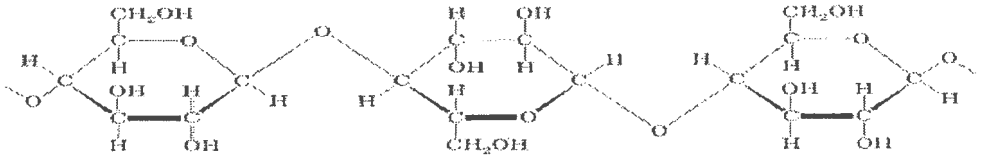

Figure 2.8 Structural formula of a cellulose molecule

2.4.1.2 Hemicelluloses

Hemicelluloses are composed of two carbohydrate polymers, a xylose- and mannose-containing polysaccharide (Bodig *et al* (1982)). In softwood, they are mostly mannose (a 6-carbon sugar like glucose) and some xylose (Tsoumis (1991)). The molecules of hemicelluloses are also chain like, as in cellulose, but both the degree of crystallization and polymerization are low, and the molecule contains less than 150 units.

2.4.1.3 Lignin

Lignin is a three-dimensional aromatic polymer with apparently no ordered arrangement. It is a phenolic polymer, differing from the carbohydrates in its ability to repel water. The deposition of lignin is variable in different parts of the cell wall, but its prime function is to protect the hydrophilic cellulose and hemicelluloses that are mechanically weak when wet. As explained by Dinwoodie (1981), since the lignin is located only on the exterior it is responsible for cementing together the fibrils and in imparting shear resistance in the transference of stress throughout the composite.

2.4.1.4 Extractives

Extractives are not part of the wood substance, but are deposited in cell lumina and cell walls. They are compounds of varying chemical composition, such as gums, fats, resins, sugars, oils, starches, alkaloids, and tannins (Tsoumis (1991)). Extractives have little or no direct effect on the mechanical properties of wood, however, they are responsible for increasing the specific gravity and lowering the equilibrium moisture content. They can also control durability, color and odor. The sapwood is usually considered extractive free; hence it is less durable than heartwood which generally has some extractives (Bodig *et al* (1982)).

2.4.2 Microfibril

The primary wall and each layer of the secondary wall consist of long thread-like structural units called *microfibrils* that can be seen readily with an electron microscope. The aggregates of microfibrils are called *macrofibrils* or *fibrillar structures* and are visible using optical microscopy. Each microfibril is composed of crystalline cellulose chains embedded in an amorphous matrix of hemicelluloses and lignin similar to glass fibres in the polymer matrix of a composite material. Two possible structural models of microfibril, as shown in Figure 2.9, were developed by Dinwoodie (1981) and Tsoumis (1991). According to the model in Figure 2.9B, the microfibrils are composed of small units called *elementary fibrils*, which have an average diameter of 3 nm and each contains 40 cellulose chains. Gaps of approximately 1 nm between these units are filled with hemicelluloses while hemicelluloses and lignin form the sheath. In the second model the crystalline core is considered to be about 5 nm x 3 nm containing about 48 chains.

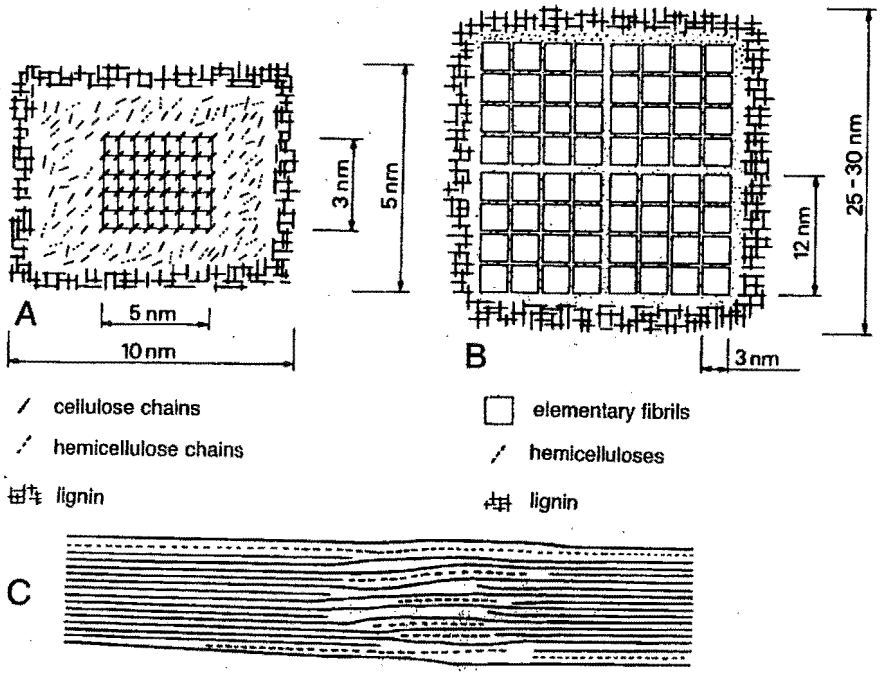

Figure 2.9 Models of the cross section of a microfibril (source: Tsoumis (1991)), (A) the core is homogeneous, (B) crystalline is divided into elementary fibrils, and (C) crystalline and amorphous regions in a fibril.

The cellulose chains are generally arranged lengthwise with regards to the microfibril axis, but are parallel to each other only in portions. In these portions, which are called *crystalline regions*, the molecular chains are strongly connected to each other by hydrogen bonds. The portions in which these molecules are somewhat disorganized in arrangement and not strongly connected are called *amorphous regions* (Tsoumis (1991)). The crystalline regions are followed by the amorphous regions as shown in Figure 2.9C. The relative quantities of crystalline and amorphous regions which is known as the *degree of crystallinity* is about 90-95% in softwood. As explained by Walker (1993a) the cellulose crystalline regions can be represented by unit cells. Each unit cell has a central chain and four chains at the cell corners, which are shared by four adjacent unit cells as illustrated in Figure 2.10. The unit cell therefore contains (1 + 4 x (1/4) = 2) two cellulose chains.

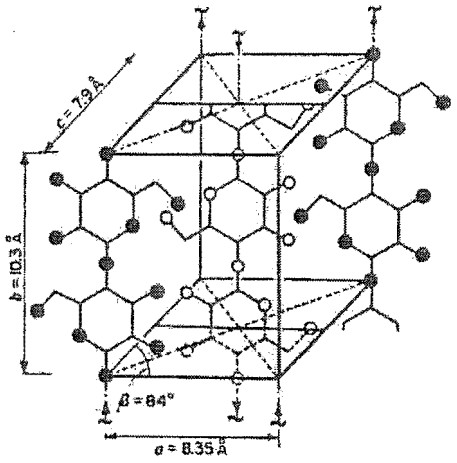

Figure 2.10. The cellulose unit cell (source: McGinnis *et al* (1991) after Meyer *et al*)

2.4.3 Orientation of Microfibrils and Cell Wall Layers

From Walker (1993a), the primary wall is thin (0.1-0.2 μm) and can be hard to distinguish from or isolate from the middle lamella. Some studies consider the two together (ML+PW) for analysis and relate results to the compound middle lamella (CML), a term which embraces both middle lamella and primary wall. The microfibrils are highly ordered and lie parallel to one another within the S_1, S_2 and S_3 layers, however they are at different orientations in each layer. In the thin S_1 layer (0.1-0.3 μm) the microfibrils are wound round the cell at an angle of between 50 and 75° to the cell axis. The S_1 wall itself comprises a number of thin concentric lamellae (Figure 2.11). Within each lamella the microfibrils are aligned very closely and the orientation between adjacent lamellae may differ slightly. The fibrils wound around the cell can be completely reversed, switching from the S to the Z helix orientation or vice versa. Both S and Z lamella are found in the S_1 layer. After a few lamellae of S_1 have been laid down the orientation of the microfibrils rapidly changes to that found in the S_2 layer. The microfibrils in the S_2 layer are densely packed and steeply inclined, making an angle of only 10 to 30° with the tracheid axis. There are a large number of lamellae in this layer ranging from 30 in earlywood to 150 in latewood. All are similarly orientated and wind around the cell in the Z direction. The S_2 layer is 1-2 μm thick in earlywood and 3-5 μm thick in latewood. In the thin S3 layer (0.1 μm) the orientation of the microfibrils changes again to an S helix with the microfibrils making an angle of 60 to 90° with tracheid axis. Therefore, the predominant

orientation of microfibrils across the secondary wall is S-Z-S in the S_1, S_2 and S_3 layers respectively.

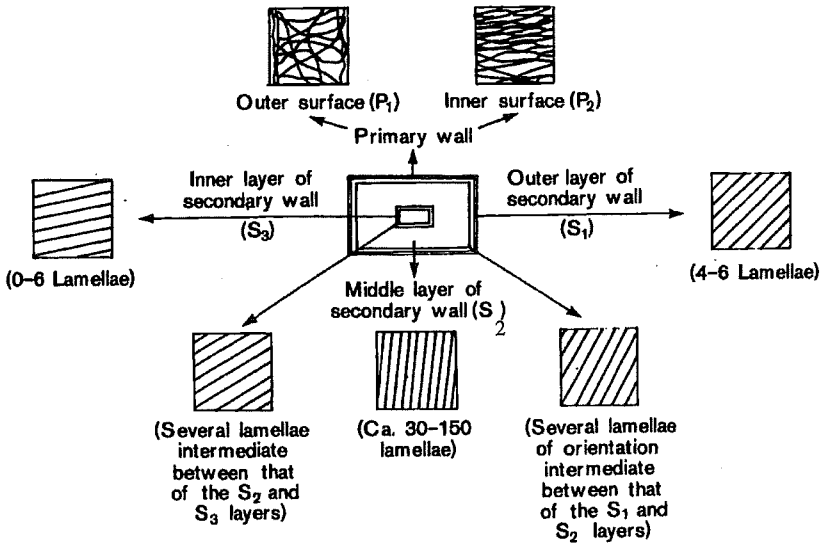

Figure 2.11 Structure of the cell wall of a tracheid and the orientation of microfibrils within each wall layers (source: Kininmonth and Whitehouse (1991)).

The angle of the helix is known as *microfibril angle* (MFA). Generally latewood microfibril angles are lower than earlywood microfibril angles for the same growth ring. The MFA decreases with ring number from the pith for earlywood as well as for latewood (Nicholls, 1986). As stated by Donaldson (1992), the MFA also decreases with the height of a tree from butt to top. Figure 2.12 shows the variation of average MFA of a log of *pinus radiata* from pith to bark in radial direction.

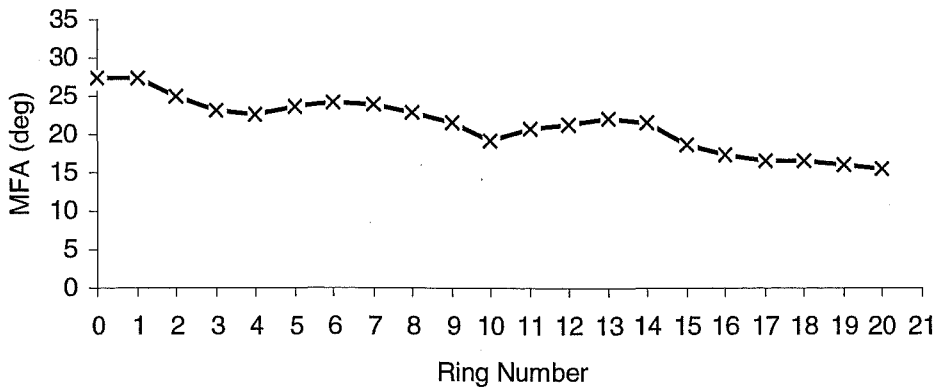

Figure 2.12. Variation of average MFA from pith in radial direction

As reported by Walker (1993b) the MFA has major effects on wood properties, especially stiffness since the S_2 layer is the thickest and is the major contributor to the mechanical properties of a tracheid (Mott *et al.*, (1996)). The stiffness of the cell wall increases from pith to cambium as the MFA decreases from 40° to 10°. Even though S_1 and S_3 are thin layers, their overall effects on the properties must be taken into consideration, however not much work has been conducted into understanding their contribution. Investigations made by Abe *et al.* (1991 and 1992) into the secondary cell walls of tracheids shows that the microfibril angles in the innermost S_3 vary among early wood tracheids, and range from approximately 30° in an S-helix to approximately 90°, although it has been generally accepted that the S_3 consists of microfibrils having a flat S-helix at 90° to the cell axis.

Several techniques are available to measure the MFA, and the merits of these techniques were discussed in a workshop held at Westport, New Zealand (Butterfield (1997)). The X-ray diffraction techniques are popular in the determination of the MFA. One of the techniques is known as the SilviScan method, which was developed by Evans (1994). It can estimate the MFA rapidly in samples cut from increment cores. The X-ray method involves irradiating a specimen that is mounted with its cell axes vertical. The determination of the MFA from the distribution of the intensity round the (002) diffraction circle commonly assumes an idealized structure in which all the cell walls were oriented precisely in either the radial or the transverse direction. The real cell structure diverges significantly from this ideal. The error involved in assuming the ideal structure has been assessed by Entwistle and Navaranjan (2001 and 2002) by making a quantitative image analysis of the length and orientations of the cell walls in a section of the specimen comparable in cross-section to that irradiated by the x-rays. From these studies it was demonstrated that the error is not more than one degree in the range of MFA 20-30°.

2.5 Density

Density is a measure of weight of wood substance in a unit volume. It is influenced by the presence of moisture in wood. Adsorption of moisture increases density and desorption results in a reduction. Density is therefore generally expressed in three different terms referring to moisture conditions. These three terms are *basic density*, *air-dry density* and *green density*. The basic density is calculated from the oven-dry

weight. The air-dry density is measured when wood has 12% moisture content which is the average equilibrium moisture content. The green density is determined on freshly felled timber. These three densities are given by:

$$\rho_b = \frac{w_o}{v_g}, \qquad \rho_a = \frac{w_a}{v_a} \qquad \text{and} \qquad \rho_g = \frac{w_g}{v_g} \tag{2.1}$$

where
ρ_b = basic density, ρ_a = air-dry density, ρ_g = green density
w_o = oven-dry weight, w_a = air-dry weight, w_g = green weight
v_o = oven-dry volume, v_a = air-dry volume, v_g = green volume

Density increases from earlywood to latewood within a growth ring in the radial direction as illustrated in Figure 2.13. The latewood has high density since it comprises tracheids with thick walls and small apertures.

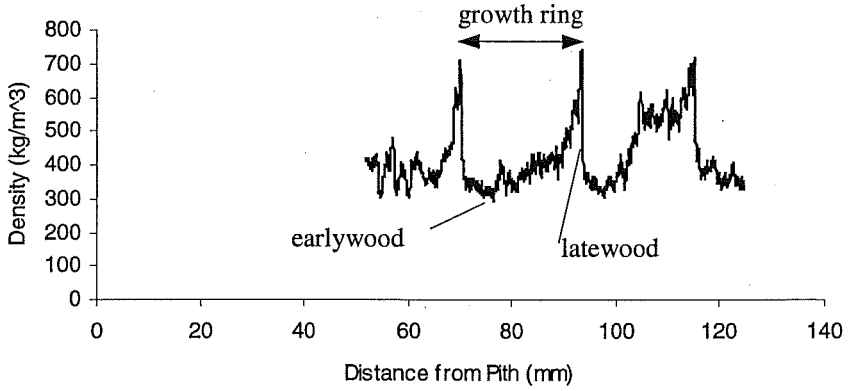

Figure 2.13. Density variation within growth ring in radial direction.

As stated by Cown and McConchie (1980), Kininmonth and Whitehouse (1991), and Tsoumis (1991), density varies in horizontal and vertical directions within a log. Near the pith, growth rings have a wide band of earlywood with a border of narrow latewood. Further from the pith, the proportion of the early wood band decreases, resulting in the average density increasing from the pith to bark in the radial direction as shown in Figure 2.14.

Cown and McConchie (1980) showed that the average density has a tendency to decreases with the height. This is because of the formation of heartwood at the base of a tree. The variation of density is also influenced by external factors such as wind and these external factors are beyond the scope this work.

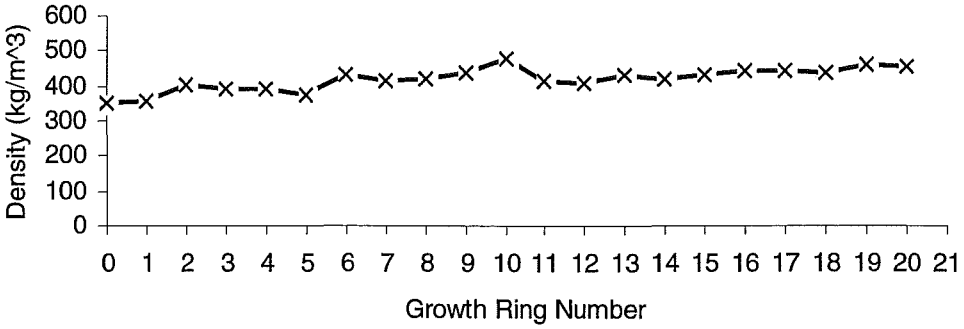

Figure 2.14. Average density variation from pith to bark in radial direction

2.6 Variation in Structure

The structure of wood varies within a tree. The variation can be related *as horizontal variations* - from pith to bark and *vertical variations* - from butt to top. The width of growth rings is not uniform. Structural variations within the trunk such as spiral grain, knots, pith alignment and conical effect of the trunk has a strong influence in the wood properties.

The properties of wood are related to the three principal directions of growth in a tree. In the Cartesian coordinate system, the two axes are taken in the radial direction (R) and tangential direction (T) to the growth ring, and the third axis is taken in the longitudinal direction (L) of the stem (see Figure 2.15).

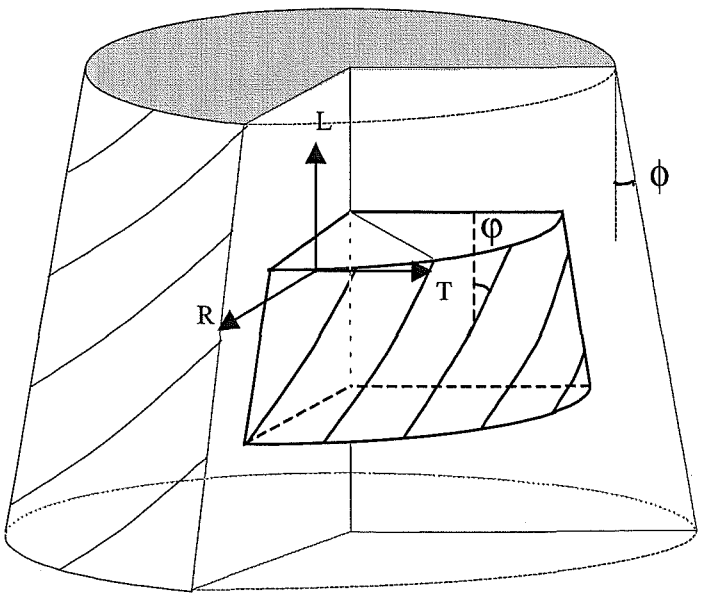

Figure 2.15. RTL is the coordinate systems of the stem. φ is the spiral grain angle and ϕ is the conical angle.

Spiral grain arises from the cells being oriented in a spiral rather than parallel to the pith. The angle at which the cells are lying with respect to the pith axis is called the *spiral grain angle* (SGA). Knots disturb the cell orientation and thus weaken the wood however their effects are neglected as this study considers only clear wood. The pith is usually straight but the trunk is slightly conical. The deviation of the trunk from the vertical axis is called *the conical angle*. On some occasions the pith of a tree is not straight although it is usually assumed to be straight. Figure 2.15 shows diagrammatically the spiral grain angle and conical angle.

According to Cown *et al* (1991b), as shown in Figure 2.16, the SGA is large near the pith and decreases with distance in radial direction from the pith. This Figure also shows that the SGA increases with height.

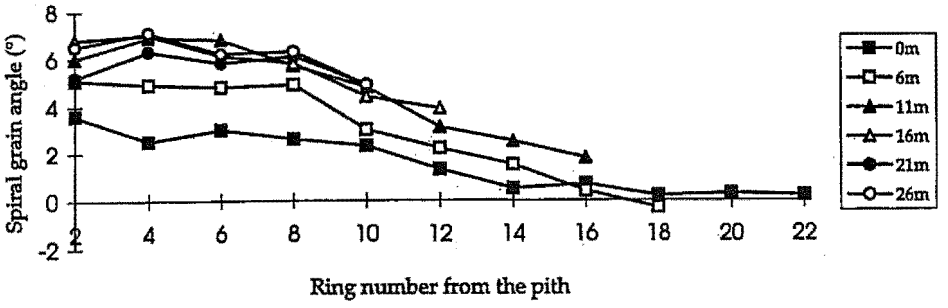

Figure 2.16. Variation of SGA in a *pinus radiata* log (souce: Cown *et al* (1991b)).

2.7 Hygroscopic Properties

Wood is a hygroscopic material. In an unstressed state it can undergo dimensional changes following variations in its moisture content and/or temperature. Changes of moisture content give rise to larger dimensional changes than do changes of temperature (Dinwoodie (1981)). The dimensional changes that occur when green wood is dried are known as *shrinkage*. Whereas if such changes taken place due to the changes in the relative humidity when the wood is at a low moisture content, it is called *movement*.

2.7.1 Moisture Content

Moisture content (MC) of wood is expressed in terms of its oven-dry weight and it is calculated from the loss in weight after oven drying at 102-105°C to approximately constant weight. It is defined by:

$$MC = \frac{W_{or} - W_o}{W_o} \times 100 \qquad (2.2)$$

where w_{or} is original weight, w_o is oven-dry weight and MC is moisture content in %

2.7.2 Moisture in Wood

Description of the role and location of water in wood is detailed elsewhere, for example Siau (1995), Walker (1993c), Dinwoodie (1981) and Tsoumis (1991). As an example, radiata pine is characterised by a wide sapwood zone and a newly felled tree has a high sapwood moisture content in the range of 120-180%. The heartwood moisture content averages about 45% as explained by Kininmonth and Whitehouse (1991). In this state the wood is referred to as *green*. For moisture contents from green to approximately 30%, the water is present both within the cell wall as *bound water* and as *free water* in cell cavities (cell lumina). The bound water is held due to strong attraction of water molecules to the hydroxyls of the non-crystalline cellulose. Formation of such bonds results in the cellulose chains being pushed apart in the amorphous and crystalline regions of the microfibrils. The rest of the wood constituents mainly lignin, and hemicelluloses also swell by taking up moisture. Due to these effects, wood cells swell when adsorbing moisture. After saturation of the cell wall, the water occupies cell cavities as free water without affecting the dimensions of wood.

When the wood is dried, the free water is removed easily without changing the properties and dimensions of the wood. Below 30%, a somewhat arbitrary value known as the *fibre saturation point*, water is present primarily within the cell wall as bound water. The removal of bound water usually takes place by liquid water diffusion across cell walls and by water vapor diffusion across void structures. The mechanism of water diffusion is beyond the scope of this project and is well described elsewhere Walker (1993c), Siau (1983) and Skaar (1988). The removal of bound water results in the microfibrils moving into a closer proximity, thereby increasing

inter-microfibrillar bonding. This process therefore causes the wood cells to shrink. In some wood species, an excessive shrinkage or collapse is displayed during drying. As explained by Cowin (1985), capillary tension forces in the water that completely fill the cell lumen cause this excessive shrinkage. These forces pull the cell walls into the lumen as the lumen water evaporates, and increases shrinkage. It can be then concluded that decreasing the moisture content below the fibre saturation point causes wood to shrink while increasing moisture above this point causes swelling.

2.7.3 Adsorption and Desorption

When structural wood is exposed to an atmosphere of constant temperature and relative humidity (RH) it will eventually reach a stable moisture content (Figure 2.17), referred to as the *equilibrium moisture content.* This moisture content for a particular atmospheric condition depends upon whether the wood is losing moisture to the atmosphere known as *desorption* or gaining moisture called *adsorption* from the atmosphere.

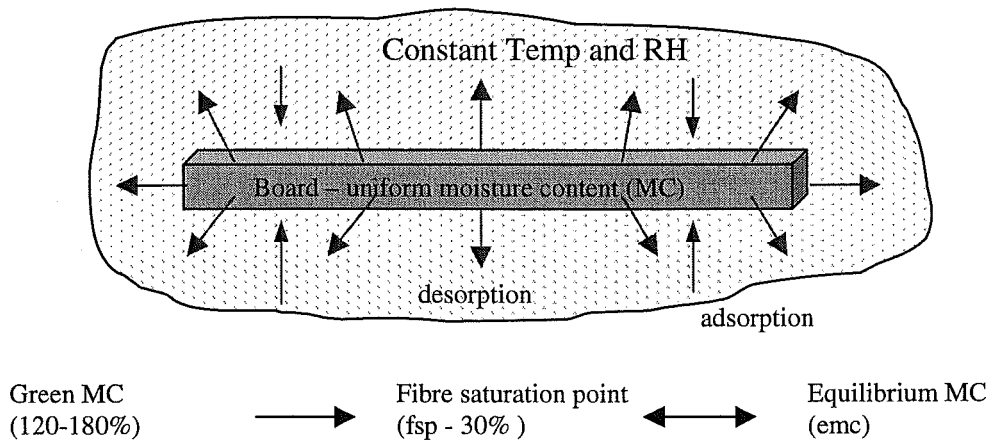

Figure 2.17. Natural drying of board

There is a difference in the equilibrium moisture content when the wood loses moisture, or adsorbs moisture after drying, or desorbs moisture, which has been previously adsorbed. Kininmonth and Whitehouse (1991) illustrated (Figure 2.18) that the equilibrium point is greater during desorption than during adsorption.

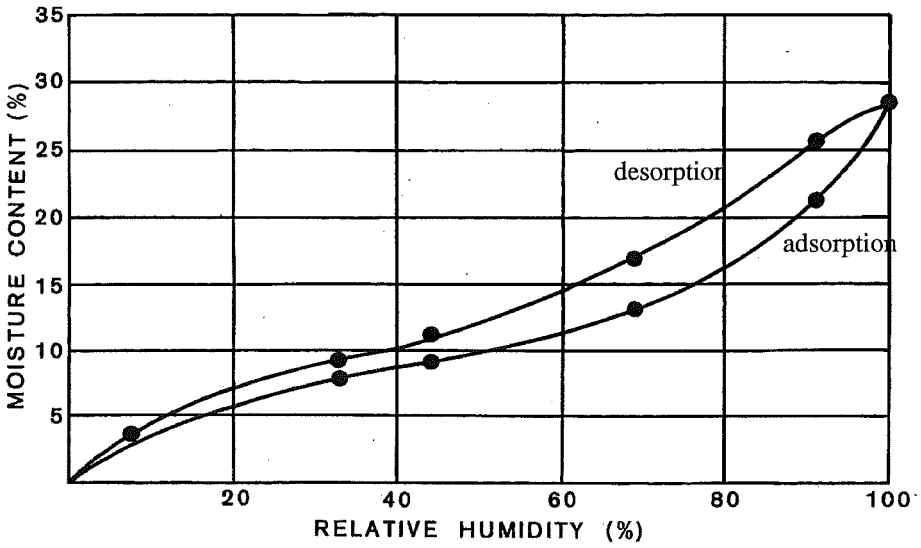

Figure 2.18. Adsorption and desorption of water by radiata pine sapwood at 15 °C (source: Kininmonth and Whitehouse (1991) – after Cunningham and Sprott)

This *hysteresis* phenomenon is a characteristic property of all cellulosic materials. In a large structural wood member, where conditions are not controlled reaching equilibrium is difficult, and desorption and adsorption takes place simultaneously. The magnitude of hysteresis may be expressed by the ratio of adsorption to desorption equilibrium moisture contents at the same relative humidity. The ratio is generally constant, with an average of approximately 0.8 according to Tsoumis (1991).

2.7.4 Wood in Service

The equilibrium moisture content of wood in service keeps on changing from day to night, from wet weather to dry, and from season to season as the atmospheric conditions change, and these changes are accompanied by shrinkage or swelling of the wood. The prevailing moisture contents of *pinus radiata* in January and July for 14 cities in New Zealand are listed by Kininmonth and Whitehouse (1991), and Christchurch has 12.3 and 19.3% respectively. Radiata pine exposed outside under cover in the main population centres has an annual mean value of 14-16% moisture content with considerable variation between summer and winter.

2.7.5 Shrinkage and Swelling

Shrinkage is the reduction, and swelling is the increase of the dimensions due to the fluctuation of moisture in wood below fibre saturation point. The percentages of volumetric and dimensional shrinkage are determined from the equations:

$$V_{sa} = \frac{v_g - v_a}{v_g} \times 100 \qquad V_{so} = \frac{v_g - v_o}{v_g} \times 100 \qquad (2.3)$$

$$D_{sa} = \frac{D_g - D_a}{D_g} \times 100 \qquad D_{so} = \frac{D_g - D_o}{D_g} \times 100 \qquad (2.4)$$

where

V_{sa} - volumetric shrinkage to air-dry, V_{so} - volumetric shrinkage to oven-dry

D_{sa} - dimensional shrinkage to air-dry, D_{so} - dimensional shrinkage to oven-dry

v_g - green volume, v_a - air-dry volume, v_o - oven-dry volume

D_g - green dimension, D_a - air-dry dimension, D_o - oven-dry dimension

The dimensional changes are expressed in the *i* (i = R, T, L) direction of wood as shown in Figure 2.15.

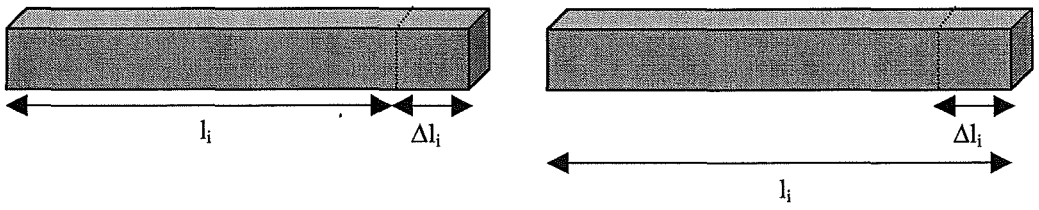

Figure 2.19 Hygroscopic expansion or contraction in the *i* direction.

The *shrinkage/swelling coefficient* (α_i) and the linear moisture-induced strain (ε_i) in the direction *i* is given by

$$\Delta l_i = l_i \alpha_i \Delta w \quad \text{and} \quad \varepsilon_i = \frac{\Delta l_i}{l_i} = \alpha_i \Delta w \qquad (i = T, R, L) \qquad (2.5)$$

respectively

where δl_i is the change in length due to contraction/expansion, l_i is the original length, and Δw is the change of moisture content in percentage. Hence, the linear orthotropic moisture-induced strain (ε_s) is defined by

$$\varepsilon_s = \begin{pmatrix} \alpha_T \\ \alpha_R \\ \alpha_L \\ 0 \\ 0 \\ 0 \end{pmatrix} \Delta w \qquad (2.6)$$

Density, moisture content, structure of wood, and presence of extractives and compression wood affect the magnitudes of shrinkage and swelling coefficients. Wood of high density has thick cell walls and therefore has more moisture in the cell walls resulting in high magnitudes of shrinkage and swelling. Density also affects the *coefficient of anisotropy of shrinkage or swelling* (ratio of tangential to radial shrinkage or swelling). The coefficient becomes smaller with increasing density. As explained by Walker (1993c) the removal of extractives increases shrinkage. Compression wood has high longitudinal shrinkage when compared to normal wood since it has thicker tracheids and a higher MFA. The structure of wood plays a major role in anisotropic shrinkage and swelling.

2.7.6 Anisotropic Shrinkage and Swelling

The shrinkage coefficients are different in the three principal directions. Dinwoodie (1981) explained that longitudinal shrinkage is an order of magnitude less than the transverse, while in the transverse plane radial shrinkage is usually 60-70% of the corresponding tangential shrinkage. He further stated that the anisotropy ratio between transverse and longitudinal shrinkage amounting to approximately 40:1 was due in part to the arrangement of cells in wood and in part to the particular orientation of the microfibrils in the cell wall layers.

As explained previously in this chapter microfibrils are approximately parallel to the tracheid length in the S_2 layer and approximately perpendicular to the tracheid length in the S_1 and S_3 layers. The S_2 layer tends to shrink with decreasing moisture in proportion to the number of microfibrils present whereas S1 and S3 layers restrain

this effect due to the differing orientation of their microfibrils. The small longitudinal shrinkage is the result of the orientation of microfibrils in the S_2 layer. A larger deviation of microfibrils in the S_2 layer contributes to a higher longitudinal shrinkage. Further details on the effects of cell wall structure on the anisotropy of shrinkage has been reviewed elsewhere Barber and Meylan (1964), and Walker (1993c). Meylan (1972) and Megraw *et al.* (1998) showed that the longitudinal shrinkage is independent of fibril angle up to MFA values of approximately 25°, and increases sharply after 40°. According to Meylan, although transverse shrinkage tended to decrease with increasing MFA, the scatter was much greater than that observed for the longitudinal shrinkage. Meylan thought that this was due to both differences in cell geometry and to the restraining effect of the outer layers in the cell wall.

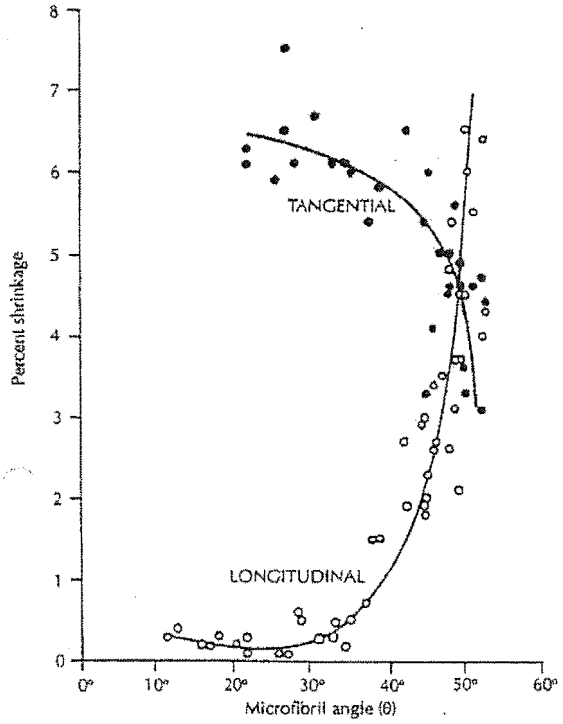

Figure 2.20. Variation of longitudinal and transverse shrinkage with MFA (from Walker and Butterfield – NZ Forestry, Nov 1995, 34-40)

The investigation made by Megraw *et al.* (1998) showed that there are very strong positional variations in the longitudinal shrinkage. Values were found to be higher near to the butt of the tree than even a few meters up the stem. The longitudinal shrinkage was also found to decrease with increasing ring number from pith at the

butt of the tree. The significant effect of longitudinal shrinkage is that the larger the shrinkage, the greater the possibility of warping.

According to Boutelje (1962) and Kifetew (1997) the transverse shrinkage anisotropy is mainly based on the following factors.

- *Difference between the fibril angles in radial and tangential walls*; The MFA of the middle secondary cell wall layer of radial walls is greater than that of the tangential walls. Moreover the average microfibril orientation around the pits on the radial walls is higher than in the tangential walls. This might reduce the radial shrinkage. However this effect on the transverse shrinkage is small.
- *Difference in lignin content of the radial and tangential walls*; Lignin content is higher in the radial walls than in the tangential walls of latewood. In fact the radial middle lamella is thicker than the tangential middle lamella. Therefore the radial middle lamella is the major cause for transverse shrinkage.
- *The effects of rays*; both authors concluded that rays are not an important cause of transverse shrinkage anisotropy in softwood.
- *The interaction between earlywood and latewood*; the differential transverse shrinkage is caused by the alternation of early- and latewood increments within the annual rings.

Differential shrinkage and swelling also depends upon the spiral grain, the sawing pattern, and the shrinkage properties of the species.

2.7.7 Significance of Shrinkage and Swelling

Shrinkage and swelling cause defects that reduce the commercial value of normal wood. The most common defects, encountered in the structural applications of the wood, are the opening or tightening of joints, change of cross-sectional shape, warping, and loosened or raised grains. The opening or tightening of joints is caused by the dimensional variations. The change of cross-sectional shape and warping are a function of the anisotropy of shrinkage, and are caused by differences in moisture distribution in log and sawing pattern as shown in Figure 1.2. The types of warping are bow, crook, cup and twist as shown in Figure 1.1.

2.8 Stiffness Properties

Throughout history wood has proved to be a popular structural material that can withstand loading even under severe weather conditions for many years. Wood is generally regarded in solid mechanics as a porous and orthotropic linearly elastic material. The properties differ with respect to three orthogonal planes of symmetry and show linear elastic behaviour below the limit of proportionality. Its constitutive properties can be related by the Hooke's generalised law as described by Lai *et al* (1993) for an orthotropic elastic material. By taking T, R and L, as defined in Figure 2.15, as the three principal directions of wood; the constitutive equation in matrix the form is given by

$$\begin{bmatrix} \varepsilon_{TT} \\ \varepsilon_{RR} \\ \varepsilon_{LL} \\ \gamma_{TR} \\ \gamma_{TL} \\ \gamma_{RL} \end{bmatrix} = \begin{bmatrix} \frac{1}{E_T} & -\frac{\nu_{RT}}{E_R} & -\frac{\nu_{LT}}{E_L} & 0 & 0 & 0 \\ -\frac{\nu_{TR}}{E_T} & \frac{1}{E_R} & -\frac{\nu_{LR}}{E_L} & 0 & 0 & 0 \\ -\frac{\nu_{TL}}{E_T} & -\frac{\nu_{RL}}{E_R} & \frac{1}{E_L} & 0 & 0 & 0 \\ 0 & 0 & 0 & \frac{1}{G_{TR}} & 0 & 0 \\ 0 & 0 & 0 & 0 & \frac{1}{G_{TL}} & 0 \\ 0 & 0 & 0 & 0 & 0 & \frac{1}{G_{RL}} \end{bmatrix} \begin{bmatrix} \sigma_{TT} \\ \sigma_{RR} \\ \sigma_{LL} \\ \tau_{TR} \\ \tau_{TL} \\ \tau_{RL} \end{bmatrix} \tag{2.7}$$

and in the simplified vector form as

$$\boldsymbol{\varepsilon}^* = \mathbf{C}^* \boldsymbol{\sigma}^* \tag{2.8}$$

or in the inverse form as

$$\boldsymbol{\sigma}^* = \mathbf{D}^* \boldsymbol{\varepsilon}^*, \qquad \mathbf{D}^* = \mathbf{C}^{*-1} \tag{2.9}$$

where $\boldsymbol{\sigma}^*$ is the stress vector, $\boldsymbol{\varepsilon}^*$ is the strain vector, $\mathbf{C}^*$ is the compliance matrix and $\mathbf{D}^*$ is the stiffness matrix.

Since the material is linear elastic, the compliance matrix $\mathbf{C}^*$ is symmetric and hence

$$\frac{\nu_{RT}}{E_R} = \frac{\nu_{TR}}{E_T}, \quad \frac{\nu_{LT}}{E_L} = \frac{\nu_{TL}}{E_T}, \quad \frac{\nu_{LR}}{E_L} = \frac{\nu_{RL}}{E_R} \tag{2.10}$$

The matrix $\mathbf{C}^*$ has nine independent constants specified as follows:

E_T, E_R and E_L are the moduli of elasticity in T, R and L directions respectively.
G_{TR}, G_{TL} and G_{RL} are the shear moduli in the planes of T-R, T-L and R-L respectively.
ν_{RT}, ν_{LT} and ν_{LR} are three Poisson's ratios and ν_{TR}, ν_{TL} and ν_{RL} are dependent Poisson's ratios, where the first suffix indicates the direction of the load and the second suffix denotes the direction of strain.

2.8.1 Factors Affecting Stiffness Parameters

The modulus of elasticity is generally greater in the longitudinal direction than in the transverse direction, because the tracheids are oriented approximately along the stem. In the transverse plane, the stiffness is higher in the radial direction than in the tangential direction. This is a function of the differing cells structure in these directions, the aspect ratio of the cells and the reinforcing effect of rays. The stiffness parameters are also influenced by properties of the wood and the environmental conditions. **Density** is a significant property since it depends upon the cell wall thickness. Increasing cell wall thickness will increase density and consequently increase the stiffness of the wood. **Moisture** affects the stiffness when it changes below fibre saturation point. When moisture content decreases the stiffness increases and *vice versa*. As explained previously, when moisture is reduced, microfibrils come closer together and the attractive forces between cellulose molecules become stronger, and thus stiffness increases. Another property is grain angle due to **spiral grain**, the conical shape of log and the variability of structure that can cause the deviation of the principal axes from the global axes. In mathematical calculation of the stiffness parameters, the parameters are subjected to transformation by suitable rotation of the axes. The theory of rotation will be dealt in the next chapter. The **MFA** also has a

significant effect on stiffness parameters, for example increasing MFA results in decreasing longitudinal modulus. The significant of MFA will be considered in detail in latter chapters.

Chapter 3

Mechanics of Continuum and Finite Element Theory

3.1 Introduction

In this chapter, the necessary theory and equations of continuum mechanics and the finite element method are presented. These relationships are the basis of the homogenization and modelling of the moisture-induced behaviour of softwood in the subsequent chapters.

3.2 Continuum Mechanics

3.2.1 Continuum Equations

The generalized continuum mechanics equations given below provide a basis for the finite element method and the homogenisation procedure. If a linear elastic continuum has domain V and boundary S as shown Figure 3.1,

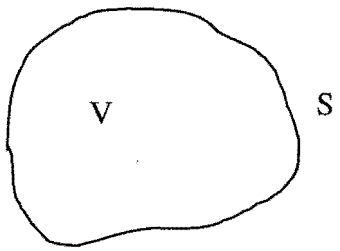

Figure 3.1. Elastic body with volume V and boundary S

as explained by Malvern (1969), Lai *et al* (1993), and Chen and Saleeb (1994), the equilibrium stress equations for the three-dimensional stress state with reference to a global coordinate system are given by

$$\nabla^T \boldsymbol{\sigma} + \mathbf{b} = \mathbf{0} \quad \text{in V} \tag{3.1}$$

and

$$\mathbf{n}\boldsymbol{\sigma} = \hat{\mathbf{t}} \qquad \text{at S} \tag{3.2}$$

where ∇ is a matrix differential operator, $\boldsymbol{\sigma}$ is a stress vector, $\mathbf{b}$ is the body force vector, $\hat{\mathbf{t}}$ is the surface traction acting on the boundary S, and $\mathbf{n}$ is the outward unit vector normal to the boundary S. These parameters are given by

$$\nabla = \begin{bmatrix} \frac{\partial}{\partial x} & 0 & 0 \\ 0 & \frac{\partial}{\partial y} & 0 \\ 0 & 0 & \frac{\partial}{\partial z} \\ \frac{\partial}{\partial y} & \frac{\partial}{\partial x} & 0 \\ \frac{\partial}{\partial z} & 0 & \frac{\partial}{\partial x} \\ 0 & \frac{\partial}{\partial z} & \frac{\partial}{\partial y} \end{bmatrix}, \tag{3.3}$$

$$\boldsymbol{\sigma} = \begin{bmatrix} \sigma_{xx} \\ \sigma_{yy} \\ \sigma_{zz} \\ \tau_{xy} \\ \tau_{xz} \\ \tau_{yz} \end{bmatrix}, \tag{3.4}$$

$$\mathbf{b} = \begin{bmatrix} b_x \\ b_y \\ b_z \end{bmatrix}, \tag{3.5}$$

$$\mathbf{t} = \begin{bmatrix} t_x \\ t_y \\ t_z \end{bmatrix} \tag{3.6}$$

and

$$\mathbf{n} = \begin{bmatrix} n_x & 0 & 0 & n_y & n_z & 0 \\ 0 & n_y & 0 & n_x & 0 & n_z \\ 0 & 0 & n_z & 0 & n_x & n_y \end{bmatrix} \tag{3.7}$$

If the change in position of a point in the continuum is defined by the Cartesian displacement field u, v and w in the x, y and z directions respectively, the six strain components are given by

$$\boldsymbol{\varepsilon} = \nabla \mathbf{u} \tag{3.8}$$

where

$$\boldsymbol{\varepsilon} = \begin{bmatrix} \varepsilon_{xx} \\ \varepsilon_{yy} \\ \varepsilon_{zz} \\ \gamma_{xy} \\ \gamma_{xz} \\ \gamma_{yz} \end{bmatrix} \tag{3.9}$$

and

$$\mathbf{u} = \begin{bmatrix} u \\ v \\ w \end{bmatrix} \tag{3.10}$$

3.2.2 Orthotropic Heterogeneous Material

If there are two orthogonal planes of symmetry with respect to material properties, symmetry will exist relative to a third mutually orthogonal plane. This material is referred to as being orthotropic. A material is described as being heterogeneous if its properties vary from point to point or are dependent on location.

The classical elastic constitutive equations, often called the generalized Hooke's law, express the linear elastic stress-strain relation for an orthotropic heterogeneous material, and are given by

$$\boldsymbol{\sigma} = \mathbf{D}(\mathbf{x})\boldsymbol{\varepsilon} \tag{3.11}$$

If the material is subjected to temperature changes, equation (3.11) can be rewritten as

$$\boldsymbol{\sigma} = \mathbf{D}(\mathbf{x})(\boldsymbol{\varepsilon} - \boldsymbol{\varepsilon}_T) \tag{3.12}$$

while the thermal induced strain is given by

$$\boldsymbol{\varepsilon}_T = \boldsymbol{\alpha}_T(\mathbf{x})\ \Delta T \tag{3.13}$$

where ΔT is the change of temperature

If the material is wood, as explained in chapter two it has greater sensitive to moisture changes when compared with temperature changes, a moisture induced strain (hygroexpansion strain or shrinkage strain) ε_s has greater significance and replaces ε_T in the equation (3.12).

ε_s is given by

$$\varepsilon_s = \alpha_s(\mathbf{x})\ \Delta w \tag{3.14}$$

where Δw is the change of moisture content in percentage.

"Note that moisture and thermal effects are equivalent and interchangeable in the derivation and application of the relationships."

Since the material is heterogeneous, the stiffness matrix $\mathbf{D}(\mathbf{x})$ and the vector of thermal expansion coefficients $\alpha_T(\mathbf{x})$ vary with the spatial coordinates $\mathbf{x}$. $\mathbf{D}(\mathbf{x})$ is a symmetric matrix and its components can be expressed in terms of three elastic moduli, three shear moduli and six Poisson ratios. Where cavities occur in the structure both $\mathbf{D}(\mathbf{x})$ and $\alpha_T(\mathbf{x})$ take a zero value.

If an equivalent homogeneous material is substituted for the orthotropic heterogeneous material, then the equivalent stiffness matrix $\mathbf{D}'$ and thermal expansion coefficients α' will be constant over the material space and the equivalent stress and strain will be related by the equations

$$\boldsymbol{\sigma}' = \mathbf{D}'(\boldsymbol{\varepsilon}' - \boldsymbol{\varepsilon}'_T) \tag{3.15}$$

and

$$\boldsymbol{\varepsilon}'_T = \alpha' \Delta T \tag{3.16}$$

Inverting equation (3.15) gives

$$(\boldsymbol{\varepsilon}' - \boldsymbol{\varepsilon}'_T) = \mathbf{C}'\boldsymbol{\sigma}', \text{ and } \mathbf{C}' = \mathbf{D}'^{-1} \tag{3.17}$$

where $\mathbf{C}'$ is the equivalent compliance matrix and α' is the vector of equivalent thermal expansion coefficients (or shrinkage coefficients) of the homogeneous solid, and they are given accordance to global coordinate system (x, y, z) by

$$\mathbf{C}' = \begin{bmatrix} \frac{1}{E_x} & -\frac{\nu_{yx}}{E_y} & -\frac{\nu_{zx}}{E_z} & 0 & 0 & 0 \\ -\frac{\nu_{xy}}{E_x} & \frac{1}{E_y} & -\frac{\nu_{zy}}{E_z} & 0 & 0 & 0 \\ -\frac{\nu_{xz}}{E_x} & -\frac{\nu_{yz}}{E_y} & \frac{1}{E_z} & 0 & 0 & 0 \\ 0 & 0 & 0 & \frac{1}{G_{xy}} & 0 & 0 \\ 0 & 0 & 0 & 0 & \frac{1}{G_{xz}} & 0 \\ 0 & 0 & 0 & 0 & 0 & \frac{1}{G_{yz}} \end{bmatrix} \tag{3.18}$$

and

$$\boldsymbol{\alpha}' = \begin{bmatrix} \alpha'_x \\ \alpha'_y \\ \alpha'_z \\ 0 \\ 0 \\ 0 \end{bmatrix} \tag{3.19}$$

where

E_x, E_y, E_z = Young's moduli in the directions x, y and z respectively

G_{xy}, G_{xz}, G_{yz} = Shear moduli for planes that are parallel to the coordinate planes x-y, x-z and y-z respectively

ν_{ij} $(i,j=x,y,z)$ = Poisson's ratio which characterizes the compressive strain in the j direction produced by a tensile stress in the i direction

α'_x, α'_y, α'_z = thermal expansion coefficients in the directions x, y and z respectively

To comply with the requirements of symmetry,

$$E_x\nu_{yx}=E_y\nu_{xy},\ E_z\nu_{xz}=E_x\nu_{zx} \text{ and } E_z\nu_{yz}=E_y\nu_{zy}$$

3.2.3 Transformation of Constitutive Properties

The principal material axes at a local point of an orthotropic heterogeneous continuum do not necessarily coincide with the global coordinate system. The transformation of

material properties from local axes to global axes can be obtained by one or more of the three principal rotations about the x, y and z axes as illustrated in Figure 3.2 (Hughes (1986)).

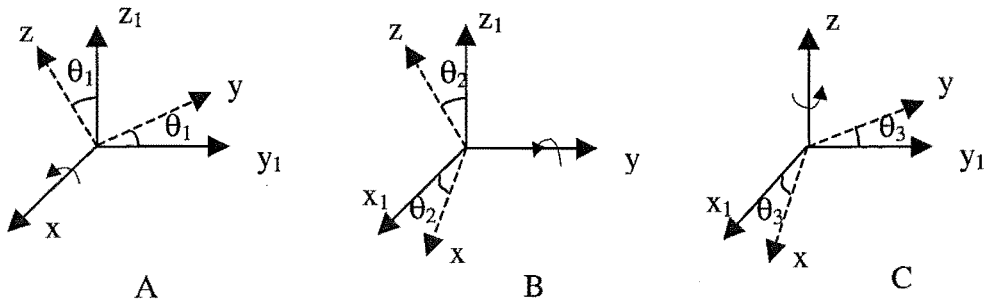

Figure 3.2. Three principal rotations

The unit vectors of the axes in the case (A) can be related by the equation

$$\begin{bmatrix} \mathbf{x} \\ \mathbf{y} \\ \mathbf{z} \end{bmatrix} = \begin{bmatrix} 1 & 0 & 0 \\ 0 & \cos\theta_1 & \sin\theta_1 \\ 0 & -\sin\theta_1 & \cos\theta_1 \end{bmatrix} \begin{bmatrix} \mathbf{x}_1 \\ \mathbf{y}_1 \\ \mathbf{z}_1 \end{bmatrix} \tag{3.20}$$

where $\mathbf{M}_1 = \begin{bmatrix} 1 & 0 & 0 \\ 0 & \cos\theta_1 & \sin\theta_1 \\ 0 & -\sin\theta_1 & \cos\theta_1 \end{bmatrix}$ is the matrix of direction cosines between the respective axes

Similarly the matrices of direction cosines for rotation about y and z axes are given by

$$\mathbf{M}_2 = \begin{bmatrix} \cos\theta_2 & 0 & -\sin\theta_2 \\ 0 & 1 & 0 \\ \sin\theta_2 & 0 & \cos\theta_2 \end{bmatrix} \tag{3.21}$$

and

$$\mathbf{M}_3 = \begin{bmatrix} \cos\theta_3 & \sin\theta_3 & 0 \\ -\sin\theta_3 & \cos\theta_3 & 0 \\ 0 & 0 & 1 \end{bmatrix} \tag{3.22}$$

respectively

If the rotations take place according to the sequence given above, the direction cosines matrices can be combined into

$$\mathbf{M} = \mathbf{M}_1\,\mathbf{M}_2\,\mathbf{M}_3 \tag{3.23}$$

or

$$\mathbf{M} = \begin{bmatrix} c_2c_3 & c_2s_3 & -s_2 \\ -c_1s_3 + s_1s_2c_3 & c_1c_3 + s_1s_2s_3 & s_1c_2 \\ s_1s_3 + c_1s_2c_3 & -s_1c_3 + c_1s_2s_3 & c_1c_2 \end{bmatrix} \tag{3.24}$$

where $c_i = \cos\theta_i$ and $s_i = \sin\theta_i$ ($i = 1, 2, 3$)

Suppose the unit vectors **t**, **r** and **l** of the local (T R L) coordinate system are transformed to the unit vectors **x**, **y** and **z** of the global (x y z) coordinate system, as illustrated in Figure 3.3, the relationship between two systems of axes is given by

$$\begin{bmatrix} \mathbf{x} \\ \mathbf{y} \\ \mathbf{z} \end{bmatrix} = \mathbf{M} \begin{bmatrix} \mathbf{t} \\ \mathbf{r} \\ \mathbf{l} \end{bmatrix} \tag{3.25}$$

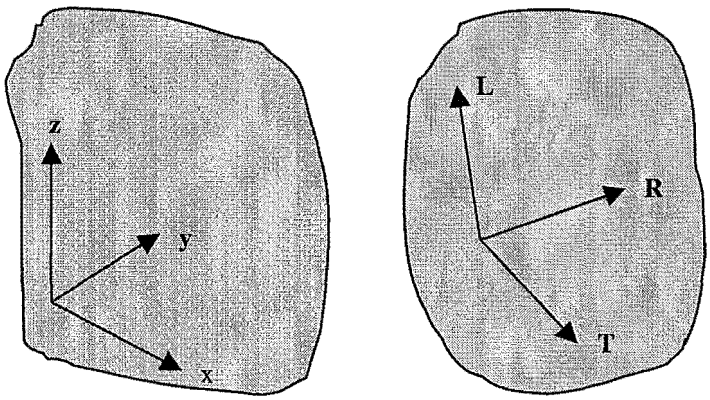

Figure 3.3. Transformation of local directions to global directions

As reported by McCullough (1990), the transformation matrix between the two systems of axes can also be given by

$$\mathbf{M} = \begin{bmatrix} m_{xt} & m_{xr} & m_{xl} \\ m_{yt} & m_{yr} & m_{yl} \\ m_{zt} & m_{zr} & m_{zl} \end{bmatrix} \tag{3.26}$$

where m_{ij} *(i=x, y, z; j=t, r, l)* are the direction cosines between the respective directions.

The stiffness equation for a continuum at a point with respect to local axes (L, T, R) is

$$\boldsymbol{\sigma}^* = \mathbf{D}^*(\boldsymbol{\varepsilon}^* - \boldsymbol{\varepsilon}_s^*)$$

while with respect to the global axes (x, y, z) it is

$$\boldsymbol{\sigma} = \mathbf{D}(\boldsymbol{\varepsilon} - \boldsymbol{\varepsilon}_s) \tag{3.28}$$

and therefore, as explained by McCullough (1990), $\boldsymbol{\sigma}^*$, $\mathbf{D}^*$ and $\boldsymbol{\varepsilon}_s^*$ are transformed according to

$$\boldsymbol{\sigma} = \mathbf{H}^T\boldsymbol{\sigma}^*, \quad \mathbf{D} = \mathbf{H}^T\mathbf{D}^*\mathbf{H} \quad \text{and} \quad \boldsymbol{\varepsilon}_s = \mathbf{H}^{-1}\boldsymbol{\varepsilon}_s^* \tag{3.29}$$

where $\mathbf{H}$ is given by

$$\mathbf{H} = \begin{bmatrix} m_{xt}\,m_{xt} & m_{yt}\,m_{yt} & m_{zt}\,m_{zt} & m_{xt}\,m_{yt} & m_{zt}\,m_{xt} & m_{yt}\,m_{zt} \\ m_{xr}\,m_{xr} & m_{yr}\,m_{yr} & m_{zr}\,m_{zr} & m_{xr}\,m_{yr} & m_{zr}\,m_{xr} & m_{yr}\,m_{zr} \\ m_{xl}\,m_{xl} & m_{yl}\,m_{yl} & m_{zl}\,m_{zl} & m_{xl}\,m_{yl} & m_{zl}\,m_{xl} & m_{yl}\,m_{zl} \\ 2\,m_{xt}\,m_{xr} & 2\,m_{yt}\,m_{yr} & 2\,m_{zt}\,m_{zr} & m_{xt}\,m_{yr} + m_{yt}\,m_{xr} & m_{zt}\,m_{xr} + m_{xt}\,m_{zr} & m_{yt}\,m_{zr} + m_{zt}\,m_{yr} \\ 2\,m_{xl}\,m_{xt} & 2\,m_{yl}\,m_{yt} & 2\,m_{zl}\,m_{zt} & m_{xl}\,m_{yt} + m_{yl}\,m_{xt} & m_{zl}\,m_{xt} + m_{xl}\,m_{zt} & m_{yl}\,m_{zt} + m_{zl}\,m_{yt} \\ 2\,m_{xr}\,m_{xl} & 2\,m_{yr}\,m_{yl} & 2\,m_{zr}\,m_{zl} & m_{xr}\,m_{yl} + m_{yr}\,m_{xl} & m_{zr}\,m_{xl} + m_{xr}\,m_{zl} & m_{yr}\,m_{zl} + m_{zr}\,m_{yl} \end{bmatrix} \tag{3.30}$$

3.3 Finite Element Method

The finite element method is a technique for solving partial differential equations by discretising them in the spatial domain. The discretisation is carried out locally over small and arbitrary shaped elements resulting in matrix equations relating the field variables of the continuum. Derivation of the finite element equations and formulation of the matrix equations are well known and described in many texts, for example Zienkiewicz and Taylor (2000a and 2000b). Techniques of solving these equations were also presented in many texts including Jennings (1992) and Pozrikidis (1998). The Rayleigh-Ritz procedure which is based on the application of the principle of the minimum total energy is one of the well-recognised techniques as described by Astley (1992). The basic steps of the procedure and the finite element equations are briefly presented below.

3.3.1 Element Formulation

The body which is under consideration is subdivided into discrete elements. The size and location of an element is defined by a sequence of nodes on its periphery that is known as the topology of the element. Elements with different geometries can be used depending on the underlying equations and the complexity of the body.

The element displacement field **u** is approximated by a polynomial function related to the nodal displacements, and is given by the equation

$$\mathbf{u} = \mathbf{N}^e\mathbf{d}^e \tag{3.31}$$

where $\mathbf{N}^e$ is the interpolating matrix or shape matrix whose components are the shape functions of the element, and $\mathbf{d}^e$ is the column vector that contains the nodal displacements (also known as nodal degrees of freedom) of the element.

From equations (3.8) and (3.31), the strain matrix, $\boldsymbol{\varepsilon}$ of the element is given by

$$\boldsymbol{\varepsilon} = \nabla\mathbf{N}^e\mathbf{d}^e \tag{3.32}$$

or

$$\boldsymbol{\varepsilon} = \mathbf{B}^e\mathbf{d}^e \tag{3.33}$$

where $\mathbf{B}^e = \nabla\mathbf{N}^e$, the strain displacement matrix and the components are derivatives of the shape functions.

By assuming that Hooke's law holds within the element, when there is a change in temperature, the stress field, $\boldsymbol{\sigma}$ is given by

$$\boldsymbol{\sigma} = \mathbf{D}\boldsymbol{\varepsilon} - \mathbf{D}\boldsymbol{\varepsilon}_T \tag{3.34}$$

and strain energy density of the element is given by

$$U^e = \int_v \tfrac{1}{2}\boldsymbol{\sigma}^T[\boldsymbol{\varepsilon} - \boldsymbol{\varepsilon}_T]dV \tag{3.35}$$

Using the constitutive equation

$$U^e = \int_v \tfrac{1}{2}[\boldsymbol{\varepsilon} - \boldsymbol{\varepsilon}_T]^T\mathbf{D}^T[\boldsymbol{\varepsilon} - \boldsymbol{\varepsilon}_T]dV \tag{3.36}$$

and substituting for $\boldsymbol{\varepsilon}$ from equation (3.33) and re-arranging, results in

$$U^e = \tfrac{1}{2}\mathbf{d}^{eT}\mathbf{K}^e\mathbf{d}^e - \mathbf{d}^{eT}\mathbf{f}_T^e \tag{3.37}$$

where $\mathbf{K}^e$ is the element stiffness matrix, given by

$$\mathbf{K}^e = \int_v (\mathbf{B}^{eT}\mathbf{D}\mathbf{B}^e)dV \tag{3.38}$$

and $\mathbf{f}_T^e$ is the thermal load vector[1], given by

$$\mathbf{f}_T^e = \int_v (\mathbf{B}^{eT}\mathbf{D}\boldsymbol{\varepsilon}_T)dV \tag{3.39}$$

since $\mathbf{D}$ is symmetric, $\mathbf{D}$ and $\mathbf{D}^T$ are equal and interchangeable.

Further, if the element is subjected to a body force, the potential energy density is given as the inner product of $\mathbf{u}$ and $\mathbf{g}$ (vector of body force components)

$$V^e = -\int_v \mathbf{u}^T\mathbf{g}dV \tag{3.40}$$

By substituting equation (3.31) into equation (3.40)

$$V^e = -\mathbf{d}^{eT}\mathbf{f}_g^e, \text{ where } \mathbf{f}_g^e = \int_v \mathbf{N}^{eT}\mathbf{g}dV \tag{3.41}$$

The total energy density of the element can be determined by combining equations (3.37) and (3.41)

$$\chi^e = U^e + V^e$$

or

$$\chi^e = \tfrac{1}{2}\mathbf{d}^{eT}\mathbf{K}^e\mathbf{d}^e - \mathbf{d}^{eT}[\mathbf{f}_T^e + \mathbf{f}_g^e] \tag{3.42}$$

3.3.2 Total Energy

The total energy of the body is the sum of the energy, χ^e of each element. Summing of the energy requires careful assembly of the $\mathbf{K}^e$, $\mathbf{f}_T^e$ and $\mathbf{f}_g^e$ matrices for each element

[1] Moisture and thermal effects are equivalent and interchangeable in the derivation of the relationships.

based on their nodal connectivity. The assembly procedure is explained in the general references previously mentioned. The total energy is given by

$$\chi = \sum_{e=1}^{m} \chi^e = \tfrac{1}{2}\mathbf{d}^T\mathbf{K}\mathbf{d} - \mathbf{d}^T[\mathbf{f}_g + \mathbf{f}_T] \tag{3.43}$$

where m is the number of discrete elements. $\mathbf{K}$, $\mathbf{f}_g$, $\mathbf{f}_T$ and $\mathbf{d}$ are the system stiffness matrix, nodal force vectors and displacement vector for the body.

The potential energy due to nodal loads by surface tractions is not associated with the sum of the element energies and must be included in the total system energy. The energy by the surface tractions is given by $-\mathbf{d}^T\mathbf{f}_t$, and on being added to equation (3.43) the total energy becomes

$$\chi = \tfrac{1}{2}\mathbf{d}^T\mathbf{K}\mathbf{d} - \mathbf{d}^T[\mathbf{f}_g + \mathbf{f}_T + \mathbf{f}_t] \tag{3.44}$$

where $\mathbf{f}_t$ is the column matrices containing nodal forces by surface tractions

3.3.3 Minimisation of System Energy

The derivative of the total energy with respect to displacements must be zero for the system to be at minimum energy. By differentiating χ with respect to the nodal displacements where $\mathbf{d} = [\delta_1, \delta_2, \delta_3, \ldots\ldots\ldots\ldots, \delta_n]^T$ for the system,

$$d\chi = \begin{bmatrix} \frac{\partial \chi}{\partial \delta_1} \\ \frac{\partial \chi}{\partial \delta_2} \\ \cdot \\ \cdot \\ \frac{\partial \chi}{\partial \delta n} \end{bmatrix}$$

or

$$d\chi = \mathbf{K}\mathbf{d} - \mathbf{f} \tag{3.45}$$

where $\mathbf{f} = \mathbf{f}_g + \mathbf{f}_T + \mathbf{f}_t$

$d\chi = 0$ for minimum energy and hence

$$\mathbf{Kd} = \mathbf{f} \tag{3.46}$$

3.3.4 Boundary Conditions

The boundary conditions are applied to prevent rigid body motion and rotation of the body. The wiping row and column method is used to implement the boundary conditions. For example, the displacement of node i has a known value i.e. $\delta_i = B_i$ then the number of degrees of nodal freedom is reduced and the system equation (4.46) can be modified to give

$$\begin{bmatrix} K_{1,1} & \cdot & K_{1,i-1} & \overset{i}{0} & K_{1,i+1} & \cdot & K_{1,n} \\ \cdot & \cdot & \cdot & \cdot & \cdot & \cdot & \cdot \\ K_{i-1,1} & \cdot & K_{i-1,i-1} & 0 & K_{i-1,i+1} & \cdot & K_{i-1,n} \\ 0 & . & 0 & 1 & 0 & . & 0 \\ K_{i+1,1} & \cdot & K_{i+1,i-1} & 0 & K_{i+1,i+1} & \cdot & K_{i+1,n} \\ \cdot & \cdot & \cdot & \cdot & \cdot & \cdot & \cdot \\ K_{n,1} & \cdot & K_{n,i-1} & 0 & K_{n,i+1} & \cdot & K_{n,n} \end{bmatrix} \begin{bmatrix} \delta_1 \\ \cdot \\ \delta_{i-1} \\ \delta_i \\ \delta_{i+1} \\ \cdot \\ \delta_n \end{bmatrix} = \begin{bmatrix} f_1 - K_{1,i} B_i \\ \cdot \\ f_{i-1} - K_{i-1,i} B_i \\ B_i \\ f_{i+1} - K_{i+1,i} B_i \\ \cdot \\ f_n - K_{n,i} B_i \end{bmatrix} \tag{3.47}$$

If B_i is zero, the i^{th} row and column in **K** and i^{th} load in **f** can be avoided during the assembly of the **K**, and **f** matrices. The resultant equation (3.47) is a set of linear equations containing the unknown nodal (degrees freedom) displacements which can be solved for the given loading conditions to obtain the resultant displacements.

Chapter 4

Homogenization of Elastic Composite Continuum

4.1 Introduction

Wood has complex microstructures with a periodic nature at several levels and is regarded as an elastic composite continuum. The equivalent properties of composite materials are evaluated from the properties of their constituents by an averaging method, an analytical method or a homogenization method. In the first method, the properties of a composite are determined by applying the law of mixtures using the known weight fraction or volume fraction of the constituent components and their respective properties (Matthews *et al* (2000)). Gibson and Ashby (1997) presented a selection of methods to calculate the effective properties of the cellular materials using analytical approaches. These methods have limitations:

(a) only one cell at a time can be analysed and hence they are only suitable for uniform density materials,
(b) only regular two dimensional honeycomb structures can be analysed.

Since 1970, significant developments in computer technology and the advanced applications of composite materials have lead to micromechanical models of increasing complexity to evaluate the equivalent homogeneous or overall properties. These developments have been reviewed in many articles and texts including; Hashin (1983), Halpin (1984), Aboudi (1991), Kalamkarov (1992), Nemat-Nasser and Hori (1993), Persson *et al* (1993), Ghosh *et al* (1995), Kalamkarov and Kolpakov (1997), Luciano and Sacco (1998), Lee *et al* (1999), Hori and Nemat-Nassar (1999), Sluis *et al* (2000), and Kaminski and Kleiber (2000). One of the homogenization methods used by these authors was based on the representative volume element as an effective numerical tool that models multi-component structures and provides systematic analysis of the stress-strain behaviour at microstructural level when the microstructure is periodic.

Hollister *et al* (1991) applied the homogenisation method based on representative volume elements to study the mechanics of trabecular bone tissue, which is a periodic porous composite similar to wood. Subsequently, Hollister and Kikuchi (1992)

compared the representative volume element based homogenization method with standard mechanics analyses for periodic porous composites. Both methods were implemented using a displacement based finite element formulation and it was found that the homogenization theory was preferable, in predicting the effective stiffness, to the standard mechanics of materials approaches. Lee *et al* (1996) used homogenization with asymptotic expansion and a finite element method to determine the effective properties of re-entrant honeycomb structures while Astley *et al* (1997 & 1998) and Persson (1997) used the representative volume element based homogenization theory to analyse the behaviour of wood at a microstructural level.

Recently, a new approach which applies constraints to the representative volume element, known as full cyclic constraint, has been used by Astley *et al* (1998). Persson (1997) made use of a similar concept. There is a need to fully describe the practical implementation of this method and to demonstrate that it is effective. The full cyclic constraint is implemented in this work by generating the constraint equations linking the points on opposite faces of the representative volume element. The finite element method is then used to model and analyze the mechanical response of the representative volume element. The accuracy and effectiveness of this method is evaluated using test models.

4.2 Homogenization Principle

4.2.1 Composite Continuum

Composites are materials that contain two or more dissimilar constituents, a subset of which are natural materials such as wood and human bone tissue. The composite continuum consists of regions with well-defined interfaces. A region is occupied by a constituent. The constituents that provide stiffness are called reinforcements, whereas the constituent that bonds the reinforcements in the composite continuum is called the matrix. The geometry, distribution, and properties of each constituent determines the resultant property of the continuum which differs from that of the individual constituents. An important parameter is the volume fraction of the constituents. The distribution of the constituents determines the homogeneity of the continuum, and the geometry and orientation of the reinforcement affects the anisotropy of the system as stated by Daniel (1994). In the homogenization approach, as described by authors such

as Nemat-Nasser and Hori (1993) and Persson *et al* (1993), the structure (microstructure) of the continuum is considered to consist of an infinite number of regular periodic structures (unit cells) with shapes and material properties that are similar. Moreover the individual regions (constituents) in each cell are also treated as consisting of an orthotropic homogeneous material. In this method, a unit cell is chosen as a representative volume element (RVE), which is repeated throughout the continuum as shown in Figure 4.1.

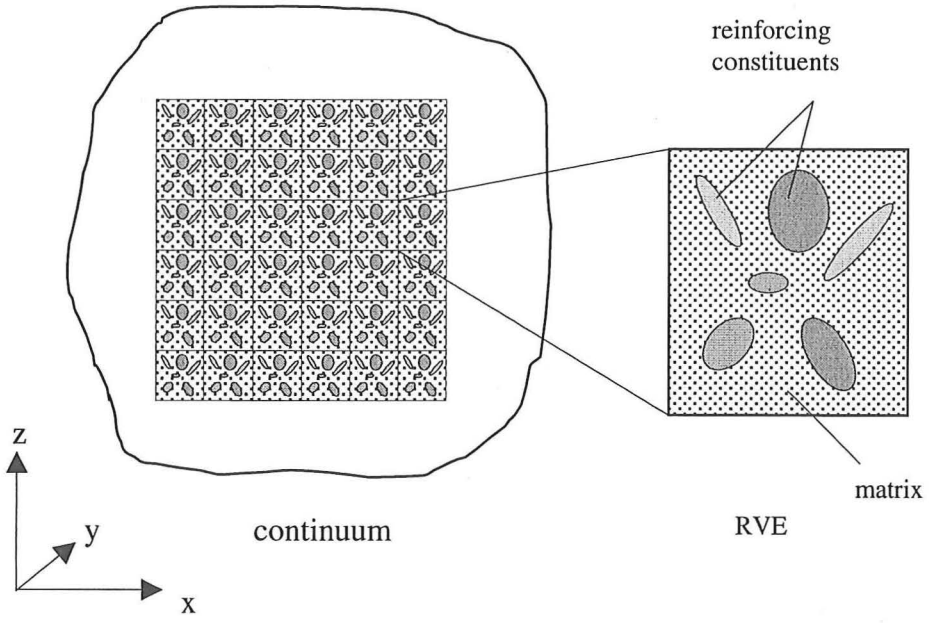

Figure 4.1. An elastic composite continuum with infinitely extended periodic structure.

4.2.2 Representative Volume Element

The concept of a representative volume element (RVE) was initially introduced by Hill (1963) and detailed in Hashin's (1983) survey. As explained by Nemat-Nasser and Hori (1993), the continuum with a periodic structure must consist of monolithic collections of RVEs, satisfying the continuity of displacements and tractions across all the RVE boundaries. For the RVE, the average strains and stresses can be calculated in terms of the geometry and properties of the constituents, and the overall average elasticity and compliance tensors can be defined. The RVE based homogenisation method has been extensively used to predict the effective stiffness and strain properties of composite materials. This is because of the ease of applying boundary conditions to the RVE and solving the resultant boundary value problem instead of analysing the entire composite

continuum. However, the accuracy of the prediction depends on how well the boundary conditions describe the actual nature of the RVE in the continuum.

As Hollister and Kikuchi (1992) pointed out, consider a case where the actual boundary conditions differ from the applied boundary conditions, but produce the same average RVE strain. In this case, by the principle of minimum potential energy, the average stiffness predicted by the RVE analysis would be greater than the actual stiffness. The actual boundary conditions minimise the energy while the assumed boundary conditions are admissible and by definition produce greater energy. The average stress within the RVE under the assumed boundary conditions must be higher to produce a higher energy. The same argument holds for applied tractions boundary conditions from the principle of minimum complementary energy resulting in an actual traction boundary condition for the same average stress giving a higher compliance and therefore a lower stiffness. Thus, RVE analysis under applied displacements gives an upper bound on apparent stiffness while the applied tractions give a lower bound.

According to Gusev (1997), larger RVEs increase the complexity of the resulting boundary value problem and therefore it is desirable to choose a method that gives the greatest accuracy for the smallest RVE. For periodic materials this is the smallest repeating unit. Natural materials, like wood and human bone tissue, are heterogeneous composites with complex microstructures. Therefore predicting the mechanical behaviour of such materials relies on the RVE selection and the RVE boundary conditions.

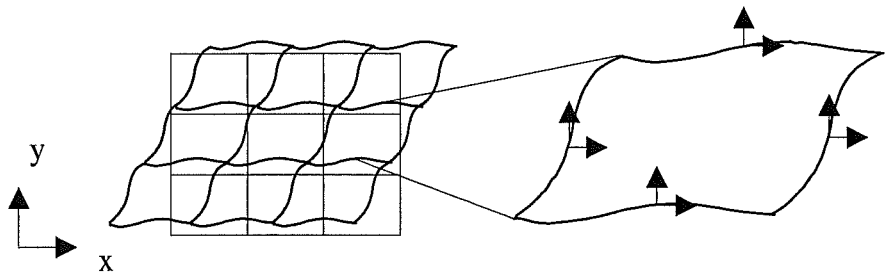

Figure 4.2. Undeformed and deformed periodic cells

It is assumed that each RVE deforms repetitively, and the neighbouring boundaries coincide in the deformed and undeformed conditions. Figure 4.2 illustrates such behaviour for the two-dimensional case. It is assumed that the unit cell consists of four connected corners with four curves. In a body at a distance from the physical

boundaries, as explained by Sluis *et al* (2000), a homogeneous stress field exists. Therefore, because the structure can be considered as a continuum, in these areas, the RVEs deform in a similar manner. The possible shape of the cell is therefore limited based on the assumption that the boundaries of opposing sides of a unit cell must have the same shape. This approach, termed *full cyclic constraint*, was proposed by Astley *et al* (1997 & 1998).

4.2.3 Full Cyclic Constraint

The orthogonal RVE shown in Figure 4.3 represents a repeating unit in the continuum shown in Figure 4.1. The RVE does not need to be in the shape of a parallelepiped but for a broad class of periodic structures, a RVE of that kind is often chosen. The parallelepiped RVE lends itself to simpler analysis and, therefore, is considered in this work. The RVE has x, y, and z as orthotropic axes with dimensions l_x, l_y and l_z, and vertices V_n (n=1,2,....,8). It satisfies the compatibility requirements resulting in full cyclic constraint equations defining the periodic cyclic boundary conditions.

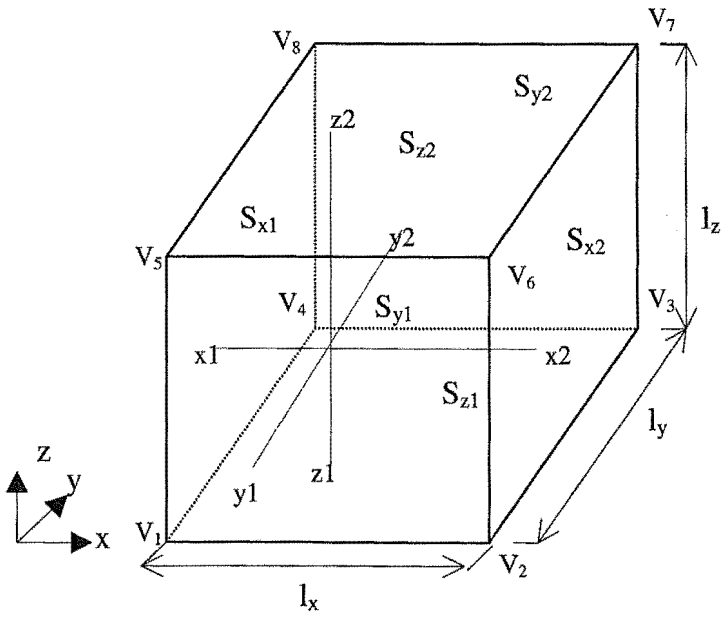

Figure 4.3. An orthogonal RVE

The RVE has a boundary surface S that includes three boundary surface pairs, S_i (i=x, y, z), which are perpendicular to the x, y and z axes respectively. Each pair has two opposite surfaces, S_{im} (m=1,2). Each boundary surface includes one face, four edges and four vertices. Each boundary pair of S_i should be periodic for the compatibility, resulting in the opposite boundary surfaces being identical in shape and size as shown in

Figure 4.4, with the stress vectors being equal and opposite in direction at each pair of surfaces. Based on these boundary conditions appropriate displacement equations are derived.

Each of the column matrices δ_x, δ_y and δ_z has three constants, which describe the overall displacements of the boundary pairs of S_x, S_y and S_z respectively in the global axis system.

$$\delta_x = \begin{bmatrix} \delta_{xx} \\ \delta_{xy} \\ \delta_{xz} \end{bmatrix}, \quad \delta_y = \begin{bmatrix} \delta_{yx} \\ \delta_{yy} \\ \delta_{yz} \end{bmatrix}, \quad \delta_z = \begin{bmatrix} \delta_{zx} \\ \delta_{zy} \\ \delta_{zz} \end{bmatrix} \tag{4.1}$$

where the first subscript of the displacement indicates the direction of load and the second subscript shows the direction of the displacement

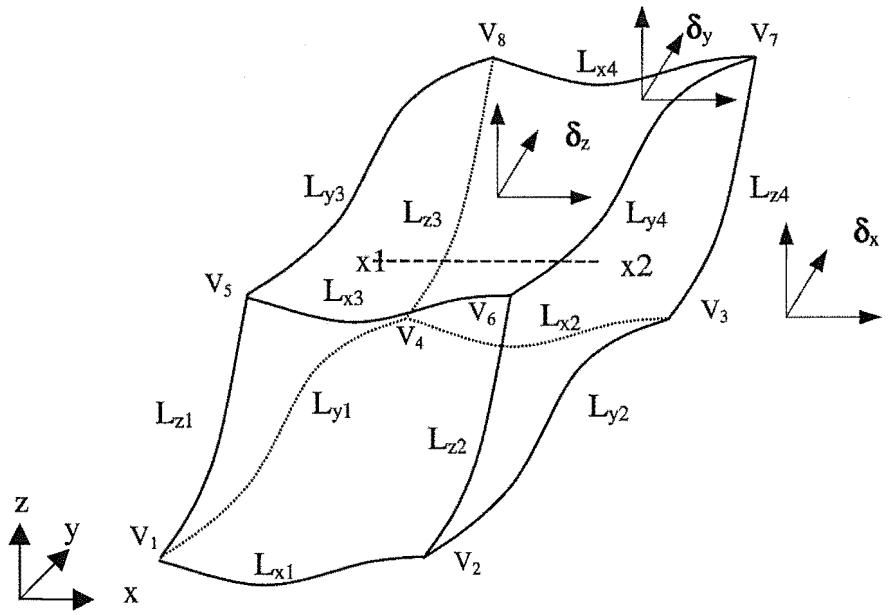

Figure 4.4. Deformed RVE

To maintain the identical shape and size of the opposite pairs of boundaries, the displacements of any corresponding points on the opposite boundary surfaces and their respective overall displacements are related as described below:

By relating the displacements of corresponding points x1 and x2 on the faces of the boundary surfaces S_{x1} and S_{x2}, the overall displacements are given by the linear constraint equations

$$\begin{bmatrix} u_{x2} \\ v_{x2} \\ w_{x2} \end{bmatrix} - \begin{bmatrix} u_{x1} \\ v_{x1} \\ w_{x1} \end{bmatrix} = \begin{bmatrix} \delta_{xx} \\ \delta_{xy} \\ \delta_{xz} \end{bmatrix} \tag{4.2}$$

where u, v and w are the displacement of a point in x, y and z directions. The subscripts of u, v and w indicate the points on the faces of the boundary S_{x1} and S_{x2}.

In a simplified general vector form, for any corresponding points on the opposite faces S_{x2} and S_{x1}, equation (4.2) is given by

$$\mathbf{u}_{x2} - \mathbf{u}_{x1} = \boldsymbol{\delta}_x \tag{4.3}$$

or

$$\mathbf{u}_{x2} = \mathbf{u}_{x1} + \boldsymbol{\delta}_x \tag{4.4}$$

Similarly the general form of linear constraint equations for faces of S_{y2} and S_{y1} is

$$\mathbf{u}_{y2} = \mathbf{u}_{y1} + \boldsymbol{\delta}_y \tag{4.5}$$

and for faces of S_{z2} and S_{z1} is

$$\mathbf{u}_{z2} = \mathbf{u}_{z1} + \boldsymbol{\delta}_z \tag{4.6}$$

A set of four edges that are parallel to each axis in the undeformed RVE can be represented by L_i, and each edge can then be represented by L_{ik}, where i=x, y, z (*i* indicates the axis for which the edges are parallel) and k=1,2,3,4 (*k* - number of edges). For compatibility, all four parallel edges deform in a similar manner as shown in Figure 4.4.

By considering the displacements of the corresponding points on L_{x1} and L_{x2} edges that are parallel to x-axis, the overall displacements of the related points L_{x1} and the overall displacements of the RVE are given by the linear constraint equations

$$\begin{bmatrix} u_{Lx2} \\ v_{Lx2} \\ w_{Lx2} \end{bmatrix} - \begin{bmatrix} u_{Lx1} \\ v_{Lx1} \\ w_{Lx1} \end{bmatrix} = \begin{bmatrix} \delta_{yx} \\ \delta_{yy} \\ \delta_{yz} \end{bmatrix} \tag{4.7}$$

or in a simplified vector form

$$\mathbf{u}_{Lx2} - \mathbf{u}_{Lx1} = \boldsymbol{\delta}_y \tag{4.8}$$

or

$$\mathbf{u}_{Lx2} = \mathbf{u}_{Lx1} + \boldsymbol{\delta}_y \tag{4.9}$$

Similarly, the linear constraint equations for the rest of the edges that are parallel to x-axis are given in relation to the points in L_{x1} as

$$\mathbf{u}_{Lx3} = \mathbf{u}_{Lx1}+\delta_z, \qquad \mathbf{u}_{Lx4} = \mathbf{u}_{Lx1}+\delta_y+ \delta_z \tag{4.10}$$

the linear constraint equations for the edges parallel to y-axis in relation to the points in L_{y1} can be given in vector form by

$$\mathbf{u}_{Ly2} = \mathbf{u}_{Ly1}+\delta_x, \qquad \mathbf{u}_{Ly3} = \mathbf{u}_{Ly1}+\delta_z, \qquad \mathbf{u}_{Ly4} = \mathbf{u}_{Ly1}+\delta_x+ \delta_z \tag{4.11}$$

and the linear constraint equations for the edges parallel to z-axis in relation to the points in L_{z1} are given in vector form by

$$\mathbf{u}_{Lz2} = \mathbf{u}_{Lz1}+\delta_x, \qquad \mathbf{u}_{Lz3} = \mathbf{u}_{Lz1}+\delta_y, \qquad \mathbf{u}_{Lz4} = \mathbf{u}_{Lz1}+\delta_x+ \delta_y \tag{4.12}$$

All eight vertices "V_n" (numbered as shown in Figure 4.3 and 4.4) of the RVE must adjoin the corresponding vertices of the neighbouring unit cells for compatibility of the continuum. Therefore, the displacements of the vertices and the overall displacements are related by the vector equations;

$$\mathbf{u}_{v2} = \mathbf{u}_{v1}+\delta_x, \quad \mathbf{u}_{v3} = \mathbf{u}_{v1}+\delta_x+\delta_y, \qquad \mathbf{u}_{v4} = \mathbf{u}_{v1}+\delta_y, \quad \mathbf{u}_{v5} = \mathbf{u}_{v1}+\delta_z$$

$$\mathbf{u}_{v6} = \mathbf{u}_{v1}+\delta_x+\delta_z, \qquad \mathbf{u}_{v7} = \mathbf{u}_{v1}+\delta_x+\delta_y+\delta_z, \quad \mathbf{u}_{v8} = \mathbf{u}_{v1}+\delta_y+\delta_z \tag{4.13}$$

where $\mathbf{u}_{v1}, \mathbf{u}_{v2}, \ldots\ldots, \mathbf{u}_{v8}$ are the column matrices of the displacements of vertices $V_1, V_2, \ldots\ldots, V_n$ respectively.

For compatibility, in addition to these linear constraint equations, the outward normal vectors, $\mathbf{n}_i$ to the RVE have opposite directions on the opposite surfaces of the RVE. Since $\mathbf{n}_i\boldsymbol{\sigma}_{ij} = \hat{\mathbf{t}}_j$, the surface tractions $\hat{\mathbf{t}}_j$ are opposite in direction on opposing boundaries of the RVE.

The global state of strain of the RVE is determined from the overall displacements given in equations

$$\varepsilon_{ij}=(\delta_{ij} + \delta_{ji})/2l_i \qquad i=x,y,z \text{ and } j=x,y,z \tag{4.14}$$

4.3 Implementation of full cyclic constraints by the Finite Element Method

4.3.1 Energy Concept

Consider a global region in the Cartesian coordinate system (x, y, z), which has a large number of similar RVEs of the composite of interest as shown in Figure 4.1. Since the shape of the RVE has already been considered as parallelepiped in section 4.2, the shape of the global region is also assumed to be parallelepiped to simplify the analysis. Figure 4.5 shows an orthogonal RVE in the global region. The dimensions of the RVE are l_i (i=x, y, z) in the x, y, z directions and if 'η' is the dimensional ratio of the global region to the RVE, the dimensions of the global region are ηl_i. The boundaries of the RVE and the global region are S_i and Π_i respectively, and the corresponding boundaries are parallel to each other.

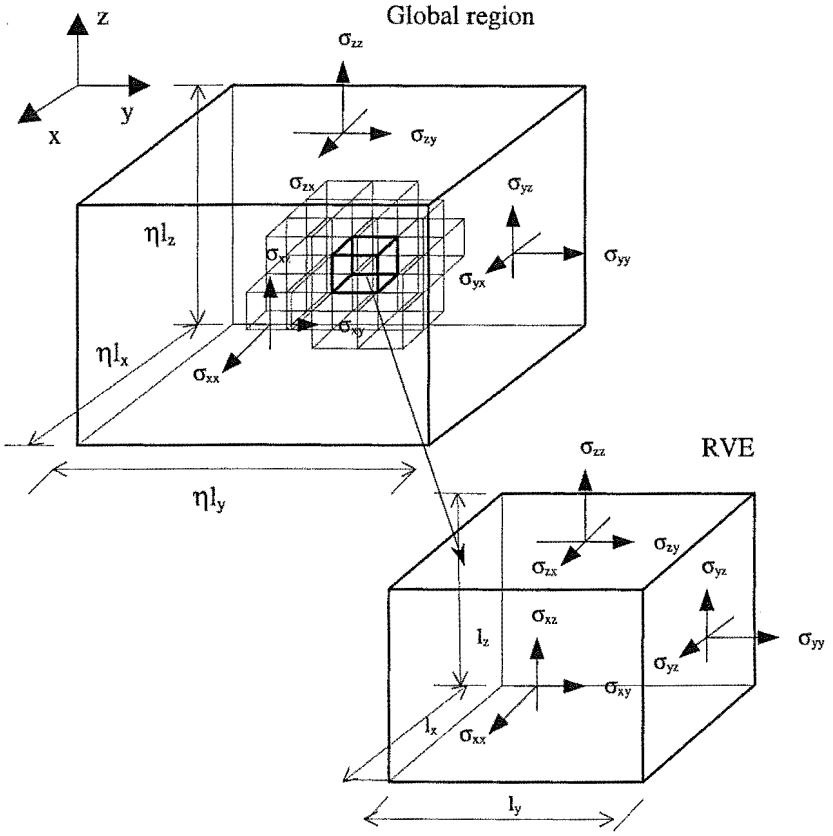

Figure 4.5. An RVE is represented in a selected global region of the continuum.

For the analysis, consider a case where the boundaries, Π_i of the global region are subjected to an external uniform stress field, σ while the global region is subjected to

the thermal-induced forces due to a temperature variation ΔT. **F** is the resultant force on each face of the global region and is given by the equation:

$$F_{ij}=\sigma_{ij}\Pi_i = \int_{\Pi_i} \hat{t}_j d\Pi \tag{4.15}$$

where $F_{ij} = F_{ji}$, $\sigma_{ij} = \sigma_{ji}$ and $\hat{t}_j$ is the surface traction by the uniform stress field acting on the boundary, Π_i

The overall global displacements, $\boldsymbol{\delta}$ of each RVE caused by the uniform stress field and the thermal forces are equal since the global region produces a linear uniform displacement field from the periodicity of the structure and the compatibility condition. Hence the overall displacement of the global region is given by $\eta\boldsymbol{\delta}$.

The total energy of the global region, χ_{reg} is given by the sum of the strain energy, U_{reg} of the global region and the work done by the external force, **F** on the global region.

$$\chi_{reg} = U_{reg} + V_{reg} \tag{4.16}$$

where V_{reg}, is the work done by **F** and given by

$$V_{reg} = -\mathbf{F}\eta\boldsymbol{\delta}$$

or

$$V_{reg} = -\boldsymbol{\sigma}\Pi_i\eta\boldsymbol{\delta} \tag{4.17}$$

By substituting equation (4.17) into (4.16),

$$\chi_{reg} = U_{reg} - \eta\Pi_i\boldsymbol{\sigma}\boldsymbol{\delta}$$

or

where $\Pi_i = \eta^2 S_i$ giving

$$\chi_{reg} = U_{reg} - \eta^3 S_i\boldsymbol{\sigma}\boldsymbol{\delta} \tag{4.18}$$

If equation (4.18) is divided by η^3,

$$(1/\eta^3)\,\chi_{reg} = (1/\eta^3)U_{reg} - S_i\boldsymbol{\sigma}\boldsymbol{\delta} \tag{4.19}$$

Since there is a homogeneous stress field existing in the continuum for periodic conditions, the boundaries, S_i of each RVE are subjected to the same uniform stress field, $\boldsymbol{\sigma}$. Therefore, the work done on an RVE by this stress is given by

$$V_{rve} = - S_i \sigma \delta \tag{4.20}$$

The number of RVEs in the global region is η^3, hence the equation (4.19) must represent the energy equation of an RVE. The strain energy of each RVE is equal due to the similarity of the periodic structure and therefore the equation (4.19) can then be rewritten as

$$\chi_{rve} = U_{rve} - S_i \sigma \delta \tag{4.21}$$

where χ_{rve} is the total energy and U_{rve} is the strain energy of an RVE.

An RVE is descretised in such a way that the corresponding nodes of the opposite boundaries should satisfy the compatibility condition. According to the finite element concept U_{rve} can be given by

$$\mathbf{U}_{rve} = \tfrac{1}{2}\mathbf{d}^T\mathbf{K}\mathbf{d} - \mathbf{d}^T\mathbf{f}_T \tag{4.22}$$

The system thermal force vector, $\mathbf{f}_T$, and the system stiffness matrix, $\mathbf{K}$, are numerically computed according to equations (3.33) and (3.32) respectively. The stiffness matrix $\mathbf{D}(x)$ and the thermal expansion coefficient $\boldsymbol{\alpha}(\mathbf{x})$ are spatial variables in the RVE. Each constituent in the RVE is assumed to have orthotropic homogeneous properties and therefore stiffness matrix and the thermal expansion coefficient are constant for each constituent. $\mathbf{d}$ is the vector of nodal displacements (nodal degrees of freedom) for the RVE and is given by

$$\mathbf{d} = [u_1, \ldots\ldots, u_p, \ldots\ldots, u_q, \ldots\ldots, u_n]^T \tag{4.23}$$

where n is the number of nodal degrees of freedom.

By substituting equation (4.22) into (4.21),

$$\chi_{rve} = [\tfrac{1}{2}\mathbf{d}^T\mathbf{K}\mathbf{d} - \mathbf{d}^T\mathbf{f}_T] - S_i \sigma \delta \tag{4.24}$$

If $\mathbf{f}$ is the resultant force field corresponding to σ at the boundary, S_i of RVE, equation (4.24) can then be written to give the total energy of RVE

$$\chi_{rve} = [\tfrac{1}{2}\mathbf{d}^T\mathbf{K}\mathbf{d} - \mathbf{d}^T\mathbf{f}_T] - \mathbf{f}\delta \tag{4.25}$$

where $S_i\sigma = \mathbf{f}$

4.3.2 Applying Constraint Equations

The constraint conditions described by equations (4.2) – (4.13) can be given in a general vector form for two nodal points np and nq

$$\mathbf{u}_{nq} = \mathbf{u}_{np} + \delta_x + \delta_y + \delta_z \tag{4.26}$$

where degrees of freedom of node nq are constraint to degrees of freedom of node np and the overall displacements of the RVE

The rest of the three global overall displacement vectors can be taken as zero in equation (4.26) if the constraint equations have one or two overall displacement vectors. If equation (4.26) is written in degrees of freedom

$$\begin{bmatrix} u_q \\ u_{q+1} \\ u_{q+2} \end{bmatrix} = \begin{bmatrix} u_p \\ u_{p+1} \\ u_{p+1} \end{bmatrix} + \begin{bmatrix} \delta_{xx} \\ \delta_{xy} \\ \delta_{xz} \end{bmatrix} + \begin{bmatrix} \delta_{yx} \\ \delta_{yy} \\ \delta_{yz} \end{bmatrix} + \begin{bmatrix} \delta_{zx} \\ \delta_{zy} \\ \delta_{zz} \end{bmatrix} \tag{4.26}$$

where p and q (freedom numbers) denote the positions of the degrees of freedom in the system displacement matrix, **d** of the RVE as given in equation (4.23).

Incorporating the global overall displacements in the last rows of **d**, the new displacement matrix can be written as

$$\mathbf{d}_g = [u_1, \ldots\ldots\ldots\ldots, u_n, \delta_{xx}, \delta_{xy}, \delta_{xz}, \ldots\ldots, \delta_{zx}, \delta_{zy}, \delta_{zz}]^T$$

or

replacing δ_{xx}, δ_{xy}, δ_{xz}, δ_{yx}, δ_{yy}, δ_{yz}, δ_{zx}, δ_{zy}, δ_{zz} by δ_{n+1}, δ_{n+2}, $\delta_{n+3}, \ldots\ldots$, δ_{n+7}, δ_{n+8}, δ_{n+9} respectively to have a sequence of the overall displacements

$$\mathbf{d}_g = [u_1, \ldots\ldots\ldots\ldots, u_n, \delta_{n+1}, \delta_{n+2}, \delta_{n+3}, \ldots\ldots, \delta_{n+7}, \delta_{n+8}, \delta_{n+9}]^T \tag{4.27}$$

or in a partitioned matrix form

$$\mathbf{d}_g = \begin{bmatrix} \mathbf{d} \\ \hline \bar{\boldsymbol{\delta}} \end{bmatrix} = \begin{bmatrix} u_i \\ \hline \bar{\delta}_j \end{bmatrix} \tag{4.28}$$

where $i = 1,2,\ldots,n$ and $j = n+1, n+2, \ldots, n+9$

The size of the system stiffness matrix **K** is increased with zero columns and rows that are equal to the number of overall displacements of the RVE to form a modified stiffness matrix ($\mathbf{K}_g$), while the same number of zero rows are added to $\mathbf{f}_T$ to form a modified thermal force vector ($\mathbf{f}_{gT}$). Since there is no change in the total energy of the RVE, by rewriting equation (4.25) in terms of $\mathbf{K}_g$ and $\mathbf{f}_{gT}$, the equation

$$\chi_{rve} = \frac{1}{2}\begin{bmatrix} \mathbf{d} \\ \hline \bar{\boldsymbol{\delta}} \end{bmatrix}^T \left[\begin{array}{c|c} \mathbf{K} & \mathbf{0} \\ \hline \mathbf{0} & \mathbf{0} \end{array}\right] \begin{bmatrix} \mathbf{d} \\ \hline \bar{\boldsymbol{\delta}} \end{bmatrix} - \begin{bmatrix} \mathbf{d} \\ \hline \bar{\boldsymbol{\delta}} \end{bmatrix}^T \begin{bmatrix} \mathbf{f}_T \\ \hline \mathbf{0} \end{bmatrix} - \mathbf{f}\boldsymbol{\delta} \tag{4.29}$$

or

$$\chi_{rve} = [\tfrac{1}{2}\mathbf{d}_g^T\mathbf{K}_g\mathbf{d}_g - \mathbf{d}_g^T\mathbf{f}_{gT}] - \mathbf{f}\boldsymbol{\delta} \tag{4.30}$$

is obtained.

By imposing the constraint equations (4.2) – (4.13) into the displacement matrix $\mathbf{d}_g$, a transformation matrix **A** between a new nodal displacement matrix $\mathbf{d}_n$ and $\mathbf{d}_g$ can be obtained.

For simple demonstration to implement a constraint equation in the system matrices, consider one of the constraint equations in (4.27)

$$u_q = u_p + \delta_{xx} + \delta_{yx} + \delta_{zx} \tag{4.31a}$$

or

$$u_q = u_p + \delta_{n+1} + \delta_{n+4} + \delta_{n+7} \tag{4.31b}$$

where *p*, *q*, *n+1*, *n+2* and *n+3* are freedom numbers that denote the position of u_p, u_q and δ_{n+1}, δ_{n+4}, $\delta_{n+}7$ in $\mathbf{d}_g$ and $\mathbf{d}_n$

If the constraint equation (4.31b) is imposed on the RVE then the transformation is given by

$$\begin{bmatrix} u_1 \\ \cdot \\ u_p \\ \cdot \\ u'_q \\ \cdot \\ u_n \\ \delta_{n+1} \\ \cdot \\ \delta_{n+4} \\ \cdot \\ \delta_{n+7} \\ \cdot \end{bmatrix} = \begin{bmatrix} & p & q & & n+1 & n+4 & n+7 & \\ 1 & & & & & & & \\ & \cdot & & & & & & \\ & 1 & & & & & & \\ & & \cdot & & & & & \\ & 1 & 0 & & 1 & 1 & 1 & \\ & & & \cdot & & & & \\ & & & & 1 & & & \\ & & & & & 1 & & \\ & & & & & & \cdot & \\ & & & & & 1 & & \\ & & & & & & \cdot & \\ & & & & & & 1 & \\ & & & & & & & \cdot \end{bmatrix} \begin{bmatrix} u_1 \\ \cdot \\ u_p \\ \cdot \\ u_q \\ \cdot \\ u_n \\ \delta_{n+1} \\ \cdot \\ \delta_{n+4} \\ \cdot \\ \delta_{n+7} \\ \cdot \end{bmatrix} \tag{4.32}$$

where u'_q is the new freedom for u_q in $\mathbf{d}_n$

Similarly all the constraint conditions described by equations (4.2) – (4.13) can be imposed on the system and the new $\mathbf{d}_n$ matrix would be given by

$$\mathbf{d}_n = \mathbf{A}\mathbf{d}_g \tag{4.33}$$

By replacing $\mathbf{d}_g$ by $\mathbf{d}_n$ in (4.30), the total energy of RVE does not change, hence

$$\chi_{rve} = \frac{1}{2}\mathbf{d}_n^T \mathbf{K}_n \mathbf{d}_n - \mathbf{d}_n^T \mathbf{f}_{nT} - \mathbf{f}\delta \tag{4.34}$$

where $\mathbf{K}_n$ and $\mathbf{f}_{nT}$ are the new system stiffness matrix and system thermal force matrix of the RVE respectively and are given by

$$\mathbf{K}_n = \mathbf{A}^T \mathbf{K}_g \mathbf{A} \tag{4.35}$$

$$\mathbf{f}_{nT} = \mathbf{A}^T \mathbf{f}_{gT} \tag{4.36}$$

The work done by the $\mathbf{f}$, ($\delta\mathbf{f}$) is also equal to $\mathbf{d}_n^T \mathbf{f}_n$, since $\mathbf{d}_n^T \mathbf{f}_n = [\,.\ u_i\ .\,|\,\delta] \begin{bmatrix} \mathbf{0} \\ \hline \mathbf{f} \end{bmatrix}$

Substituting $\mathbf{d}_n^T \mathbf{f}_n$ in equation (4.34) does not change the energy of the RVE, and hence

$$\chi_{rve}=\frac{1}{2}\mathbf{d}_n^T\mathbf{K}_n\mathbf{d}_n-\mathbf{d}_n^T\mathbf{f}_{nT}-\mathbf{d}_n^T\mathbf{f}_n \tag{4.37}$$

By minimizing the energy of the RVE, equation (4.37) can be rewritten as

$$\mathbf{K}_n\mathbf{d}_n=\mathbf{f}_{nT}+\mathbf{f}_n \tag{4.38}$$

The $\mathbf{K}_n$ and $\mathbf{f}_{nT}$ can easily be computed from $\mathbf{K}_g$ and $\mathbf{f}_{gT}$ respectively by performing the transformations given in equations (4.35) and (4.36) as explained in Appendix (A).

By removing the zero rows and columns from the system matrices (this does not have any effect in the system equation), a new system stiffness matrix $\mathbf{K}_{nc}$ and thermal load vector $\mathbf{f}_{ncT}$ that are smaller than $\mathbf{K}_n$ and $\mathbf{f}_{nT}$ respectively can be formed. The size of $\mathbf{d}_n$ is also reduced since all constraint freedoms are removed and take a new form as $\mathbf{d}_{nc}$. The resultant external loads do not change although the zero rows are reduced in the upper part of the matrix, $\mathbf{f}_{nc}=\begin{bmatrix}\mathbf{0}\\ \hline \mathbf{f}\end{bmatrix}$. Hence equation (4.38) can be rewritten without having zero rows and columns after the transformation as

$$\mathbf{K}_{nc}\mathbf{d}_{nc}=\mathbf{f}_{ncT}+\mathbf{f}_{nc} \tag{4.39}$$

However, modifying a large system stiffness matrix by the above method generally requires a large computer memory and takes significant computer time to obtain the solutions. This problem can be avoided by doing the column and row operation at the element level and then assembling to form the new system matrices without zero columns and rows. Applying linear constraint equations at an element level was introduced by Dhatt and Touzot (1985) without detailing the method. In this study the linear constraint equations are imposed on the finite element analysis at element level as explained in Appendix (B).

To solve equation (4.39) the rigid body motion of the RVE can be eliminated by suppressing all the displacements of the vertex V_1 ($\mathbf{u}_{v1}=\mathbf{0}$). The rotation of the RVE is prevented by suppressing the overall shear displacements, i.e. $\delta_{xy}=\delta_{xz}=\delta_{yz}=0$. The rows and columns related to these displacements are not incorporated in $\mathbf{K}_{nc}$ and $\mathbf{f}_{ncT}$.

The unconstraint degrees of freedom and overall global displacements can be determined by solving the equation (4.39). The constraint degrees of freedom can be determined by substituting for the unconstraint degrees of freedom and overall displacements in the equations (4.2) – (4.13).

4.4 Determining the Equivalent Properties

4.4.1 Six Elementary Stress Cases

Assume that the orthotropic heterogeneous material within the RVE is replaced by an equivalent orthotropic homogeneous material which has a stiffness matrix **D'**, a compliance matrix **C'**, and thermal coefficient α' (Figure 4.6).

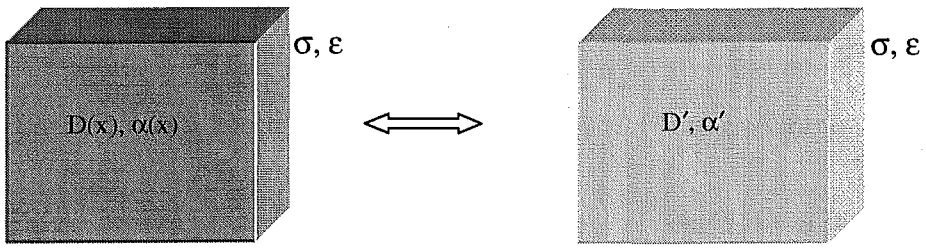

Figure 4.6. Heterogeneous RVE (A) and equivalent homogeneous RVE (B) are under same stress and strain fields.

If both RVEs are subjected to same stress field, they produce an equivalent strain field and equal energy.

As explained in the previous chapter, the constitutive equation for the equivalent homogenized RVE is given by equation (3.17). At a constant temperature ($\Delta T=0$), the induced thermal strain is zero ($\boldsymbol{\varepsilon}'_T = \boldsymbol{\alpha}'\Delta T = \mathbf{0}$), and equation (3.17) reduces to

$$\boldsymbol{\varepsilon}' = \mathbf{C}'\boldsymbol{\sigma}' \tag{4.40}$$

Equation (4.40) can be solved for the following six unit stress cases to find the stiffness parameters in $\mathbf{C}'$ if the strain components in $\boldsymbol{\varepsilon}'$ are known.

$$\sigma=\begin{bmatrix}1\\0\\0\\0\\0\\0\end{bmatrix}, \sigma=\begin{bmatrix}0\\1\\0\\0\\0\\0\end{bmatrix}, \sigma=\begin{bmatrix}0\\0\\1\\0\\0\\0\end{bmatrix}, \sigma=\begin{bmatrix}0\\0\\0\\1\\0\\0\end{bmatrix}, \sigma=\begin{bmatrix}0\\0\\0\\0\\1\\0\end{bmatrix} \text{ and } \sigma=\begin{bmatrix}0\\0\\0\\0\\0\\1\end{bmatrix} \tag{4.41}$$

The strain components can be found by solving equation (4.39) for each of the unit stress cases when the RVE is maintained at a constant temperature. If the stress acting on the RVE is unity then the resultant load for the given case is equal to the area of the boundary, S_i while the rest of the forces are equated to zero. Equation (4.39) is solved separately for each $\mathbf{f}_{nc}$ of the six elementary stress cases to determine $\boldsymbol{\delta}$, for a constant temperature ensuring that the thermal forces are zero.

The overall global strain $\boldsymbol{\varepsilon}'$ is determined for each case using equation (4.14), and the respective components of $\mathbf{C}'$ are determined using equation (4.40).

4.4.2 Thermal Load Case

For $\boldsymbol{\sigma}' = \mathbf{0}$ and a unit change of temperature ($\Delta T=1$), equation (3.17) reduces to

$$\boldsymbol{\varepsilon}'_T = \boldsymbol{\varepsilon}' \tag{4.42}$$

Hence

$$\boldsymbol{\alpha}' = \boldsymbol{\varepsilon}' \tag{4.43}$$

To determine $\boldsymbol{\delta}$, solve equation (4.39) only for the thermal forces since the resultant forces at the boundary of the RVE by the external stress field are zero. This is referred to as the seventh load case. The value of $\boldsymbol{\varepsilon}'$ is calculated from the equation (4.14) and the coefficients of $\boldsymbol{\alpha}'$ can be determined using equation (3.19).

4.5 Test Models

Two different test models were used to evaluate the proposed *full cyclic constraint* boundary conditions by applying a finite element method based on the homogenization procedure. The materials used for these models were assumed to satisfy all the previously described requirements of the homogenization procedures. In the first model,

the equivalent properties were determined using both the homogenization procedure and an analytical method. The procedure of full cyclic constraint was validated by a comparison of the calculated results. The validity of different possible RVEs for a continuum was evaluated in the second test model.

4.5.1 First Test Model

An elastic composite continuum, which consisted of a matrix reinforced by a hard uniform strip (fibre) with a 1:2 fibre-matrix volume ratio, was used for the homogenization analysis. The matrix and fibre were assumed to be isotropic with respect to their local axes. Two different representative volume elements with the same volume fraction, identified as RVE1 and RVE2 were chosen to define the microstructure of the continuum with respect to global (x, y, z) and local (t, r, l) axes respectively. These elements are illustrated in Figure 4.7, and were analysed for the selected stiffness and thermal expansion properties. The properties of fibre were E=350 GPa, ν=0.2, G=150 GPa and α=0.1, while the properties of matrix were E=3 GPa, ν=0.4, G=1 GPa and α=0.4. Both the RVE1 and RVE2 models were analysed using the numerical homogenization procedure in a finite element method. An analytical method was also applied to RVE2.

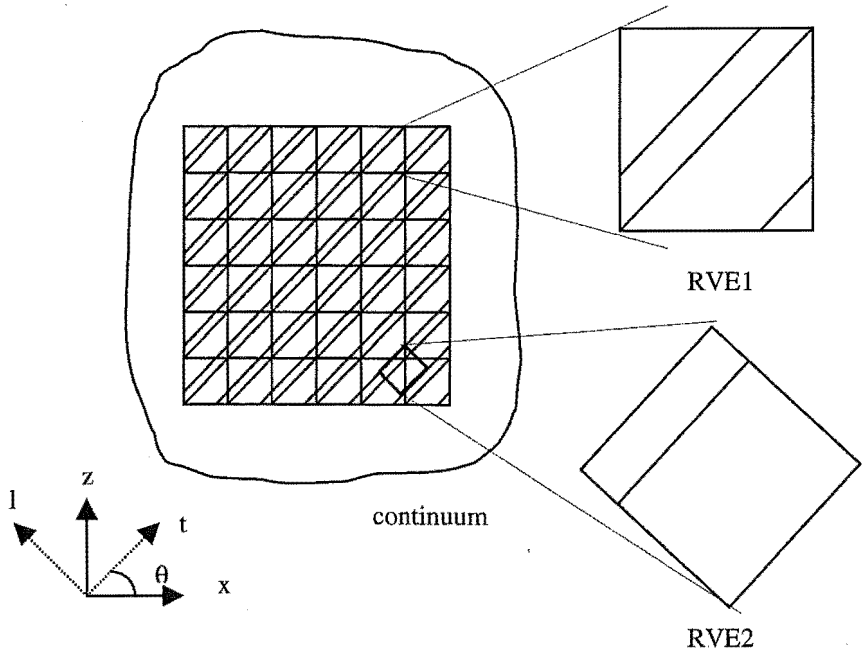

Figure 4.7. x-z face of a composite with strips

4.5.1.1 Homogenization Analysis

For the numerical procedure, the finite element mesh of RVE1 was generated using 4-node tetrahedron elements and the equivalent properties were determined oriented with respect to the global axes for the seven load cases and under full cyclic constraints.

The equivalent compliance matrix $\mathbf{C}_g'$ and effective thermal expansion coefficient α_g' of RVE1 determined by the homogenization procedure are

$$\mathbf{C}_g' = \begin{pmatrix} 0.1946 & -0.0026 & -0.1398 & 0.0000 & -0.0499 & 0.0000 \\ -0.0026 & 0.0084 & -0.0026 & 0.0000 & 0.0018 & 0.0000 \\ -0.1398 & -0.0026 & 0.1946 & 0.0000 & -0.0499 & 0.0000 \\ 0.0000 & 0.0000 & 0.0000 & 0.3443 & 0.0000 & -0.3246 \\ -0.0499 & 0.0018 & -0.0499 & 0.0000 & 0.1238 & 0.0000 \\ 0.0000 & 0.0000 & 0.0000 & -0.3246 & 0.0000 & 0.3443 \end{pmatrix} \text{ and } \alpha_g' = \begin{pmatrix} 0.3331 \\ 0.1066 \\ 0.3331 \\ 0.0000 \\ -0.4529 \\ 0.0000 \end{pmatrix}$$

where subscript g of $\mathbf{C}_g'$ and α_g' refers to the x,y,z coordinate system

The properties $\mathbf{C}_g'$ and α_g' of RVE1 were transformed to the local axes according to the procedure described in Section (3.2.3). The transformed equivalent compliance matrix $\mathbf{C}_l'$ and effective thermal expansion coefficient α_l' are given below.

$$\mathbf{C}_l' = \begin{pmatrix} 0.0084 & -0.0017 & -0.0035 & 0.0000 & 0.0000 & 0.0000 \\ -0.0017 & 0.0084 & -0.0035 & 0.0000 & 0.0000 & 0.0000 \\ -0.0035 & -0.0035 & 0.1083 & 0.0000 & 0.0000 & 0.0000 \\ 0.0000 & 0.0000 & 0.0000 & 0.0197 & 0.0000 & 0.0000 \\ 0.0000 & 0.0000 & 0.0000 & 0.0000 & 0.6689 & 0.0000 \\ 0.0000 & 0.0000 & 0.0000 & 0.0000 & 0.0000 & 0.6689 \end{pmatrix} \text{ and } \alpha_l' = \begin{pmatrix} 0.1067 \\ 0.1067 \\ 0.5596 \\ 0.0000 \\ 0.0000 \\ 0.0000 \end{pmatrix}$$

where subscript l of $\mathbf{C}_l'$ and α_l' refers to the t,r,l coordinate system

The mesh for RVE2 was generated using an 8-node brick element with respect to the local axes and the equivalent properties were determined by the numerical procedure. The derived equivalent compliance matrix and effective thermal expansion coefficient of RVE2 are equal to $\mathbf{C}_l'$ and α_l' respectively.

4.5.1.2 Analytical Method

The representative element RVE2, in which the axes of the fibre are orientated with respect to the local (t, r, l) axes as shown in Figure 4.8, was used in the analytical procedure to determine the equivalent properties. The stresses normal to the interface of the fibre and matrix as well as the strain components parallel to the interface are compatible. The remaining relationships between the stress and strain components of the fictitious homogenized material can be related to

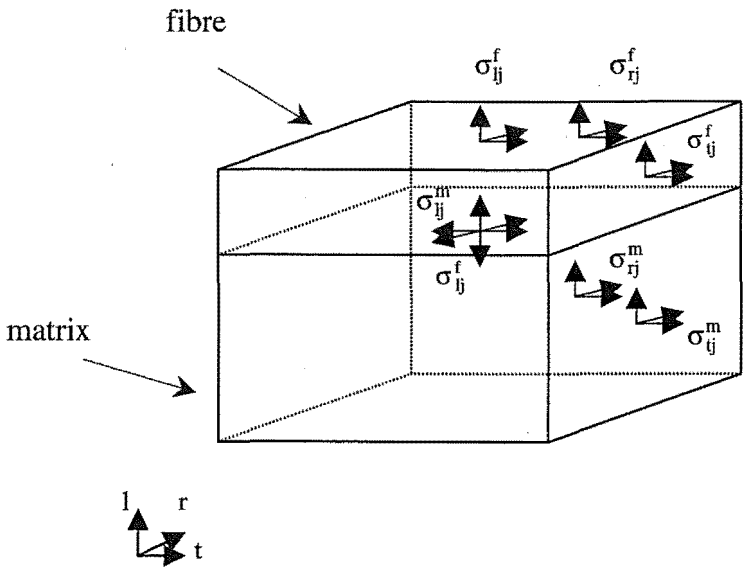

Figure 4.8. RVE2 referred to t ,r, l axes

the stress strain components of the fibre and matrix by the constitutive equations as explained by Chou and Carleone (1972) for a periodic layered composite. The constitutive equation for the fibre is

$$\begin{bmatrix} e_t \\ e_r \\ \gamma_{tr} \\ \hline e_l^f \\ \gamma_{lt}^f \\ \gamma_{rl}^f \end{bmatrix} = \left[\begin{array}{cc|cc} & & & \\ & C_{11}^f & & C_{12}^f \\ & & & \\ \hline & & & \\ & C_{21}^f & & C_{22}^f \\ & & & \end{array}\right] \begin{bmatrix} \sigma_t^f \\ \sigma_r^f \\ \tau_{tr}^f \\ \hline \sigma_l \\ \tau_{lt} \\ \tau_{rl} \end{bmatrix} \tag{4.44}$$

where the suffix *f* refers to the components for the fibre and no suffix is used for the components of the fictitious homogenized material

The constitutive equation for the matrix is,

$$\left[\begin{array}{c} e_t \\ e_r \\ \gamma_{tr} \\ \hline e_l^m \\ \gamma_{lt}^m \\ \gamma_{rl}^m \end{array}\right] = \left[\begin{array}{c|c} C_{11}^m & C_{12}^m \\ \hline C_{21}^m & C_{22}^m \end{array}\right] \left[\begin{array}{c} \sigma_t^m \\ \sigma_r^m \\ \tau_{tr}^m \\ \hline \sigma_l \\ \tau_{lt} \\ \tau_{rl} \end{array}\right] \tag{4.45}$$

where again no suffix is used for the components of the fictitious homogenized material and the suffix *m* refers to the components of the matrix

If the volume ratio of the fibre and the matrix is $v_f : v_m$, the following relationships can be developed for the stress and strain components that are not parallel to the interface.

$$\begin{bmatrix} e_l \\ \gamma_{lt} \\ \gamma_{rl} \end{bmatrix} = v_m \begin{bmatrix} e_l^m \\ \gamma_{lt}^m \\ \gamma_{rl}^m \end{bmatrix} + v_f \begin{bmatrix} e_l^f \\ \gamma_{lt}^f \\ \gamma_{rl}^f \end{bmatrix} \tag{4.46}$$

$$\begin{bmatrix} \sigma_t \\ \sigma_r \\ \tau_{tr} \end{bmatrix} = v_m \begin{bmatrix} \sigma_t^m \\ \sigma_r^m \\ \tau_{tr}^m \end{bmatrix} + v_f \begin{bmatrix} \sigma_t^f \\ \sigma_r^f \\ \tau_{tr}^f \end{bmatrix} \tag{4.47}$$

The constitutive equation for the equivalent fictitious homogenized material with respect to local, l, t & r, axes is

$$\left[\begin{array}{c} e_t \\ e_r \\ \gamma_{tr} \\ \hline e_l \\ \gamma_{lt} \\ \gamma_{rl} \end{array}\right] = \left[\begin{array}{c|c} C_{11} & C_{12} \\ \hline C_{21} & C_{22} \end{array}\right] \left[\begin{array}{c} \sigma_t \\ \sigma_r \\ \tau_{tr} \\ \hline \sigma_l \\ \tau_{lt} \\ \tau_{rl} \end{array}\right] \tag{4.48}$$

By solving equations (4.44) to (4.47), the sub-matrices C_{11}, C_{12}, C_{21} and C_{22} of the equation (4.48) can be related to the sub-matrices of equations (4.44) and (4.45) as follows:

$$C_{11} = (v_m (C_{11}^m)^{-1} + v_f (C_{11}^f)^{-1})^{-1} \tag{4.49}$$

$$C_{12} = C_{11}(v_m (C_{11}^m)^{-1} C_{12}^m + v_f (C_{11}^f)^{-1} C_{12}^f) \tag{4.50}$$

$$C_{21} = (v_m C_{21}^m (C_{11}^m)^{-1} + v_f C_{21}^f (C_{11}^f)^{-1}) C_{11} \tag{4.51}$$

$$C_{22} = (v_m C_{21}^m (C_{11}^m)^{-1} + v_f C_{21}^f (C_{11}^f)^{-1}) C_{12} + v_m (C_{22}^m - C_{21}^m (C_{11}^m)^{-1} C_{12}^m) + v_f (C_{22}^f - C_{21}^f (C_{11}^f)^{-1} C_{12}^f) \tag{4.52}$$

Since the sub-matrices of equations (4.44) and (4.45) are known, C_{11}, C_{12}, C_{21} and C_{22} can be determined from equations (4.49) to (4.52). Hence the equivalent compliance matrix **C** of the representative element RVE2 can be determined and is given by

$$\mathbf{C} = \begin{pmatrix} 0.0084 & -0.0017 & -0.0035 & 0.0000 & 0.0000 & 0.0000 \\ -0.0017 & 0.0084 & -0.0035 & 0.0000 & 0.0000 & 0.0000 \\ -0.0035 & -0.0035 & 0.1083 & 0.0000 & 0.0000 & 0.0000 \\ 0.0000 & 0.0000 & 0.0000 & 0.0197 & 0.0000 & 0.0000 \\ 0.0000 & 0.0000 & 0.0000 & 0.0000 & 0.6689 & 0.0000 \\ 0.0000 & 0.0000 & 0.0000 & 0.0000 & 0.0000 & 0.6689 \end{pmatrix}$$

The transformed equivalent compliance matrix $\mathbf{C}_l'$ that was determined by the homogenization method and the equivalent compliance **C** are equal.

4.5.2 Second Test Models

For the second test case, an elastic composite continuum reinforced with uniform hollow hard spherical particles (fibres) consisting of repeating unit cells was analysed. This was carried out for a matrix and fibre that had similar stiffness and thermal expansion properties to that used for first test model. A finite element mesh of the representative element RVE was generated using 8-node brick elements to accommodate various positions of the sphere. For the homogenization process two different unit cells with the same volume fraction were chosen as illustrated in figure (4.9), i.e. RVES1 and RVES2. The numerical procedures were carried out on both RVES1 and RVES2 for the seven cases and full cyclic constraints.

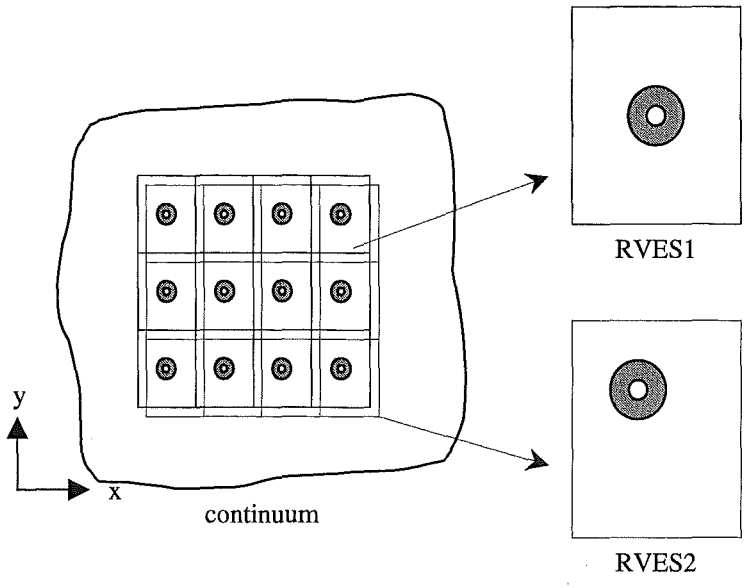

Figure 4.9. x-z face of composite with sphere particles

The equivalent properties were determined for various numbers of elements of RVES1 and RVES2. The stiffness matrices and thermal expansion coefficients which were determined using a fine mesh with 1764 elements are given below for RVES1

$$\mathbf{D}_{s1}=\begin{pmatrix} 8.32516 & 4.97893 & 4.97891 & 0.00000 & 0.00000 & 0.00000 \\ 4.97893 & 8.32515 & 4.97892 & 0.00000 & 0.00000 & 0.00000 \\ 4.97891 & 4.97892 & 8.32515 & 0.00000 & 0.00000 & 0.00000 \\ 0.00000 & 0.00000 & 0.00000 & 1.36618 & 0.00000 & 0.00000 \\ 0.00000 & 0.00000 & 0.00000 & 0.0000 & 1.36618 & 0.00000 \\ 0.00000 & 0.00000 & 0.00000 & 0.0000 & 0.00000 & 1.36618 \end{pmatrix} \text{ and } \alpha_{s1}=\begin{pmatrix} 0.06887 \\ 0.06887 \\ 0.06887 \\ 0.00000 \\ 0.00000 \\ 0.00000 \end{pmatrix}$$

For RVES2 the stiffness matrices and thermal expansion coefficients are

$$\mathbf{D}_{s2}=\begin{pmatrix} 8.32510 & 4.97890 & 4.97893 & 0.00000 & 0.00004 & -0.00003 \\ 4.97890 & 8.32511 & 4.97890 & -0.00003 & -0.00002 & 0.00002 \\ 4.97893 & 4.97890 & 8.32510 & -0.00001 & -0.00002 & -0.00003 \\ 0.00000 & -0.00003 & -0.00001 & 1.36616 & 0.00001 & 0.00001 \\ 0.00004 & -0.00002 & -0.00002 & 0.00001 & 1.36616 & 0.00002 \\ -0.00003 & 0.00002 & -0.00003 & 0.00001 & 0.00002 & 1.36616 \end{pmatrix} \text{ and } \alpha_{s2}=\begin{pmatrix} 0.06889 \\ 0.06889 \\ 0.06889 \\ 0.00000 \\ 0.00001 \\ 0.00000 \end{pmatrix}$$

The properties produced by the fine mesh for both RVEs were found to be almost equal whereas the coarse mesh produces errors especially in RVES2 due to the dissimilar

shape and size of the element. The graph in Figure (4.10) shows the variation of equivalent modulus of elasticity in x-direction from both RVEs with the number of elements used in the FEM analysis.

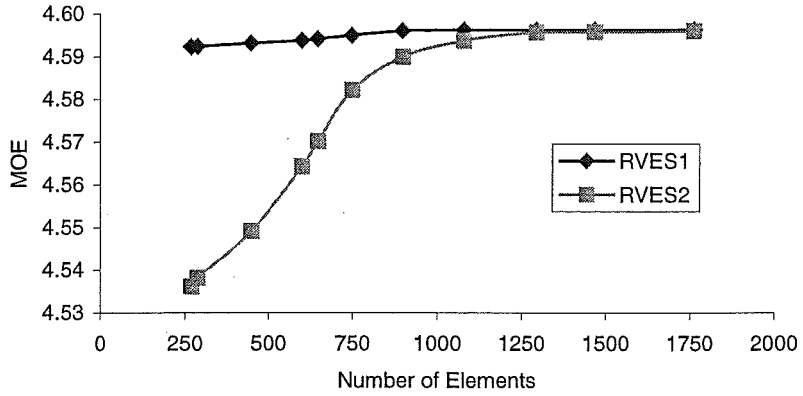

Figure 4.10. Variation of equivalent MOE with mesh number

4.6 Discussion

The objective of the study was to implement and evaluate the homogenization procedure using FEM with full cyclic constraint conditions. Two test models were designed for the computer simulation and the results were analysed to validate the cyclic constraint procedure. For the first model, strip-shaped fibres were regularly aligned at a fixed angle with the stiffness compliance matrix and thermal expansion coefficients being determined by the cyclic constraint approach and using analytical methods. The results were found to be equal and hence the cyclic constraint approach was verified.

In the second test model, the cyclic constraint approach was applied to two different representative volume elements of a composite that consisted of regularly distributed hollow spherical particles. The first RVE, RVES1, had a hollow sphere at its centre whereas the second RVE, RVES2, had the hollow sphere at a position one third of the length of the side along the x, y and z axis from the corner. The homogenization procedure was carried out for different number of finite element meshes of both RVEs. Each analysis of RVES1 produced the same stiffness matrix and thermal expansion coefficients. The analysis of RVES2 with fine finite element mesh produced results that were equal to the results of RVES1 as shown Figure (4.8). The accuracy of the results

from RVES2 with a coarse mesh were lower than that with a refined mesh due to the unsymmetrical shape and size of elements. From the analysis of the second model, it is proved that the cyclic constraint based RVE method is independent of the geometry of inclusions present and the choice of RVE in the continuum although with increasing asymmetry in the location of the inclusion a finer mesh is required.

The test models therefore prove that the homogenization procedure based on the application of full cyclic constraint by the finite element method provides reliable homogenized properties irrespective of the choice of RVE. Furthermore the constraint relationships of the degrees of freedom were based on the linear equations and thus minimising the computing truncation errors. The full cyclic constraint requires less effort to implement in the finite element method. The application does not depend on the volume fraction, size, shape and orientation of the constituents. It is therefore a suitable method to determine the equivalent properties of complex natural composite materials like wood and bone tissue. However in a composite with complex structure, the number of RVEs might be chosen at different levels of structure and analysed from lower level to the highest. It is a general practice to homogenize the wood from its ultrastructure to macrostructure and it has been reported elsewhere, for example Astley *et al* (1998).

Chapter 5

Modelling Wood Behaviour at Micro Level

5.1 Introduction

As explained in chapter 2 softwood is a heterogeneous fibrous material. The complex microstructure and inhomogeneity that exist at different levels make computer models necessary to predict the shrinkage and stiffness properties. Computer simulation using numerical modeling can be carried out at three different geometrical scales. These are at the microfibril, cellular structure and board levels. The sequence of modelling is illustrated in Figure 1.3.

The microfibrils are the repeating units of the cell wall layers and can be chosen as the representative volume element of each cell wall layer. The microfibril model accepts as input data the estimated local values of volume fractions and elastic properties of the chemical constituents of each cell wall layer and converts these into effective orthotropic stiffness and shrinkages for a representative microfibril element. The cellular model combines these data with further cellular information such as the distribution of microfibril angle (MFA) throughout the cell wall layers, volume fraction of the cell wall layers, cell aspect ratios and density variation of wood as the basis for computing the equivalent local values for the clearwood stiffness and shrinkage properties.

These properties of clearwood were predicted by modelling a cell as a representative volume element and are listed in Appendix (C) as a function of density and microfibril angle. The procedures for modelling the cell, validating the results of the cell models, and the experimental method used at cellular level to determine the shrinkage coefficients for the clearwood are presented in this chapter.

5.1.1 Cell Wall Model

Persson (2000) predicted the equivalent stiffness and shrinkage properties of cell wall layers by using the representative volume element based the homogenization method. The resultant models used the properties of the chemical constituents as the input data

to determine the equivalent properties of different cell wall layers from the microfibril models. This is briefly discussed since these properties were used in the simulation of the cell. Persson used simple geometrical models of the microfibrils that have a rectangular cross section similar to the illustrations in Figure 2.9 and on infinite length. In cross-section the cellulose chains are assumed to be located in the center surrounded by a matrix of hemicellulose and lignin. The volume fractions of the chemical constituents differ within the different layers of cell wall as shown in Figure 2.7. The values of the volume fractions at 0% and 12% moisture contents for the five layers, middle lamella (ML), primary wall (PW), S_1, S_2, and S_3 are given in Table 5.1. In the microfibril model, the variations of the volume fractions were defined by the variations of thickness of each chemical constituent since each constituent was assumed to be distributed evenly in the microfibril.

Table 5.1. Volume fractions of the chemical constituents of the cell wall layers used in the microfibril model.

Cell wall layers	Fraction at 0% moisture content			Fraction at 12% moisture content		
	Cellulose (%)	Hemicell-ulose (%)	Lignin (%)	Cellulose (%)	Hemicell-ulose (%)	Lignin (%)
S_2 and S_3 layers	49	27	24	44.3	31.6	24.1
ML, PW and S_1 layers	20	15	65	18.0	17.4	64.6

The stiffness and shrinkage properties of the chemical constituents used in the microfibril model were reported by Cave (1978). Cellulose and hemicellulose are transversely isotropic materials, whereas lignin is an isotropic material. A transversely isotropic material is isotropic in one plane and has different properties in the direction normal to the plane. Persson used three sets identified as low, medium and high stiffness and moisture-induced coefficients for the constituents as input data to model the microfibril structure. The second set of medium coefficients at 12% moisture content which is the average of the first and the third sets is listed in Table 5.2. These coefficients are given in relation to the local axes of the microfibril, where the 1-axis, 2-axis and 3-axis are oriented in the circumferential, cell wall thickness and longitudinal direction of microfibril respectively. Cellulose was assumed to be

unaffected by moisture changes in all three directions while in hemicellulose, the longitudinal properties were assumed to be independent of moisture effects. The stiffness properties of cellulose, hemicellulose and lignin were also assumed to be constant for a change in moisture from 0 to 12%.

Table 5.2. Stiffness and shrinkage coefficients of the chemical constituents.

Constituent	Coefficient	Property
Cellulose	E_{33} (Gpa)	150.0
	E_{11} (Gpa)	17.5
	G_{31} (Gpa)	4.5
	ν_{13}	0.01
	ν_{21}	0.50
Hemicellulose	E_{33} (Gpa)	16.0
	E_{11} (Gpa)	3.5
	G_{31} (Gpa)	1.5
	ν_{13}	0.10
	ν_{21}	0.40
	α_{33}	0.000
	$\alpha_{11} = \alpha_{22}$	1.368
Lignin	E (Gpa)	2.75
	ν	0.33
	$\alpha_{11} = \alpha_{22} = \alpha_{33}$	0.351

Computer simulation using microfibril models for each layer of cell wall were implemented by the finite element based homogenization procedure. The equivalent properties were obtained from the microfibril models for changes of moisture content from 0% to 12% at constant temperatures. The predicted equivalent properties of the cell wall layers are given in Table 5.3. These layer properties were used as input data to the cell models to determine the equivalent macroscopic properties of the wood in this study.

Table 5.3. Equivalent stiffness and hygroexpansion coefficients for the five layers of cell wall from the microfibril model.

Coefficient	S_2 and S_3 layers	ML, PW and S_1 layers
E_{11} GPa	7.48	4.69
E_{22} GPa	6.13	3.17
E_{33} GPa	72.6	31.7
G_{31} (Gpa)	3.13	1.85
G_{32} (Gpa)	2.97	1.68
G_{12} (Gpa)	1.75	1.18
ν_{13}	0.0234	0.0419
ν_{23}	0.0199	0.0377
ν_{21}	0.433	0.467
α_{11}	0.353	0.477
α_{22}	0.587	0.477
α_{33}	0.0093	0.0089

5.1.2 Existing Cell Models

Various mathematical models were proposed and developed to predict stiffness and shrinkage properties of wood at cellular levels. Most of these models are based on analytical approaches. Shrinkage anisotropy in terms of the shrinkage behaviour of the cellular components of the cell wall models were developed in 1942 by considering a cell as consisting as a rectangular tube. This is known as the Preston models (Barrett *et al.* 1972). Deformation patterns were calculated in the single-layer in terms of the MFA and the swelling potential of cellulose. However these models do not account for restraint effects produced by differences in swelling potential of the cell wall constituents. Barber *et al.* (1964), Barber (1968), Cave (1972) and Barrett *et al.* (1972) considered multi-layer models of the cell with its anisotropic constituents. These models were then further improved by Cave (1978) incorporating swelling and stiffness properties of the constituents. Koponen *et al.* (1989 and 1991) refined the previous models by estimating elastic and shrinkage properties of softwood using a

two-dimensional honeycomb structure. The properties of the earlywood and latewood were determined separately using different densities and cell properties for these two differing regions. The complete growth ring properties were not derived.

The elastic properties of cell wall constituents were modeled by Navi and Huet (1989a) based on the homogenization of the cell wall as the rectangular tube. Yamamoto (1994) developed a model based upon Barber's work incorporating all the cell-wall layers to represent the anisotropic swelling process during water adsorption. In this model, the stiffness and strain in the longitudinal and transverse directions were determined as a function of moisture content. Improved finite element models of the elastic properties of softwood were presented by Astley *et al.* (1998). The finite element models enabled the stiffness to be determined as a function of the MFA by homogenizing the cell wall structure. This homogenization of cell wall structure was further extended to model the variation of longitudinal, transverse and radial shrinkage with MFA by Astley *et al.* (1997). The radial and tangential walls were assumed to have the same MFA in the model while the effects of the pit apertures in the radial walls were not taken into account in the calculation of radial shrinkage. The concluding remarks made by Astley *et al.* (1997) are the basis for this study of the cell models. Those remarks are: "the availability of better and more detailed information on cell wall structure and composition, and a systematic study of the sensitivity of output assumptions in conjunction with further experiments are important next steps in the further development of this approach".

5.2 New Cell Model

5.2.1 Periodic Nature of Wood at Micro Level

The tracheids of late- and transitionwood in *pinus radiata* are shaped more or less as rectangles, whereas the tracheids of the earlywood usually have the shape of irregular hexagons. Experimental results giving the distribution of *pinus radiata* cell wall length and orientation relative to the radial direction are shown in Figure 5.1, and show that nearly 60% of cell walls are orientated predominately along the radial and tangential directions. The cell wall length and orientation relative to the radial direction as zero were measured for more than 1000 walls using images obtained from a recently developed microscopic technique that will be described later in the chapter.

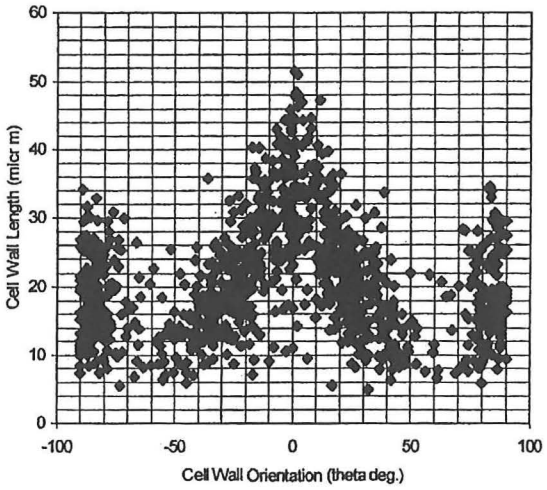

Figure 5.1. Distribution of cell wall length and orientation relative to the radial direction (Entwistle and Navaranjan (2001)).

The tracheids are the major contributors to the stiffness and shrinkage properties of softwood as explained in chapter 2. For the simplification of the homogenization procedure, the wood can be assumed to be a heterogeneous continuum which consists of periodically arranged rectangular long narrow straight tracheids (cells) as shown in Figure 5.2.

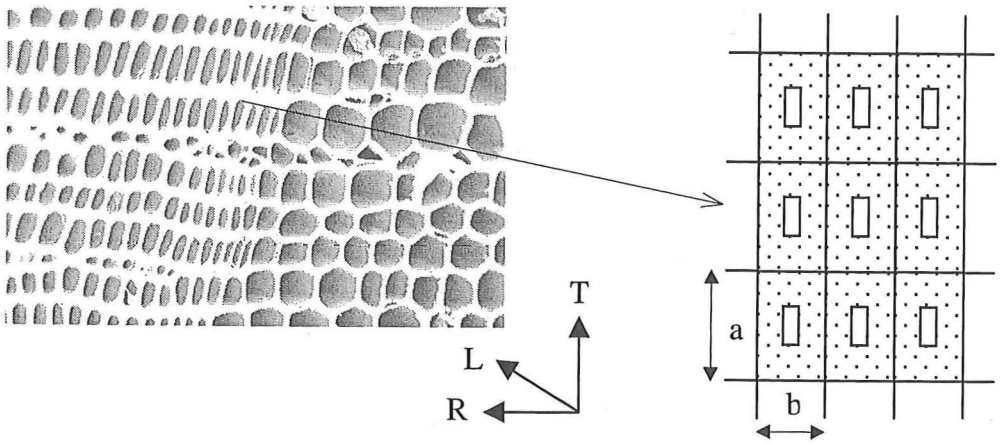

Figure 5.2. Simplified model of periodic cells in *pinus radiata* softwood.

In this arrangement a tracheid can be chosen as a representative volume element (RVE) and the wood continuum can be assumed to satisfy all compatibility conditions for the periodic nature of the structure. Consequently the homogenization procedure

using cyclic boundary conditions that have been described in chapter 4 can readily be implemented to predict the equivalent properties of wood as a function of density and microfibril angle (MFA).

The average aspect ratios (a:b) of the cells for earlywood, transitionwood and latewood are assumed to be 2:3, 1:1 and 3:2 respectively. From the experimental results as shown by the graphs in Appendix (F), the density of earlywood, transitionwood and latewood of *pinus radiata* can be considered to vary within the range of 200-450, 450-500 and 500-900 kg/m^3 respectively.

5.2.2 Homogenization of Cell Model

To model a cell as an RVE of the wood continuum, a three-dimensional cell was considered to consist of a long narrow tube made up of five layers: middle lamella (ML), primary wall (PW), S_1, S_2 and S_3. The PW, S_1, S_2 and S_3 were assumed to have uniform thickness over the cell wall. The distribution of material in the ML layer can be seen in Figure 5.3 showing an increased thickness at the corners.

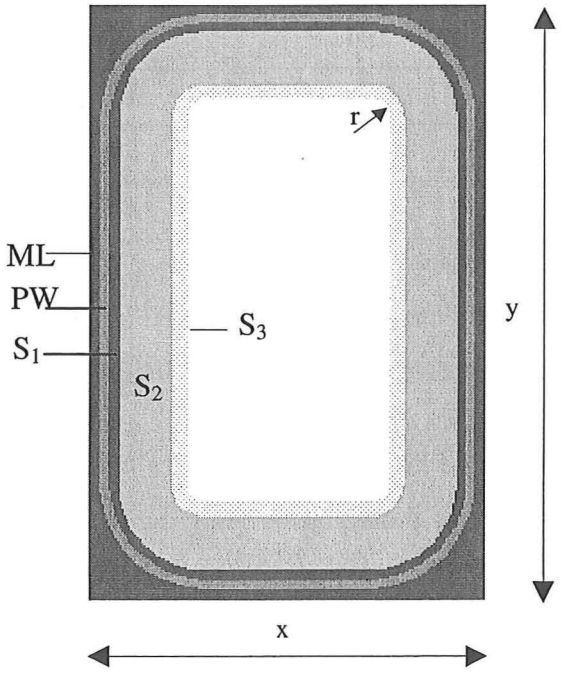

Figure 5.3. Cross-section of cell model with five cell wall layers.

The volume fractions of the cell layers of early- and latewood for *loblolly pine* were reported by Saka (2001) and the densities of these layers were listed by Harrington (2002). These parameters for the S_1, S_2 and S_3 layers, and the combination of ML and PW (listed as CML) layers are given in Table 5.4. Since the ML and PW layers have identical properties, either the volume fraction of the CML can be conveniently considered to consist of two separate layers, ML and PW in the model or can be combined to a single layer representing both ML and PW layers. The cell wall layers of transitionwood were assumed to have the same volume fractions and densities as the latewood.

Table 5.4. Volume fractions and densities of cell wall layers of early- and latewood.

Wood	Cell wall layer	Tissue Volume (%)	Density (kg/m^3)
Earlywood	S_1	13	1393
	S_2	60	1424
	S_3	9	1408
	CML	18	1329
Latewood	S_1	6	1393
	S_2	80	1424
	S_3	5	1408
	CML	9	1329

The volume fractions and the densities of the cell wall layers were used to determine the thickness of the representative layers in the cell model for a given wood density.

The volume fractions of ML, PW, S_1, S_2 and S_3 are taken as v_1, v_2, v_3, v_4 and v_5 respectively, with the density of those layers being d_1, d_2, d_3, d_4 and d_5 respectively. The thickness of ML, PW, S_1, S_2 and S_3 are taken as t_1, t_2, t_3, t_4 and t_5.

The density of the cell wall material can be given by

$$d_w = \sum_{i=1}^{5} d_i v_i \qquad (5.1)$$

Volume ratio of the cell and cell wall material is proportional to area ratio of the cross section of the cell and cell wall. Since the mass of the cell is equal to the mass of the cell wall material, the area of the cell wall section is represented by

$$A_w = \frac{d_c A_c}{d_w} \tag{5.2}$$

where d_c is the density of the cell, A_c ($A_c = xy$) is the area of the cross-section of cell, and A_i ($A_i = A_c - A_w$) is the area of the section of lumen

By considering the area of the cross section of the cell and each cell layer the following thicknesses were obtained;

the cell wall

$$t = (x + y - ((x + y)^2 - 4(A_w + (\pi - 4)r^2))^{\frac{1}{2}} \tag{5.3}$$

S_3 layer

$$t_5 = \frac{((x + y - 4r - 4t + \pi r)^2 + \pi v_5 A_w)^{\frac{1}{2}} - (x + y - 4r - 4t + \pi r)}{\pi} \tag{5.4}$$

S_2 layer

$$t_4 = \frac{((x + y - 4r - 4t + \pi(r + t_5))^2 + \pi v_4 A_w)^{\frac{1}{2}} - (x + y - 4r - 4t + \pi(r + t_5))}{\pi} \tag{5.5}$$

S_1 layer

$$t_3 = \frac{((x + y - 4r - 4t + \pi(r + t_5 + t_4))^2 + \pi v_3 A_w)^{\frac{1}{2}} - (x + y - 4r - 4t + \pi(r + t_5 + t_4))}{\pi} \tag{5.6}$$

primary wall

$$t_2 = \frac{((x + y - 4r - 4t + \pi(r + t_5 + t_4 + t_3))^2 + \pi v_2 A_w)^{\frac{1}{2}} - (x + y - 4r - 4t + \pi(r + t_5 + t_4 + t_3))}{\pi} \tag{5.7}$$

middle lamella

$$t_1 = \frac{(x+y-(4-\pi)(r+t))-((x+y-(4-\pi)(r+t))^2-\pi(v_1A_w-(4-\pi)(r+t)))^{\frac{1}{2}}}{\pi} \quad (5.8)$$

A finite element mesh was generated using 8-nodes brick elements to carry out the numerical simulations, as shown in Figure 5.4, to model the five wall-layers that make up the cell.

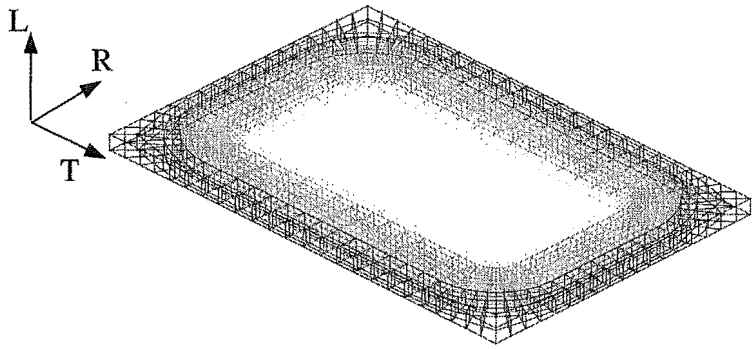

Figure 5.4. Cell mesh.

The mesh has the capability to adapt to any number of elements, different thickness of the layers and different radius of curvature of the layers. The thickness of each layer is a function of the volume fraction, density of the layer, aspect ratio of the cell and density of the wood.

The equivalent stiffness and shrinkage properties of each layer listed in Table 5.3 for 12% moisture content are given referring to the local Cartesian coordinate system (1, 2, 3) of the microfibril. These properties were used as input constitutive coefficients for the cell model. Each of the cell wall layers was considered as a homogeneous orthotropic material. The microfibrils in S_1, S_2 and S_3 layers are oriented at different microfibril angles with respect to the local coordinate system (c1, c2, c3) of the cell walls as shown in Figure 5.5. The c1- axis is along the circumferential direction of

cell wall, c2- axis is oriented in the direction of the cell wall thickness and c3- axis is oriented in the longitudinal direction. The microfibril angles (MFA) of S_1 and S_3 were taken as a fixed value of 75°, and that of S_2 was considered varying from 0° to 50°. The MFA of the ML and PW layers were taken as zero. The four walls of the rectangular cell are orientated at 0°, 90°, 180° and 270° angles with the local T-axis of the cell (Figure 5.4).

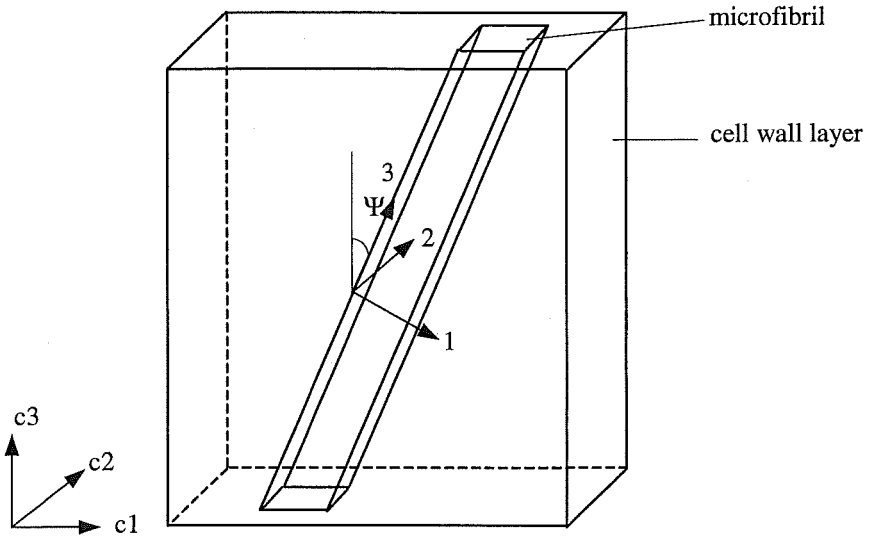

Figure 5.5. Orientation of microfibril in a cell wall layer.

As the microfibrils are wound around the cell wall in each layer, two transformations are therefore necessary to refer the constitutive properties of the layers to the local coordinate system of the cell. The first transformation relates the properties from the local coordinates of microfibril to the local coordinates of the cell wall. The second transformation relates the properties of the cell wall to global coordinate system using the transformation procedure from chapter 3. If the microfibril angle is ψ and the rotation is around the axis (2) perpendicular to the cell wall, the direction cosine matrix $M(\psi)$ can be determined from equation (3.21). Similarly if the orientation of the cell wall with the local axis of the cell is ω in the T-R plane and rotated about the c3-axis, the direction cosine matrix $M(\omega)$ can be determined. The second rotation is performed for the elements from corner to corner of each of the four walls. By combining both rotations as in equation (3.23)

$$M = M(\psi)M(\omega) \tag{5.9}$$

M is used to obtain the transformation matrix **T** based upon equation (3.30). By using **T**, the stiffness matrix $\mathbf{D}_{cl}$ and the shrinkage coefficient matrix α_{cls} of a cell wall layer with respect to local axis of cell can be determined from the local constitutive coefficients of the respective layers.

$$\mathbf{D}_{cl} = \mathbf{T}^T\mathbf{D}_m\mathbf{T}, \qquad \alpha_{cls} = \mathbf{T}^T\alpha_{ms} \tag{5.10}$$

where $\mathbf{D}_m$ and α_{ms} are the matrices of stiffness and shrinkage coefficients of a layer referring to the local coordinate system of the microfibril

The equivalent stiffness and shrinkage properties were predicted by the finite element method based homogenization procedure as described in chapter 4. For each of the six load cases, the cyclic boundary conditions were applied and the equivalent constitutive coefficients of wood were calculated from the cell model. Subsequently for the seventh case which is for the moisture-induced load resulting from a unit increase of moisture, the swelling coefficients (equal to shrinkage coefficients) were calculated from the cell model. The simulations were carried out for every 5^o of MFA from 0^o to 50^o as well as for every 50 kg/m^3 of cell density from 200 to 900 kg/m^3. The aspect ratios of the cell and the densities of wood were changed depending on whether early-, transition- and latewood were being modelled. These equivalent properties are listed in Appendix (C) as a function of the MFA of S_2 and the density of wood. The deformed meshes of the cell models for the seven load cases are also shown in Appendix (D). For all simulations of the cell models, the programme codes were written in FORTRAN 90 and the meshes were plotted in TECPLOT.

5.3 Measuring Transverse Shrinkage Coefficients at Cellular Level

Investigation and measurement of the transverse shrinkage properties at a cellular level needs well-defined images of the cell structure at different moisture contents. Thin sections of wood can be used to produce images using an optical microscope, but cracking and damage to the cell wall is possible when preparing the sections. Further, the sections do not always represent the ensemble of wood. To replicate the

wood surface, Watanabe *et al* (1998a and 1998b) pushed a small wood specimen (5mm x 5mm x 30mm) onto a polyethylene film that has been softened at 130°C to transfer topographical surface information into the film. Subsequently the film was examined using either an optical microscope or a scanning electron microscope and analyzed using a power spectrum analysis method. The procedure was repeated at different moisture contents, and the changes of cell geometry and shrinkage properties were determined. The replica method has drawbacks:

(a) when small cross-sections (5mm x 5mm) are forced into contact with the film at 130° C the change of temperature will cause thermal strain, while the applied force will result in elastic strain on the structure of the specimen surface,
(b) requires equipment to ensure that the surface is normal to the film and that a repeatable interface pressure is applied,
(c) error might arise while tracing the image from the replica prior to transfer to the power spectrum analysis.

To overcome these difficulties, a new technique was developed to measure the changes of dimensions and geometry of cells due to moisture variation using optical microscopy. This technique reveals the microstructure of a surface of the specimen in the wet or dry conditions without any surface treatments or use of replicas. This method was also used to measure cell wall lengths as explained in Appendix (E) and reported in an article by Entwistle and Navaranjan (2001).

5.3.1 Specimen Preparation and Measurement

A log from a selected 20 years old *pinus radiata* tree in the Bottle Lake plantation forest was sawn into four sections, identified as A, B, C and D (from butt to top) in Figure 5.6.

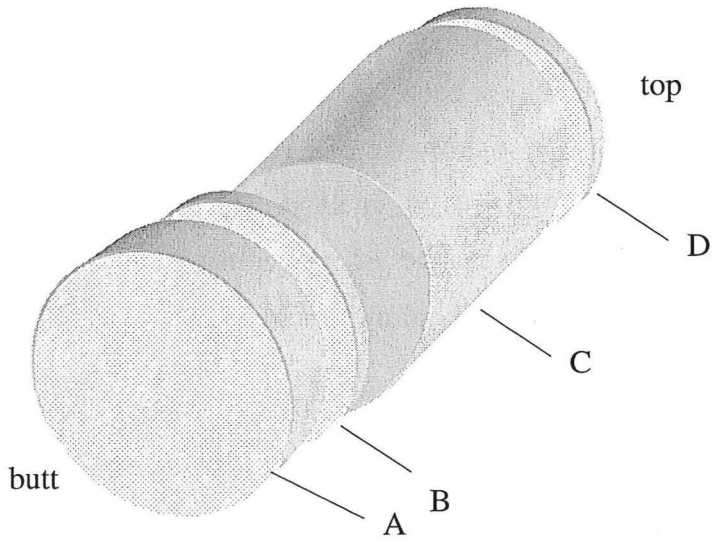

Figure 5.6. Sections of log used for specimen preparation.

The 160 mm thick disc A was used for another research project. The 50 mm thick discs B and D were used to make specimens for the measurement of microfibril angle (MFA), spiral grain angle (SGA), density and shrinkage parameters at a micro or cellular level. Specimens for the investigation of board shrinkage behaviour, which will be discussed in the next chapter, were made from the Log C that had a metre length.

Eight clear specimens of known MFA and densities were made from the discs B and D (four specimens from each disc) to investigate shrinkage behaviour at cellular level. The size of each specimen was 3 mm in the radial direction, 2 mm in the tangential direction and 10 mm in the longitudinal direction. The specimens were cut along the R-T plane using a sharp blade to give a fine surface. No tearing damage could be observed after saturating in water. The resultant surface gave images from which repeatable measurements could be taken under an incident-light optical microscope using dark field lenses. These images were used to determine changes in dimensions as a function of moisture content. Figure 5.7 shows an image of a colony of cells at fibre saturation point.

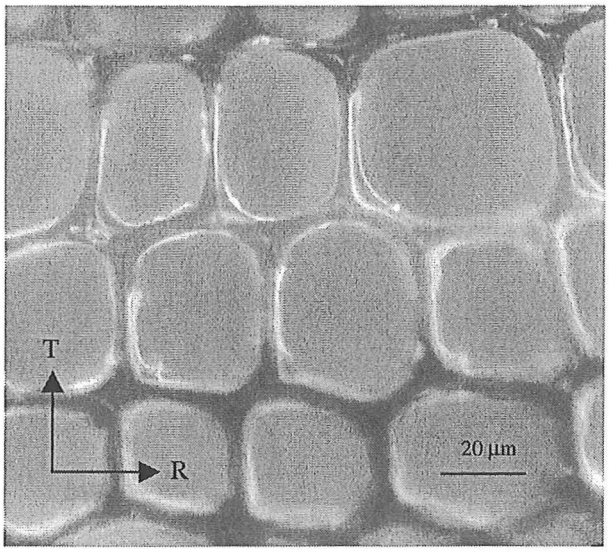

Figure 5.7. Cell image at fibre saturation.

The specimens were then dried slowly in a controlled environment to bring the cell wall moisture content down to nearly 3.8%. This was achieved by controlling the humidity using a saturated solution of Sodium Iodide in an airtight box with gentle air circulation at the ambient temperature as shown in Figure 5.8.

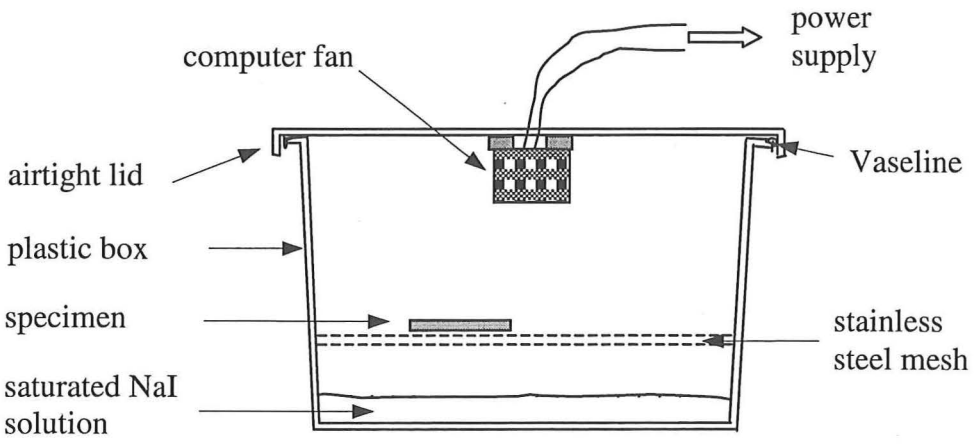

Figure 5.8. Simplified environmental chamber.

The images of the same colonies of cells were taken immediately after drying. Figure 5.9 shows the image of the cells previously presented in Figure 5.7 after drying.

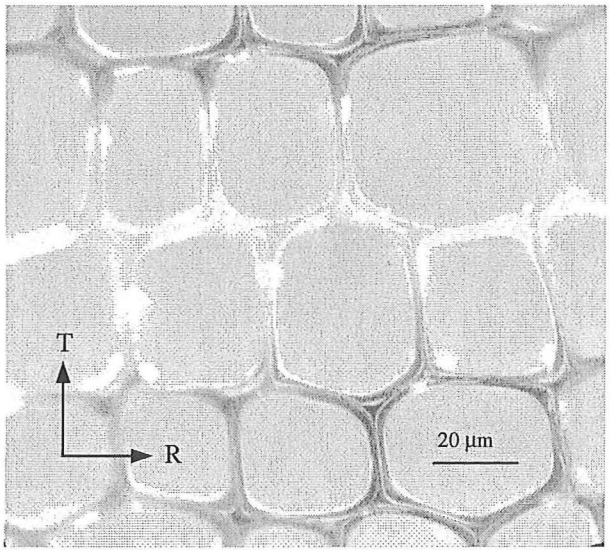

Figure 5.9. Cell image after drying.

Images were analysed using a Scion Image Analyser. Two-dimensional co-ordinates were set up in the field of view with x-direction coinciding with the radial direction and the y-direction oriented in the tangential direction. The co-ordinates of three particular cell junctions P_1, P_2 and P_3 of the images from wet and dry conditions were determined referring to a fixed junction "O" in the field of view as indicated in Figure 5.10.

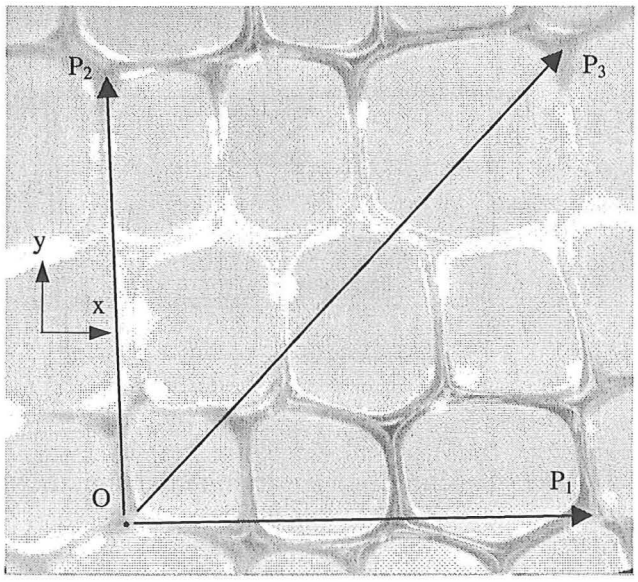

Figure 5.10. Points for measurements in the field of view.

The position of junction "O" would have changed slightly due to moisture variation between wet and dry conditions. However this change is minor and the errors caused by this change in the coordinate measurement are neglected.

If (x_{wi}, y_{wi}) and (x_{di}, y_{di}) are the coordinates of P_i from the images of wet and dry cell respectively referring to the fixed origin, O, where $i = 1, 2$ and 3, then

the linear shrinkage strain in the radial and tangential directions are given by

$$\varepsilon_R^s = \frac{x_{wi} - x_{di}}{x_{wi}} \tag{5.11}$$

and

$$\varepsilon_T^s = \frac{y_{wi} - y_{di}}{y_{wi}} \tag{5.12}$$

respectively.

The linear shrinkage coefficients in radial and tangential directions are given by

$$\alpha_R = \frac{\varepsilon_R^s}{\Delta w} = \frac{x_{wi} - x_{di}}{x_{wi}\Delta w} \tag{5.13}$$

and

$$\alpha_T = \frac{\varepsilon_T^s}{\Delta w} = \frac{y_{wi} - y_{di}}{y_{wi}\Delta w} \tag{5.14}$$

respectively, where Δw is the change of moisture content.

Shear strain is given by

$$\gamma_{RT} = \frac{x_{w2} - x_{d2}}{y_{w2}} + \frac{y_{w1} - y_{d1}}{x_{w1}} \tag{5.15}$$

and shear strain coefficient is given by

$$\alpha_{RT} = \frac{x_{w2} - x_{d2}}{y_{w2}\Delta w} + \frac{y_{w1} - y_{d1}}{x_{w1}\Delta w} \tag{5.16}$$

For each specimen, the linear transverse shrinkage coefficients were determined from the coordinates of P_1, P_2 and P_3 using equations (5.13) and (5.14). Subsequently the average linear transverse shrinkage coefficient and strain coefficient of each specimen

were calculated from the three values. The shear strain coefficients were calculated using equation (5.16). These average values are given in Table 5.5. There was negligible shear strain found in any of these colonies of cells. The distances of P_1, P_2 and P_3 from O are above 600 pixels. In reading the coordinates of a point the limit is one pixel and the probable uncertainty associated with the calculation of a distance can be taken to be ±2 pixels. Hence the measurement of distance between two point is reasonably accurate, within about ±0.3 %.

Table 5.5. Measured transverse shrinkage coefficients.

Density (kg/m^3)	MFA (deg)	Tangential shrinkage coefficient	Radial shrinkage coefficient	Shear strain coefficient
300	15	0.2300	0.2100	0.003
300	23	0.2100	0.1700	0.000
300	25	0.2400	0.2300	0.001
350	23	0.2200	0.2000	0.000
350	25	0.2100	0.2000	0.003
450	30	0.2700	0.2200	0.002
550	30	0.2800	0.2600	0.000
600	10	0.3600	0.3300	0.001

5.4 Comparison of Results and Discussion

The data which were calculated from the cell model provide a table (Appendix (C)) of stiffness and shrinkage properties of *pinus radiata* for varying densities from 200 to 900 kg/m^3 and microfibril angles of the S_2 layer ranging 0 to 50°. For a selected density and microfibril angle, the stiffness and shrinkage properties of wood at a local point in a log can be determined from the table using an interpolation method which will be discussed in the next chapter. It is necessary to validate the calculated data against experimental results before using the table.

5.4.1 Shrinkage/Swelling Coefficients

The transverse shrinkage/swelling coefficients from the models and experiments are compared in Figure (5.11). The graphs of shrinkage/swelling coefficients against microfibril angle are plotted for known densities. The graphs which are given in A, B and C are for the earlywood that have densities of 300, 350 and 450 kg/m^3

respectively and cell aspect ratio of 2:3. The results show that the predicted swelling coefficients are close to most of the measured shrinkage coefficients. As given in D, since the observed aspect ratio of the cell is 1:1 in the transitionwood the calculated swelling coefficients in the radial and tangential direction are equal for a density of 550 kg/m^3, and the values are close to the measured values.

Keys used in the graphs are: ETM – tangential swelling coefficient from the cell model, ERM – radial swelling coefficient from the cell model, ETE – tangential shrinkage coefficient from the experiment, ERE – radial shrinkage coefficient from the experiment.

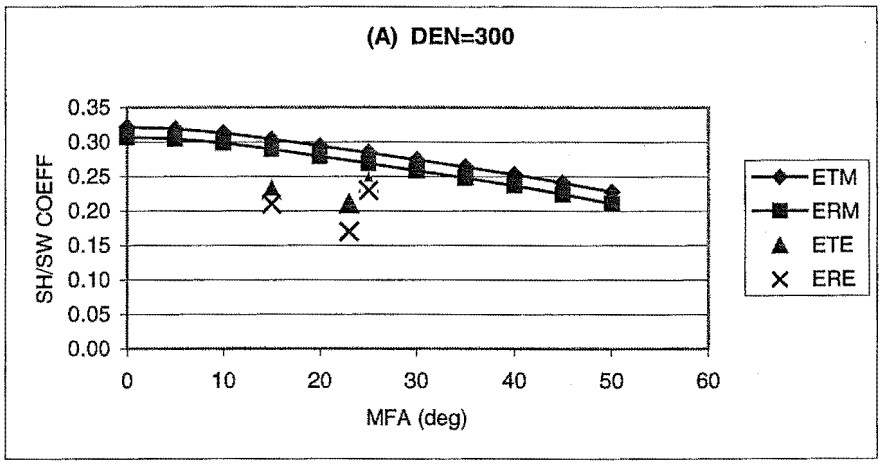

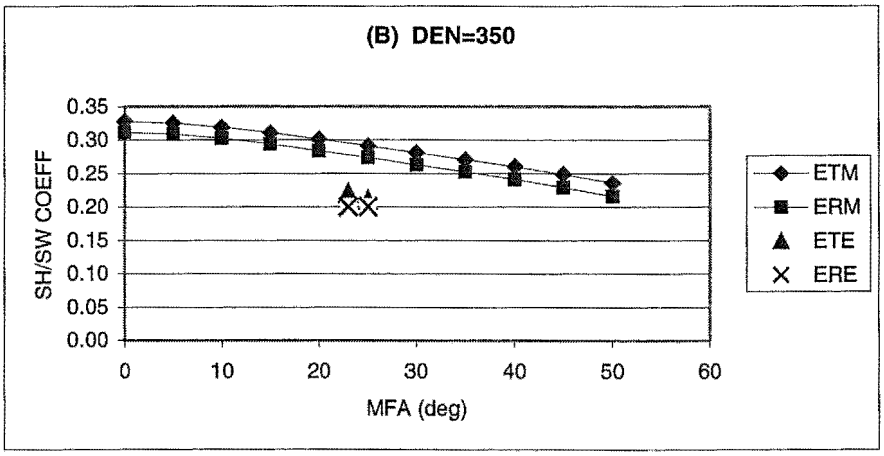

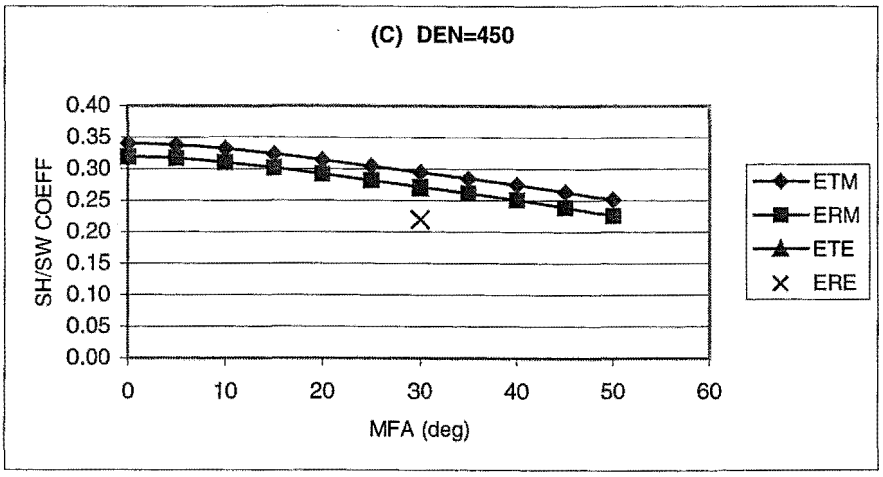

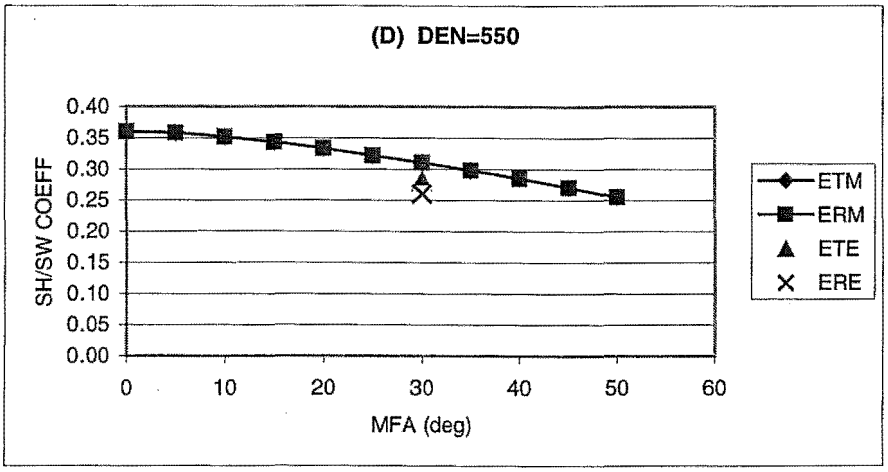

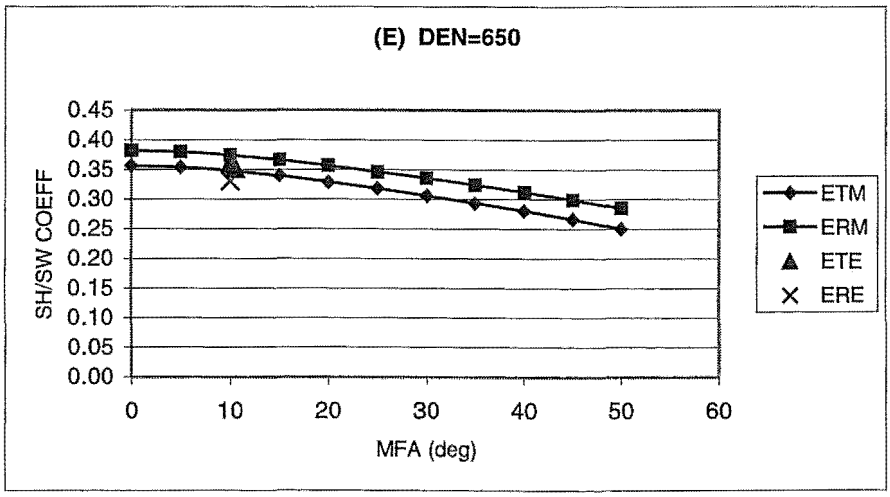

Figure 5.11. A – E: Comparisons of transverse shrinkage/swelling coefficients vs. microfibril angle from the model and experiments.

A comparison of the predicted swelling coefficients and measured shrinkage coefficients of latewood with density 650 kg/m^3 and aspect ratio 3:2 is made in E. Although the predicted radial swelling coefficients are higher than the tangential swelling coefficients, these values are close to the measured values.

From the comparisons, it can be concluded that the cell models predict shrinkage/swelling coefficients close to the measured values and hence the predicted results can be used in the board model as the properties of wood for given the microfibril angles and density.

Measuring the longitudinal shrinkage at cellular level as well as from small clear specimens is a difficult task because the value is very small and thus needs sensitive measuring facilities. However, the predicted values that are shown in Figure 5.12 are in reasonable range.

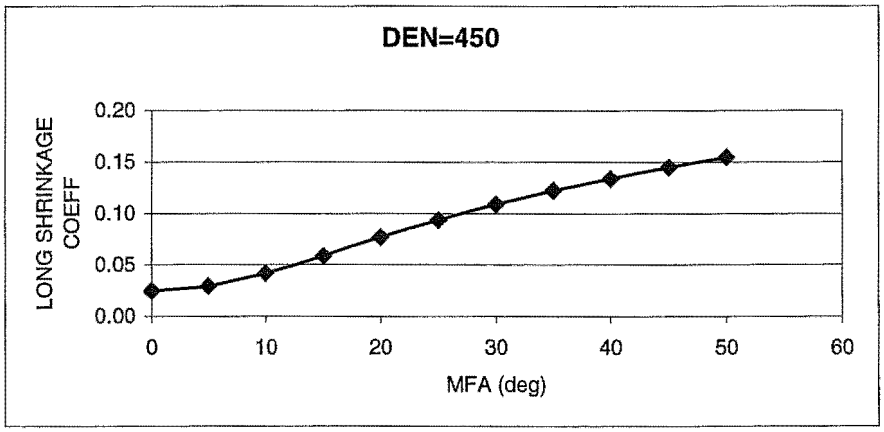

Figure 5.12. Predicted longitudinal shrinkage coefficient vs. MFA for earlywood with density 450 kg/m^3.

The measured longitudinal shrinkage coefficient of *pinus radiata* with an average density of 450 kg/m^3 is 0.013, as was calculated from the average longitudinal shrinkage reported by Pang (2001). The average microfibril angle of the wood was not reported. The calculated values from the numerical model are higher but where based upon assumptions that included the microfibril angle and density whereas in the actual wood cells are not aligned perfectly.

As from the graphs in Figures 5.11 and 5.12, increasing microfibril angle reduces the transverse shrinkage and increases the longitudinal shrinkage. The aspect ratio of the cell causes anisotropy in the transverse shrinkage as explained in chapter 2. The shrinkage values increase with increasing density, however the change of density has little effect in the shrinkage.

5.4.2 Elastic Properties

The graphs of modulus of elasticity that were calculated from the cell model against microfibril angle for density 450 kg/m^3 are given in Figure 5.13. The graphs that are given in A are for longitudinal modulus of elasticity (EL), and in B for radial modulus of elasticity (ER) and tangential modulus of elasticity (ET). The graphs for shear modulus and Poisson's ratios are given in C and D. For the keys G - shear modulus, NU - Poisson's ratio, R - radial direction, T - tangential direction and L - longitudinal direction.

Little information is available on the stiffness properties of *pinus radiata* at cellular levels. Measuring these properties is beyond the scope of this study.

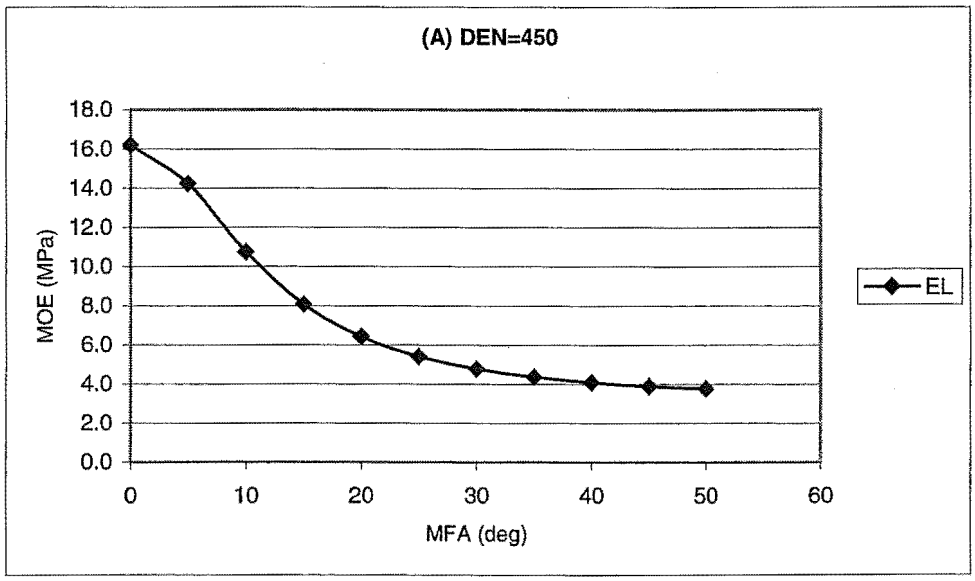

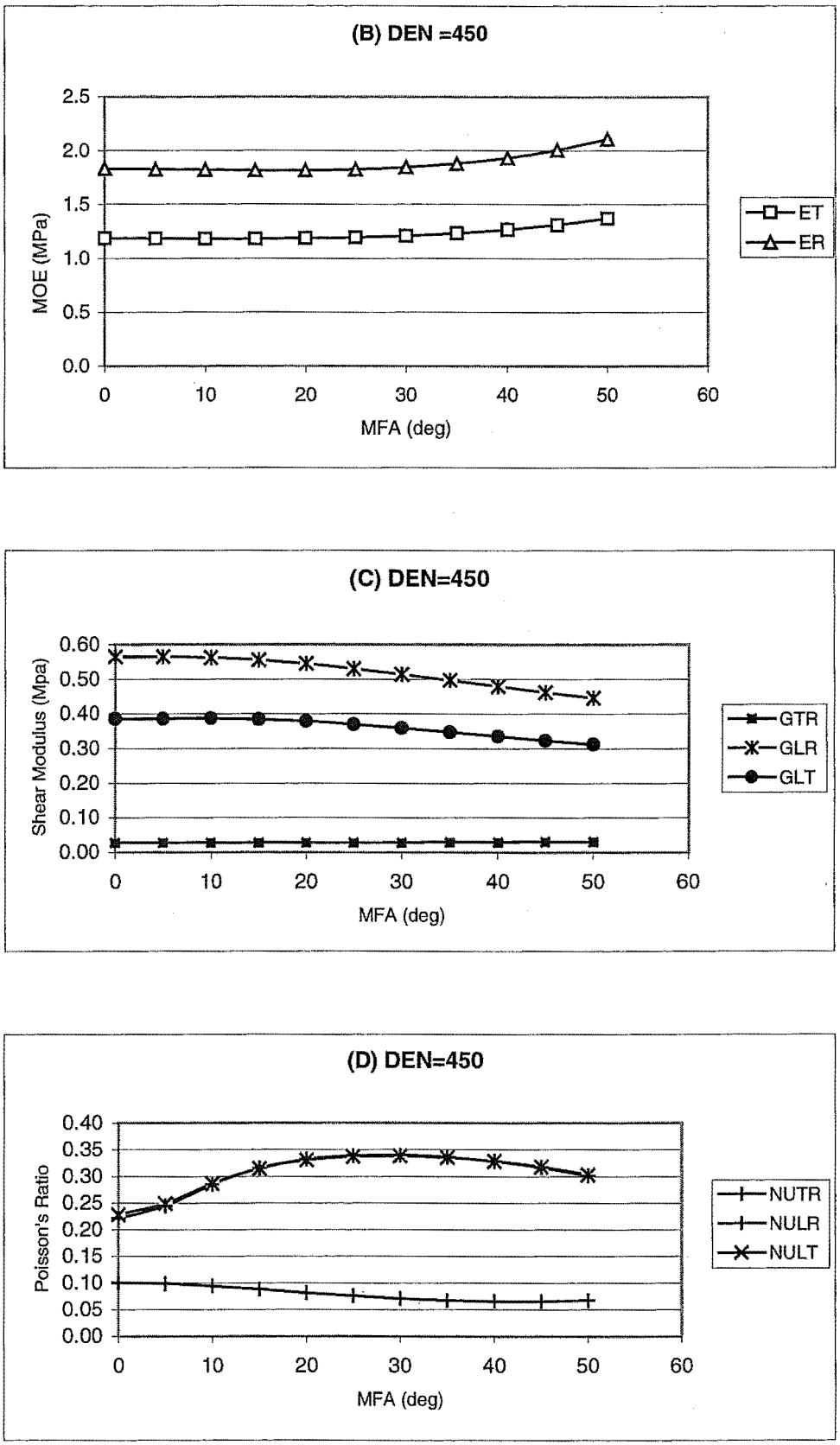

Figure 5.13. A – D: predicted stiffness coefficients vs. MFA for earlywood with density of 450 kg/m^3.

The influence of microfibril angle and density can be seen in the results given in Figure 5.13. The longitudinal modulus of elasticity decreases with microfibril angle and has a strong dependency on the angle from 5° to 30°. The radial and tangential moduli are almost constant when the microfibril angle increases up to 20°, and then increases only slightly with angles above 20°. The shear modulus along the T-R plane of the cell has a limited dependency on an increasing microfibril angle until 25°, and then it increases while the shear moduli along the vertical walls of the cell decrease with increasing microfibril angle. The Poisson's ratio along the T-R plane decreases slightly as the microfibril angle increases beyond 10°. Poisson's ratios in the vertical walls of the cell coincide and increase as the angle increases up to 25° at which point they and then decrease when the microfibril angle increases from 30°.

Figure 5.14 gives graphs of stiffness properties against density for microfibril angle 25°. As shown in Figure 5.14, the stiffness properties increase with density. The thicker the cell wall is the higher the density of wood. Therefore, the increasing cell wall thickness enhances the stiffness properties of the wood. Graphs in Figure 5.14 (B) show that ET is higher than ER for earlywood and they are equal for transitionwood. ET is lower than ER for latewood. Similar change is also shown in Figure 5.14 (C). These step changes with increasing density occurred due to difference in aspect ratios of the three different woods.

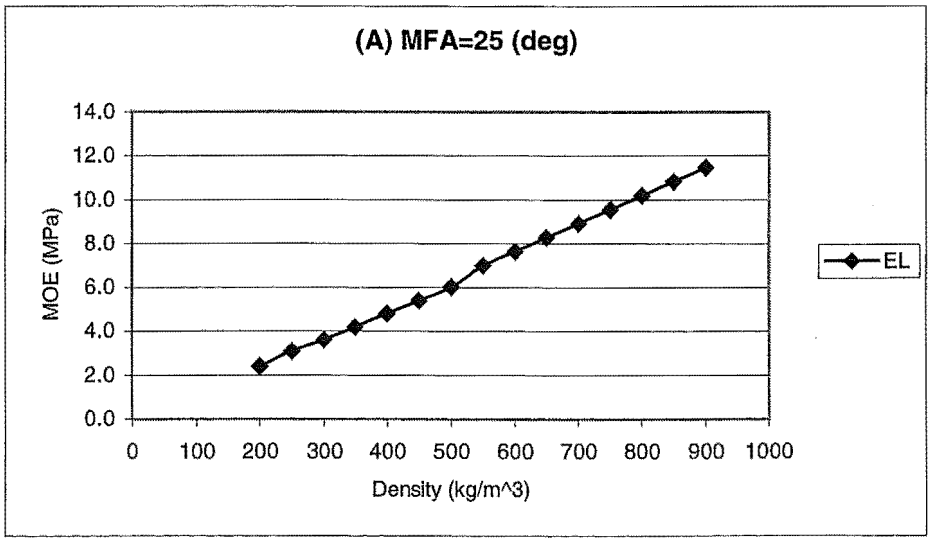

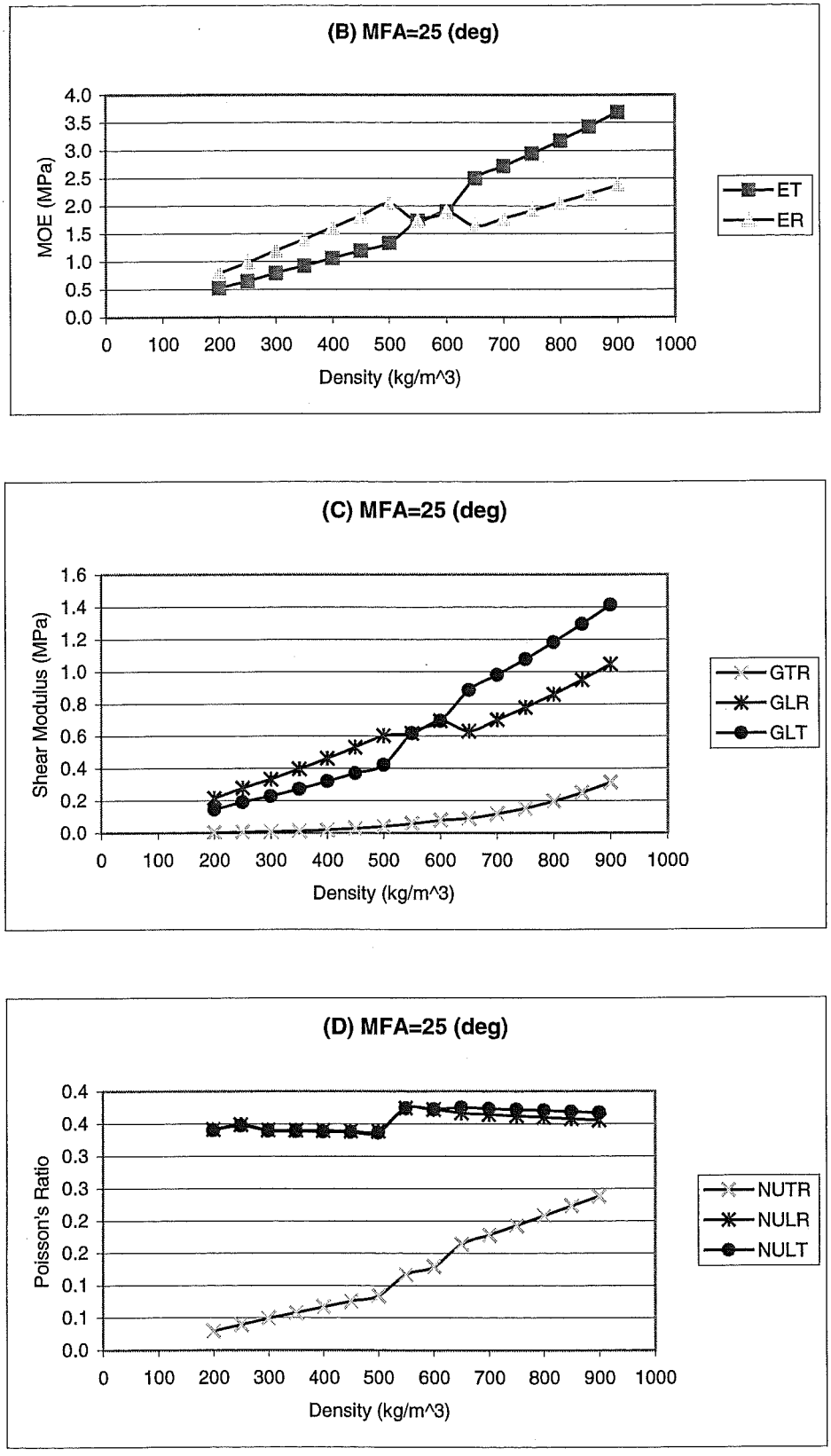

Figure 5.14. A – D: predicted stiffness coefficients vs. density for wood with MFA of S_2 layer is 25°.

Chapter 6

Modelling Moisture-Induced Behaviours of Board

6.1 Introduction

6.1.1 A Brief Review of Existing Models

There are various mathematical models of moisture-induced behaviour of wood at a macro level. The important models relevant to this research are reviewed in this chapter. Shrinkage in wood along the longitudinal, radial and tangential directions was modelled by Zhang *et al.* (1994) as a function of density, and analyzed mathematically by Hunter (1996) ignoring the micro-mechanical behaviour. A finite element model based on heat and mass transfer principles was developed to analyse the time-dependence of moisture distribution in drying wood by Gui *et al.* (1994). The model did not include stress, strain and other micro-mechanical variables. A two dimensional model was developed by Martensson and Svensson (1997) to explain the dimensional changes due to drying wood in the direction perpendicular to the grain. Ormarsson (1999) performed numerical analysis of moisture related distortions in sawn timber during drying using the finite element method. Ormarsson's model used the macro level constitutive properties of wood as the input data. The influence of growth rings, spiral grain and conical shape of the log was taken into account in the model.

Most of these numerical methods are based upon the drying of freshly sawn wood using macro level constitutive properties, and only limited numerical analyses have been done to predict moisture induced distortions of boards in-service by incorporating nano- to macro-scale effects. To advance our understanding of these important effects the following investigation was carried out.

6.1.2 Present Modelling

The magnitude of the dimensional changes caused by moisture changes varies with wood species and the location and orientation of the board in a log. Since the orientation of the board in relation to the log is an influencing factor, the shape

stability in service is also dependent on the sawn pattern as illustrated in Figure 1.2. The main factors which determine the stiffness and dimensional stability of wood are the microfibril angle (MFA), density and the spiral grain angle (SGA) while other contributing factors are the orientation of the pith and the growth ring pattern. The stiffness of wood is also a function of the moisture content when it is below the fibre saturation point with an increase in moisture content decreasing the stiffness.

The relationship between the microstructure of wood and the mechanical properties is complex and the development of numerical models to define this relationship at microfibril and cellular levels have been reported in previous chapters. In the this chapter, the development of two numerical models mapping the information from the cell models to describe the dimensional behaviour of boards as a function of the in-service variations of moisture content are reported. In all models, in-service temperature is assumed to be constant and the wood is assumed to be an elastic continuum. Hence creep and mechano-sorptive behaviors are neglected. The first model developed herein is based on the work of Astley (1999) and calculates the dimensional change as a function of moisture content using finite element methods. This model uses the assumptions that the pith is straight and is taken as the longitudinal axis, the log is conical and the properties vary linearly with radius from the pith to the bark as well as with height from the butt to the top of the log. In the second model, actual pith orientation and growth ring pattern were used to interpolate the properties for the analysis. Predicted board distortions from both analyses models were compared with the experimentally obtained results from boards cut from a selected *pinus radiata* log.

6.2 Properties for Board Models

6.2.1 Generating Input Properties from Experiment

Sections of the log as previously illustrated in Figure 5.6 are shown in Figure 6.1. From the pictures of the log: the pith is neither straight nor is it coincidental with the global axis; the shape of the cross sections of the log are neither conical nor uniformly cylindrical; the growth rings are not perfectly circular; and the width of the growth rings is not uniform.

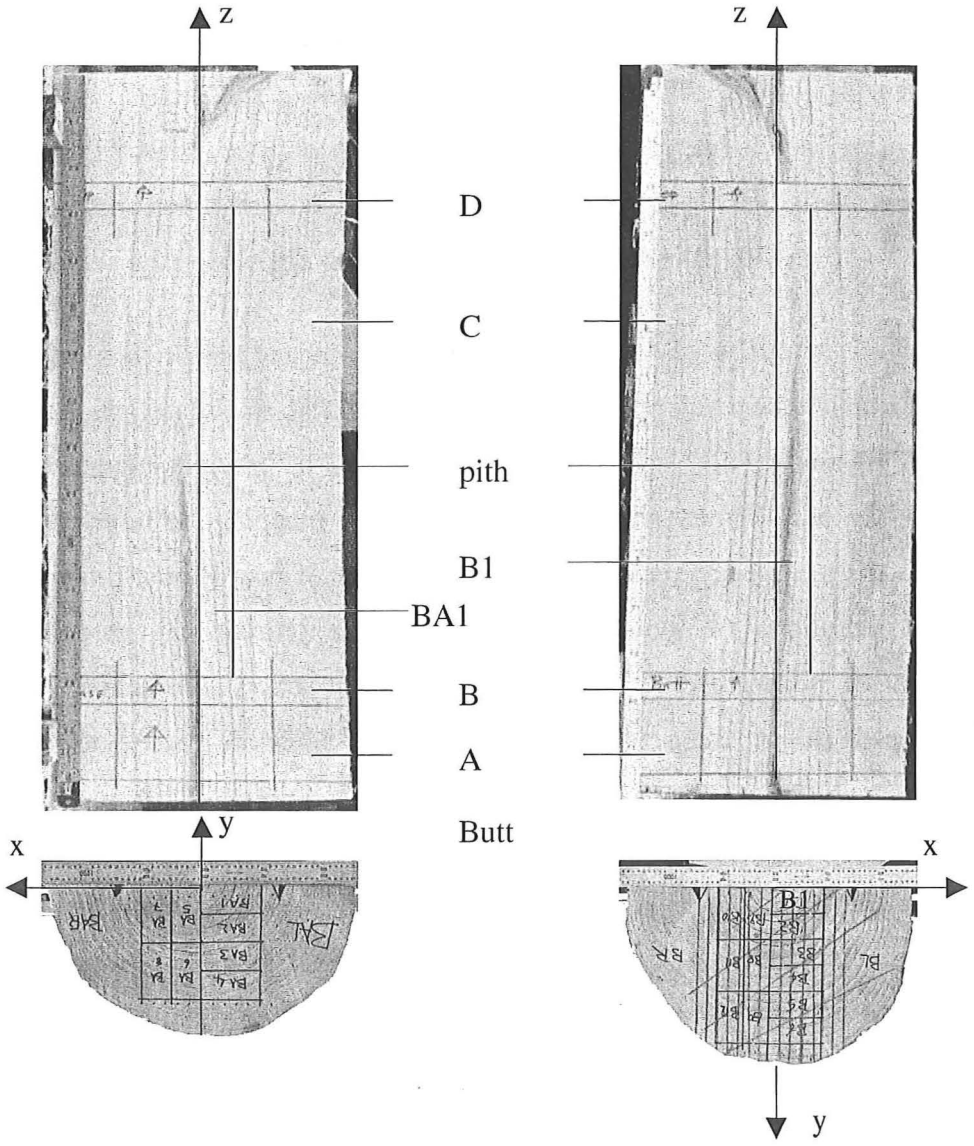

Figure 6.1. Sections of *pinus radiata* log used for experimental studies.

Density, microfibril angle and spiral grain angle are the input properties for the board models in addition to the equivalent properties that were predicted from the cell model. Specimens for the measurement of density, microfibril angle and spiral grain angle were taken at 45° intervals from the 50mm thick discs B and D (see Figure 6.2) that were sawn from the log. The three parameters were measured for each specimen by the SilviScan method at CSIRO, Australia (Evans 1997) as a function of distance from pith to bark. These properties from the sixteen specimens were plotted against the radial distance and are given in Appendices F, G and H.

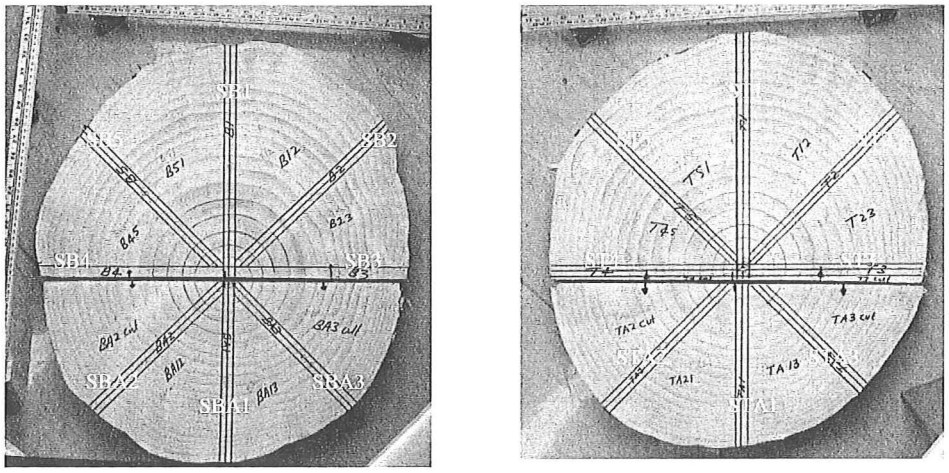

Butt Disc B Top Disc D

Figure 6.2. Specimens obtained at 45° from the discs.

Average values of these properties from the butt and top discs were calculated separately, and plotted against the growth ring number from pith to bark. These results are presented in Figures 6.3 – 6.8, where DEN refers to the density, MFA is the microfibril angle and SGA is the spiral grain angle. From Figures 6.3 – 6.8, the average density of the butt and the top shows a slight increase with the radial distance from the pith. The average microfibril angle from both butt and top decreases from pith to bark while the average spiral grain angle fluctuates around an increasing angle from the pith to the twelfth growth ring and then remains almost constant.

Keys to the graphs in Figure 6.3:

— regression line - — - trendline * average

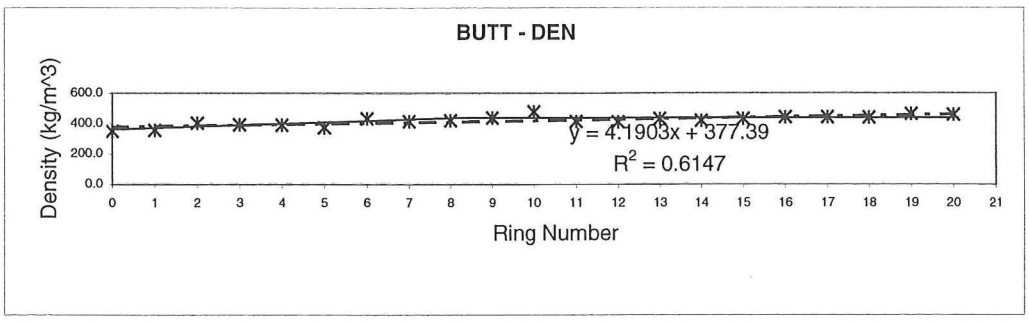

Figure 6.3. Average density from butt disc B.

Keys to the graphs in Figures 6.4 - 6.8:

— regression line - — - trendline * average

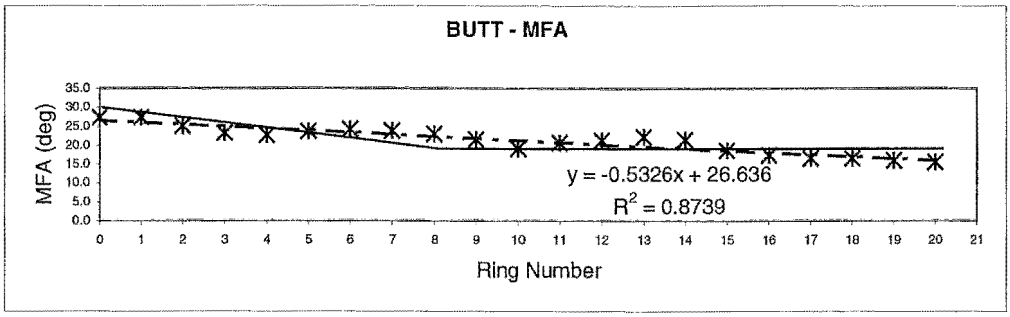

Figure 6.4. Average microfibril angle from butt disc B.

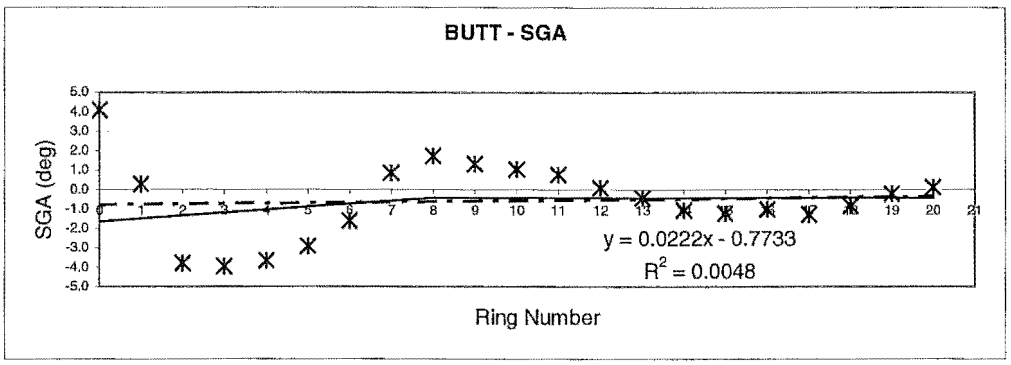

Figure 6.5. Average spiral grain angle from butt disc B.

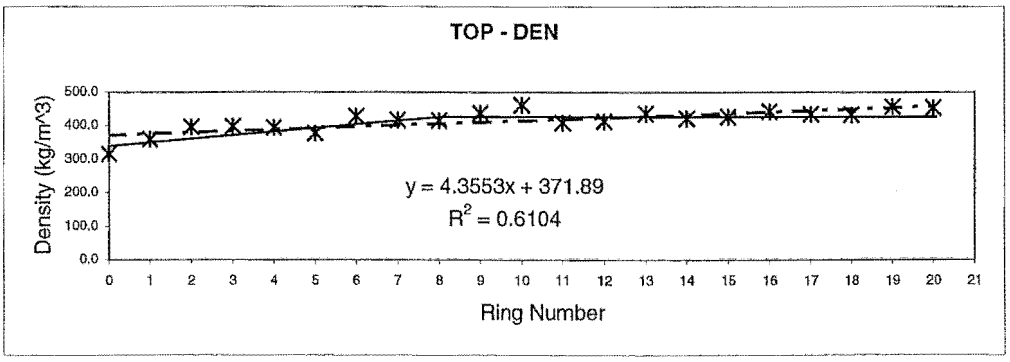

Figure 6.6. Average density from top disc D.

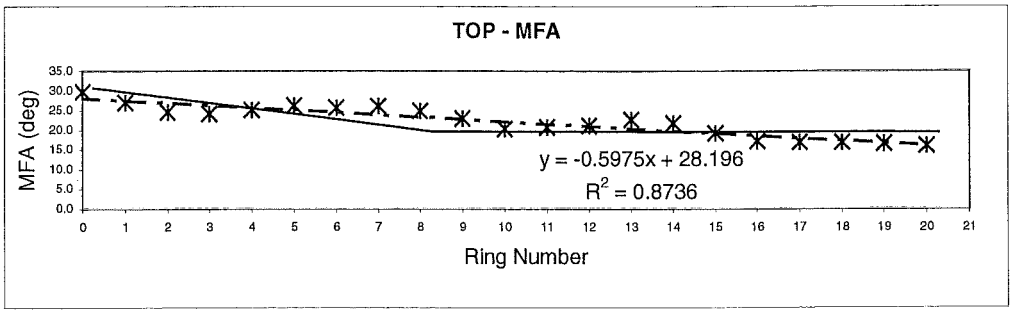

Figure 6.7. Average microfibril angle from top disc D.

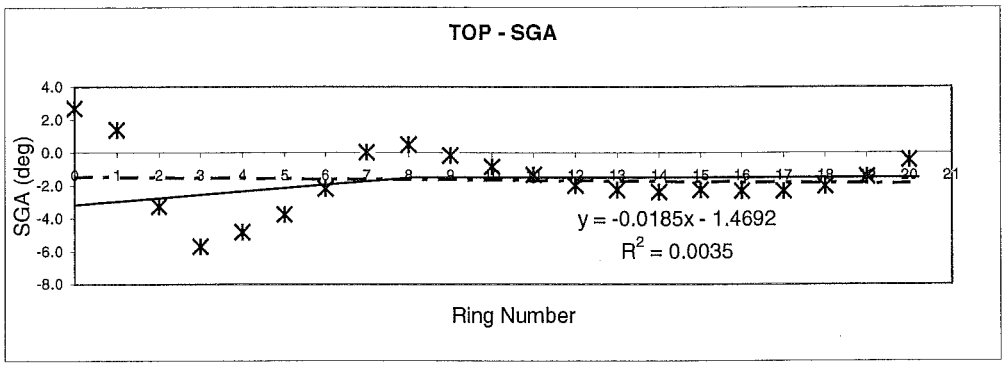

Figure 6.8. Average spiral grain angle from top disc D.

The assumed linear variations of the average properties are given by the trendlines as shown in the graphs. The continuous regression line graphs are sketched for best fits by assuming that the average properties vary linearly in the corewood which is up to the eighth growth ring and remain constant in the outerwood. The average properties of the log obtained from the graphs are given in Figure 6.9.

6.2.2 Property Variation in Log

In the first model, the log is assumed to have a perfect conical shape with a straight pith at the center of the log. As shown in Figures 6.3 – 6.8, the radial distributions of density, microfibril angle and spiral grain angle are assumed to vary linearly with axial distance along the log and with radius from the pith reaching constant values at a prescribed corewood/outerwood boundary. Hence a linear interpolation can be used to calculate the properties at a specific point as a function of axial distance and radial position in the log.

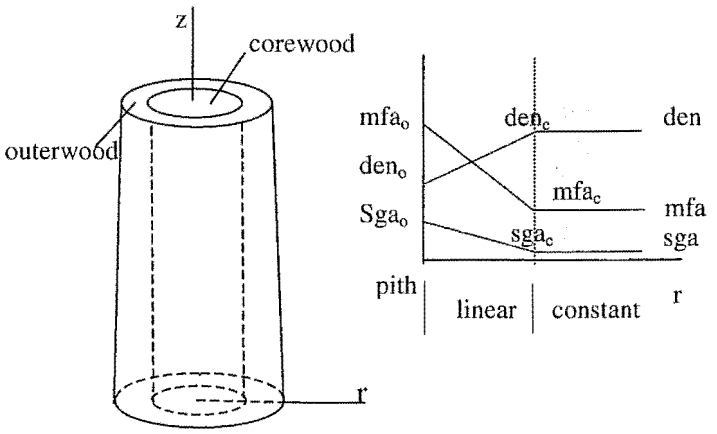

Log data for first model

Log
Average diameter (butt) : 0.66m
Average diameter (top) : 0.64m
Average diameter (core): 0.32m
Length: 1.00m

Butt
$MFA_{bo}=32^{o}$, $MFA_{bc}=20^{o}$
$den_{bo}=351$ kg/m^3, $den_{bc}=439$ kg/m^3
$SGA_{bo}=-1.60^{o}$, $SGA_{bc}=-0.44^{o}$

Top
$MFA_{to}=30^{o}$, $MFA_{tc}=19^{o}$
$den_{to}=315$ kg/m^3, $den_{tc}=426$ kg/m^3
$SGA_{to}=-3.00^{o}$, $SGA_{tc}=-1.34^{o}$

Figure 6.9. Variation of average MFA, SGA and density in the radial direction, and input log properties.

In Figure 6.9:

MFA_{bo}, SGA_{bo} and den_{bo} refer to the microfibril angle, spiral grain angle and density of the pith in the butt respectively.

MFA_{bc}, SGA_{bc} and den_{bc} denote the microfibril angle, spiral grain angle and density of the corewood/outerwood boundary in the butt respectively.

MFA_{to}, SGA_{to} and den_{to} refer to the microfibril angle, spiral grain angle and density of the pith in the top respectively.

MFA_{tc}, SGA_{tc} and den_{tc} denote the microfibril angle, spiral grain angle and density of the corewood/outerwood boundary in the top respectively.

The density, microfibril angle and spiral grain angle that are given in Appendices (F, G and H) are used as input data in the second model without making any assumption. The actual pith orientation and log shape is used as the basis of the interpolation used to determine these properties in the board. However each growth ring is assumed to be uniformly distributed around the pith.

6.2.3 Interpolations of Properties

6.2.3.1 Interpolations for First Model

Distribution of the properties in a log is calculated using the following interpolation equations based on Lagrange interpolation as explained by Wood (1999) and Pozrikidis (1998).

If the linear variations, as shown in Figure 6.9, are assumed, linear interpolation equation can be used to determine the distribution of properties in a log.

If "pro" refers to a property such as density, MFA or SGA, then the value of the property "pro" at a point within the corewood ($r_{bp} < r_c$) of the butt is given by

$$pro_{bp} = \frac{(pro_{bc} - pro_{bo})r_{bp}}{r_c} + pro_{bo} \tag{6.1}$$

where r_c is the radius of corewood, pro_{bo} is a property at the center (pith) of the butt, pro_{bc} is the property at the corewood boundary of the butt, r_{bp} is the radius of the point at the butt

"pro"at a point within the corewood ($r_{tp} < r_c$) of the top is given by

$$pro_{tp} = \frac{(pro_{tc} - pro_{to})r_{tp}}{r_c} + pro_{to} \tag{6.2}$$

where pro_{to} is a property at the center of the top, pro_{tc} is the property at the corewood boundary of the top, r_{tp} is the radius of the point at the top.

If $r_{bp} \geq r_c$ and $r_{bp} \geq r_c$, pro_{bp} and pro_{tp} at the radii r_{bp} and r_{tp} in the outerwood of the butt and the top respectively are given by

$$pro_{bp} = pro_{bc} \text{ and } pro_{tp} = pro_{tc} \tag{6.3}$$

The property of a specific point which is at a radius, r_p and a height, l_p in the log is calculated using the linear interpolation equation

$$pro_p = \frac{(pro_{tp} - pro_{bp})l_p}{L} + pro_{bp} \tag{6.4}$$

where L is the length of the log

The elastic stiffness and shrinkage coefficients of a point F (see Figure 6.10), whose MFA and density are known, are calculated by interpolating the stiffness and shrinkage coefficients from the database (table) in Appendix (C) which were obtained as the function of MFA and density as output from the cellular model.

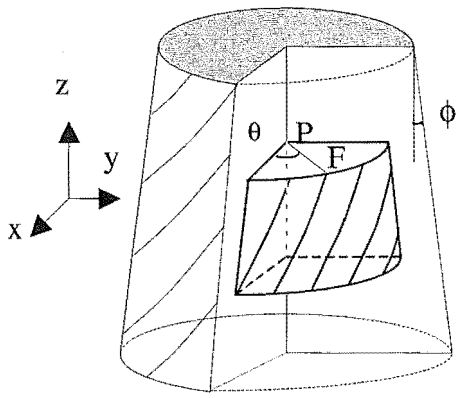

Figure 6.10. Material point in a conical log with pith as the centre line.

If one of the elastic stiffness and shrinkage coefficients at F is $E_{d\psi}$ for the density, d and MFA, ψ, $E_{d\psi}$ is given by

$$E_{d\psi} = \frac{\psi_2 - \psi}{\psi_2 - \psi_1}\frac{d_2 - d}{d_2 - d_1}E_{d_1\psi_1} + \frac{\psi_2 - \psi}{\psi_2 - \psi_1}\frac{d_1 - d}{d_1 - d_2}E_{d_2\psi_1} + \frac{\psi_1 - \psi}{\psi_1 - \psi_2}\frac{d_1 - d}{d_1 - d_2}E_{d_2\psi_2} + \frac{\psi_1 - \psi}{\psi_1 - \psi_2}\frac{d_2 - d}{d_2 - d_1}E_{d_1\psi_2} \tag{6.5}$$

where

$d_1 \le d \le d_2$ and $\psi_1 \le \psi \le \psi_2$

$E_{d_1\psi_1}$ is the coefficient from the database for the density, d_1 and MFA, ψ_1

$E_{d_2\psi_1}$ is the coefficient from the database for the density, d_2 and MFA, ψ_1

$E_{d_2\psi_2}$ is the coefficient from the database for the density, d_2 and MFA, ψ_2

$E_{d_1\psi_2}$ is the coefficient from the database for the density, d_1 and MFA, ψ_2

6.2.3.2 Interpolations for Second Model

Coordinates of the pith with respect to the global axes were measured by sectioning the board B1 since it includes the whole pith (see Figure 6.1), and the pith location could then be defined using a cubic-spline interpolation. The cubic-spline interpolation is well described in many texts including Wood (1999) and Pozrikidis (1998).

Consider a material point F in the log as shown in Figure 6.11 to calculate the density, microfibril angle and spiral grain angle at this location by interpolation using the data from the butt and the top of the log.

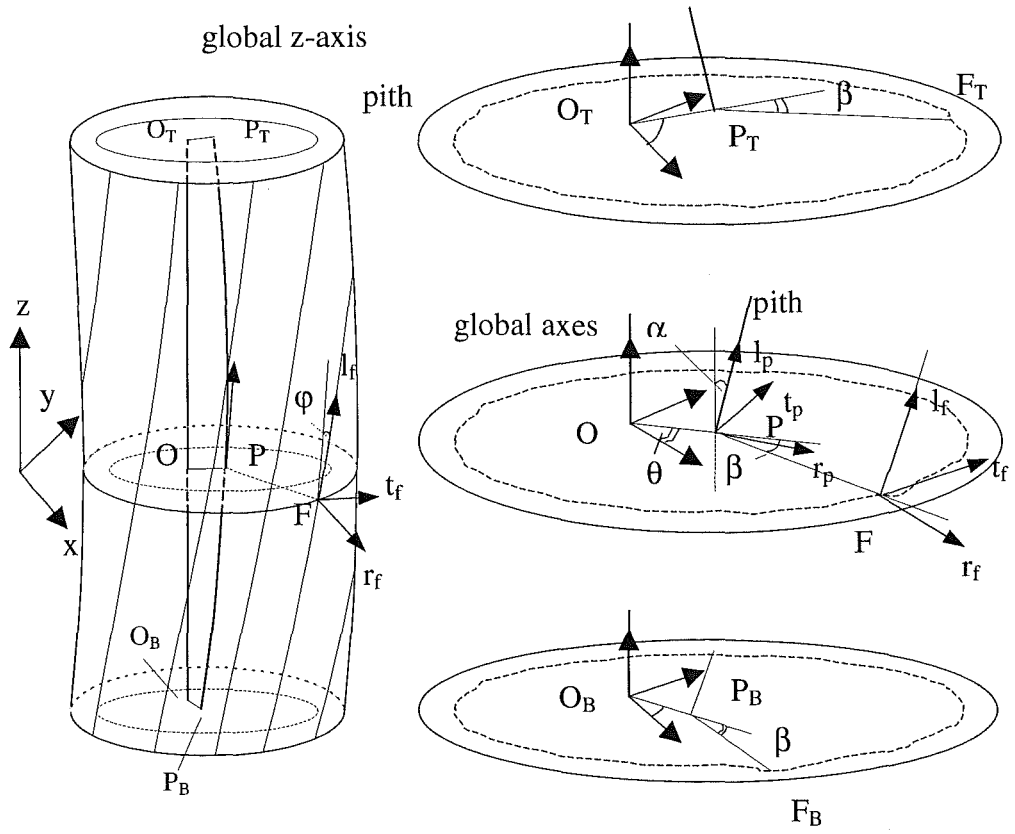

Figure 6.11. Material point in the log considered for interpolation.

The polar coordinates of F with respect to the local coordinate system of the pith P in the same plane are calculated. The density, microfibril angle and spiral grain angle of

the points F_B and F_T (see Figure 6.11), which have the same polar coordinates as F with respect to the piths P_B in the butt and P_T in the top, are calculated from the data using a cubic-spline interpolation. Subsequently density, microfibril angle and spiral grain angle at F are calculated from the interpolated properties of points F_B and F_T using a linear interpolation (equation (6.4)). Elastic stiffness and shrinkage coefficients at F are calculated using equation (6.5) as explained above.

6.2.4 Transformation of Properties

In this study to model the moisture-related behaviour, the board is assumed to be an elastic continuum at a constant temperature that consists of clear wood subject to only moisture-induced loads due to a small uniform variation of moisture below the fibre saturation moisture content. Hence when modelling the deformation, only elastic strain and moisture-induced strain are taken into account since mechano-sorptive strain and creep strain are neglected. The stress-strain relationship can then be defined in the local coordinate system by the constitutive equation reported in chapter 3,

$$\sigma_L = \mathbf{D}_L (\varepsilon_L - \varepsilon_{Ls}) \tag{6.6}$$

and the moisture-induced strain

$$\varepsilon_{Ls} = \alpha_{Ls} \Delta w \tag{6.7}$$

The relationships in equations (6.6) and (6.7) need to be transformed from the local coordinate system to the global coordinate system (x, y, z).

6.2.4.1 Transformation in First Model

For the first model, based on the assumptions made as shown in Figure 6.9, three transformations are necessary. If a material point F as illustrated in Figure 6.12 is considered, the first coordinate transformation is performed for the spiral grain angle, φ that is the angle in the $l_f t_f$-plane between the l_f and l_c axes.

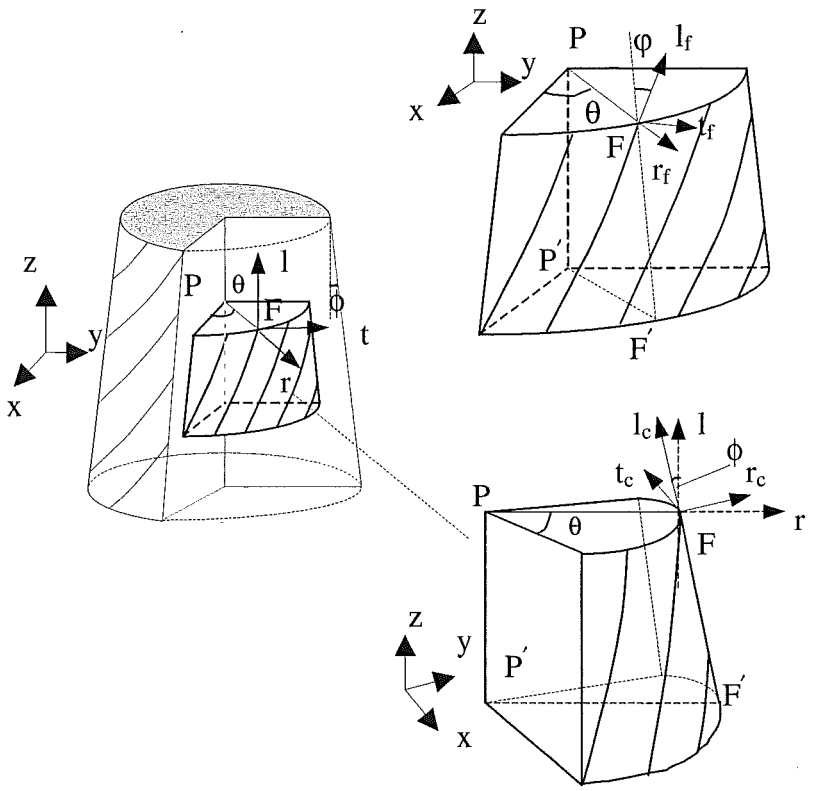

Figure 6.12. Coordinate transformations of a material point in a log.

When transforming the local coordinate system (r_f, t_f, l_f) of spiral grain to the local coordinate system (r_c, t_c, l_c) of the conical axes, the orthogonal transformation matrix of direction cosines M(φ), as reported in chapter 3, is given by

$$M(\varphi) = \begin{bmatrix} 1 & 0 & 0 \\ 0 & \cos\varphi & \sin\varphi \\ 0 & -\sin\varphi & \cos\varphi \end{bmatrix} \tag{6.8}$$

The second transformation is carried out for the conical angle, ϕ that is the angle in the $l_c r_c$-plane between l_c and l axes. An orthogonal transformation matrix of direction cosines, M(ϕ) can be obtained by transforming the coordinate system (r_c, t_c, l_c) to the coordinate system (r, t, l).

$$M(\phi) = \begin{bmatrix} \cos\phi & 0 & -\sin\phi \\ 0 & 1 & 0 \\ \sin\phi & 0 & \cos\phi \end{bmatrix} \tag{6.9}$$

The third transformation is to relate the local coordinate system (r, t, l) to the global coordinate system (x, y, z), and the orthogonal transformation matrix of direction cosines, M(θ) is given by

$$M(\theta) = \begin{bmatrix} \cos\theta & \sin\theta & 0 \\ -\sin\theta & \cos\theta & 0 \\ 0 & 0 & 1 \end{bmatrix} \tag{6.10}$$

Hence the relationship between the local and the global coordinate system are expressed by the transformation matrix

$$M_f = M(\theta)M(\phi)M(\varphi) \tag{6.11}$$

allowing the constitutive properties at point F to be transformed from the local coordinate system (r_f, t_f, l_f) to the global coordinate system (x, y, z). The constitutive equation at F with respect to global axes is given by

$$\boldsymbol{\sigma} = \mathbf{D}(\boldsymbol{\varepsilon} - \boldsymbol{\varepsilon}_s) \tag{6.12}$$

where

$$\mathbf{D} = \mathbf{H}^T\mathbf{D}_L\mathbf{H} \text{ and } \boldsymbol{\varepsilon}_s = \mathbf{H}^{-1}\boldsymbol{\varepsilon}_{Ls} \tag{6.13}$$

6.2.4.2 Transformation in Second Model

In the second model, the actual pith orientation is taken into account for the coordinate transformations from the local axis of the grain to the global axis as illustrated in Figures 6.13 and 6.14.

The transformation due to spiral grain angle is similar to that of the first model, and the transformation matrix of direction cosines of angles between (r_f, t_f, l_f) and (r_c, t_c, l_c) systems is given by equation (6.8).

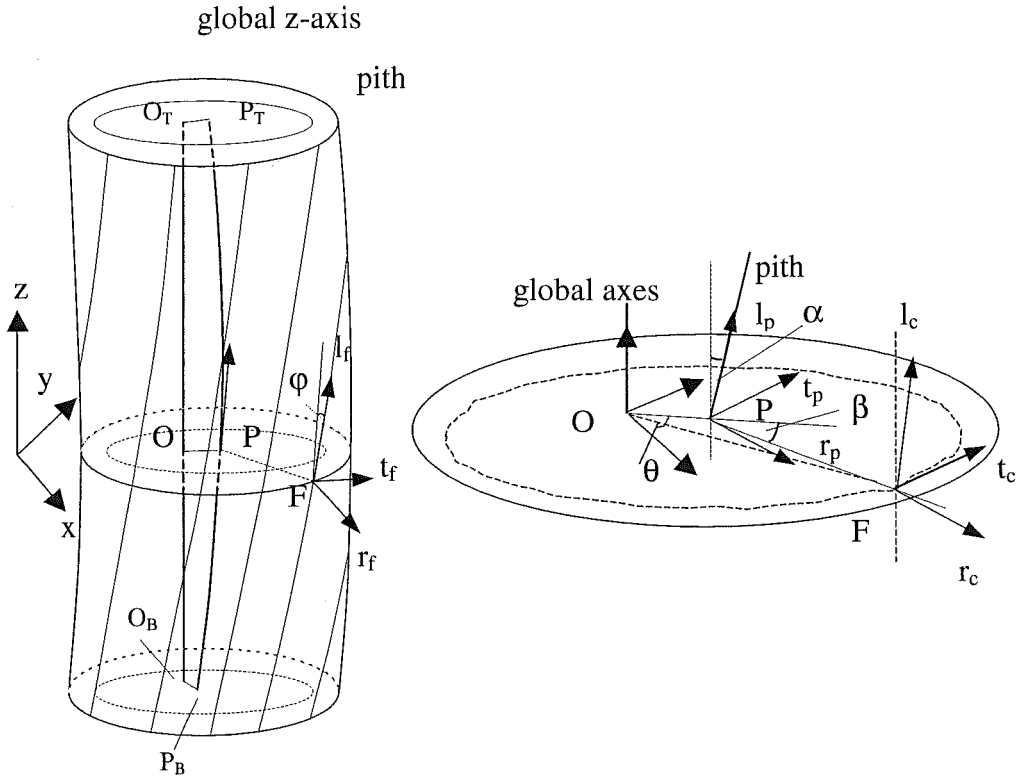

Figure 6.13. Pith orientation and transformation due to spiral grain, conical angle and pith orientation.

The second transformation allows the transformation of conical axes (r_c, t_c, l_c) to the local axes of the pith (r_p, t_p, l_p), and then to local axes (r, t, l) as shown in Figure 6.14. This can be done in a single transformation of the coordinate system (r_c, t_c, l_c) to the coordinate system (r, t, l) by the angle (α-ϕ), where ϕ is the conical angle. The log used for the experiments does not have a conical shape and hence ϕ is zero. α is the pith angle which is the angle between the z-axis and the local longitudinal axis l_p of the pith. The pith angle at P is calculated from the global coordinates of the pith.

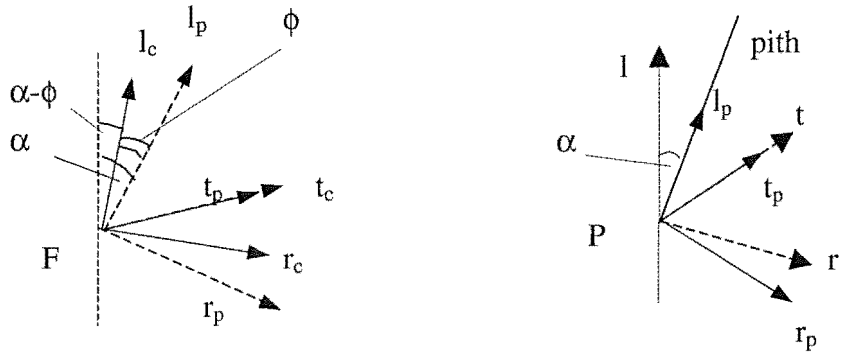

Conical angle (ϕ) is the angle between l_c and l_p in the $l_c t_c$ - plane. Pith angle (α) is the angle between l_p and l in the $l_p t_p$ plane. A single transformation can be performed to transform (r_c, t_c, l_c) to (r, t, l) by angle (α-ϕ).

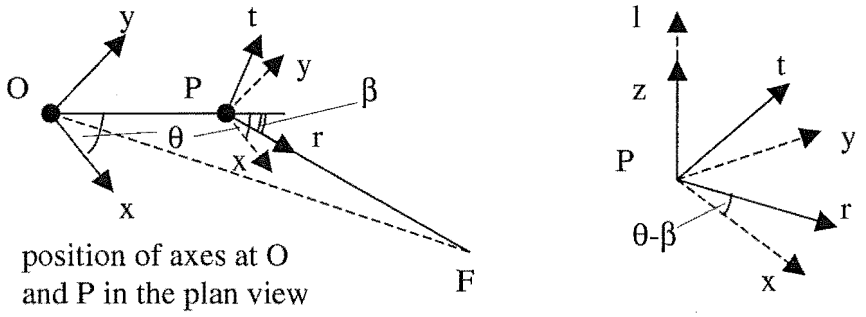

Angle between r and x in the rt plane is (θ-β). The local axis system (r, t, l) at P is transformed to global axis system (x, y, z).

Figure 6.14. Transformation due to conical angle, pith orientation.

The orthogonal transformation matrix of direction cosines, M(α-ϕ) is given by

$$M(\alpha\text{-}\phi)=\begin{bmatrix}\cos(\alpha-\phi) & 0 & -\sin(\alpha-\phi)\\ 0 & 1 & 0\\ \sin(\alpha-\phi) & 0 & \cos(\alpha-\phi)\end{bmatrix} \tag{6.14}$$

The coordinate system of the local axes (r, t, l) is transformed to the global coordinate system (x, y, z) by the angle (θ-β) as illustrated in Figure 6.14. The orthogonal transformation matrix of direction cosines, M(θ-β) is given by

$$M(\theta\text{-}\beta) = \begin{bmatrix} \cos(\theta-\beta) & \sin(\theta-\beta) & 0 \\ -\sin(\theta-\beta) & \cos(\theta-\beta) & 0 \\ 0 & 0 & 1 \end{bmatrix} \tag{6.15}$$

By combining equations (6.8), (6.14) and (6.15), the relationship between the local and the global coordinate system are expressed by the transformation matrix

$$M_s = M(\theta\text{-}\beta)M(\alpha\text{-}\phi)M(\varphi) \tag{6.16}$$

As expressed in equations (6.12) and (6.13) the constitutive properties at point F in the second model can be transformed from the local coordinate system (r_f, t_f, l_f) to global coordinate system (x, y, z).

6.3 Implementation of Board Model

6.3.1 First Model

The first board model consists of a suite of FORTRAN 90 programs which perform the computer simulation and plot undeformed and deformed finite element meshes of board in TECPLOT.

Initially, key input property data was generated based on the assumptions that are shown in Figure 6.8. Secondly, key input information of a finite element model of the board was generated. The information supplied defines the location, size and orientation of the board within a log. The resulting finite element model was formed from three-dimensional, 27-node blocks. The key input values of microfibril angle, density and spiral grain angle were interpolated using equations (6.1) – (6.4) and assigned to each node of the finite element model. The direction cosines of a local axis set parallel to the grain were also assigned to each node of the finite element model. A database of elastic stiffness and shrinkage coefficients, which were obtained

as a function of microfibril angle and density by running the cellular model, given in Appendix, was interrogated to determine the interpolated values of stiffness and shrinkage for each node of the finite element model. The interpolation was done using equation (6.5). The constitutive properties were transformed from the local axis of the grain to global axis of board using equation (6.13). The system stiffness matrix and moisture-induced load matrix were then computed for a given uniform change in moisture content as explained in chapter 3. Equation (4.46) was solved for the boundary conditions (see Figure 6.15) preventing rigid body motion and rotation to determine the displacements at all points in the board.

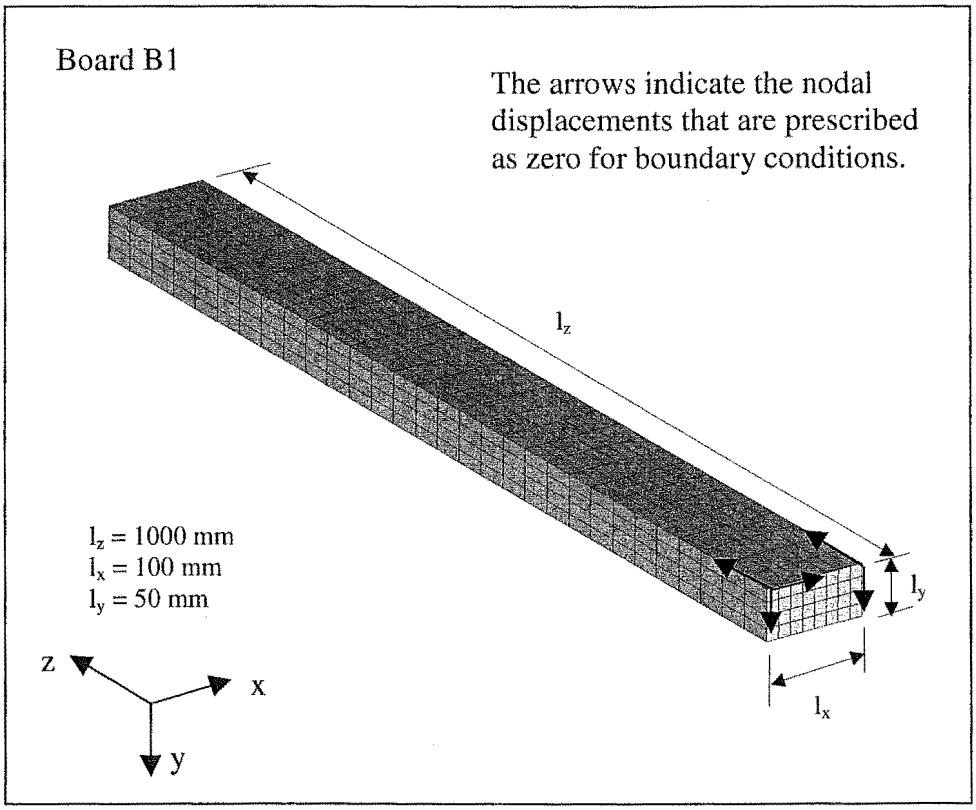

Figure 6.15. Dimensions of board and boundary conditions.

6.3.2 Second Model

The second board model also consists of a suite of FORTRAN 90 programs that perform the computer simulation and plot the undeformed and deformed finite element meshes of the board in TECPLOT.

Information on log dimensions, board dimensions, the location of the boards in the log and the board topology for the finite element model were generated from the key input data. As described previously in this chapter the pith location was defined with respect to the global axis using a cubic-spline interpolation and subsequently the polar co-ordinates of the finite element nodes with respect to a local axis were obtained. The local axis was based upon the pith orientation. Using a cubic-spline interpolation, the polar coordinates of the nodes and the measured data from the disks B and D, the microfibril angle, spiral grain angle and density were calculated and assigned to the corresponding nodes. A finite element model was formed with 27-node three dimensional block elements for each board.

The cellular models were used to obtain a database of elastic stiffness and shrinkage coefficients based upon the local values of microfibril angle and density. These stiffness and shrinkage properties were mapped onto the nodes of the finite element model. Similar to the first model, a finite element analysis was carried out to obtain the displacements at all points in the board for a given uniform change in moisture content.

6.4 Results

6.4.1 Results from the Board Models

Using both models, shrinkage along the longitude, width and thickness of the boards were calculated from the nodal displacements in the respective directions. The warping properties were also calculated using the nodal displacements as illustrated in Figure 6.16 and given in equations (6.17) – (6.20).

The following equations are used to determine warping such as bow, crook, cup and twist:

for bow

$$d_{bow} = \frac{u_{yb} + u_{yt}}{2} - u_{ym} \qquad (6.17)$$

for crook

$$d_{crook} = \frac{u_{xb} + u_{xt}}{2} - u_{xm} \tag{6.18}$$

for cup

$$d_{cup} = \frac{u_{c1} + u_{c3}}{2} - u_{c2} \tag{6.19}$$

for twist

$$\theta_{twist} = \tan^{-1}\left(\frac{u_{y4} - u_{y3}}{l_x}\right) - \tan^{-1}\left(\frac{u_{y1} - u_{y2}}{l_x}\right) \tag{6.20}$$

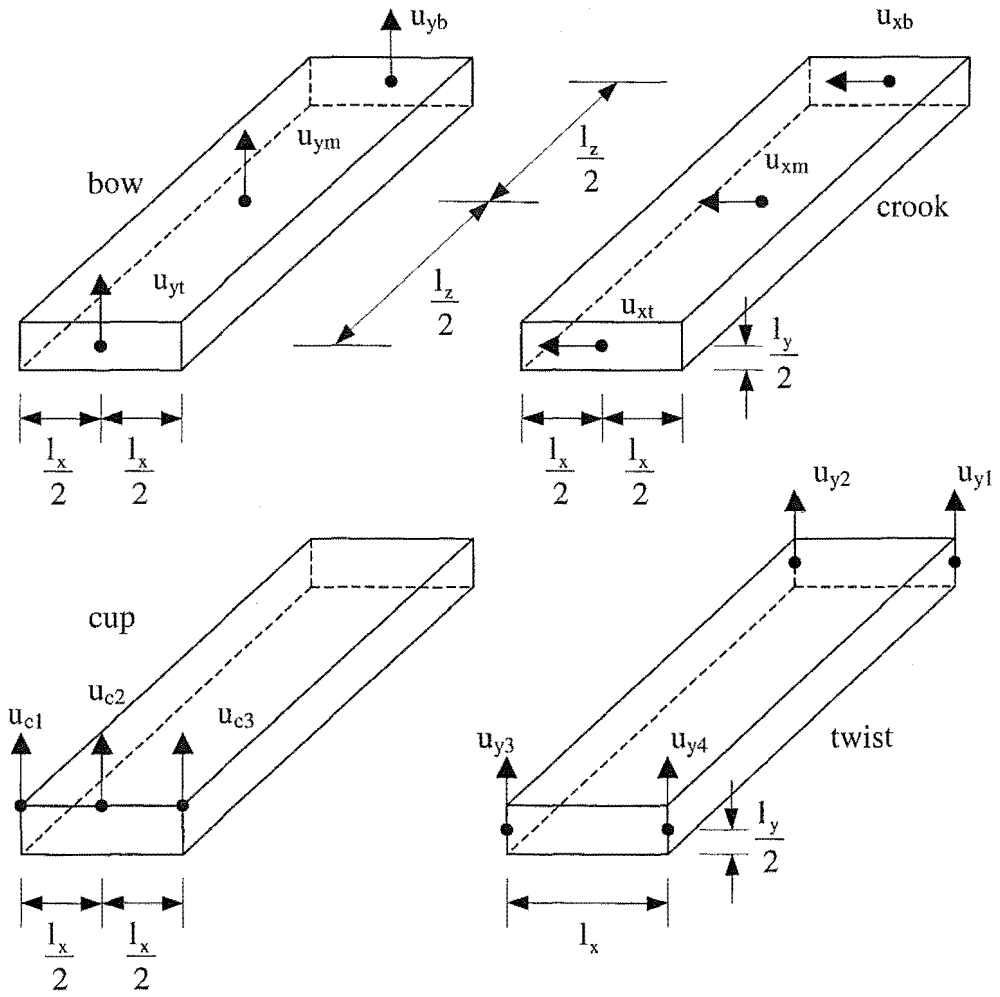

Figure 6.16. Nodal displacements to determine bow, crook, cup and twist.

The sign of the twist is positive if the twisting occurs in the clockwise direction about the longitudinal direction of the board. The bow, crook and cup have a positive sign if the mean value of the end displacements is greater than the midpoint displacement.

The shrinkage and warping results were obtained by applying the first and the second models to twenty boards from different locations in the log as shown in Figures 6.1, 6.17 and 6.18.

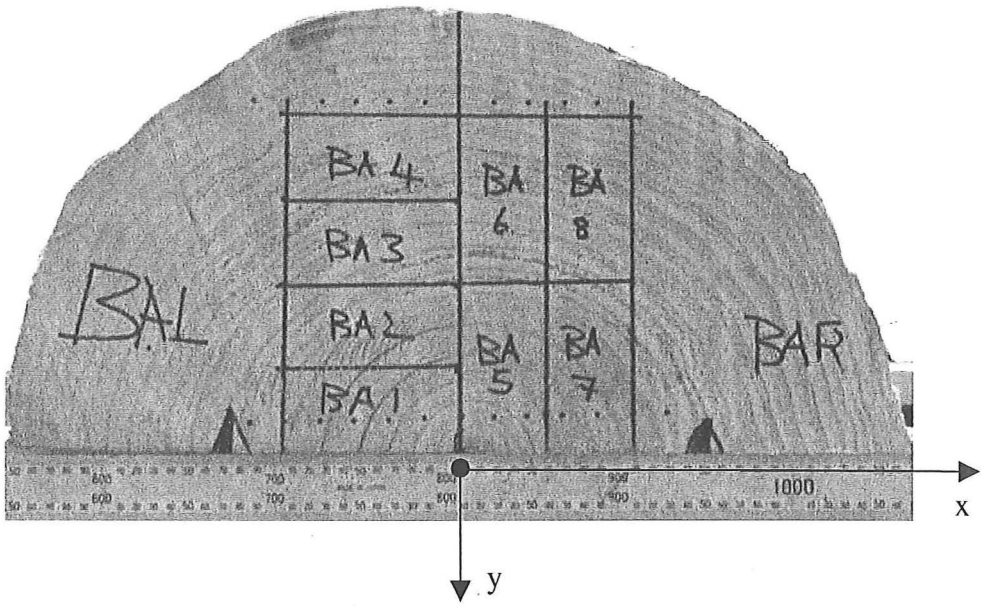

Figure 6.17. Board numbers and locations with respect to global axes are indicated in the butt of the one half of the log.

The dimensions of each board for both models were taken as 1000mm in length and 50mm x 100mm in cross section. In each case, the finite element analysis was performed for changes of moisture content of ±1% about an initial moisture content of 12%.

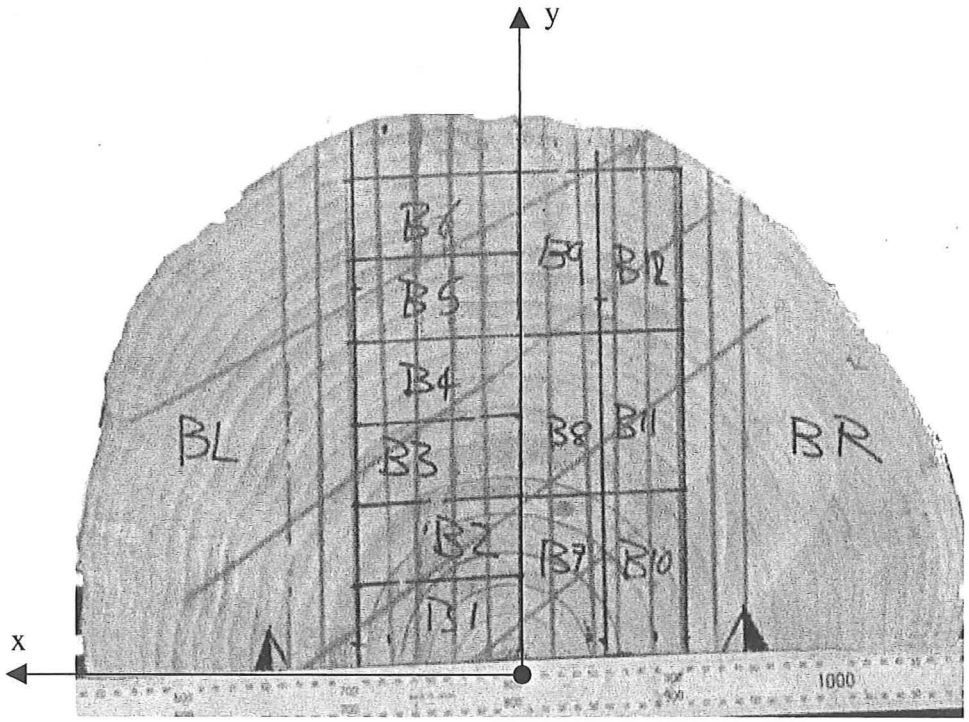

Figure 6.18. Board numbers and location with respect to global axes are indicated in the butt of the other half of the log.

The warping properties such as bow, crook, cup and twist of twenty boards from both models are listed in Tables 6.1 and 6.2.

Table 6.1. Board deformation in (m) from the first model.

BOARD	BOW	CROOK	CUP	TWIST(deg)
B1	0.0173	0.0240	0.0001	-5.5626
B2	0.0239	0.0146	-0.0005	-2.5151
B3	0.0278	0.0095	-0.0005	-0.5639
B4	0.0028	-0.0002	-0.0002	-1.0930
B5	0.0002	-0.0009	-0.0002	-0.9280
B6	0.0002	-0.0009	-0.0002	-0.7866
B7	-0.0172	0.0239	-0.0002	5.5502
B8	-0.0043	0.0188	0.0002	0.7991
B9	-0.0010	-0.0001	0.0000	0.8954
B10	-0.0240	0.0146	0.0005	2.5041
B11	-0.0078	0.0105	0.0003	0.8402
B12	-0.0009	-0.0003	0.0000	0.8636
BA1	-0.0168	-0.0237	0.0009	-5.5093
BA2	-0.0239	-0.0146	0.0008	-2.5027
BA3	-0.0259	-0.0095	0.0006	-0.6134
BA4	-0.0025	0.0002	0.0003	-1.0712
BA5	0.0168	-0.0238	-0.0009	5.4929
BA6	0.0042	-0.0205	0.0001	0.6792
BA7	0.0237	-0.0145	-0.0008	2.5671
BA8	0.0078	-0.0114	0.0001	0.7528

Table 6.2. Board deformation in (m) from the second model.

BOARD	BOW	CROOK	CUP	TWIST(deg)
B1	0.0023	0.0073	-0.0008	-16.4072
B2	0.0039	0.0040	-0.0013	8.0223
B3	0.0039	0.0117	0.0002	11.9182
B4	0.0072	0.0052	-0.0003	-8.6321
B5	0.0043	0.0024	-0.0011	-3.4835
B6	0.0294	0.0094	-0.0005	-13.2191
B7	0.0026	0.0012	-0.0002	3.8290
B8	-0.0022	0.0261	-0.0010	3.6570
B9	-0.0131	0.0283	0.0004	10.9584
B10	-0.0032	-0.0045	0.0012	-15.1648
B11	-0.0189	0.0162	0.0002	7.4726
B12	-0.0190	0.0266	0.0006	8.1402
BA1	-0.0167	0.0021	0.0010	6.0100
BA2	-0.0180	-0.0068	0.0000	14.8242
BA3	-0.0257	0.0024	0.0000	-5.9071
BA4	-0.0253	0.0053	0.0016	-7.6599
BA5	-0.0004	-0.0104	-0.0027	24.3772
BA6	0.0078	-0.0117	0.0009	11.7319
BA7	0.0000	-0.0025	-0.0012	-7.4740
BA8	0.0119	-0.0177	-0.0005	8.2785

The shrinkage/swelling coefficients along the directions of longitude, width and thickness for twenty boards from both models are listed in Tables 6.3 and 6.4. The shrinkage/swelling coefficients along the width and the thickness were calculated at the butt, middles and top of the boards and are listed in the separate columns of the tables. The average of these values are also listed in the tables.

The deformed and undeformed finite element (FE) meshes of twenty boards from both models are given in Appendix (I). The contour plots of the distribution and variation of density (RO), microfibril angle (MFA), spiral grain angle (PSI), modulus of elasticity in the radial direction (ER), modulus of elasticity in the tangential direction (ET), modulus of elasticity in the longitudinal direction (EL), shrinkage/swelling coefficients in the radial direction (ALPH-R), shrinkage/swelling coefficients in the tangential direction (ALPH-R) and shrinkage/swelling coefficients in the longitudinal direction (ALPH-R) for board B1 are illustrated in Appendix (J).

Table 6.3. Shrinkage/Swelling coefficients in longitude, width and thickness of boards from the first model.

BOARD	LONGITU	WIDTH				THICKNESS			
		BASE	MIDLE	TOP	AVERAGE	BASE	MIDLE	TOP	AVERAGE
B1	0.100	0.271	0.270	0.274	0.272	0.281	0.283	0.278	0.281
B2	0.092	0.295	0.292	0.295	0.294	0.279	0.284	0.279	0.281
B3	0.082	0.305	0.304	0.305	0.305	0.276	0.277	0.277	0.277
B4	0.075	0.310	0.311	0.310	0.310	0.282	0.282	0.282	0.282
B5	0.075	0.312	0.312	0.312	0.312	0.280	0.281	0.281	0.281
B6	0.075	0.312	0.312	0.312	0.312	0.280	0.281	0.281	0.281
B7	0.100	0.271	0.270	0.274	0.272	0.281	0.283	0.278	0.281
B8	0.079	0.297	0.300	0.298	0.298	0.311	0.309	0.311	0.310
B9	0.075	0.303	0.304	0.304	0.304	0.313	0.313	0.313	0.313
B10	0.092	0.295	0.292	0.295	0.294	0.279	0.284	0.279	0.281
B11	0.077	0.301	0.306	0.302	0.303	0.313	0.308	0.313	0.311
B12	0.075	0.304	0.306	0.306	0.305	0.311	0.311	0.311	0.311
BA1	0.100	0.271	0.270	0.274	0.272	0.281	0.283	0.278	0.281
BA2	0.092	0.295	0.292	0.295	0.294	0.279	0.284	0.279	0.281
BA3	0.082	0.305	0.304	0.305	0.305	0.299	0.301	0.300	0.300
BA4	0.075	0.310	0.311	0.310	0.310	0.305	0.305	0.306	0.305
BA5	0.100	0.271	0.270	0.274	0.272	0.281	0.283	0.278	0.281
BA6	0.079	0.275	0.277	0.275	0.276	0.311	0.309	0.311	0.310
BA7	0.092	0.295	0.292	0.295	0.294	0.279	0.284	0.279	0.281
BA8	0.077	0.278	0.283	0.279	0.280	0.312	0.307	0.312	0.310

Table 6.4. Shrinkage/Swelling coefficients in longitude, width and thickness of boards from the second model.

BOARD	LONGITU	WIDTH				THICKNESS			
		BASE	MIDLE	TOP	AVERAGE	BASE	MIDLE	TOP	AVERAGE
B1	0.094	0.271	0.276	0.275	0.274	0.300	0.289	0.271	0.287
B2	0.095	0.307	0.291	0.290	0.296	0.255	0.283	0.286	0.275
B3	0.095	0.310	0.297	0.304	0.304	0.257	0.268	0.267	0.264
B4	0.086	0.296	0.305	0.295	0.299	0.287	0.281	0.287	0.285
B5	0.092	0.308	0.303	0.304	0.305	0.268	0.270	0.277	0.272
B6	0.080	0.310	0.310	0.304	0.308	0.280	0.284	0.277	0.280
B7	0.097	0.276	0.278	0.276	0.277	0.296	0.289	0.280	0.288
B8	0.092	0.292	0.296	0.306	0.298	0.311	0.304	0.292	0.302
B9	0.086	0.298	0.297	0.307	0.301	0.305	0.308	0.293	0.302
B10	0.097	0.294	0.291	0.283	0.289	0.280	0.282	0.293	0.285
B11	0.087	0.291	0.304	0.290	0.295	0.321	0.308	0.311	0.313
B12	0.081	0.291	0.306	0.301	0.299	0.319	0.307	0.301	0.309
BA1	0.091	0.276	0.280	0.282	0.279	0.290	0.291	0.284	0.288
BA2	0.086	0.313	0.297	0.288	0.299	0.261	0.287	0.303	0.284
BA3	0.076	0.306	0.307	0.304	0.306	0.326	0.306	0.299	0.310
BA4	0.074	0.318	0.310	0.310	0.313	0.301	0.304	0.301	0.302
BA5	0.089	0.263	0.284	0.291	0.279	0.333	0.294	0.272	0.300
BA6	0.075	0.282	0.275	0.279	0.279	0.322	0.302	0.314	0.313
BA7	0.089	0.300	0.295	0.306	0.300	0.276	0.290	0.272	0.279
BA8	0.073	0.285	0.286	0.305	0.292	0.308	0.307	0.302	0.306

6.4.2 Results from the Experiments

Twenty boards of one-meter long and 50mm x 100mm in cross section were cut from log C (see Figures 5.6, 6.1, 6.16 and 6.17) to study shrinkage and warping properties. Initially, the boards were naturally dried over four months at 20 °C and 60% relative humidity until they reached a moisture content of 10% and subsequently nine of the boards were artificial dried to 3% moisture content at 110°C and 30% relative humidity. Then their moisture content was increased to nearly 15% moisture content in a controlled environment at 20°C and 78% relative humidity without applying any external loads. The changes in the dimensions, distortions and weight of the boards were recorded. The method of measuring the changes of dimensions and distortion of boards is explained in Appendix (K). The calculated shrinkage/swelling and warping properties from the experimental measurements against the moisture content are illustrated in Appendix (L). The shrinkage graphs were extrapolated to zero moisture content as shown in these figures. Shrinkage/swelling coefficients at 12% moisture content were calculated from the gradient of the graphs by assuming that the variation of shrinkage was linear from 15% to 0% moisture content. Keys for the graphs: DVS – volumetric shrinkage for desorption, DLS – longitudinal shrinkage for desorption, DWS – shrinkage along the width for desorption, DTS – shrinkage along the thickness for desorption, AVS – volumetric swelling for adsorption, ALS – longitudinal swelling for adsorption, AWS – swelling along the width for adsorption, ATS – swelling along the thickness for adsorption, Keys for the graphs: DCR – crooking for desorption, DBO – bowing for desorption, DCU – cuping for desorption, DTW – twisting the thickness for desorption, ACR – crooking for adsorption, ABO – bowing for adsorption, ACU – cuping for adsorption and ATW – twisting for adsorption.

6.5 Comparisons, Verification and Discussion

6.5.1 Results from the First and Second Models

6.5.1.1 Longitudinal Shrinkage/Swelling Coefficients

The first model: The predicted longitudinal shrinkage coefficients of the boards B1, B7, BA1 and BA7 that are near the pith are greater than that of other boards. These

values decrease with the varying location of the board from the pith in the radial direction, and reach constant values at the corewood/outerwood boundary. The variation of the longitudinal shrinkage coefficient can also be observed within a board as shown by the contour plot of the board B1 in Figure J9 in Appendix (J). The contour plot also shows that the longitudinal shrinkage coefficient decreases with the height of the board. The reason for the variation in the longitudinal shrinkage coefficient is that the longitudinal shrinkage is influenced significantly by the density and the microfibril angle. According to the assumption made for the first model, these properties decrease linearly with the axial distance along the log as well as with radial distance from the pith reaching constant values at the corewood/outerwood boundary. As illustrated in the contour plots of the board B1 from the first model (Figures J6 and J9 in Appendix (J)), increasing longitudinal elastic modulus reduces the longitudinal shrinkage.

The second model: The contour plots of the longitudinal shrinkage coefficient, density and microfibril angle for the board B1 show that these properties are non-linearly distributed in the board. Because, the pith is not parallel to the board direction and hence all the parameters that vary in the radial direction from the pith also vary in the longitudinal direction of the board. However the predicted longitudinal shrinkage coefficient of the board does not show significant variation from the value that was calculated by the first model. Also the calculated longitudinal shrinkage coefficients of the eighteen boards are not significantly different and have greater values than that of the boards BA3, BA4, BA6 and BA8. From the graphs (specimens SBA1, SBA2, SBA3, STA1, STA2 and STA3 as shown in Figure 6.2) of the microfibril angle (Appendices (G)), the microfibril angle is low in the zone of the log from where the boards BA3, BA4, BA6 and BA8 were obtained.

6.5.1.2 Transverse Shrinkage/Swelling Coefficients

The first model: The transverse shrinkage coefficients were calculated along the width and thickness of the boards. The shrinkage coefficients that were predicted by the first model along the width of the boards B1, B7, BA1 and BA5 are equal, and similarly the shrinkage coefficients along the thickness of these boards are also equal. Although the directions along the width and the thickness of the boards are parallel to the radii in the respective directions, the coefficients along the thickness are higher

than that of along the width. This is due to the width having a greater number of growth rings than the thickness (see Figures 6.17 and 6.18). The boards B2, B3, B4, B5, B6, BA2, BA3 and BA4 predict higher shrinkage along the width than the thickness, because the section of the growth rings are larger along the width than along the thickness. A similar variation in the growth ring distribution is observed in the rest of the boards that have higher shrinkage along the thickness than along the width. The contour plots of board B1 from the first model (Figures J6 and J7 in Appendix (J)) show that the transverse shrinkage increases with radius from the pith since the density increases and the microfibril angle decreases in the radial direction.

The second model: The predicted transverse shrinkage coefficients from the second model do not differ significantly from the results obtained from the first model. However the contour plots of B1 shows the random distribution of these coefficients within the board due to the random distribution of density and microfibril angle since the pith deviates from the board direction.

6.5.1.3 Warping Properties

Twist, bow and crook are the significant warping properties that were predicted by the first and second models. The predicted values of the cup by these models for all the boards are very small since there is little difference between the shrinkage values along the width and the thickness of the boards. Further, as discussed in the previous chapter the shrinkage coefficient in the radial direction is less than in the tangential direction, and consequently this reduces the potential for cupping. As a result of the sawing pattern, the boards do not have a plane of symmetry with respect to the curvature of growth rings in their cross section. It may therefore produce a skew deformation in the cross section of a board due to the inclined orientation of the growth rings.

The warping deformation is dependent on the location of the board in a log. The main factors responsible for warping deformation are the cylindrical orientation of the wood fibres, the difference between the radial and tangential shrinkage coefficients, and the radial variation in the longitudinal shrinkage coefficients, longitudinal elastic modulus and the spiral grain angle.

Twist: The spiral grain angle, curvature of the growth ring and deviation of pith have a strong influence in the formation of twist. The first model, in which the pith is assumed to be parallel to the longitudinal direction of the boards, predicted a large twist in the boards B1, B7, BA1 and BA5 that were cut from near the pith where the spiral grain angle is high.

The twist deformation predicted by the second model is considerably greater than that from the first model. The main reason for such a high value is due to the large variation of spiral grain angle in the butt and the top as shown in the graphs of spiral grain angle in Appendix (H). The twist deformations calculated by the second model also varies significantly among the boards. The boards from near the pith have large values of twist due to the pith's deviation from a straight line. The actual spiral grain angle in some boards has an opposite sign from that assumed in the first model. Therefore, a few boards, for example B2, B10 and BA7 have twist with opposite signs when comparing the results from both models.

Bow: The boards that are near the pith bow towards the pith since the longitudinal shrinkage coefficient is large at the pith. Although all boards have the same dimensions, they have different values of bow. For example B2 has higher value than B1 even though B1 is from near the pith. This is mainly due to the curvature of growth rings. The curvature becomes less when the location of board is further away from the pith. The internal constraint is less if the curvature is less and thus results in a greater bow. The bow deformation also increases with increasing spiral grain angle.

The lower half of the pith is shared between the boards B1and BA5 while the upper half of the pith is in the board B1and has a curved shape (see Figure 6.1). Since the shape of pith located in the board B1is non-linear, the lower part of the board bows toward the pith while the upper part bows in the opposite, and hence the overall bow is reduced. This results in the second model predicting a small value of bow for board B1, than the first model. This reason is also applicable to the difference in results for board BA5 because of the absence of the upper portion of the pith. Some of the boards have the same values of bow from both models and some have higher values from the first model than from the second model. The main reason for this variation is that the distribution of properties is not linear in the second model.

Crook: According to the assumption made in the first model one of the longitudinal edges of each of the boards, B1, B7, BA1 and BA5, is aligned with the pith and therefore these boards have a large crook deformation. The crook deformation becomes less when the location of board moves away from the pith because the curvatures of growth rings become less.

The calculated crook deformations by both models show similar differences as for the calculated bow deformations. Hence, as for the bow, the distribution of the properties is significant.

6.5.2 Experimental Results and Verification

Moisture distribution throughout a board could be considered to be uniform since the change of moisture in the board was achieved by slow desorption and adsorption processes to ensure that an equilibrium conditions had been achieved with no moisture gradient within the board. Consequently the stress distribution due to hygroscopic strain is uniform in the board.

Measured shrinkage against the moisture content in the directions of longitude, width and thickness of the twenty boards are shown in Figures L1 – L7 of Appendix (L). The resultant shrinkage coefficients from the experiments at 12% moisture content are compared in Table 6.5 and in Figures 6.19 – 6.21. The measured variation in warping deformation against the moisture content are shown in Figures L8 – L12 of Appendix (L), and resultant warping deformations per unit moisture change at 12% moisture content are compared in Table 6.6 and in Figures 6.22 – 6.25. As for Figures L1 – L7 of Appendix (L), shrinkage in the directions of all the boards show almost linear variation against the moisture content from 15% to 0%. For the nine boards, swelling in the three directions and warping behaviours during the adsorption of moisture are also presented in Figures for the nine boards B1, B2, B3, B4, B7, B8, BA4, BA5 and BA7.

Table 6.5 Shrinkage/swelling coefficients along the longitude, width and thickness of twenty boards from the first (1ST) and second (2ND), and experiment (EXP).

	LONGITUTE			WIDTH			THICKNESS		
BOARD	1ST	2ND	EXP	1ST	2ND	EXP	1ST	2ND	EXP
B1	0.100	0.094	0.070	0.272	0.274	0.226	0.281	0.287	0.252
B2	0.092	0.095	0.050	0.294	0.296	0.210	0.281	0.275	0.250
B3	0.082	0.095	0.050	0.305	0.304	0.250	0.277	0.264	0.230
B4	0.075	0.086	0.050	0.310	0.299	0.280	0.282	0.285	0.260
B5	0.075	0.092	0.050	0.312	0.305	0.250	0.281	0.272	0.200
B6	0.075	0.080	0.050	0.312	0.308	0.300	0.281	0.280	0.270
B7	0.100	0.097	0.080	0.272	0.277	0.250	0.281	0.288	0.300
B8	0.079	0.092	0.050	0.298	0.298	0.250	0.310	0.302	0.360
B9	0.075	0.086	0.050	0.304	0.301	0.250	0.313	0.302	0.300
B10	0.092	0.097	0.070	0.294	0.289	0.260	0.281	0.285	0.250
B11	0.077	0.087	0.060	0.303	0.295	0.290	0.311	0.313	0.320
B12	0.075	0.081	0.060	0.305	0.299	0.280	0.311	0.309	0.300
BA1	0.100	0.091	0.070	0.272	0.279	0.270	0.281	0.288	0.280
BA2	0.092	0.086	0.070	0.294	0.299	0.300	0.281	0.284	0.260
BA3	0.082	0.076	0.060	0.305	0.306	0.290	0.300	0.310	0.260
BA4	0.075	0.074	0.050	0.310	0.313	0.320	0.305	0.302	0.310
BA5	0.100	0.089	0.080	0.272	0.279	0.250	0.281	0.300	0.290
BA6	0.079	0.075	0.050	0.276	0.279	0.270	0.310	0.313	0.300
BA7	0.092	0.089	0.070	0.294	0.300	0.270	0.281	0.279	0.280
BA8	0.077	0.073	0.060	0.280	0.292	0.300	0.310	0.306	0.280

Table 6.6 Bow, crook, cup and twist of twenty boards from the first (1ST) and second (2ND), and experiment (EXP).

	BOW			CROOK			CUP			TWIST		
BOARD	1ST	2ND	EXP	1ST	2ND	EXP	1ST	2ND	EXP	1ST	2ND	EXP
B1	0.0173	0.0023	0.0020	0.0240	0.0073	0.0030	0.0001	-0.0008	0.0000	-5.5626	-16.4072	-4.0000
B2	0.0239	0.0039	0.0041	0.0146	0.0040	0.0020	-0.0005	-0.0013	0.0000	-2.5151	8.0223	1.0000
B3	0.0278	0.0039	0.0020	0.0095	0.0117	0.0010	-0.0005	0.0002	0.0000	-0.5639	11.9182	2.0000
B4	0.0028	0.0072	0.0030	-0.0002	0.0052	0.0010	-0.0002	-0.0003	0.0000	-1.0930	-8.6321	-3.0000
B5	0.0002	0.0043	0.0032	-0.0009	0.0024	0.0000	-0.0002	-0.0011	0.0000	-0.9280	-3.4835	-1.5000
B6	0.0002	0.0294	0.0030	-0.0009	0.0094	0.0000	-0.0002	-0.0005	0.0000	-0.7866	-13.2191	-2.0000
B7	-0.0172	0.0026	0.0015	0.0239	0.0012	0.0010	-0.0002	-0.0002	0.0000	5.5502	3.8290	2.0000
B8	-0.0043	-0.0022	-0.0020	0.0188	0.0261	0.0250	0.0002	-0.0010	0.0000	0.7991	3.6570	1.5000
B9	-0.0010	-0.0131	-0.0040	-0.0001	0.0283	0.0010	0.0000	0.0004	0.0000	0.8954	10.9584	2.5000
B10	-0.0240	-0.0032	-0.0050	0.0146	-0.0045	0.0000	0.0005	0.0012	0.0000	2.5041	-15.1648	-1.0000
B11	-0.0078	-0.0189	-0.0060	0.0105	0.0162	0.0010	0.0003	0.0002	0.0000	0.8402	7.4726	2.7000
B12	-0.0009	-0.0190	-0.0050	-0.0003	0.0266	0.0020	0.0000	0.0006	0.0000	0.8636	8.1402	1.5000
BA1	-0.0168	-0.0167	-0.0040	-0.0237	0.0021	0.0000	0.0009	0.0010	0.0000	-5.5093	6.0100	0.0000
BA2	-0.0239	-0.0180	-0.0040	-0.0146	-0.0068	-0.0020	0.0008	0.0000	0.0000	-2.5027	14.8242	1.0000
BA3	-0.0259	-0.0257	-0.0030	-0.0095	0.0024	0.0000	0.0006	0.0000	0.0000	-0.6134	-5.9071	0.0000
BA4	-0.0025	-0.0253	-0.0020	0.0002	0.0053	0.0000	0.0003	0.0016	0.0000	-1.0712	-7.6599	-1.5000
BA5	0.0168	-0.0004	0.0000	-0.0238	-0.0104	-0.0020	-0.0009	-0.0027	0.0000	5.4929	24.3772	4.0000
BA6	0.0042	0.0078	0.0020	-0.0205	-0.0117	-0.0020	0.0001	0.0009	0.0000	0.6792	11.7319	2.0000
BA7	0.0237	0.0000	0.0025	-0.0145	-0.0025	-0.0010	-0.0008	-0.0012	0.0000	2.5671	-7.4740	-1.0000
BA8	0.0078	0.0119	0.0020	-0.0114	-0.0177	-0.0010	0.0001	-0.0005	0.0000	0.7528	8.2785	1.0000

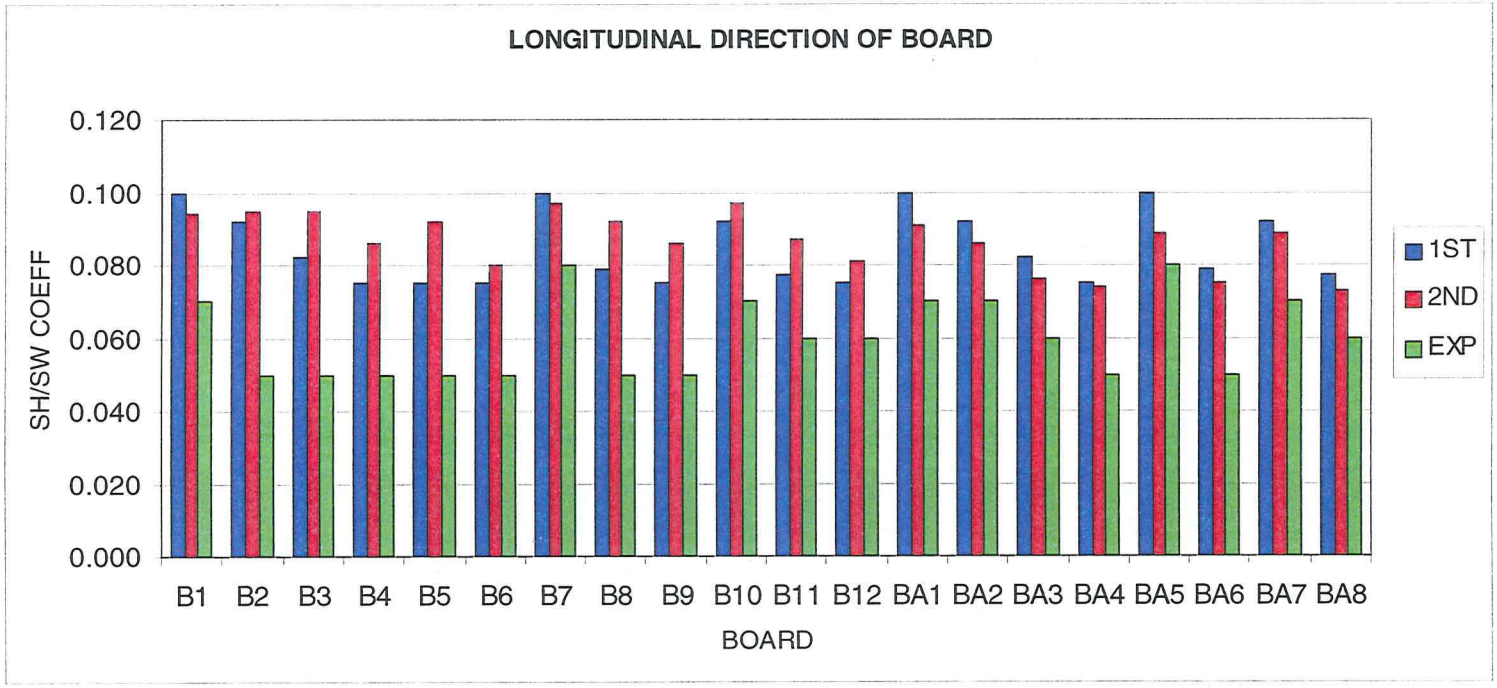

Figure 6.19. Comparison of shrinkage/swelling coefficients in the longitudinal direction of twenty boards from the first (1ST) and second (2ND) models, and experiments (EXP).

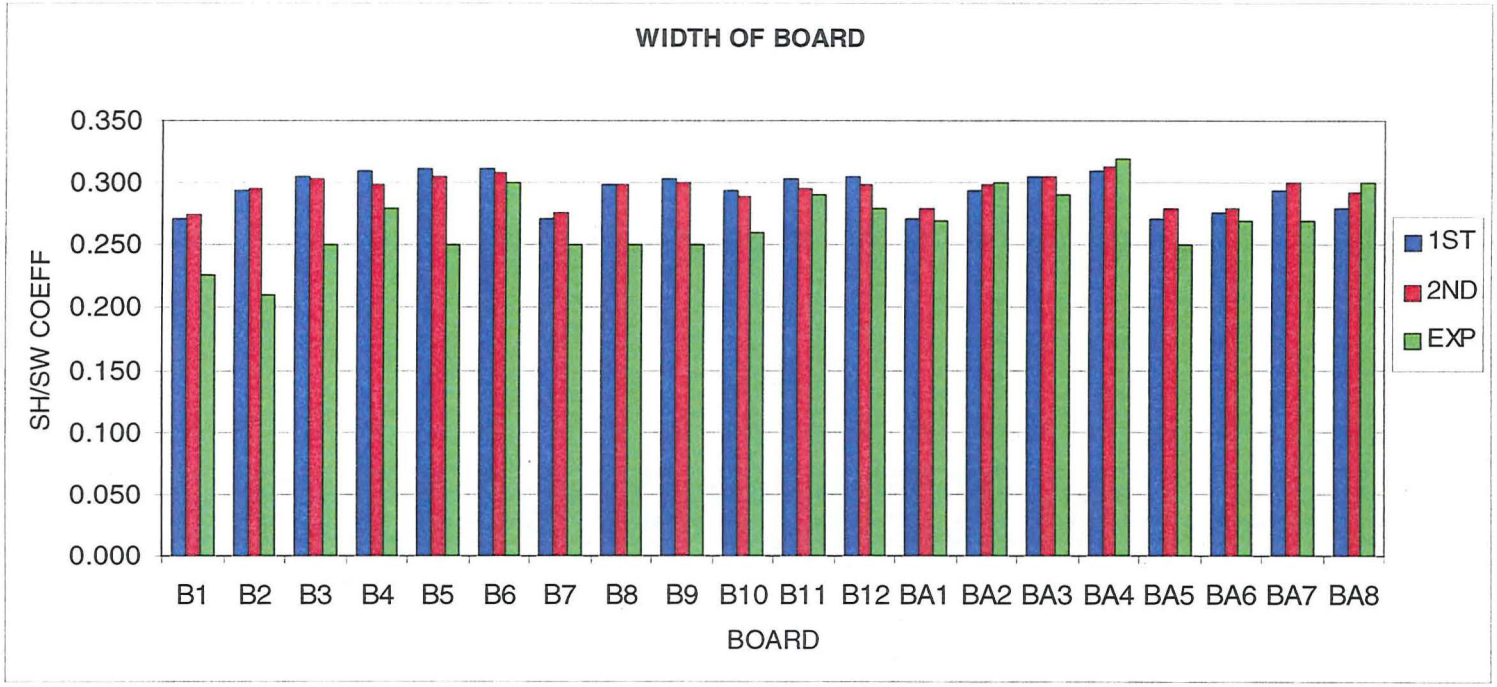

Figure 6.20. Comparison of shrinkage/swelling coefficients along the width of twenty boards from the first (1ST) and second (2ND) models, and experiments (EXP).

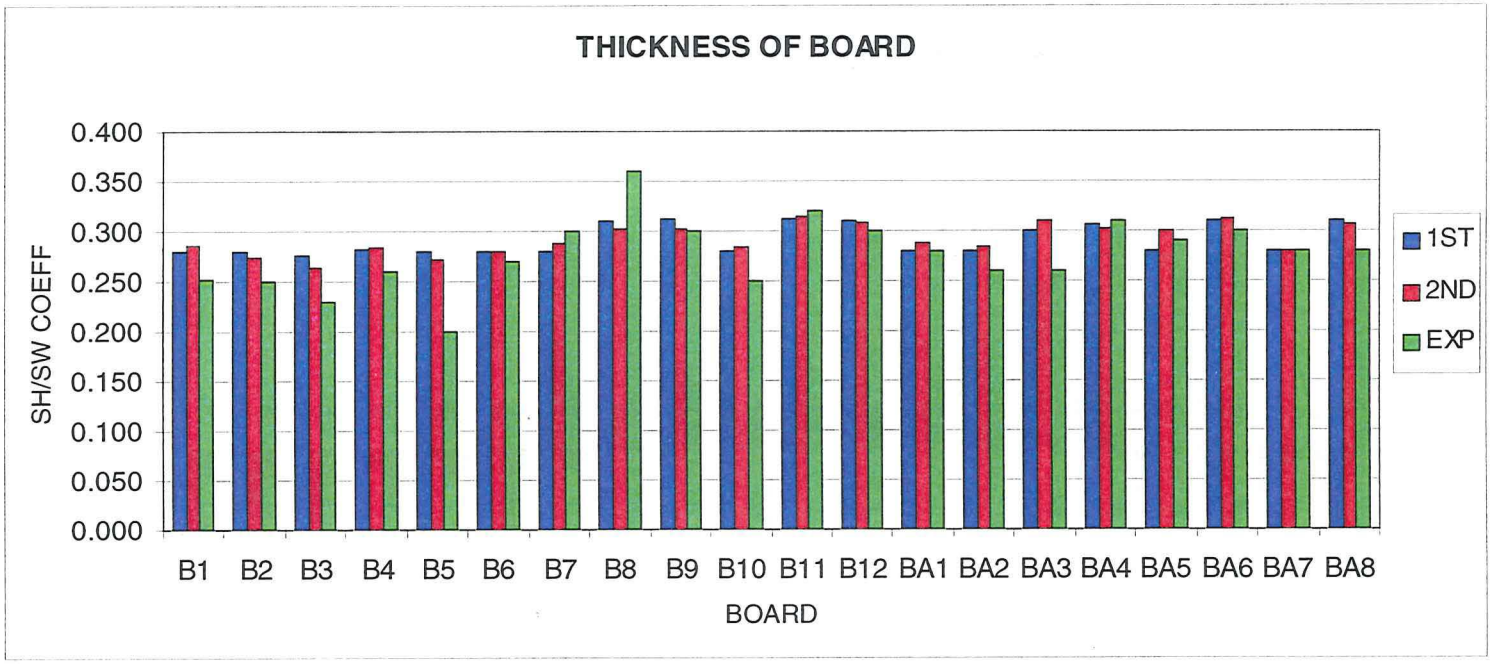

Figure 6.21. Comparison of shrinkage/swelling coefficients along the thickness of twenty boards from the first (1ST) and second (2ND) models, and experiments (EXP).

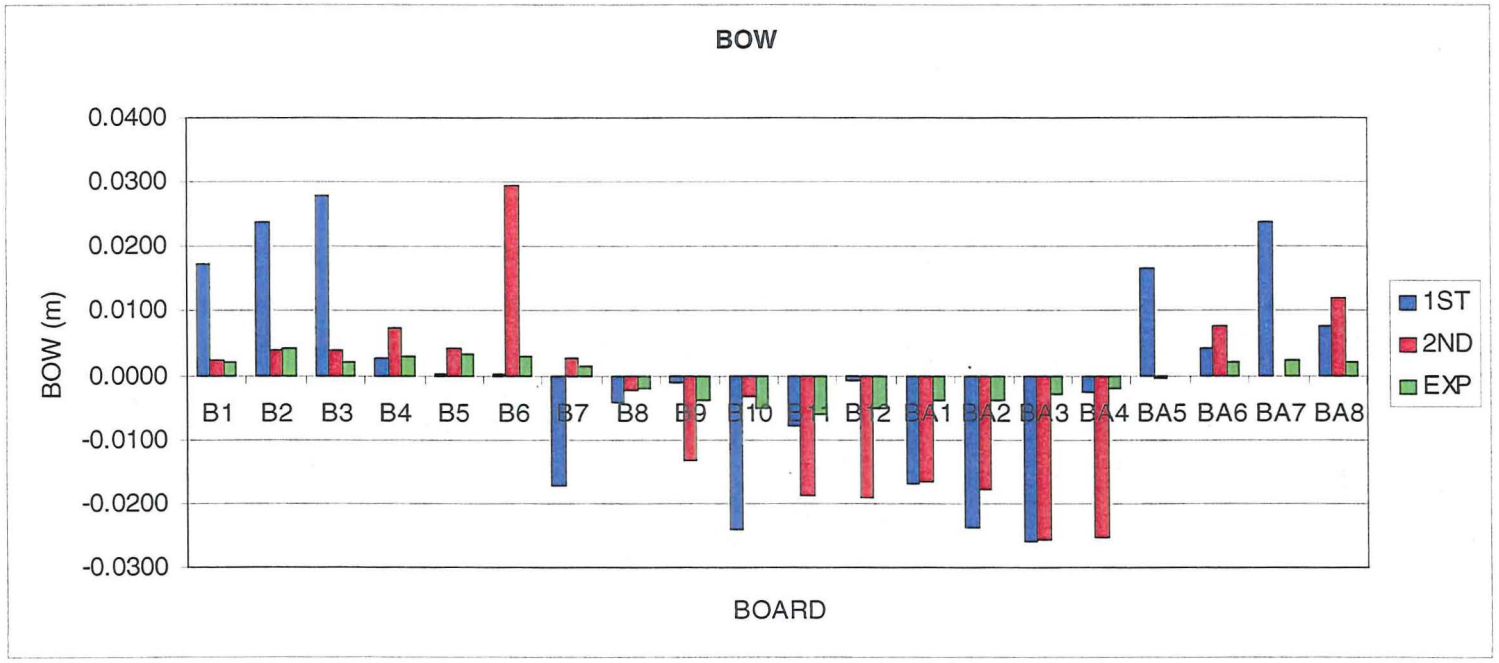

Figure 6.22. Comparison of bows of twenty boards from the first (1ST) and second (2ND) models, and experiments (EXP).

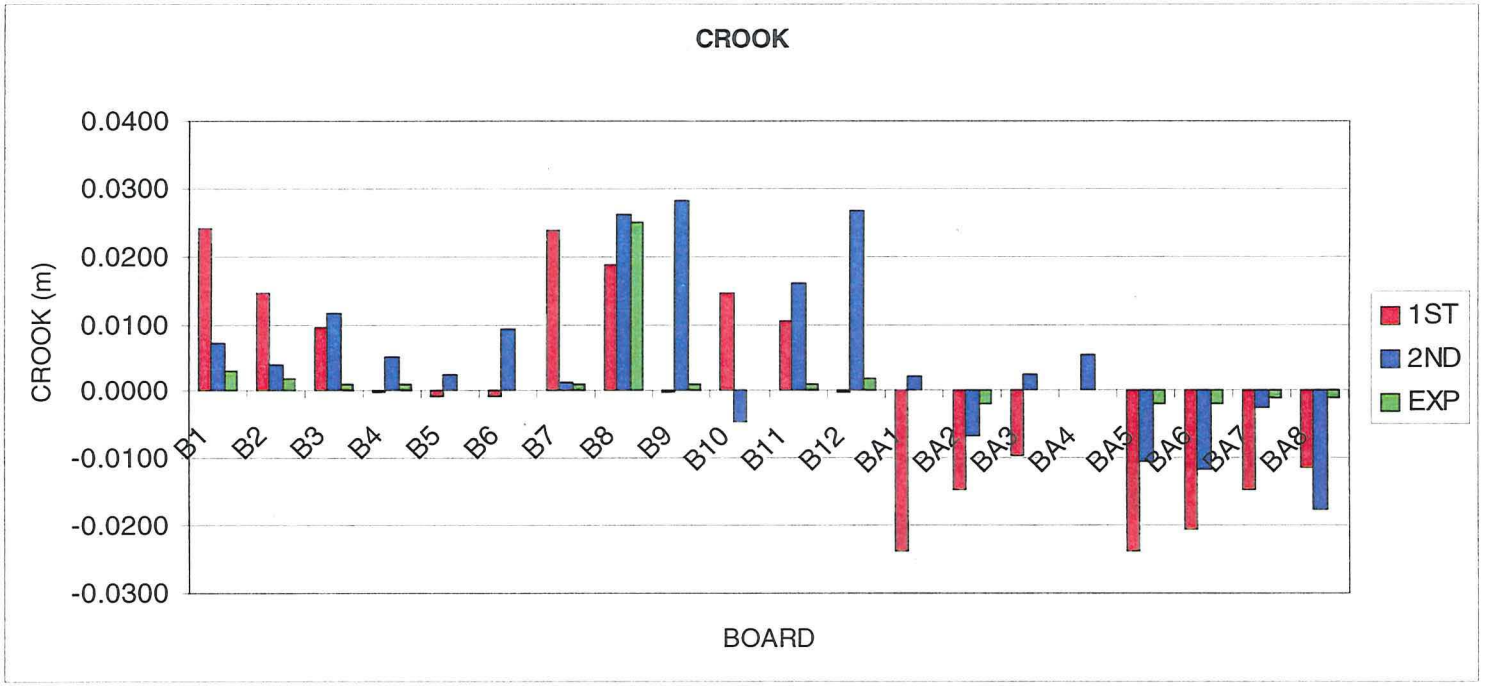

Figure 6.23. Comparison of crooks of twenty boards from the first (1ST) and second (2ND) models, and experiments (EXP).

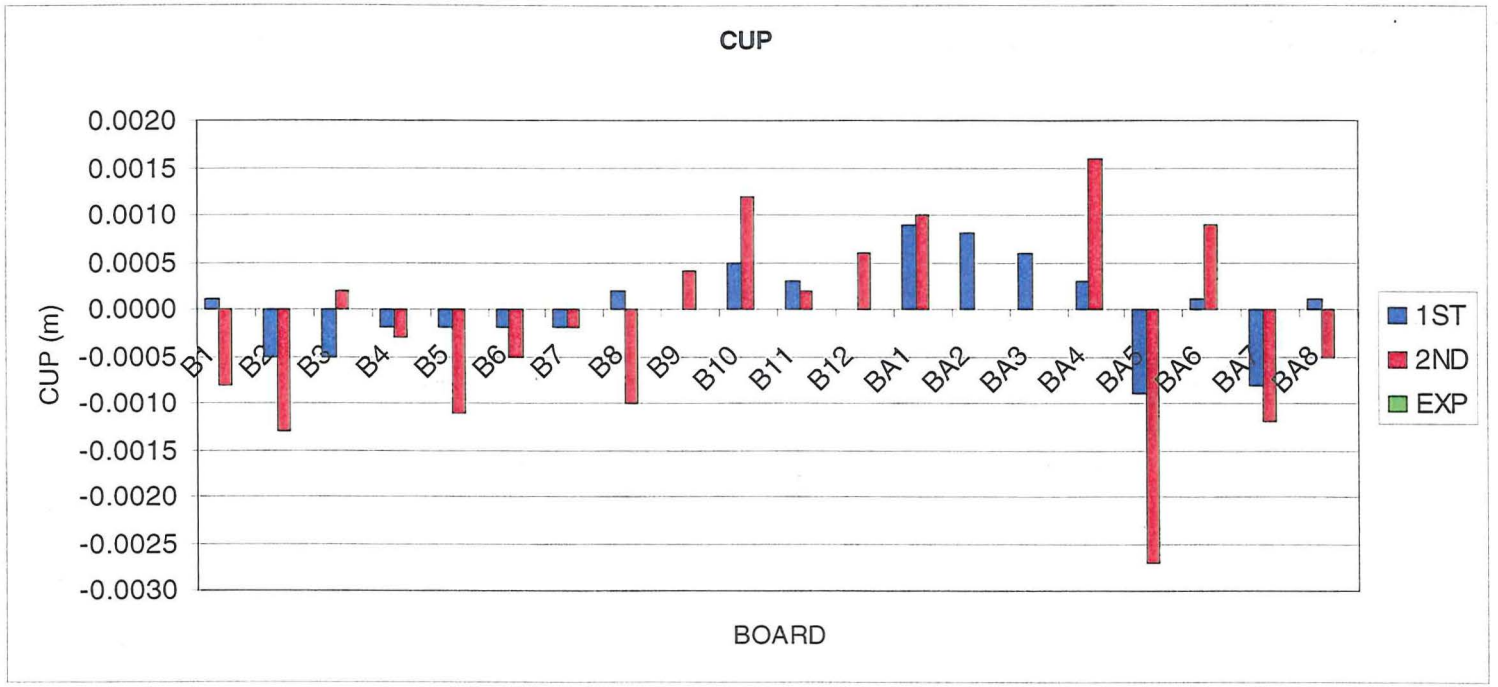

Figure 6.24. Comparison of cups of twenty boards from the first (1ST) and second (2ND) models, and experiments (EXP).

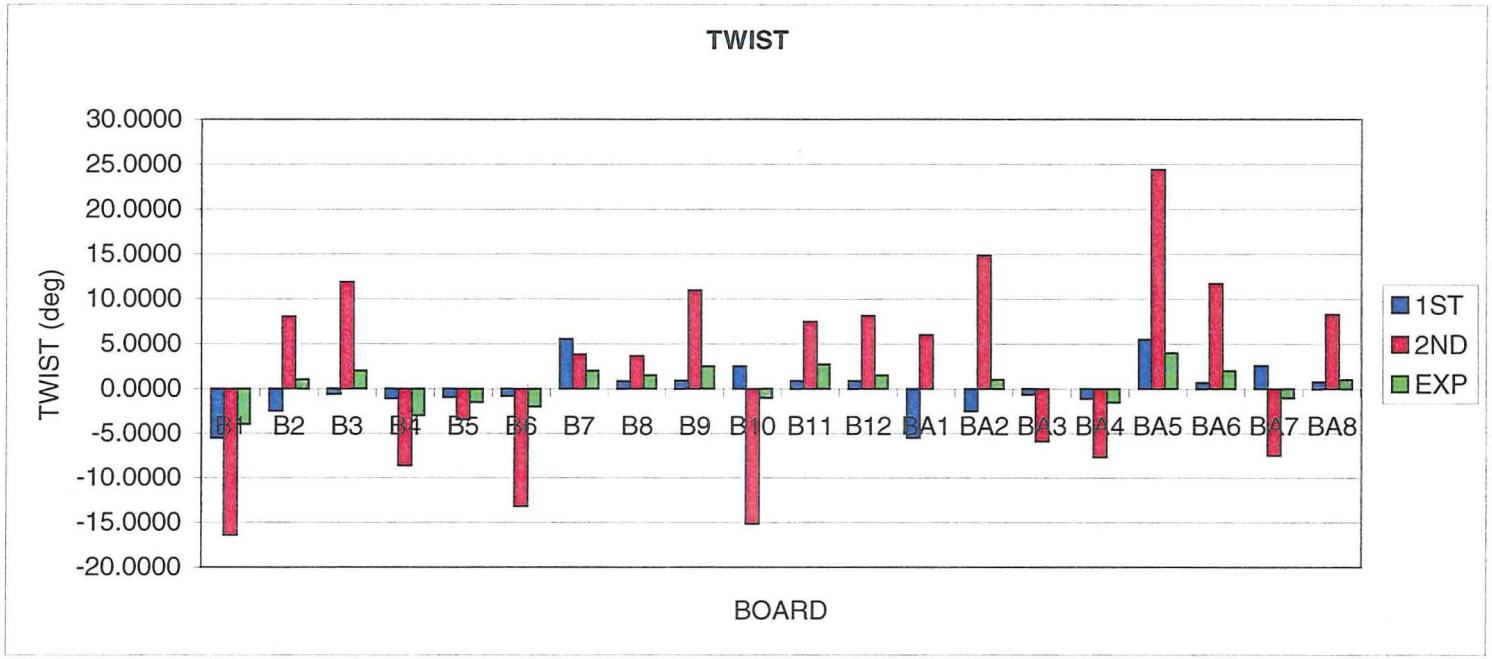

Figure 6.25. Comparison of twists of twenty boards from the first (1ST) and second (2ND) models, and experiments (EXP).

6.5.2.1 Longitudinal Shrinkage

The longitudinal shrinkage coefficients for the twenty boards calculated from the experimental measurements were less than that predicted by both models. The measurements of longitudinal dimensional changes were made using a metre scale. The limit reading of this scale is 1.0 mm and the probable uncertainty associated with reading the scale can be taken to be ±0.5 mm. Hence the measurements may not have accuracy due to very small variation in the dimensional changes.

6.5.2.2 Transverse Shrinkage

As illustrated in Figures 6.22 and 6.23, measured shrinkage coefficients in the directions of width and thickness correlated with the calculated shrinkage coefficients obtained from both models in the respective directions.

6.5.2.3 Warping Properties

By making an overall comparison of the results a common conclusion can be drawn as all measured warping deformations are slightly smaller than those calculated by the numerical models. No cup deformation was found in any of those boards during the desorption and adsorption experiments.

The measured values of the twist deformation of most of the boards are almost equal to the values determined from the first model, and smaller than the values obtained from the second model. In the case of bow and crook, the measured values of these deformations for some boards are almost equal to the values predicted by the first model and values of the other boards were close to the values predicted by the second numerical model. The reasons for these differences are considered to be due to:

a) the equivalent stiffness and shrinkage properties that were calculated by the cell models are slightly higher than the actual values due to the assumption discussed in the previous chapter,
b) in the first model the density, microfibril angle and spiral grain angle were assumed to vary linearly,
c) in the second model, the actual position of the pith was considered, but the shape of the growth rings was not taken into account, while the longitudinal

variation of properties was considered with respect to the longitudinal axis of the board rather than the pith,

d) the moisture was assumed to be distributed uniformly all over a board, however, although boards were dried very slowly without any external constraint, there may be an uneven variation of moisture between the surface and core of the board. This results a tensile stress at the surface and a compressive stress in the core since the surface dries and shrinks faster than the core.

6.6 Validation

Both models predict almost equal transverse shrinkage and have close correlation to the observed experimental results. With respect to the board distortion, both models have closer correlation to the observed experimental results only from a few boards. The second model slightly improves the prediction. The accuracy of the prediction is dependent on the quality of the stiffness and shrinkage coefficients and the complexity of the microfibril and the cell models. The first model requires less computational effort than the modified model. However provided the board/log has the assumed distribution of density, microfibril angle and spiral grain in the radial and longitudinal directions, the first model can predict the behaviour accurately. The significance of the modified model is that it can accommodate irregularities in the alignment of the pith.

6.7 Limitation

The constitutive equations which are used in the finite element model are straightforward. Elastic behaviour is assumed and the moisture content is taken to be uniform throughout the model. Technically, the model should only be applied to boards which experience small variations of moisture content about an in-service mean. In reality, it is likely that predictions for larger variations in moisture content will be valid provided that the board is dried slowly without constraint so that internal stresses remain at levels below those at which time dependent creep and other time-dependent effects are appreciable. More complex constitutive relationships which include creep and mechano-absorbtive effects can readily be incorporated within such FE models. These modifications would require a significant change, as they are time

dependent and would significantly increase the requirements by introducing the time domain.

Chapter 7

Conclusion and Future Work

7.1 Conclusion

An attempt has been made to model moisture-induced distortion in softwood by linking the structure and properties at different levels and beginning with the properties of the chemical constituents. Experimental work concerning the shrinkage behaviours at cellular level, and the warp and dimensional stability of boards were carried out and the results were used to test the models.

Specimens for experiments were obtained from a selected 20 years old *pinus radiata* tree. Microfibril angle, spiral grain angle and density were measured from the specimens obtained at 45^{o} interval from the butt and top of the log. The method of selection of specimens gave a good distribution of these properties in the butt and the top. These properties were found to vary almost linearly along the radius.

A new microscopic technique was developed to measure the changes of dimensions and geometry of cells due to moisture variation. The new technique examined the microstructure of a surface of the specimen in the wet or dry conditions without any surface treatment or use of replicas. This new microscopic technique was used to measure the change of dimensions and geometry of cells as a function of variation of moisture content.

In the first step of modelling, the equivalent properties of a heterogeneous continuum were determined by homogenization. The homogenization procedures were achieved by use of the finite element method in the repeating microstructure of the continuum using a representative volume element. The representative volume element was subjected to periodic cyclic boundary conditions and the deformations of its boundaries were related by linear constrained equations. A new approach was used to apply the constrained equations in the element stiffness and force matrices and then these matrices were appropriately assembled to form the system stiffness and force matrices. This approach helped to reduce the number of equations and optimize the computer memory and solution time. The newly developed homogenization method

was validated using two test models. The test models proved that the homogenization procedure based on the application of full cyclic constraint by a finite element method provides reliable homogenized properties for the continuum that has an orthogonal parallelepiped representative volume element.

A mesh to accommodate the five wall-layers that make up a periodic cell of wood was generated and numerical simulations were carried out using this model to calculate the equivalent stiffness and shrinkage properties. These properties were found to be dependent on the density and microfibril angle of S_2 layer. They were also found to vary along the radius and the height of the log. The shrinkage coefficients from eight specimens that were selected to have good distribution of density and microfibril angle were measured using the new microscopic method and the results were found to correlate closely with the predicted results from the model.

Simulation and numerical analysis of the distortion of two board models were performed as a function of small changes of moisture content using the equivalent properties of wood that were predicted from the cell model. The major assumptions made for the first model were a) the pith is a straight line and taken as the longitudinal axis, b) the log is perfectly conical, c) the properties vary linearly from pith to bark as well as from bottom to top. In the second model, the actual shape of the pith was considered. Both models predicted board distortion that has a close correlation to the observed experimental results. The accuracy of the prediction is dependent on the quality of the stiffness and shrinkage coefficients and the complexity of the microfibril and the cell models. The predicted deformation was found to vary with density, microfibril angle, spiral grain angle and location of the board in a log. The first model requires less computational effort than the modified model. However provided the board/log has the assumed distribution of density, microfibril angle and spiral grain in the radial and longitudinal directions, the first model can predict the behaviour accurately. The significance of the modified model is that it can accommodate irregularities in the alignment of the pith.

7.2 Limitation of Models and Future Work

Specimens from *pinus radiata* log used in experimental studies to validate the models. Volume fractions of cell wall layers of *pinus radiata* are not available. Also limited

information is available on the stiffness properties of *pinus radiata* at cellular levels to validate the cell model. More experimental work on shrinkage behaviour at cellular level using the newly developed microscopic technique is necessary to obtain a statistical representation for the validation. In the cell model, several assumptions were made, for example, the periodic cell was assumed to have rectangular section. Difference in microfibril angle in radial and tangential cell walls, pits in the radial wall and the rays were not taken into account in the model.

In board models, elastic behaviour was assumed and the moisture content was taken to be uniform throughout the model. Technically, the model should only be applied to boards which experience small variations of moisture content about an in-service mean. In reality, it is likely that predictions for larger variations in moisture content will be valid provided that the board is dried slowly without constraint so that internal stresses remain at levels below those at which time dependent creep and other time-dependent effects are appreciable. More complex constitutive relationships which include creep and mechano-absorbtive effects can be incorporated within such finite element models. In the model, a board was assumed to have only clear wood. Further studies are necessary to incorporate the variability of the structure of wood into the models.

In this study the influence of growth stress has not been taken into account and this could be a significant reason for the difference between the predicted and measured values of bow and twist. The spiral grain angle is another factor that influences the bow and twist deformations. In both models, the spiral grain angle was assumed to vary linearly between the butt and the top. The log used in this study has an irregular variation in growth structure. This would be a limitation to the difference in bow and twist predicted by the first model when compared with the second model. To validate the models, it is necessary to test using data from a number of different logs. This could not be done due to the limited time frame of this study.

It is necessary to experiment and model the complete chain of properties from the chemical constituents to the board by focusing on *pinus radiata* since it is a species of

economic significance in New Zealand. The board models can be incorporated into the development of the sawing patterns to optimize the sawn wood products.

References

Abe, H., Ohtani, J. and Fukszawa, K. (1991) FE-SEM observations on the microfibrillar orientation in the secondary wall of tracheids, *IAWA Bulletin* 12(4). p. 431-438.

Abe, H., Ohtani, J. and Fukszawa, K. (1992) Microfibrillar orientation of the innermost surface of conifer tracheid walls, *IAWA Bulletin* 13(4). p. 411-417.

Abe, H., Ohtani, J. and Fukszawa, K. (1994) A scanning electron microscopic study of changes in microtubule distributions during secondary wall formation in tracheids. *IAWA Journal* 15(2). 185-189.

Aboudi, J. (1991) *Mechanics of Composite materials-A unified micromechanical approach*. Amsterdam. Elsevier.

Astley, R. J. (1992) *Finite Elements in Solids and Structures*. Chapman & Hall. 345p.

Astley, R. J., Harrington, J. J., Tang, S. and Neumann, J. (1997) Modelling the influence of microfibril angle on stiffness and shrinkage in radiata pine. In Butterfield, B. G. *Microfibril angle in wood*. The proceeding of the international Workshop on the significance of microfibril angle to wood quality. Westport, New Zealand. 272-295.

Astley, R. J., Stol, K. A. and Harrington, J. J. (1998) Modelling the elastic properties of softwood - part II the cellular microstructure. *Holzals Rohund Werkstoff*. 56. 43-50.

Astley, R. J. (1999) Predicting movement in boards due to in-service variation in moisture content. *Workshop 1999*. Wood technology research center, University of Canterbury, Christchurch, New Zealand.

Barber, N.F. (1968) A theoretical model of shrinking wood. *Holzforschung* Bd. 22: 97-103.

Barber, N.F. and Meylan, B.A. (1964) The anisotropic shrinkage of wood. *Holzforschung* 18(5): 146-156.

Barrett, J. D., Schniewind, A. P. and Taylor, R. L. (1972) Theoretical shrinkage model for wood cell walls. *Wood science* 4(3): 178-192.

Bodig, J. and Jayne, B. A. (1982) *Mechanics of wood and wood composites*. New York, Van Nostrand Reinhold. 712 p.

Boutelje, J.B. (1962) The relationship of structure to transverse anisotropy in wood with Reference to shrinkage and elasticity, *Holzforschung* 16(2): 33-46.

Boutelje, J.B. (1968) A theoretical model of shrinkage, *Holzforschung* 22(4): 97-103.

Butterfield, B. G. (1997) Microfibril angle in wood. The proceeding of the international Workshop on the significance of microfibril angle to wood quality. Westport, New Zealand. 410p.

Cave, I.D. (1972) A theory of the shrinkage of wood. Part 2. *Wood science and technology* 6: 284-292.

Cave, I.D. (1978) Modelling moisture-related mechanical properties of wood. Part 1. *Wood science and technology* 12: 75-86.

Cave, I.D. (1996) Theory of X-ray measurement of microfibril angle in wood. Part 1. *Wood science and technology* 30: 143-152.

Cave, I.D. (1997) Theory of X-ray measurement of microfibril angle in wood. Part 2. *Wood science and technology* 31: 225-234.

Chen, W. F. and Saleeb, A. F. (1994) *Constitutive equations for engineering materials.* Volume1: Elasticity and modeling. Elsevier. 580p.

Chou, P.C. and Carleone, J. (1972) Elastic constants of layered media. *Journal of composite Materials* 6: 80-93.

Cousins, W.J. Young's modulus of hemicellulose as related to moisture content, *Wood science and technology* 12(2): 161-167, 1978.

Cown, D. J. Variation in tracheid dimensions in the stem of a 26-year-old radiata pine tree, *Appita* 28 (4): 237-245, 1975.

Cown, D. J. and McConchie, D. L. (1980) Wood property variations in an old-crop stand of radiata pine, *New Zealand Journal of forestry science* 10(3): 508-520.

Cown, D. J., McConchie, D. L. and Young, G. D. (1991a) *Radiata pine wood properties survey.* FRI Bulletin No. 50. Forest Research Institute, Rotorua, New Zealand. 50p.

Cown, D. J., Young, G. D. and Kimberly, M. O. (1991b) Spiral grain patterns in plantation grown *pinus radiata. New Zealand Journal of Forestry Science* 21(2/3): 206-216.

Cowin, S.C. (1985) Modeling shrinkage mechanisms in porous elastic solids, *Journal of applied mechanics* 52: 351-355.

Daniel, I. M. and Ishi, O. (1994) *Engineering Mechanics of Composite Materials.* Oxford University Press. 395p.

Datt, G. and Touzot, G. (1985) Matrix formulation of the finite element method, *The finite element method displayed.* John Wiley & Sons. p.169-239.

Dinwoodie, J. M. (1981) *Timber its nature and behaviour.* London, Van Nostrand Reinhold. p. 1-36 & 39-46.

Donaldson, L.A (1992) Within- and between-tree variation in microfibril in *pinus radiata, New Zealand Journal of forestry science* 22. p. 77-86.

Entwistle, K. M. and Navaranjan, N. (2001) X-ray diffraction from cellulose micro-fibrils in the S2 layers of structurally characterized softwood specimens. *Journal of Materials Science* 36: p. 3855-3863.

Entwistle, K. M. and Navaranjan, N. (2002) Small-angle X-ray scattering from cellulose micro-fibrils in the S2 layers of structurally characterized softwood specimens. *Journal of Materials Science* 37: p. 539-545.

Evans, R. (1994) Rapid measurement of the transverse dimensios of tracheids in radial wood section from *pinus radiata, Holzforschung* 48(2): p. 168-172.

Ghosh, S., Lee, K., Moorthy, S. (1995): Multiple scale analysis of heterogeneous elastic structures using homogenisation theory and veronic cell finite element method. *Int. J. Solids Structures*. 32(1), 27-62.

Gibson, L. J. and Ashby, M. F. (1997) *Cellular solids: structure & properties.* Cambridge, Cambridge University Press. 510p.

Gorman. P J. (1995) Future market products for forest products. In Hammond, D. *Forestry Handbook*, New Zealand Institute of Forestry. p.181-182

Gui, Y. Q. (1994) An application of finite element analysis to wood drying. *Wood and fiber science* 26 (2): 281-293.

Gusev, A. A. (1997) Representative volume element size for elastic composites: A numerical study. *Journal of Mechanics Physics and Solids*. 45(9). 1449-1459.

Halpin, J. C. (1984): Primer on composite materials: A analysis. Technomic publishing company. 187p.

Harrington, J. J. (2002) *Hierarchical modelling of softwood hygro-elastic properties.* Thesis submitted for the degree of doctor of philosophy. University of Canterbury.

Harrington, J. J., Booker, R. and Astley, R. J. (1998) Modelling the elastic properties of softwood. Part I: The cell-wall lamellae. *Holzals Rohund Werkstoff*. 56. 37-41.

Hashin, Z. (1983) Analysis of composite materials-a survey. *Journal of Applied Mechanics*. 50. 481-505.

Hill, R. (1963) Elastic properties of reinforced solids: some theoretical principles. *Journal of Mechanics Physics and Solids*. 11. 357-372.

Hollister, S. J., Fyhrie, D. P., Jepsen, K. J., Goldstein, S. A. (1991) Application of homogenization theory to the study of trabecular bone mechanics. *Journal of Biomechanics*. 24(9). 825-839.

Hollister, S. J. and Kikuchi, N. (1992) A comparison of homogenization and standard mechanics analysis for periodic composite. *Computational Mechanics* 10. 73-95

Hori, M. and Nemat-Nassar, S. (1999): On two micromechanics theories for determining micro-macro relations in heterogeneous solids. *Mechanics of Materials*. 31. 667-682

Hughes, P.C. (1986) Rotational Kinematics. *Spacecraft attitude dynamics*. John Wiley & Sons, Inc. p.7-37.

Hunter, A.J. Analysis of shrinkage in wood, *Wood science and technology* 30: 385-395, 1996.

Jackson, N. and Ravindara, K. D. (1996): *Civil engineering materials*. 5th edition. Macmillan. p. 112-160.

Jennings, A and McKeown, J. J (1992). *Matrix computation*. 2nd ed. New York, J. Wiley. 427p.

Kalamkarov, A. L. (1992): Composite and reinforced elements of construction. John Wiley & Sons. 290p.

Kalamkarov, A. L., Kolpakov, A. G. (1997): *Analysis, design and optimization of composite structures*. John Wiley & Sons. 356p.

Kaminski, M. and Kleiber, M. (2000): Numerical homogenization of N-component Composites including stochastic interface defects. *International Journal of Numerical Method in Engineering*. 47. 1001-1027.

Kifetew, G. Application of the earlywood-latewood interaction theory to the shrinkage anisotropy of scots pine, *International conference of COST action E8, Mechanical performance of wood and wood products*. Copenhagen, Denmark, June 16-17, 1997a.

Kifetew, G., Lindberg, H. and Wiklund, M. (1997b) Tangential and radial deformation field measurements on wood during drying, *Wood science and technology* 31: 35-44.

Kininmonth, J. A. and Whitehouse, L. J. (1991) *Properties and uses of New Zealand radiata pine*: Vol 1-wood properties. New Zealand ministry of forestry, Rotorua, New Zealand. 10-9p.

Koponen, T., TORATTI, T. and KANERVA, P. Modelling longitudinal elastic and shrinkage properties of wood, *Wood science and technology* 23: 55-63, 1989.

Koponen, T., TORATTI, T. and KANERVA, P. Modelling elastic and shrinkage properties of wood based on cell structure, *Wood science and technology* 25: 25-32, 1991.

Kretschmann, D.E. and Green, D.W. Modeling moisture content-mechanical property relationships for clear southern pine, *Wood and fiber science* 28(3): 320-337, 1996.

Kretschmann, D.E. and others, Variations of microfibril angle in loblolly pine: Comparison of iodine crystallization and x-ray diffraction techniques, In Butterfield, B.G. *The proceedings of the IAWA/IUFRO international workshop on the significance of microfibril angle to wood quality*, Westport, New Zealand, 1998. p 157-176.

Lai, W. M., Rubin, D. and Krempl, E. (1993*) Introduction to continuum mechanics.* 3rd ed. Pergamon Press. 556p.

Lane, P. M. (1995) New Zealand planted forest description. In Hammond, D. *Forestry Handbook*, New Zealand Institute of Forestry. p.178-179

Lee, J., Choi, J. B. and Choi, K. (1996) Application of homogenization FEM analysis to Regular and re-entrant honeycomb structures. *Journal of Materials Science*. 31. 4105-4110.

Lee, K. and Ghosh, S. (1999) A microstructure based numerical method for constitutive modeling of composite and porous materials. *Materials Science and Engineering*. A272. 120-133.

Lichtenegger, H. Determination of spiral angles of elementary fibrils in the wood cell wall: comparison of small-angle X-ray scattering and wide-angle X-ray diffraction, In Butterfield, B.G. *The proceedings of the IAWA/IUFRO international workshop on the significance of microfibril angle to wood quality*, Westport, New Zealand, 1998. p 140-156.

Luciano, R. and Sacco, E. (1998): Variational methods for the homogenization of periodic heterogeneous media. *European Journal of Mechanics - A/Solids*. 17, 599-617

Malvern, L. E. (1969) *Introduction to the Mechanics of a continuous medium*, Prentice-Hall. 713p.

Martensson, A. and Svensson, S. (1997) Behaviour of drying wood in the direction perpendicular to grain. *International conference of COST action E8. Mechanical performance of wood products.* Theme: wood-water relations. Copenhagen, Denmark. June16-17.

Matthews, F. L. and Rowlings, R. D. Composite materials: Enginering and Science, Chapman & Hall, 1st edition, 1994, pp 1-28.

Matthews, F. L., Davies, G. A. O., Hitchings, D. and Soutis, C. (2000) *Finite element modeling of composite materials and structures*: Woodhead Publishing Limited. p. 6-16.

McCullough, R. L. (1990) Introduction to anisotropic elasticity, In Whitney, J. M. and others. *Delware Composite Design Encyclopedia.* Volume 2: Micromechanical materials modelling. Technomic Publishing Company. p.3-35.

McGinnis, G. D. and Shafizadeh, F. (1991) Cellulose. In Lewin, M. and Goldstein, I. S.: *Wood structure and composition.* New York. Marcel Dekker, Inc. p.139-181

Megraw, R. A. and others. (1998) Longitudinal shrinkage and microfibril angle in loblolly pine, In Butterfield, B.G. *The proceedings of the IAWA/IUFRO international workshop on the significance of microfibril angle to wood quality,* Westport, New Zealand. p 27-61.

Meylan, B.A. Measurement of microfibril angle by X-ray diffraction, *Forest products journal* 17(5): 51-58, 1967.

Meylan, B.A. (1972) The influence of microfibril angle on the longitudinal shrinkage-moisture content relationship, *Wood science and technology* 6: 293-301.

Ministry of Forestry (1995) New Zealand production and markets 1994. In Hammond, D. *Forestry Handbook,* New Zealand Institute of Forestry. p.197-199

Mott, L., Shaler, S.M. and Groom, L.H. A. (1996) Technique to measure strain distributions in single wood pulp fibers. *Wood and fiber science* 28(4). p. 429-437.

Navi, P. and Huet, C. (1989a) A three dimensional multilevel technique to study influence of the fiber microstructure on wood microscopic elastic properties, *The third joint ASCE/ASME mechanics conference.* University of California, San Diego, La Jolla. July 9-12.

Navi, P. and others. Experimental observation of microstructural influences on the mechanics wood cell bundles in tension, *The third joint ASCE/ASME mechanics conference.* University of California, San Diego, La Jolla. July 9-12, 1989.

Nemat-Nasser, S., Hori, M. (1993): *Micromechanics: Overall properties of heterogeneous materials.* North-Holland. 687p.

Newman, R. How stiff is an individual cellulose microfibril? In Butterfield, B.G. *The proceedings of the IAWA/IUFRO international workshop on the significance of microfibril angle to wood quality,* Westport, New Zealand, 1998. p 81-93.

Nicholls, J.W.P. (1986) Within-tree variation in wood characteristics of *pinus radiata* D.Don, *Australian forest research* 16: p. 313-335.

Ormarsson, S. (1999) Numerical analysis of moisture-related distortions in sawn timber. Thesis for the degree of doctor in engineering. Chalmers University of Technology, Sweden. P. 213

Ormarsson, S., Dahlblom, O. and Petersson, H. (1998) A numerical study of the shapestability of sawn timber subjected to moisture variation. part 1: Theory. *Wood science and technology* 32(5): 325-334.

Ormarsson, S., Dahlblom, O. and Petersson, H. (1999) A numerical study of the shapestability of sawn timber subjected to moisture variation. part 2: Simulation of drying board, *Wood science and technology* 33: 407-423.

Pang, S. (2001) Anisotropic shrinkage, equilibrium moisture content and fibre saturation point of earlywood and latewood of radiata pine. *7th International IUFRO Wood Drying Conference, Japan.* p.184-191.

Patel, R.N. Anatomy of stem and root wood of *pinus radiata* D. Don, *New Zealand Journal of Forestry science* 1(1): 37-49, 1971.

Pentoney, R.E. Mechanics of affecting tangential vs radial shrinkage, *Journal of FPRS*: 27-32, 1953.

Persson, K. (1997): *Modelling of wood properties by a micromechanical approach.* PhD thesis. Lund University, Sweden. 213p.

Persson, L. E., Persson, L., Svanstedt, N. and Wyller, J. (1993) *The homogenisation method – An introduction.* British Library Cataloguing in Publication Data. 80p.

Petersson, H., Dahlblom, O., Ormarsson, K. and Persson, K. *Moisture Distortion modelling of wood and structural timber*, International conference of COST action E8, Mechanical performance of wood and wood products. Copenhagen, Denmark, June 16-17, 1997.

Pozrikidis, C. (1998) *Numerical computation in science and engineering.* Oxford University Press Inc. 627p.

Rao, S.S. The finite element method in engineering, 3rd edition, Butterworth – Heinemann, 1999.

Saka, S. (2001) Chemical composition and distribution. In Hon, D. N. S and Shiraishi, N. *Wood and cellulosic chemistry.* 2nd ed. New York. Marcel Dekker Inc. p.51-81.

Siau, J. F. (1983) *Transport processes in wood.* Springer-Verlag, London. 245p.

Siau, J. F. (1995) *Wood: Influence on moisture on physical properties.* Department of Wood Science and Forest Products, Virginia Polytechnic and State University. 227p.

Skaar, C. (1988) *Wood-Water relations.* Springer-Verlag, London. 279p.

Sluis, O. v. d., Schreurs, P. J. G., Brekelmans, W. A. M. and Meijer, H. E. H. (2000) Overall behaviour of heterogeneous elstoviscoplastic materials: effect of microstructural modeling. *Mechanics of Materials.* 32. 449-462.

Sutton. W. R. J. (1995) Future international supply and demand trends as a guide to New Zealand plantation managment. In Hammond, D. *Forestry Handbook*, New Zealand Institute of Forestry. p.179-181

Tang, R.C. The microfibrillar orientation in cell-wall layers of virginia pine Tracheids, *Wood science* 5(3): 181-186, 1973.

Tsoumis, G. (1991) *Science and technology of wood; structure, properties and utilization.* New York, Van Nostrand Reinhold. p. 1-203

Walker, J.C.F. (1993a) Basic wood chemistry and cell wall ultrastructure. In Walker, J.C.F. *Primary wood processing*. Chapman and Hall, London. p. 23-64.

Walker, J.C.F. (1993b) Water and wood. In Walker, J.C.F. *Primary wood processing*. Chapman and Hall, London. p. 68-93.

Walker, J.C.F. (1993c) Dimensional instability of timber. In Walker, J.C.F. *Primary wood processing*. Chapman and Hall, London. p. 95-120.

Walker, J.C.F. and Butterfield, B.G. (1995) The importance of microfibril angle for the processing industries, *New Zealand. Forestry*: 34-40.

Watanabe, U., Fujita, M. and Norimot, M. (1998a) Transverse shrinkage of coniferous wood cells examined using replica method and power spectrum analysis. *Holzforschung* 52(2): 200-206.

Watanabe, U., Norimot, M. and Fujita, M. (1998b) Transverse shrinkage anisotropy of coniferous wood investigated by the power spectrum analysis, *Journal of wood science* 44: 9-14.

Wiley, J.H. and Atalla, R.H. Band assignments in the Raman spectra of Celluloses, *Carbohydrate research 160*: 113-129, 1987.

Wood, A. (1999) *Introduction to numerical analysis.* Addison-Wesley. p.55-108

Yamamoto, H. (1994) A model of the anisotropic swelling and shrinkage process of wood. *Unpublished report.* Nagoya University, Japan.

Zhang, S. Y. and others. (1994) Modeling intratree wood shrinkage by measuring wood density, *Forest products journal* 44(10): 42-46.

Zienkiewicz, O. C. and Taylor, R. L. (2000a) *The finite element method.* 5th ed. Volume 1: The basis. Butterworth-Heinemann. 689p.

Zienkiewicz, O. C. and Taylor, R. L. (2000b) *The finite element method.* 5th ed. Volume 2: Solid mechanics. Butterworth-Heinemann. 459p.

Appendices

A. Computing new system stiffness matrix

The $\mathbf{K}_n$ can easily be computed from $\mathbf{K}_g$ by performing the transformations given in equation

$$\mathbf{K}_n=\mathbf{A}^T\mathbf{K}_g\mathbf{A} \tag{A1}$$

in two different steps as given below:

The steps are described to implement a constraint equation type;

$$u_q = u_p + \delta_{n+1} + \delta_{n+4} + \delta_{n+7} \tag{A2}$$

Step 1;

If $$\mathbf{K}' = \mathbf{K}_g\mathbf{A} \tag{A3}$$

The size of $\mathbf{K}'$ is same as $\mathbf{K}_g$ and should be sufficient to accommodate the rows and columns from $\mathbf{K}$ and nine rows and nine columns related to the overall global displacements. The size of $\mathbf{K}'$ is $n+9$ by $n+9$ where n is the number of degrees of freedom.

Column p of $\mathbf{K}'$ = column p of $\mathbf{K}'$ + 1 x column q of $\mathbf{K}_g$

Column $n+1$ of $\mathbf{K}'$ = column $n+1$ of $\mathbf{K}'$ + 1 x column q of $\mathbf{K}_g$

Column $n+4$ of $\mathbf{K}'$ = column $n+4$ of $\mathbf{K}'$ + 1 x column q of $\mathbf{K}_g$

Column $n+7$ of $\mathbf{K}'$ = column $n+7$ of $\mathbf{K}'$ + 1 x column q of $\mathbf{K}_g$

Column q of $\mathbf{K}'$ = 0 x column q of $\mathbf{K}_g$

The other columns of $\mathbf{K}'$ are identical to corresponding column in $\mathbf{K}_g$.

Step 2;

$$\mathbf{K}_n = \mathbf{A}^T\mathbf{K}' \tag{A4}$$

The size of $\mathbf{K}_n$ is $n+9$ by $n+9$ matrix.

Row p of $\mathbf{K}_n$ = row p of $\mathbf{K}_n$ + 1 x row q of $\mathbf{K}'$

Row $n+1$ of $\mathbf{K}_n$ = row $n+1$ of $\mathbf{K}_n$ + 1 x row q of $\mathbf{K}'$

Row $n+4$ of $\mathbf{K}_n$ = row $n+4$ of $\mathbf{K}_n$ + 1 x row q of $\mathbf{K}'$

Row $n+7$ of $\mathbf{K}_n$ = row $n+7$ of $\mathbf{K}_n$ + 1 x row q of $\mathbf{K}'$

Row q of $\mathbf{K}_n$ = 0 x row q of $\mathbf{K}'$

The load vector $\mathbf{f}_{gT}$ as given in

$$\mathbf{f}_{nT}=\mathbf{A}^T\mathbf{f}_{gT} \tag{A5}$$

can also be transformed to $\mathbf{f}_{nT}$ by a similar method that described in step 2.

After finishing the row and column operations as outlined by the two steps to implement a constraint equation (A2), the system equation can take the form given by

$$\begin{bmatrix} K_{1,1} & \cdots & \overset{p}{(K_{1,p}+K_{1,q})} & \cdots & \overset{q}{0} & \cdots & K_{1,n} & \overset{n+1}{(K_{1,n+1}+K_{1,q})} & \cdots & \to \\ \vdots & & \vdots & & \vdots & & \vdots & \vdots & & \\ (K_{p,1}+K_{q,1}) & \cdots & \begin{matrix}(K_{p,p}+K_{p,q}\\ K_{p,q}+K_{q,q})\end{matrix} & \cdots & 0 & \cdots & (K_{p,n}+K_{q,n}) & \begin{matrix}(K_{p,n+1}+K_{p,q}\\ K_{q,n+1}+K_{q,q})\end{matrix} & \cdots & \\ \vdots & & \vdots & & \vdots & & \vdots & \vdots & & \\ 0 & \cdots & 0 & \cdots & 0 & \cdots & 0 & 0 & \cdots & \\ \vdots & & \vdots & & \vdots & & \vdots & \vdots & & \\ K_{n,1} & \cdots & (K_{n,p}+K_{n,q}) & \cdots & 0 & \cdots & K_{n,n} & (K_{n,n+1}+K_{n,q}) & \cdots & \\ (K_{n+1,1}+K_{q,1}) & \cdots & \begin{matrix}(K_{n+1,p}+K_{n+1,q}\\ K_{q,p}+K_{q,q})\end{matrix} & \cdots & 0 & \cdots & (K_{n+1,n}+K_{q,n}) & \begin{matrix}(K_{n+1,n+1}+K_{n+1,q}\\ K_{q,n+1}+K_{q,q})\end{matrix} & \cdots & \\ \vdots & & \vdots & & \vdots & & \vdots & \vdots & & \\ \downarrow & \cdots & \vdots & \cdots & \vdots & \cdots & \vdots & \vdots & \cdots & \end{bmatrix} \begin{bmatrix} u_1 \\ \vdots \\ u_p \\ \vdots \\ u'_q \\ \vdots \\ u_n \\ \delta_{n+1} \\ \downarrow \\ \delta_{n+9} \end{bmatrix} = \begin{bmatrix} f_{1T} \\ \vdots \\ f_{pT}+f_{qT} \\ \vdots \\ 0 \\ \vdots \\ f_{nT} \\ f_{n+1T}+f_{qT} \\ \vdots \\ \downarrow \end{bmatrix} + \begin{bmatrix} 0 \\ , \\ 0 \\ \vdots \\ \vdots \\ \vdots \\ \underline{0} \\ f_1 \\ \vdots \\ \downarrow \end{bmatrix}$$

(A6)

where only the $(n+1)^{th}$ row and column are shown due to limited space, and the $(n+4)^{th}$ and $(n+7)^{th}$ rows and columns are also assembled in similar manner for $(n+1)^{th}$ row and column

Similarly all the linear constraint equations are implemented in the system matrices.

B Applying constraint equations at element level

Consider the type of constraint equation

$$u_q = u_p + \delta_{n+1} + \delta_{n+4} + \delta_{n+7} \tag{B1}$$

p, *q*, *n+1*, *n+4* and *n+7* refer to the freedom numbers and the position of the rows and columns corresponding to u_p, u_q, δ_{n+1}, δ_{n+4}, and δ_{n+7} as indicated in equation (B1).

Element *e* which shares u_q is considered to demonstrate the implementation of equation (B1). *e* does not share u_p (in some occasions both freedoms may be shared by the same element), but it is shared by some other elements of the system. The $\delta n+1$, $\delta n+4$, and $\delta n+7$ are not shared by any element since they are the overall global displacements of the RVE. They must be then included in the element displacement matrix. The sizes of the element stiffness matrix and load matrix should be increased to accommodate the components when row and column operations are performed in similar manner as explained for system matrices. By row and column operation, the new element stiffness matrix, $\mathbf{k}_n^e$ and the element thermal load matrix, $\mathbf{f}_{nT}^e$ are computed, and the new system matrices $\mathbf{K}_{nc}$ and $\mathbf{f}_{ncT}$ are then assembled by locating the positions of their components without accommodating the zero columns and rows. In order to carry out this procedure, the following steps can be adopted.

Step 1;

Size of element stiffness matrix is increased by the number of rows and columns of $\mathbf{k}^e$ by the number of global overall displacements of the RVE, *m* (*m* is nine for the three dimensional case). If the size of $\mathbf{k}^e$ is *l* by *l*, the new size will be *l+m* by *l+m*. Similarly the size of $\mathbf{f}_T^e$ is also increased by *m* rows. After increasing the size both matrices become:

$$\begin{bmatrix} & & & & & 0 & \xrightarrow{m} & & 0 \\ & & & & & 0 & & & 0 \\ & & \mathbf{k}_e & & & 0 & & & 0 \\ & & & & & 0 & & & 0 \\ & & & & & 0 & & & 0 \\ 0 & 0 & 0 & 0 & 0 & 0 & & & 0 \\ \overset{m}{\downarrow} & & & & & & & & 0 \\ . & & & & & & & & 0 \\ 0 & 0 & 0 & 0 & 0 & 0 & 0 & 0 & 0 \end{bmatrix} \text{ and } \begin{bmatrix} . \\ \\ \mathbf{f}_T^e \\ \\ \\ 0 \\ . \\ \overset{m}{\downarrow} \\ 0 \end{bmatrix} \tag{B2}$$

If g, h, i and j refer to the positions of rows and columns correspond to u_q, δ_{n+1}, δ_{n+4} and δ_{n+7}, in $\mathbf{k}'$ whose size is $l+m$ by $l+m$

The matrix $\mathbf{k}_e$ is transformed to $\mathbf{k}'$ as follows:

Column h of $\mathbf{k}'$ = column h of $\mathbf{k}'$ + 1 x column g of $\mathbf{k}_e$

Column i of $\mathbf{k}'$ = column i of $\mathbf{k}'$ + 1 x column g of $\mathbf{k}_e$

Column j of $\mathbf{k}'$ = column j of $\mathbf{k}'$ + 1 x column g of $\mathbf{k}_e$

The other columns of $\mathbf{k}'$ are identical to corresponding columns in $\mathbf{k}_e$.

$$\mathbf{k}' = \begin{bmatrix} & & \overset{u_q}{g} & & & \overset{\delta_{n+1}}{h} & & \overset{\delta_{n+4}}{i} & \\ k_{1,1} & . & k_{1,g} & . & k_{1,l} & k_{1,g} & . & k_{1,g} & \rightarrow \\ . & . & . & . & . & . & . & . & . \\ k_{g,1} & . & k_{g,g} & . & . & k_{g,g} & . & k_{g,g} & . \\ . & . & . & . & . & . & . & . & . \\ k_{l,1} & . & k_{l,g} & . & k_{l,l} & k_{l,g} & . & k_{l,g} & . \\ 0 & . & 0 & . & 0 & 0 & 0 & . & 0 \\ \overset{m}{\downarrow} & . & . & . & . & . & . & . & . \\ . & . & . & . & . & . & . & . & . \\ 0 & . & 0 & . & 0 & 0 & 0 & . & 0 \end{bmatrix} \tag{B3}$$

Step 2;

The matrix $\mathbf{k}'$ is transformed to $\mathbf{k}_n^e$.

g, h, i and j refer the positions of rows and columns correspond to u_q, δ_{n+1}, δ_{n+4} and δ_{n+7}, in $\mathbf{k}_n^e$ which is the new element stiffness matrix has size $l+m$ by $l+m$

Row h of $\mathbf{k}_n^e$ = row h of $\mathbf{k}_n^e$ + 1 x row g of $\mathbf{k}'$

Row i of $\mathbf{k}_n^e$ = row i of $\mathbf{k}_n^e$ + 1 x row g of $\mathbf{k}'$

Row j of $\mathbf{k}_n^e$ = row j of $\mathbf{k}_n^e$ + 1 x row g of $\mathbf{k}'$

The other rows of $\mathbf{k}_n^e$ are identical to corresponding rows in $\mathbf{k}'$.

The load vector $\mathbf{f}_T^e$ can also be modified by similar method to compute $\mathbf{f}_{nT}^e$.

$$\mathbf{k}' = \begin{bmatrix} & & \overset{u_q}{\underset{g}{}} & & & \overset{\delta_{n+1}}{\underset{h}{}} & & \overset{\delta_{n+4}}{\underset{i}{}} & \\ k_{1,1} & \cdot & k_{1,g} & \cdot & k_{1,l} & k_{1,g} & \cdot & k_{1,g} & \rightarrow \\ \cdot & \cdot & \cdot & \cdot & \cdot & \cdot & \cdot & \cdot & \cdot \\ k_{g,1} & \cdot & k_{g,g} & \cdot & k_{g,l} & k_{g,g} & \cdot & k_{g,g} & \cdot \\ \cdot & \cdot & \cdot & \cdot & \cdot & \cdot & \cdot & \cdot & \cdot \\ k_{l,1} & \cdot & k_{l,g} & \cdot & k_{l,l} & k_{l,g} & \cdot & k_{l,g} & \cdot \\ k_{g,1} & \cdot & k_{g,g} & \cdot & k_{g,l} & k_{g,g} & \cdot & k_{g,g} & \cdot \\ \cdot & \cdot & \cdot & \cdot & \cdot & \cdot & \cdot & \cdot & \cdot \\ k_{g,1} & \cdot & k_{g,g} & \cdot & k_{g,l} & k_{g,g} & \cdot & k_{g,g} & \cdot \\ \downarrow & \cdot & \cdot & \cdot & \cdot & \cdot & \cdot & \cdot & \cdot \end{bmatrix}, \qquad \mathbf{f}_{nT}^e = \begin{bmatrix} f_{1T}^e \\ \cdot \\ f_{gT}^e \\ \cdot \\ f_{lT}^e \\ f_{gT}^e \\ \cdot \\ f_{gT}^e \\ \downarrow \end{bmatrix} \tag{B4}$$

where row and column of δ_{n+7} are not shown, however they are similar to rows and columns of δ_{n+1} and δ_{n+4}

No extra rows and/or columns are necessary for the degree of freedom u_p in the element matrices for e because the row and column in $\mathbf{k}_n^e$ of the freedom u_q will be accommodated in the row and column of u_p as seen in equation (A6) when the system matrix is assembled.

Step 3;

Nodal freedom numbers array, $\mathbf{L}^e$ is created from the system nodal freedom numbers for element, *e*. This vector has the freedom numbers associated with the element in accordance with the nodal order as well as with global displacement order. The size of $\mathbf{L}^e$ is (*l*+*m*). For the element *e*, the freedom numbers *q*, *n+1*, *n+4* and *n+7* in $\mathbf{L}^e$ refer to the positions of u_q, δ_{n+1}, δ_{n+4} and δ_{n+7} respectively in the system and are shown in equation (B5). It must be noted that p^{th} freedom does not belong to the element *e*. The freedom numbers of the overall global displacements will be taken as zero for the elements that do not have constraint nodes. It should be noted that the rows and columns in the element stiffness matrix that correspond to the overall global displacements, which are not constraint to u_q, are always zero.

$$\mathbf{L}^e = [\ldots\ldots q\ldots\ldots\ldots n+1..n+4..n+7..]^T \qquad \text{(B5)}$$

The new system stiffness matrix, $\mathbf{K}_{nc}$ does not have rows and columns for freedom u_q since the components are zero after the row and column operation. To avoid that row and column, the freedom numbers of the system are rearranged and hence the number in $\mathbf{L}^e$ will also be rearranged and given by

$$\mathbf{L}^e = [\ldots\ldots q_n\ldots\ldots (n+1)_n..(n+4)_n..(n+7)_n..]^T \qquad \text{(B6)}$$

where

q_n, $(n+1)_n$, $(n+4)_n$ and $(n+7)_n$ are the new positions of the rows and columns in $\mathbf{K}_{nc}$ that are occupied by the u_q, δ_{n+1}, δ_{n+4}, and δ_{n+7} from $\mathbf{k}_n^e$ when assembling the $\mathbf{K}_{nc}$.

It is also noted that the freedom number q_n is the new freedom number of u_p in the system after rearranging the system freedom numbers, and therefore the components of row and column of freedom u_q in $\mathbf{k}_n^e$ will be added to the components of row and column of freedom u_p in $\mathbf{K}_{nc}$.

By performing the steps 2 and 3, $\mathbf{f}_T^e$ can be transformed to $\mathbf{f}_{nT}^e$, and assembled to form $\mathbf{f}_{ncT}$.

Similarly rest of the constraint equations can be implemented at the element level and the element stiffness and load matrices can be assembled to form the new system stiffness and thermal load matrices, $\mathbf{K}_{nc}$ and $\mathbf{f}_{ncT}$.

The elements which do not have constraint nodes take the element stiffness and load matrices in the form

$$\mathbf{k}_n^e = \begin{bmatrix} & & & & & & \overset{m}{\longrightarrow} & & \\ & & & & 0 & \cdots & & 0 \\ & & & & 0 & & & 0 \\ & & \mathbf{k}_e & & 0 & & & 0 \\ & & & & 0 & & & 0 \\ & & & & 0 & & & 0 \\ 0 & 0 & 0 & 0 & 0 & 0 & & 0 \\ \overset{m}{\downarrow} & & & & & & & 0 \\ \vdots & & & & & & & 0 \\ 0 & 0 & 0 & 0 & 0 & 0 & 0 \;\; 0 & 0 \end{bmatrix}, \quad \mathbf{f}_{nT}^e = \begin{bmatrix} \\ \mathbf{f}_T^e \\ \\ \\ 0 \\ \vdots \\ \overset{m}{\downarrow} \\ 0 \end{bmatrix} \tag{B7}$$

The nodal freedom numbers matrix $\mathbf{L}^e$ for each of these elements has rearranged freedom numbers for the degrees of freedom of the elements and zero for the overall global displacements. When $\mathbf{K}_{nc}$ is assembled, the coefficients of $\mathbf{k}_n^e$ will be placed in the appropriate rows and columns.

where j_n is the new position of j in $\mathbf{K}_{nc}$

Therefore by carefully constructing the element matrices $\mathbf{k}_n^e$ and $\mathbf{f}_{nT}^e$, and the nodal freedom array $\mathbf{L}^e$ for each element, the system stiffness and thermal load matrices $\mathbf{K}_{nc}$ and $\mathbf{f}_{ncT}$ can be constructed correctly without requiring a large computer memory. If the size of $\mathbf{K}_{nc}$ is *nc* by *nc*, where *nc* is given by

nc = number of total freedoms + number of overall displacements –
number of constrained freedoms (B8)

C. Predicted stiffness and shrinkage properties from the cell model as the function of density and microfibril angle

MFA	EL	ET	ER	GTR	GLR	GLT	NUTR	NULR	NULT	ALR	ALT	ALL
Density = 200 kg/m^3												
0	7.2006	0.5219	0.7923	0.0025	0.2322	0.1571	0.0527	0.2156	0.2193	0.2992	0.3093	0.0246
5	6.3214	0.5214	0.7909	0.0025	0.2316	0.1568	0.0513	0.2404	0.2428	0.2969	0.3070	0.0293
10	4.7701	0.5205	0.7878	0.0025	0.2295	0.1558	0.0470	0.2840	0.2850	0.2904	0.3007	0.0419
15	3.5913	0.5204	0.7855	0.0025	0.2257	0.1536	0.0412	0.3158	0.3157	0.2814	0.2918	0.0589
20	2.8548	0.5221	0.7859	0.0026	0.2204	0.1502	0.0351	0.3333	0.3328	0.2712	0.2818	0.0769
25	2.4035	0.5264	0.7904	0.0026	0.2140	0.1461	0.0299	0.3409	0.3402	0.2606	0.2714	0.0939
30	2.1194	0.5337	0.8002	0.0026	0.2070	0.1414	0.0260	0.3419	0.3413	0.2499	0.2609	0.1092
35	1.9346	0.5448	0.8164	0.0027	0.1998	0.1366	0.0236	0.3378	0.3374	0.2390	0.2503	0.1226
40	1.8112	0.5606	0.8404	0.0028	0.1927	0.1318	0.0227	0.3295	0.3294	0.2275	0.2391	0.1344
45	1.7279	0.5826	0.8748	0.0028	0.1860	0.1272	0.0234	0.3169	0.3173	0.2150	0.2269	0.1450
50	1.6723	0.6131	0.9233	0.0030	0.1799	0.1230	0.0259	0.2998	0.3009	0.2010	0.2134	0.1550
Density = 250 kg/m^3												
0	9.3730	0.6453	0.9820	0.0047	0.3013	0.2040	0.0629	0.2176	0.2217	0.3034	0.3152	0.0219
5	8.2230	0.6446	0.9803	0.0047	0.3006	0.2038	0.0614	0.2435	0.2462	0.3011	0.3130	0.0262
10	6.1935	0.6436	0.9766	0.0047	0.2982	0.2028	0.0571	0.2893	0.2900	0.2949	0.3069	0.0379
15	4.6512	0.6437	0.9739	0.0048	0.2935	0.2002	0.0511	0.3225	0.3220	0.2861	0.2983	0.0536
20	3.6874	0.6461	0.9748	0.0048	0.2867	0.1960	0.0448	0.3408	0.3397	0.2760	0.2884	0.0705
25	3.0970	0.6517	0.9810	0.0049	0.2783	0.1907	0.0394	0.3487	0.3474	0.2655	0.2782	0.0867
30	2.7255	0.6613	0.9939	0.0049	0.2691	0.1846	0.0352	0.3496	0.3483	0.2547	0.2677	0.1012
35	2.4839	0.6757	1.0151	0.0050	0.2596	0.1782	0.0326	0.3452	0.3442	0.2436	0.2569	0.1141
40	2.3228	0.6962	1.0464	0.0052	0.2502	0.1718	0.0316	0.3363	0.3358	0.2318	0.2455	0.1256
45	2.2142	0.7244	1.0911	0.0053	0.2413	0.1657	0.0322	0.3229	0.3231	0.2189	0.2331	0.1361
50	2.1419	0.7633	1.1538	0.0055	0.2331	0.1600	0.0347	0.3049	0.3059	0.2045	0.2192	0.1460

Key to the table: EL, ET and ER=elastic modulus in L, T and R directions, GTR, GLR and GLT= shear modulus in TR, LR and LT planes, NUTR, NULR and NULT=Poisson's ratios in TR, LR and LT planes, ALR, ALT and ALL=shrinkage coefficients in R, T and L directions

MFA	EL	ET	ER	GTR	GLR	GLT	NUTR	NULR	NULT	ALR	ALT	ALL
Density = 300 kg/m^3												
0	10.8079	0.7847	1.1994	0.0079	0.3589	0.2436	0.0726	0.2178	0.2226	0.3071	0.3214	0.0245
5	9.4889	0.7839	1.1973	0.0080	0.3584	0.2435	0.0711	0.2419	0.2452	0.3048	0.3192	0.0293
10	7.1611	0.7825	1.1927	0.0080	0.3559	0.2427	0.0668	0.2846	0.2857	0.2985	0.3130	0.0418
15	5.3921	0.7825	1.1891	0.0080	0.3507	0.2400	0.0608	0.3156	0.3153	0.2896	0.3043	0.0587
20	4.2867	0.7851	1.1896	0.0081	0.3430	0.2353	0.0545	0.3328	0.3318	0.2795	0.2945	0.0766
25	3.6094	0.7913	1.1964	0.0082	0.3333	0.2292	0.0490	0.3403	0.3391	0.2691	0.2844	0.0936
30	3.1830	0.8021	1.2109	0.0083	0.3226	0.2222	0.0448	0.3413	0.3402	0.2586	0.2742	0.1088
35	2.9055	0.8183	1.2348	0.0085	0.3115	0.2147	0.0421	0.3374	0.3366	0.2479	0.2639	0.1222
40	2.7203	0.8412	1.2703	0.0086	0.3005	0.2072	0.0408	0.3293	0.3291	0.2367	0.2530	0.1339
45	2.5953	0.8729	1.3208	0.0089	0.2900	0.2000	0.0412	0.3171	0.3176	0.2244	0.2413	0.1446
50	2.5119	0.9163	1.3917	0.0092	0.2804	0.1933	0.0434	0.3005	0.3019	0.2108	0.2282	0.1545
Density = 350 kg/m^3												
0	12.6049	0.9172	1.4066	0.0126	0.4251	0.2890	0.0821	0.2189	0.2243	0.3112	0.3277	0.0245
5	11.0669	0.9163	1.4041	0.0126	0.4247	0.2892	0.0805	0.2427	0.2464	0.3089	0.3254	0.0292
10	8.3525	0.9147	1.3987	0.0126	0.4221	0.2886	0.0761	0.2848	0.2860	0.3025	0.3193	0.0418
15	6.2895	0.9147	1.3945	0.0127	0.4164	0.2859	0.0700	0.3154	0.3151	0.2937	0.3107	0.0586
20	5.0003	0.9177	1.3950	0.0128	0.4076	0.2807	0.0637	0.3324	0.3313	0.2837	0.3010	0.0766
25	4.2104	0.9249	1.4028	0.0130	0.3964	0.2737	0.0581	0.3399	0.3385	0.2734	0.2910	0.0936
30	3.7131	0.9374	1.4196	0.0131	0.3837	0.2654	0.0537	0.3409	0.3396	0.2630	0.2810	0.1088
35	3.3895	0.9560	1.4473	0.0134	0.3705	0.2565	0.0508	0.3371	0.3362	0.2524	0.2708	0.1221
40	3.1735	0.9823	1.4884	0.0137	0.3574	0.2476	0.0494	0.3292	0.3288	0.2413	0.2602	0.1338
45	3.0277	1.0184	1.5467	0.0140	0.3449	0.2389	0.0496	0.3172	0.3176	0.2292	0.2487	0.1445
50	2.9304	1.0677	1.6283	0.0145	0.3334	0.2308	0.0515	0.3008	0.3024	0.2158	0.2359	0.1545

Key to the table: EL, ET and ER=elastic modulus in L, T and R directions, GTR, GLR and GLT= shear modulus in TR, LR and LT planes, NUTR, NULR and NULT=Poisson's ratios in TR, LR and LT planes, ALR, ALT and ALL=shrinkage coefficients in R, T and L directions

MFA	EL	ET	ER	GTR	GLR	GLT	NUTR	NULR	NULT	ALR	ALT	ALL
Density = 400 kg/m^3												
0	14.4090	1.0512	1.6173	0.0190	0.4938	0.3362	0.0913	0.2200	0.2260	0.3153	0.3341	0.0245
5	12.6507	1.0502	1.6144	0.0190	0.4934	0.3367	0.0898	0.2434	0.2476	0.3130	0.3319	0.0292
10	9.5471	1.0484	1.6082	0.0191	0.4910	0.3366	0.0853	0.2850	0.2864	0.3067	0.3258	0.0417
15	7.1881	1.0483	1.6033	0.0192	0.4849	0.3340	0.0791	0.3153	0.3149	0.2980	0.3173	0.0586
20	5.7137	1.0518	1.6039	0.0193	0.4750	0.3284	0.0727	0.3321	0.3307	0.2880	0.3077	0.0766
25	4.8103	1.0600	1.6126	0.0195	0.4621	0.3205	0.0669	0.3395	0.3378	0.2778	0.2978	0.0936
30	4.2416	1.0740	1.6317	0.0198	0.4476	0.3110	0.0624	0.3405	0.3390	0.2675	0.2880	0.1088
35	3.8714	1.0950	1.6631	0.0202	0.4322	0.3006	0.0593	0.3368	0.3357	0.2570	0.2780	0.1221
40	3.6244	1.1245	1.7097	0.0206	0.4169	0.2901	0.0577	0.3290	0.3286	0.2460	0.2675	0.1339
45	3.4578	1.1649	1.7756	0.0211	0.4023	0.2800	0.0577	0.3172	0.3177	0.2341	0.2562	0.1446
50	3.3465	1.2198	1.8677	0.0217	0.3888	0.2704	0.0594	0.3012	0.3030	0.2208	0.2437	0.1546
Density = 450 kg/m^3												
0	16.2056	1.1866	1.8316	0.0275	0.5646	0.3852	0.1004	0.2211	0.2278	0.3194	0.3406	0.0245
5	14.2288	1.1855	1.8284	0.0275	0.5646	0.3861	0.0988	0.2442	0.2488	0.3171	0.3384	0.0292
10	10.7394	1.1835	1.8213	0.0276	0.5624	0.3867	0.0943	0.2851	0.2867	0.3109	0.3324	0.0417
15	8.0867	1.1834	1.8157	0.0278	0.5560	0.3843	0.0881	0.3150	0.3145	0.3022	0.3240	0.0586
20	6.4286	1.1872	1.8162	0.0280	0.5451	0.3785	0.0815	0.3316	0.3301	0.2924	0.3145	0.0766
25	5.4126	1.1964	1.8260	0.0283	0.5307	0.3697	0.0756	0.3389	0.3371	0.2822	0.3048	0.0935
30	4.7729	1.2120	1.8473	0.0287	0.5141	0.3589	0.0709	0.3400	0.3383	0.2720	0.2951	0.1087
35	4.3566	1.2352	1.8823	0.0292	0.4966	0.3471	0.0676	0.3364	0.3351	0.2617	0.2852	0.1221
40	4.0788	1.2678	1.9342	0.0298	0.4790	0.3350	0.0658	0.3288	0.3282	0.2508	0.2750	0.1339
45	3.8914	1.3122	2.0075	0.0305	0.4622	0.3232	0.0656	0.3172	0.3178	0.2391	0.2639	0.1445
50	3.7662	1.3723	2.1097	0.0313	0.4466	0.3121	0.0671	0.3015	0.3034	0.2259	0.2517	0.1545

Key to the table: EL, ET and ER=elastic modulus in L, T and R directions, GTR, GLR and GLT= shear modulus in TR, LR and LT planes, NUTR, NULR and NULT=Poisson's ratios in TR, LR and LT planes, ALR, ALT and ALL=shrinkage coefficients in R, T and L directions

MFA	EL	ET	ER	GTR	GLR	GLT	NUTR	NULR	NULT	ALR	ALT	ALL
Density = 500 kg/m^3												
0	18.0077	1.3236	2.0500	0.0387	0.6383	0.4364	0.1094	0.2222	0.2296	0.3236	0.3472	0.0245
5	15.8121	1.3224	2.0464	0.0387	0.6386	0.4377	0.1077	0.2449	0.2500	0.3213	0.3450	0.0292
10	11.9359	1.3203	2.0385	0.0388	0.6369	0.4392	0.1032	0.2853	0.2870	0.3151	0.3391	0.0417
15	8.9887	1.3202	2.0322	0.0391	0.6303	0.4374	0.0969	0.3148	0.3142	0.3065	0.3308	0.0586
20	7.1465	1.3244	2.0326	0.0394	0.6185	0.4313	0.0902	0.3311	0.3294	0.2968	0.3215	0.0765
25	6.0175	1.3344	2.0434	0.0399	0.6026	0.4218	0.0842	0.3383	0.3363	0.2867	0.3119	0.0935
30	5.3066	1.3515	2.0668	0.0404	0.5840	0.4098	0.0793	0.3394	0.3375	0.2767	0.3023	0.1086
35	4.8441	1.3769	2.1055	0.0411	0.5641	0.3964	0.0758	0.3359	0.3345	0.2664	0.2927	0.1220
40	4.5354	1.4125	2.1626	0.0419	0.5442	0.3826	0.0738	0.3285	0.3279	0.2557	0.2827	0.1337
45	4.3271	1.4607	2.2432	0.0428	0.5250	0.3691	0.0734	0.3172	0.3178	0.2441	0.2719	0.1444
50	4.1881	1.5256	2.3551	0.0439	0.5071	0.3563	0.0746	0.3017	0.3039	0.2312	0.2599	0.1543
Density = 550 kg/m^3												
0	22.3857	1.7169	1.7169	0.0547	0.6436	0.6436	0.1530	0.2331	0.2331	0.3601	0.3601	0.0175
5	19.5720	1.7146	1.7146	0.0548	0.6457	0.6457	0.1508	0.2609	0.2609	0.3580	0.3580	0.0212
10	14.6001	1.7103	1.7103	0.0550	0.6478	0.6478	0.1445	0.3102	0.3102	0.3521	0.3521	0.0312
15	10.8166	1.7089	1.7089	0.0555	0.6447	0.6447	0.1355	0.3460	0.3460	0.3434	0.3434	0.0452
20	8.4511	1.7143	1.7143	0.0561	0.6348	0.6348	0.1258	0.3655	0.3655	0.3332	0.3332	0.0607
25	7.0024	1.7296	1.7296	0.0570	0.6191	0.6191	0.1170	0.3737	0.3737	0.3221	0.3221	0.0762
30	6.0920	1.7571	1.7571	0.0581	0.5993	0.5993	0.1100	0.3741	0.3741	0.3104	0.3104	0.0908
35	5.5017	1.7995	1.7995	0.0595	0.5774	0.5774	0.1051	0.3688	0.3688	0.2982	0.2982	0.1042
40	5.1099	1.8599	1.8599	0.0610	0.5547	0.5547	0.1026	0.3587	0.3587	0.2851	0.2851	0.1166
45	4.8481	1.9431	1.9431	0.0629	0.5325	0.5325	0.1028	0.3439	0.3439	0.2709	0.2709	0.1284
50	4.6757	2.0564	2.0564	0.0651	0.5116	0.5116	0.1056	0.3245	0.3245	0.2553	0.2553	0.1397

Key to the table: EL, ET and ER=elastic modulus in L, T and R directions, GTR, GLR and GLT= shear modulus in TR, LR and LT planes, NUTR, NULR and NULT=Poisson's ratios in TR, LR and LT planes, ALR, ALT and ALL=shrinkage coefficients in R, T and L directions

MFA	EL	ET	ER	GTR	GLR	GLT	NUTR	NULR	NULT	ALR	ALT	ALL
Density = 600 kg/m^3												
0	24.4239	1.8904	1.8904	0.0739	0.7161	0.7161	0.1654	0.2342	0.2342	0.3648	0.3648	0.0175
5	21.3552	1.8878	1.8878	0.0740	0.7191	0.7191	0.1632	0.2614	0.2614	0.3627	0.3627	0.0212
10	15.9320	1.8831	1.8831	0.0744	0.7230	0.7230	0.1568	0.3097	0.3097	0.3569	0.3569	0.0312
15	11.8046	1.8815	1.8815	0.0750	0.7209	0.7209	0.1477	0.3448	0.3448	0.3483	0.3483	0.0451
20	9.2237	1.8873	1.8873	0.0759	0.7110	0.7110	0.1378	0.3639	0.3639	0.3383	0.3383	0.0607
25	7.6431	1.9039	1.9039	0.0772	0.6942	0.6942	0.1288	0.3720	0.3720	0.3273	0.3273	0.0761
30	6.6497	1.9338	1.9338	0.0787	0.6725	0.6725	0.1214	0.3725	0.3725	0.3159	0.3159	0.0907
35	6.0055	1.9797	1.9797	0.0805	0.6480	0.6480	0.1163	0.3674	0.3674	0.3039	0.3039	0.1041
40	5.5780	2.0449	2.0449	0.0826	0.6226	0.6226	0.1135	0.3575	0.3575	0.2911	0.2911	0.1165
45	5.2923	2.1345	2.1345	0.0850	0.5976	0.5976	0.1132	0.3432	0.3432	0.2772	0.2772	0.1282
50	5.1042	2.2560	2.2560	0.0878	0.5739	0.5739	0.1157	0.3243	0.3243	0.2619	0.2619	0.1396
Density = 650 kg/m^3												
0	26.4645	2.4970	1.6158	0.0865	0.6352	0.9264	0.2100	0.2391	0.2314	0.3818	0.3564	0.0175
5	23.1373	2.4926	1.6143	0.0866	0.6397	0.9289	0.2072	0.2640	0.2600	0.3798	0.3543	0.0212
10	17.2590	2.4833	1.6122	0.0870	0.6471	0.9309	0.1992	0.3085	0.3102	0.3742	0.3483	0.0312
15	12.7864	2.4769	1.6135	0.0878	0.6495	0.9252	0.1877	0.3410	0.3466	0.3661	0.3395	0.0451
20	9.9904	2.4803	1.6212	0.0889	0.6441	0.9099	0.1752	0.3588	0.3664	0.3565	0.3292	0.0607
25	8.2783	2.4987	1.6375	0.0904	0.6313	0.8865	0.1638	0.3663	0.3746	0.3462	0.3180	0.0761
30	7.2024	2.5358	1.6640	0.0922	0.6132	0.8577	0.1545	0.3670	0.3750	0.3354	0.3062	0.0906
35	6.5046	2.5956	1.7027	0.0943	0.5918	0.8259	0.1479	0.3626	0.3696	0.3241	0.2938	0.1040
40	6.0416	2.6831	1.7561	0.0968	0.5690	0.7934	0.1441	0.3538	0.3592	0.3122	0.2806	0.1165
45	5.7321	2.8056	1.8276	0.0996	0.5461	0.7616	0.1435	0.3409	0.3442	0.2992	0.2662	0.1282
50	5.5284	2.9741	1.9226	0.1030	0.5241	0.7318	0.1461	0.3239	0.3244	0.2850	0.2503	0.1396

Key to the table: EL, ET and ER=elastic modulus in L, T and R directions, GTR, GLR and GLT= shear modulus in TR, LR and LT planes, NUTR, NULR and NULT=Poisson's ratios in TR, LR and LT planes, ALR, ALT and ALL=shrinkage coefficients in R, T and L directions

MFA	EL	ET	ER	GTR	GLR	GLT	NUTR	NULR	NULT	ALR	ALT	ALL
Density = 700 kg/m^3												
0	28.4940	2.7182	1.7540	0.1131	0.6989	1.0167	0.2253	0.2405	0.2323	0.3879	0.3603	0.0175
5	24.9130	2.7134	1.7525	0.1132	0.7046	1.0204	0.2225	0.2647	0.2603	0.3860	0.3581	0.0212
10	18.5855	2.7032	1.7502	0.1138	0.7147	1.0244	0.2143	0.3079	0.3098	0.3805	0.3522	0.0312
15	13.7704	2.6962	1.7516	0.1149	0.7194	1.0198	0.2026	0.3394	0.3456	0.3725	0.3436	0.0451
20	10.7600	2.6997	1.7599	0.1164	0.7149	1.0042	0.1899	0.3568	0.3650	0.3631	0.3334	0.0606
25	8.9163	2.7193	1.7772	0.1184	0.7019	0.9793	0.1782	0.3642	0.3732	0.3530	0.3223	0.0761
30	7.7577	2.7592	1.8056	0.1208	0.6825	0.9480	0.1686	0.3650	0.3736	0.3425	0.3107	0.0906
35	7.0063	2.8233	1.8467	0.1236	0.6590	0.9131	0.1616	0.3607	0.3684	0.3315	0.2985	0.1040
40	6.5077	2.9170	1.9032	0.1269	0.6336	0.8772	0.1574	0.3523	0.3582	0.3198	0.2855	0.1164
45	6.1744	3.0479	1.9787	0.1306	0.6079	0.8419	0.1563	0.3400	0.3435	0.3072	0.2713	0.1281
50	5.9550	3.2274	2.0784	0.1348	0.5831	0.8087	0.1585	0.3236	0.3242	0.2933	0.2557	0.1395
Density = 750 kg/m^3												
0	30.5277	2.9454	1.8949	0.1459	0.7657	1.1110	0.2409	0.2420	0.2332	0.3943	0.3643	0.0175
5	26.6921	2.9402	1.8933	0.1462	0.7730	1.1160	0.2380	0.2654	0.2607	0.3924	0.3622	0.0212
10	19.9137	2.9291	1.8909	0.1470	0.7864	1.1225	0.2297	0.3073	0.3094	0.3870	0.3563	0.0311
15	14.7547	2.9214	1.8924	0.1485	0.7938	1.1195	0.2178	0.3380	0.3446	0.3792	0.3478	0.0451
20	11.5287	2.9250	1.9012	0.1506	0.7908	1.1040	0.2048	0.3548	0.3638	0.3700	0.3377	0.0606
25	9.5530	2.9459	1.9197	0.1532	0.7778	1.0778	0.1928	0.3621	0.3718	0.3601	0.3268	0.0760
30	8.3112	2.9885	1.9497	0.1564	0.7570	1.0439	0.1828	0.3629	0.3723	0.3498	0.3154	0.0905
35	7.5060	3.0570	1.9933	0.1602	0.7314	1.0058	0.1754	0.3590	0.3672	0.3390	0.3033	0.1039
40	6.9716	3.1569	2.0528	0.1644	0.7033	0.9662	0.1708	0.3509	0.3573	0.3277	0.2905	0.1163
45	6.6144	3.2962	2.1320	0.1691	0.6746	0.9272	0.1693	0.3391	0.3430	0.3154	0.2766	0.1281
50	6.3793	3.4869	2.2360	0.1745	0.6467	0.8902	0.1710	0.3235	0.3240	0.3020	0.2613	0.1394

Key to the table: EL, ET and ER=elastic modulus in L, T and R directions, GTR, GLR and GLT= shear modulus in TR, LR and LT planes, NUTR, NULR and NULT=Poisson's ratios in TR, LR and LT planes, ALR, ALT and ALL=shrinkage coefficients in R, T and L directions

MFA	EL	ET	ER	GTR	GLR	GLT	NUTR	NULR	NULT	ALR	ALT	ALL
Density = 800 kg/m^3												
0	32.5529	3.1819	2.0402	0.1865	0.8361	1.2094	0.2567	0.2436	0.2341	0.4009	0.3683	0.0175
5	28.4653	3.1763	2.0385	0.1868	0.8453	1.2160	0.2538	0.2661	0.2611	0.3990	0.3662	0.0212
10	21.2401	3.1643	2.0359	0.1880	0.8625	1.2256	0.2453	0.3066	0.3088	0.3937	0.3604	0.0311
15	15.7399	3.1558	2.0375	0.1900	0.8735	1.2249	0.2332	0.3363	0.3434	0.3860	0.3520	0.0450
20	12.3002	3.1596	2.0469	0.1928	0.8724	1.2098	0.2200	0.3527	0.3623	0.3770	0.3421	0.0605
25	10.1933	3.1818	2.0665	0.1964	0.8596	1.1823	0.2076	0.3598	0.3702	0.3674	0.3314	0.0759
30	8.8691	3.2272	2.0982	0.2007	0.8377	1.1460	0.1973	0.3607	0.3707	0.3573	0.3201	0.0904
35	8.0103	3.3002	2.1441	0.2055	0.8098	1.1045	0.1894	0.3570	0.3658	0.3469	0.3083	0.1038
40	7.4404	3.4065	2.2065	0.2110	0.7788	1.0611	0.1844	0.3494	0.3562	0.3359	0.2957	0.1162
45	7.0594	3.5543	2.2891	0.2171	0.7468	1.0181	0.1823	0.3382	0.3422	0.3240	0.2821	0.1279
50	6.8087	3.7559	2.3971	0.2239	0.7156	0.9772	0.1834	0.3232	0.3238	0.3109	0.2671	0.1393
Density = 850 kg/m^3												
0	34.5923	3.4285	2.1900	0.2360	0.9108	1.3126	0.2728	0.2451	0.2350	0.4078	0.3725	0.0174
5	30.2503	3.4225	2.1882	0.2365	0.9222	1.3213	0.2698	0.2668	0.2614	0.4059	0.3705	0.0212
10	22.5740	3.4095	2.1855	0.2381	0.9441	1.3348	0.2611	0.3060	0.3083	0.4007	0.3647	0.0311
15	16.7293	3.4003	2.1872	0.2409	0.9594	1.3370	0.2488	0.3347	0.3422	0.3932	0.3565	0.0450
20	13.0736	3.4042	2.1971	0.2447	0.9610	1.3230	0.2353	0.3506	0.3608	0.3844	0.3467	0.0604
25	10.8342	3.4279	2.2178	0.2495	0.9489	1.2945	0.2226	0.3576	0.3686	0.3750	0.3361	0.0758
30	9.4266	3.4762	2.2512	0.2551	0.9259	1.2556	0.2118	0.3585	0.3692	0.3652	0.3250	0.0903
35	8.5137	3.5539	2.2993	0.2615	0.8956	1.2106	0.2035	0.3551	0.3644	0.3551	0.3134	0.1036
40	7.9079	3.6667	2.3645	0.2687	0.8613	1.1631	0.1979	0.3479	0.3551	0.3444	0.3011	0.1160
45	7.5029	3.8232	2.4504	0.2765	0.8257	1.1158	0.1953	0.3372	0.3415	0.3328	0.2877	0.1278
50	7.2364	4.0361	2.5621	0.2850	0.7907	1.0705	0.1957	0.3230	0.3236	0.3202	0.2729	0.1392

Key to the table: EL, ET and ER=elastic modulus in L, T and R directions, GTR, GLR and GLT= shear modulus in TR, LR and LT planes, NUTR, NULR and NULT=Poisson's ratios in TR, LR and LT planes, ALR, ALT and ALL=shrinkage coefficients in R, T and L directions

MFA	EL	ET	ER	GTR	GLR	GLT	NUTR	NULR	NULT	ALR	ALT	ALL
Density = 900 kg/m^3												
0	36.6192	3.6853	2.3443	0.2960	0.9898	1.4199	0.2892	0.2467	0.2359	0.4150	0.3768	0.0174
5	32.0250	3.6788	2.3424	0.2967	1.0038	1.4311	0.2860	0.2675	0.2618	0.4132	0.3748	0.0211
10	23.9014	3.6648	2.3396	0.2989	1.0313	1.4496	0.2772	0.3053	0.3077	0.4081	0.3692	0.0311
15	17.7147	3.6549	2.3414	0.3025	1.0520	1.4557	0.2646	0.3330	0.3410	0.4008	0.3610	0.0449
20	13.8444	3.6589	2.3518	0.3076	1.0570	1.4433	0.2508	0.3484	0.3592	0.3922	0.3514	0.0603
25	11.4734	3.6841	2.3736	0.3139	1.0460	1.4142	0.2377	0.3552	0.3669	0.3830	0.3410	0.0757
30	9.9829	3.7356	2.4087	0.3214	1.0221	1.3729	0.2264	0.3563	0.3676	0.3735	0.3301	0.0901
35	9.0162	3.8181	2.4590	0.3298	0.9893	1.3243	0.2176	0.3531	0.3630	0.3637	0.3187	0.1035
40	8.3747	3.9377	2.5269	0.3390	0.9516	1.2724	0.2115	0.3463	0.3540	0.3533	0.3066	0.1159
45	7.9459	4.1032	2.6159	0.3490	0.9119	1.2204	0.2082	0.3363	0.3408	0.3421	0.2934	0.1276
50	7.6637	4.3275	2.7310	0.3598	0.8726	1.1705	0.2079	0.3228	0.3233	0.3299	0.2790	0.1390

Key to the table: EL, ET and ER=elastic modulus in L, T and R directions, GTR, GLR and GLT= shear modulus in TR, LR and LT planes, NUTR, NULR and NULT=Poisson's ratios in TR, LR and LT planes, ALR, ALT and ALL=shrinkage coefficients in R, T and L directions

D. Deformed cell meshes for seven load cases

1st Load Case

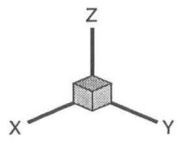

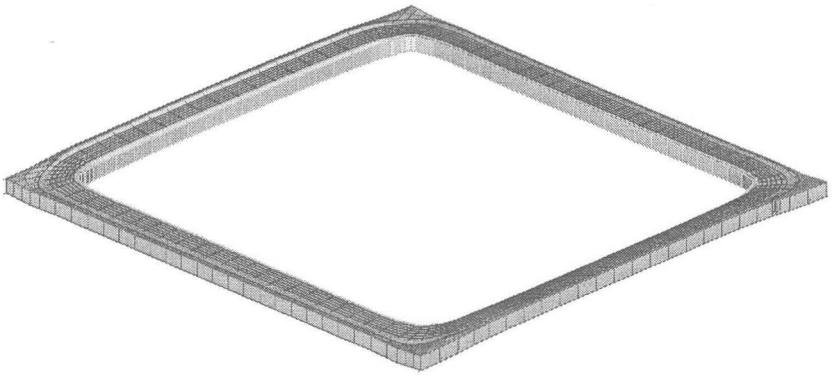

2nd Load Case

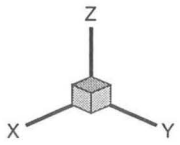

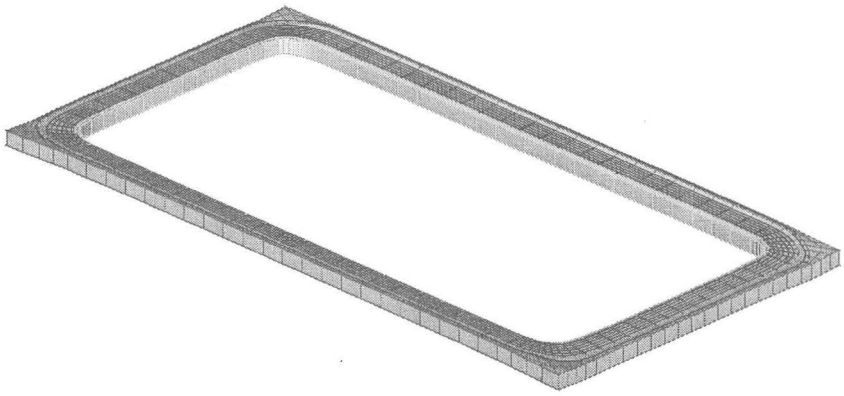

The global directions x, y and z represent the tangential, radial and longitudinal directions respectively. Finite element meshes of deformed periodic cell of wood that has density of 450 kg/m^3 and microfibril angle of 25^o in S_2 are given for first and second load cases.

3rd Load Case

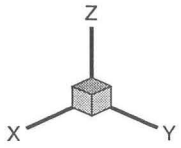

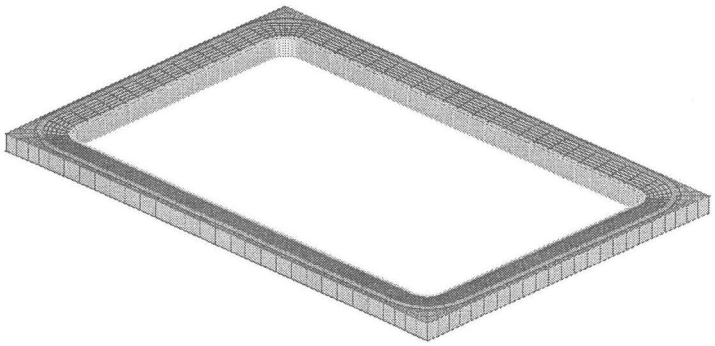

4th Load Case

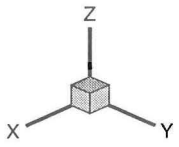

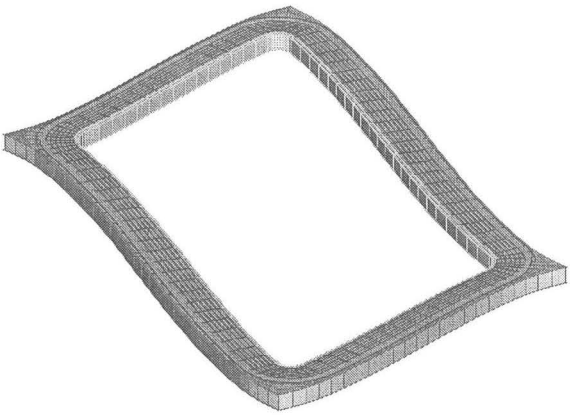

The global directions x, y and z represent the tangential, radial and longitudinal directions respectively. Finite element meshes of deformed periodic cell of wood that has density of 450 kg/m^3 and microfibril angle of 25^o in S_2 are given for third and fourth load cases.

5th Load Case

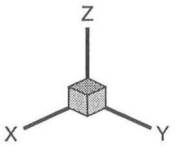

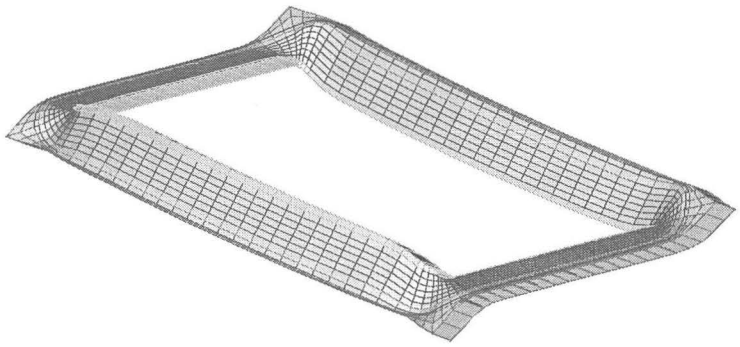

6th Load Case

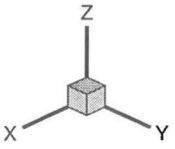

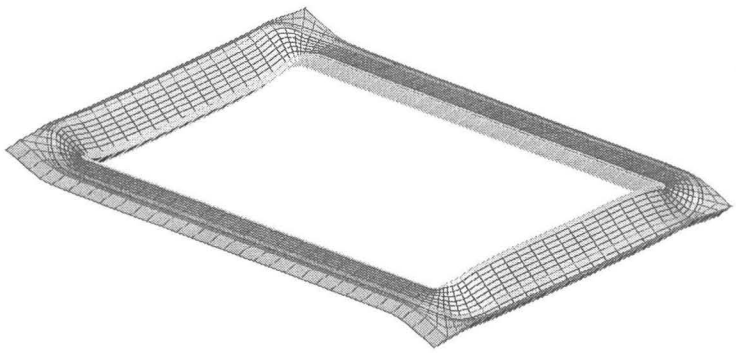

The global directions x, y and z represent the tangential, radial and longitudinal directions respectively. Finite element meshes of deformed periodic cell of wood that has density of 450 kg/m^3 and microfibril angle of 25^o in S_2 are given for fifth and sixth load cases.

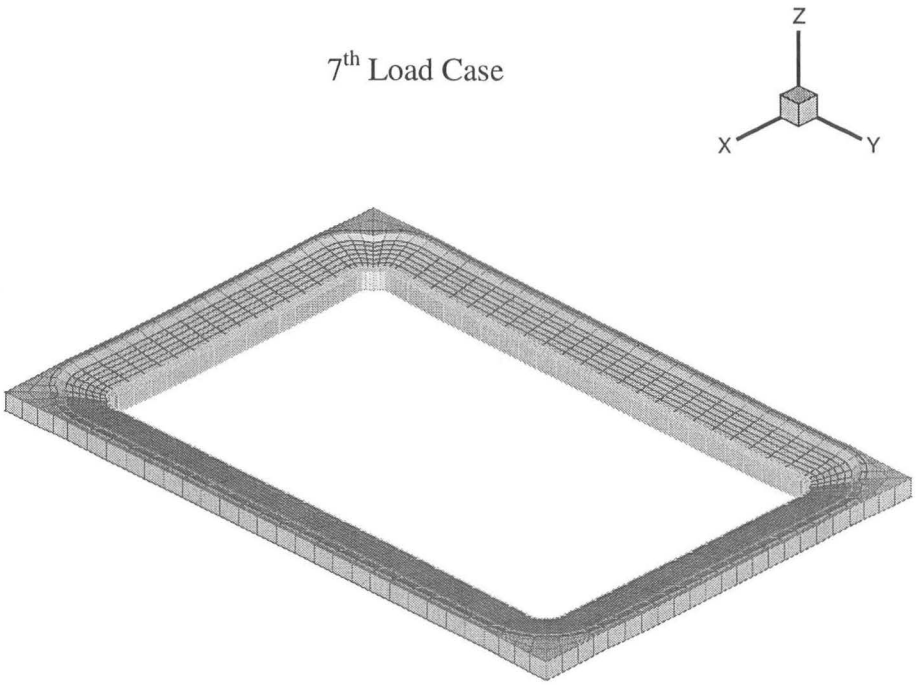

The global directions x, y and z represent the tangential, radial and longitudinal directions respectively. Finite element mesh of deformed periodic cell of wood that has density of 450 kg/m^3 and microfibril angle of 25^o in S_2 is given for seventh load case.

E. Measurement of the cell wall geometry

Specimens were prepared for optical examination by making a fine cut along the radial-tangential plane using a sharp blade. The surface produced gave a clear image of the undistorted cell structure in the optical image analyzer. A typical field view is presented in Figure E.1.

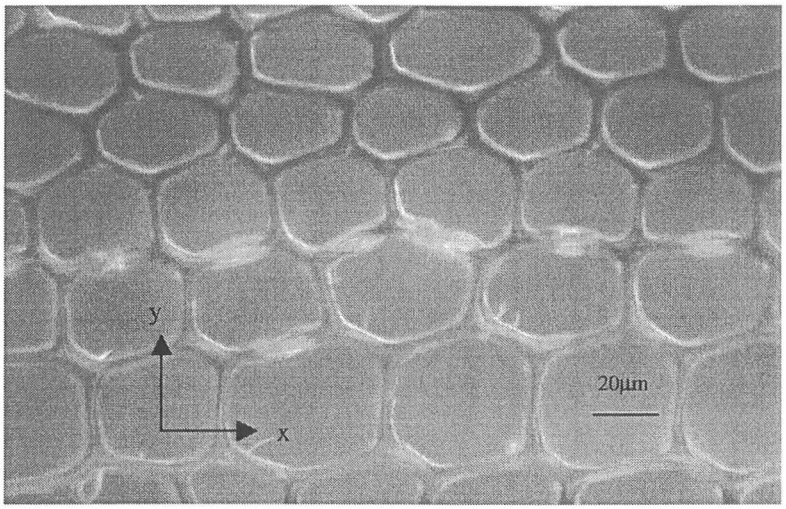

E.1. Cell image of radial-tangential plane showing the x-y coordinate axes.

Images were analysed using a Scion Image Analyser. Five images were analysed for each specimen, four near each corner of the field and one in the center. More than 1000 cell walls were measured. The length and the orientation of each cell wall were obtained in the following way. Two-dimensional coordinates were set up in the field of view with the x-direction coinciding with the radial direction and the y-direction orientated in the transverse direction. The x and y coordinates of each cell junction were then determined by the image analyzer. The length of each cell wall (l_c) and the orientation (θ), relative to the radial direction as zero, were determined by

$$l_c = ((x_j - x_i)^2 + (y_j - y_i)^2)^{\frac{1}{2}} \tag{E1}$$

$$\theta = \tan^{-1}\left(\frac{y_j - y_i}{x_j - x_i}\right) \tag{E2}$$

where (x_i, y_i) and (x_j, y_j) are the coordinates of the two ends of an individual cell wall.

The distribution of l_c with θ for one specimen is shown in Figure 5.1.

F. Density vs. radial distance graphs of sixteen specimens

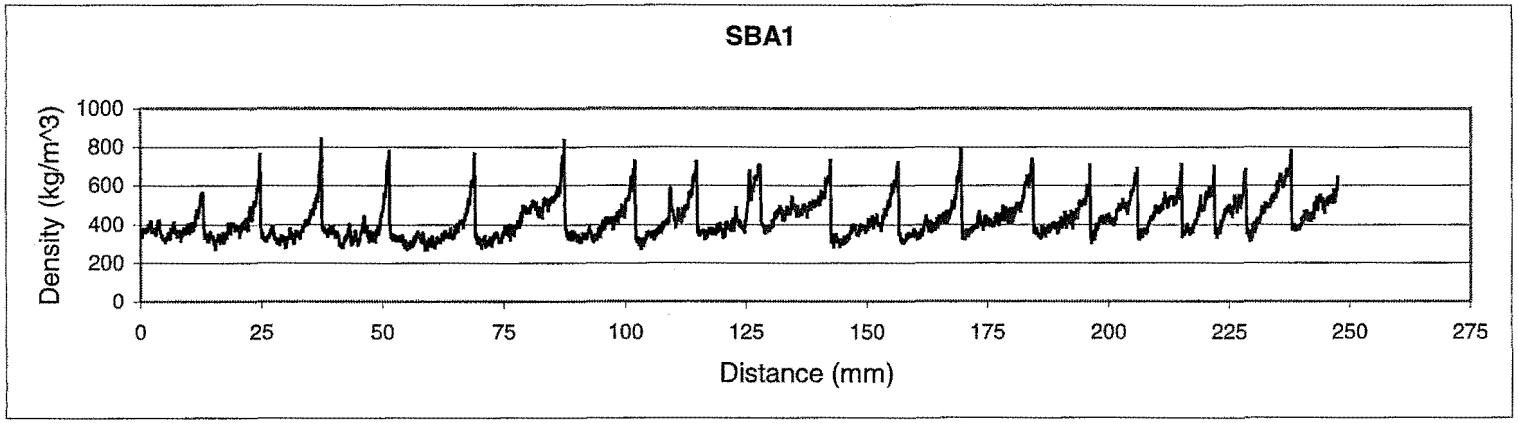

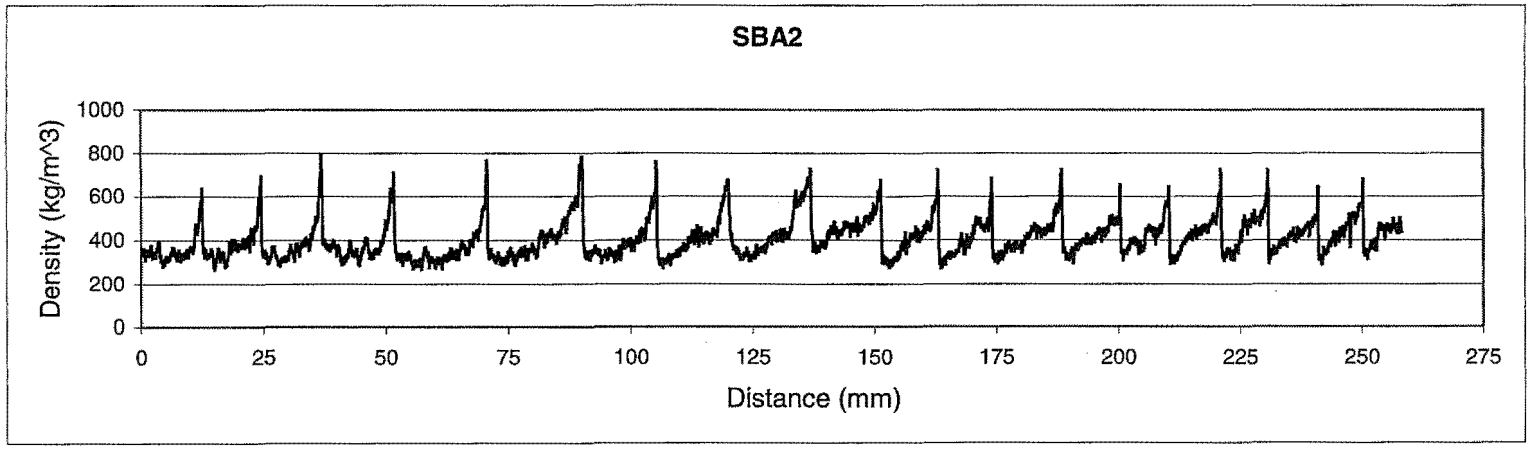

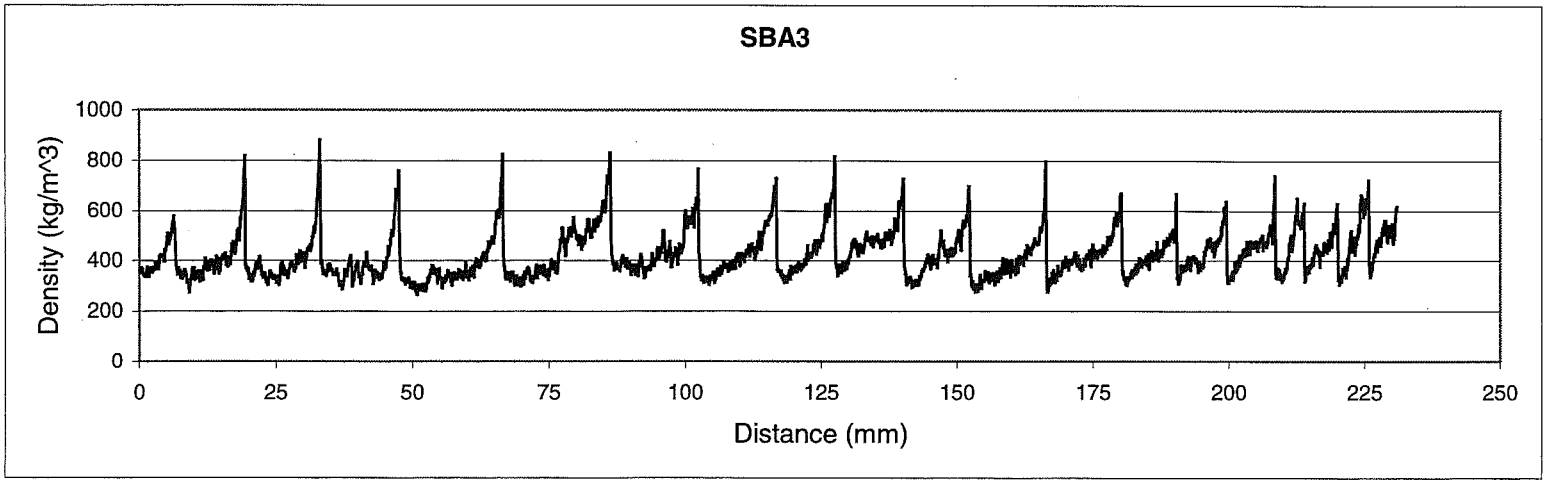
SBA3
Density (kg/m^3)
1000
800
600
400
200
0
0
25
50
75
100
125
150
175
200
225
250
Distance (mm)

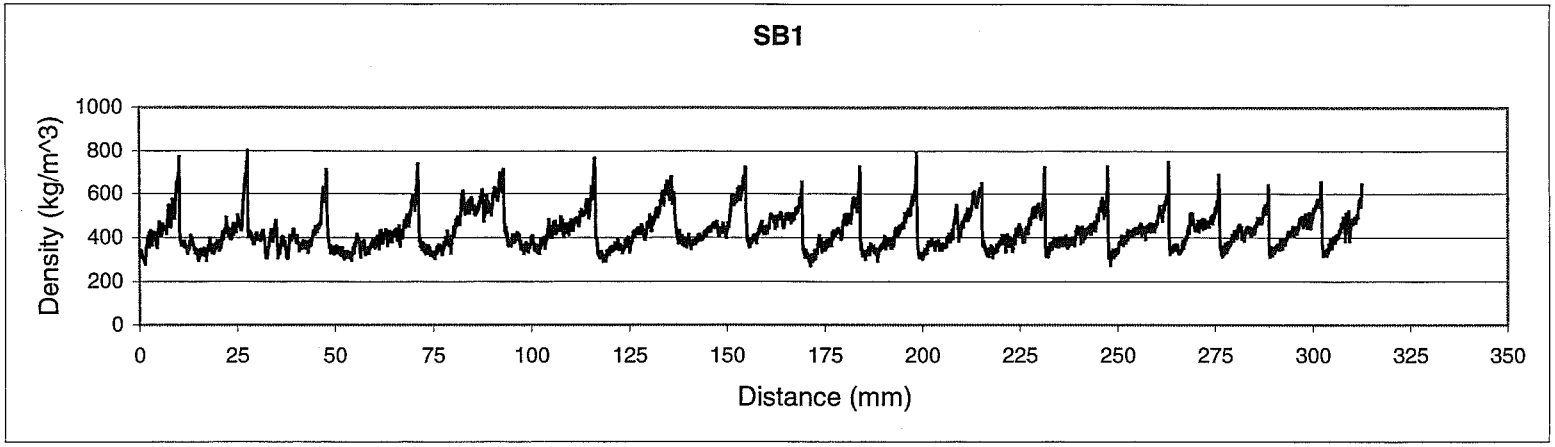
SB1
Density (kg/m^3)
1000
800
600
400
200
0
0
25
50
75
100
125
150
175
200
225
250
275
300
325
350
Distance (mm)

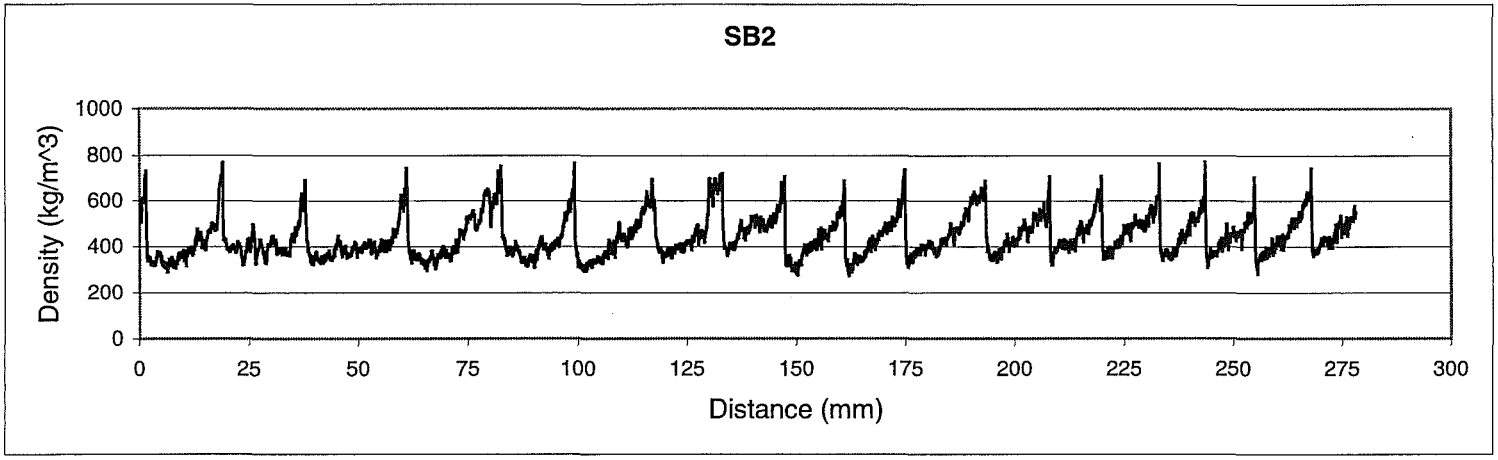
SB2
Density (kg/m^3)
1000
800
600
400
200
0
0
25
50
75
100
125
150
175
200
225
250
275
300
Distance (mm)

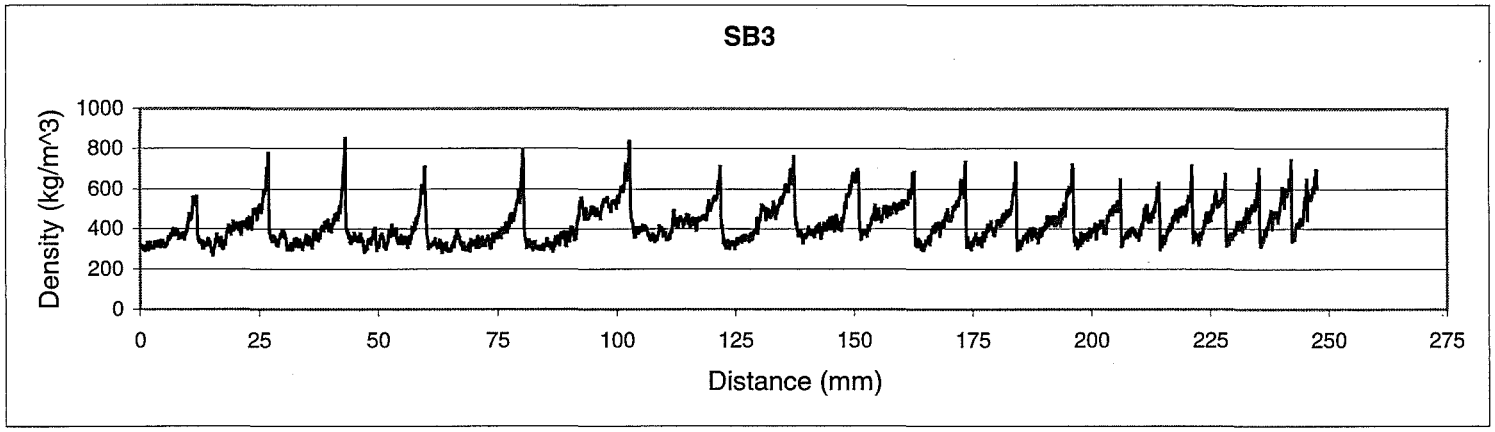
SB3
Density (kg/m^3)
1000
800
600
400
200
0
0
25
50
75
100
125
150
175
200
225
250
275
Distance (mm)

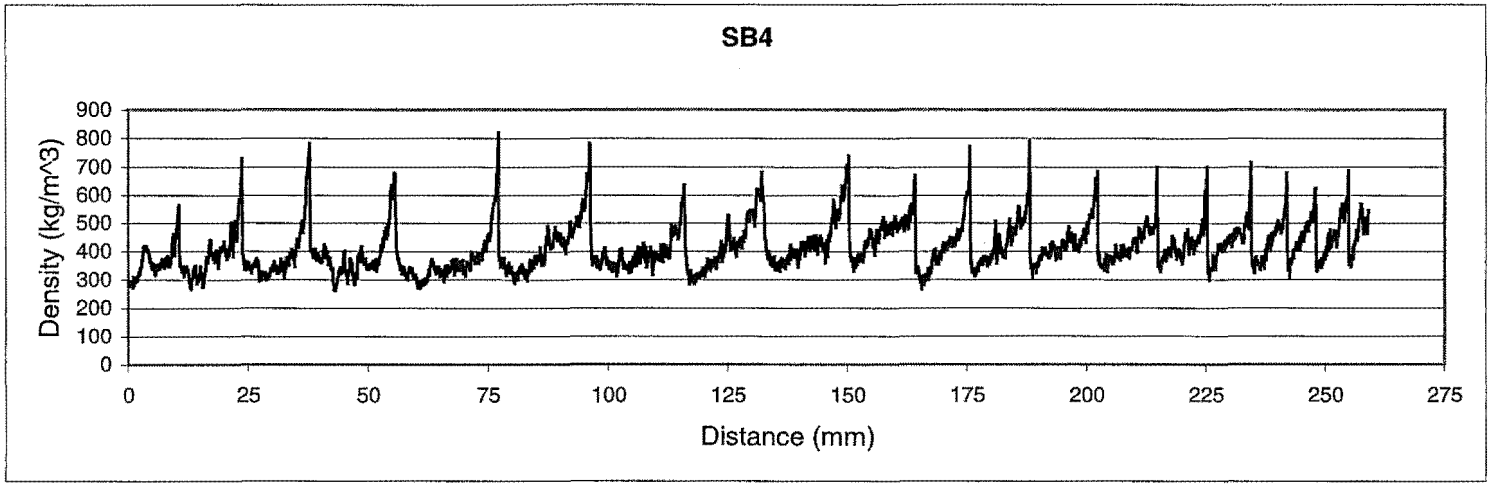
SB4
Density (kg/m^3)
900
800
700
600
500
400
300
200
100
0
0
25
50
75
100
125
150
175
200
225
250
275
Distance (mm)

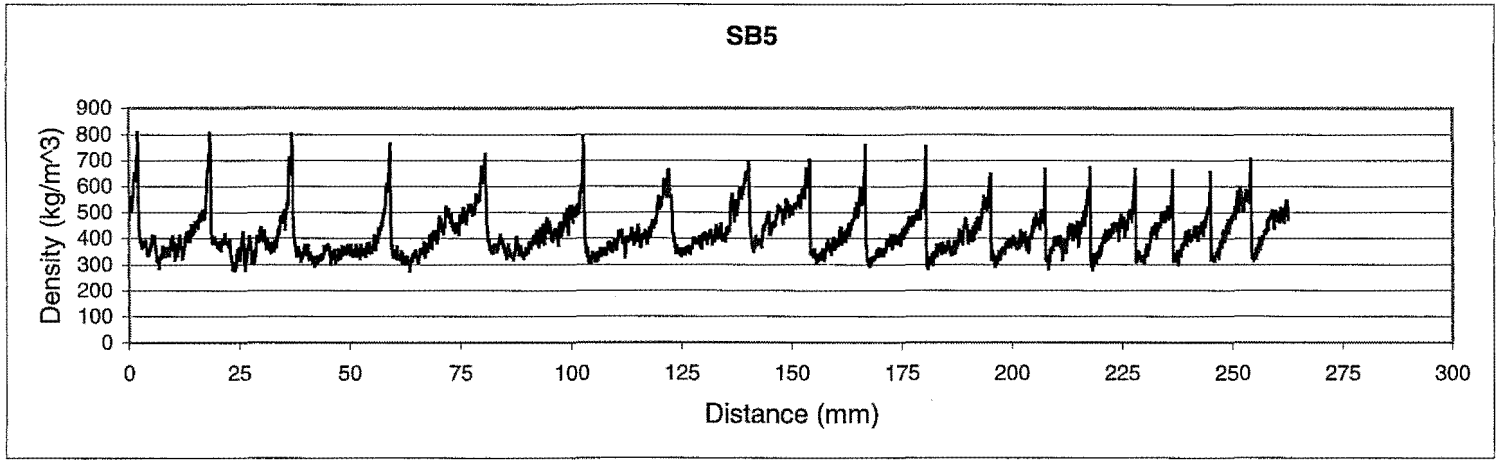
SB5
Density (kg/m^3)
900
800
700
600
500
400
300
200
100
0
0
25
50
75
100
125
150
175
200
225
250
275
300
Distance (mm)

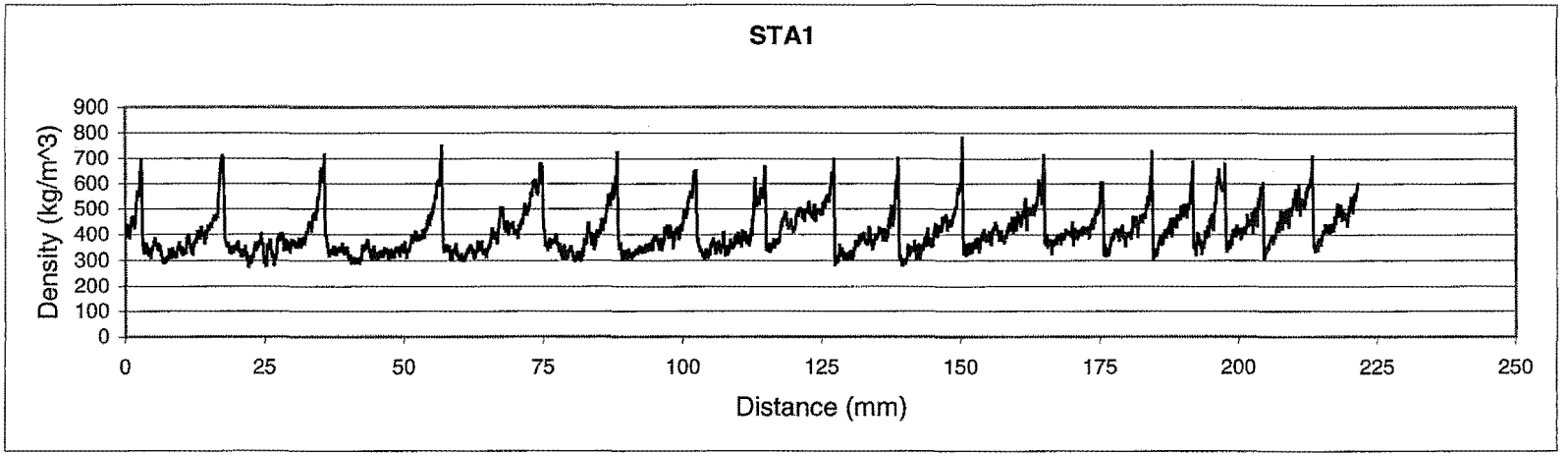
STA1
Density (kg/m^3)
900
800
700
600
500
400
300
200
100
0
0
25
50
75
100
125
150
175
200
225
250
Distance (mm)

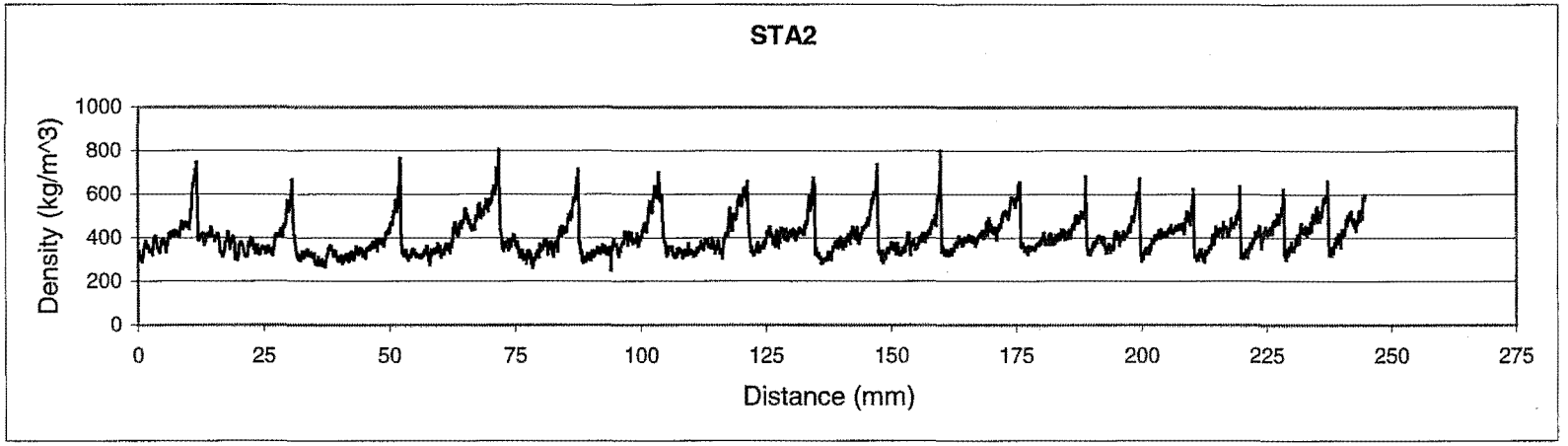
STA2
Density (kg/m^3)
1000
800
600
400
200
0
0
25
50
75
100
125
150
175
200
225
250
275
Distance (mm)

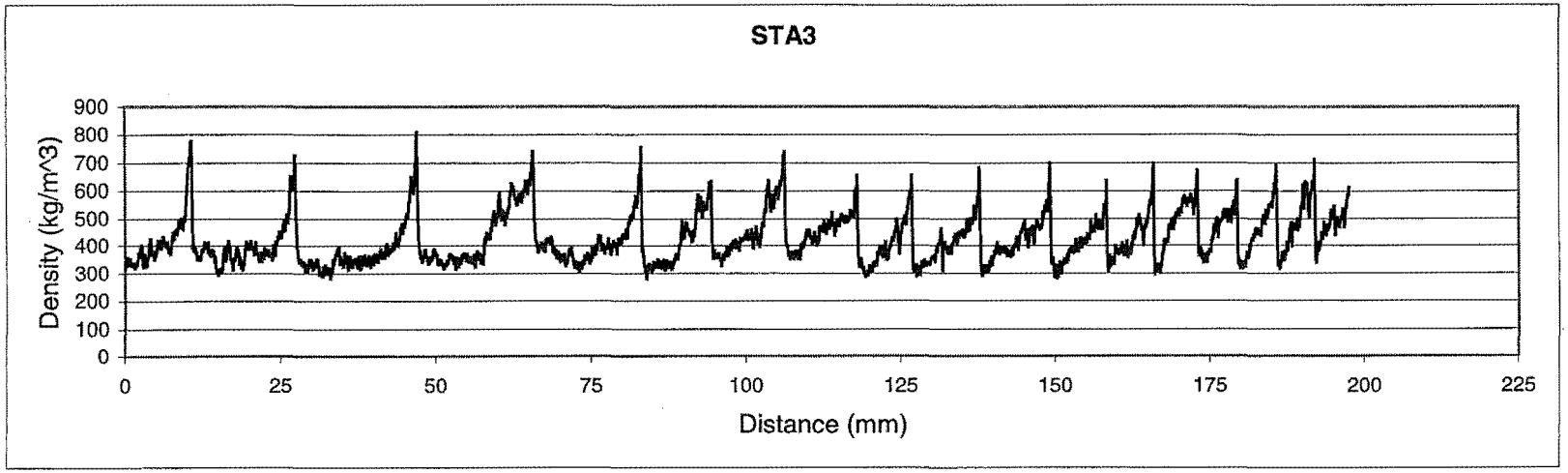
STA3
Density (kg/m^3)
900
800
700
600
500
400
300
200
100
0
0
25
50
75
100
125
150
175
200
225
Distance (mm)

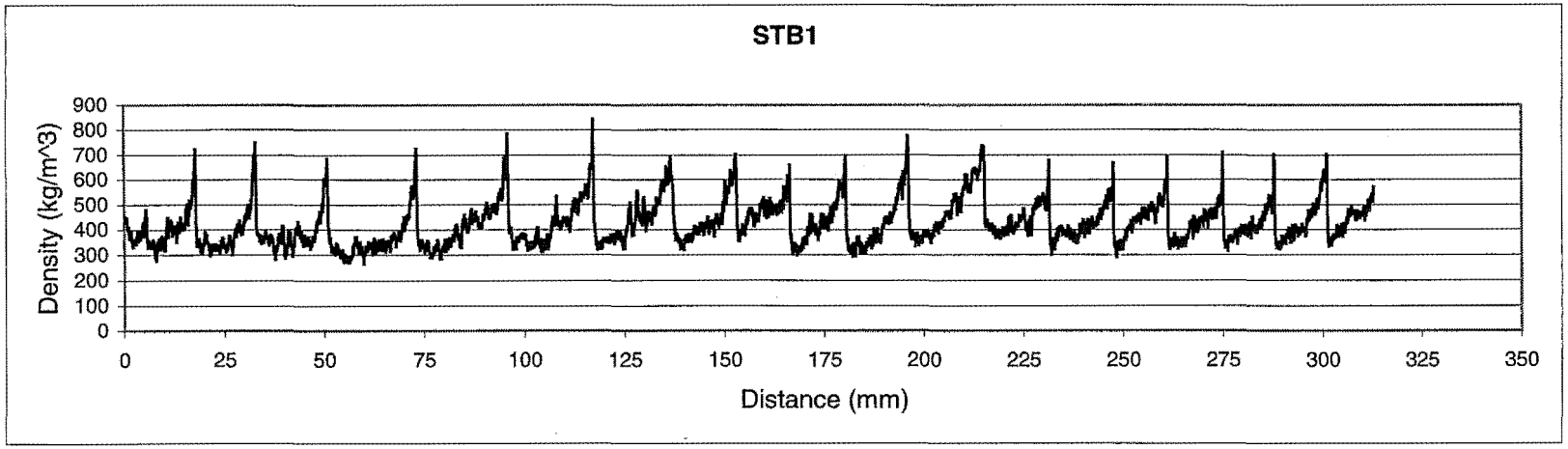
STB1
Density (kg/m^3)
900
800
700
600
500
400
300
200
100
0
0
25
50
75
100
125
150
175
200
225
250
275
300
325
350
Distance (mm)

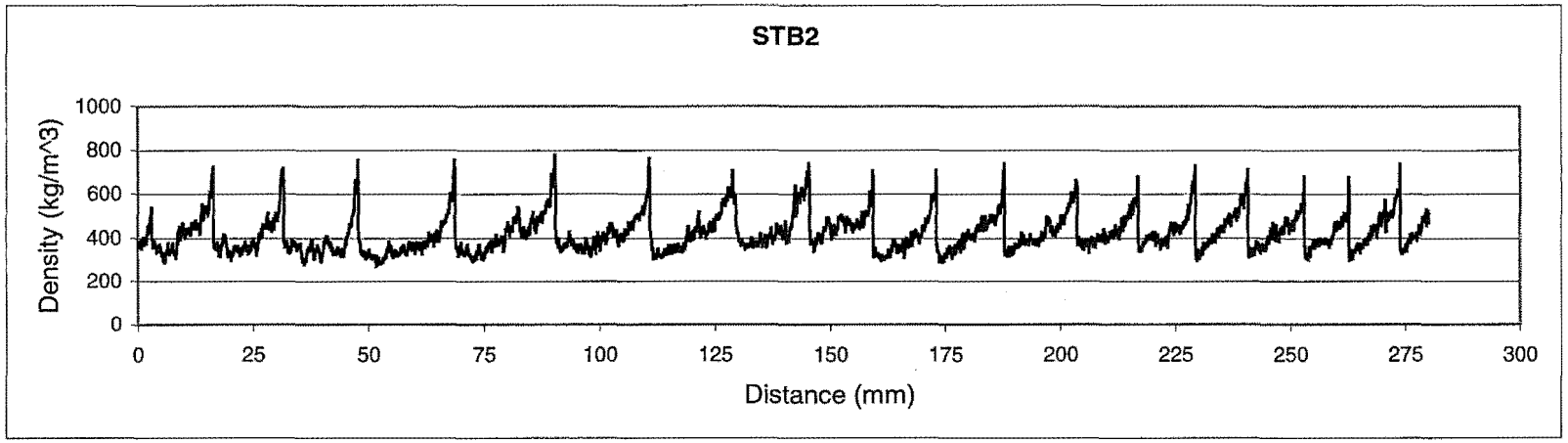
STB2
Density (kg/m^3)
1000
800
600
400
200
0
0
25
50
75
100
125
150
175
200
225
250
275
300
Distance (mm)

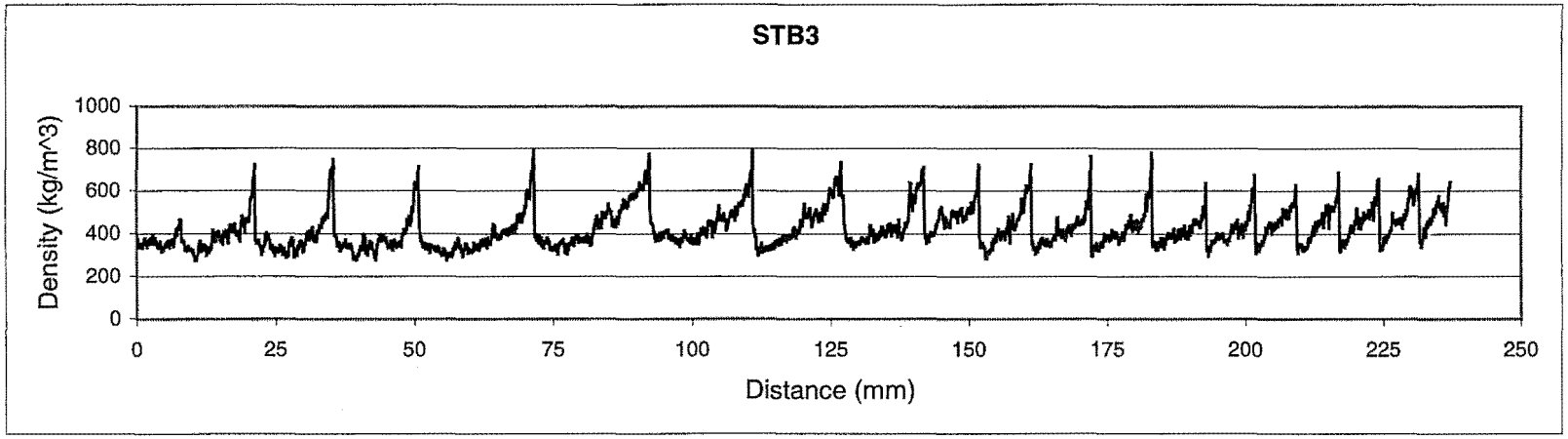
STB3
Density (kg/m^3)
1000
800
600
400
200
0
0
25
50
75
100
125
150
175
200
225
250
Distance (mm)

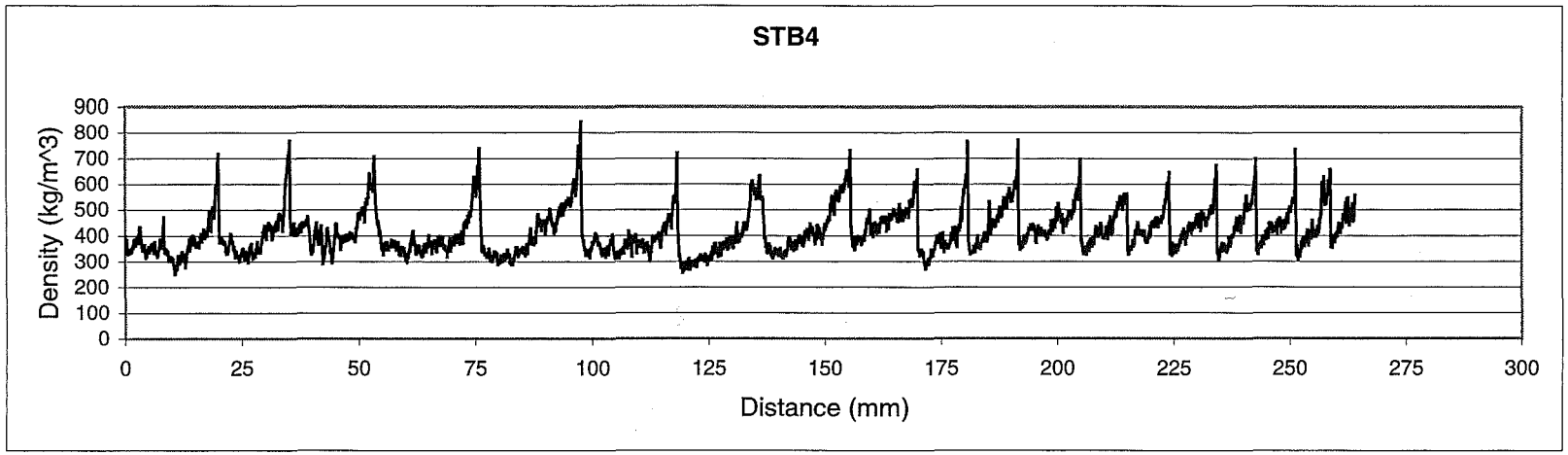
STB4
Density (kg/m^3)
900
800
700
600
500
400
300
200
100
0
0
25
50
75
100
125
150
175
200
225
250
275
300
Distance (mm)

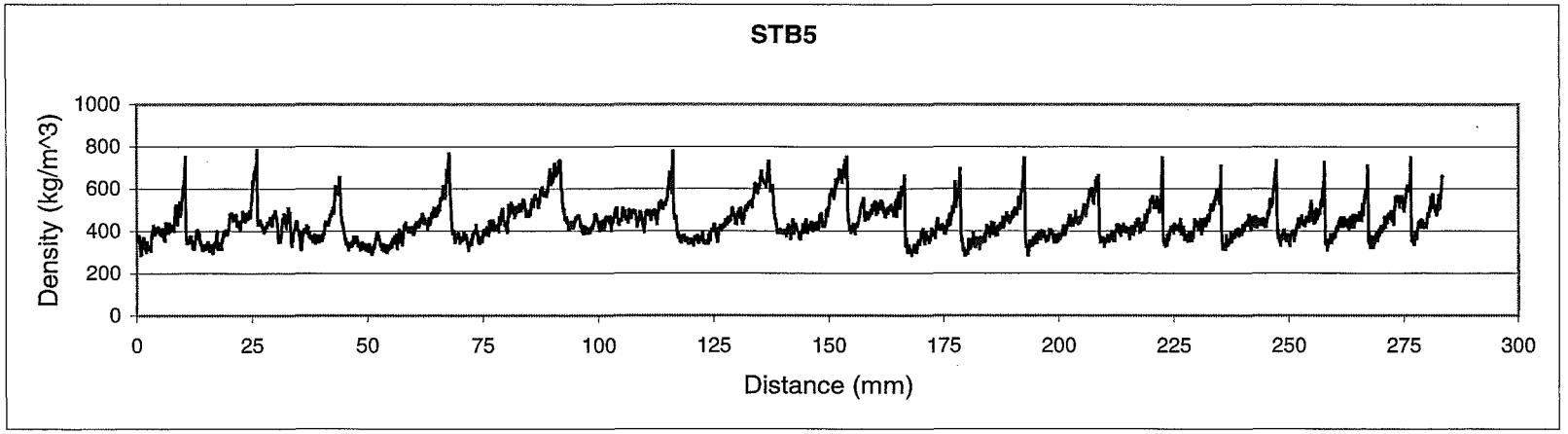
STB5
Density (kg/m^3)
1000
800
600
400
200
0
0
25
50
75
100
125
150
175
200
225
250
275
300
Distance (mm)

G. Microfibril angle (MFA) vs. radial distance graphs of sixteen specimens

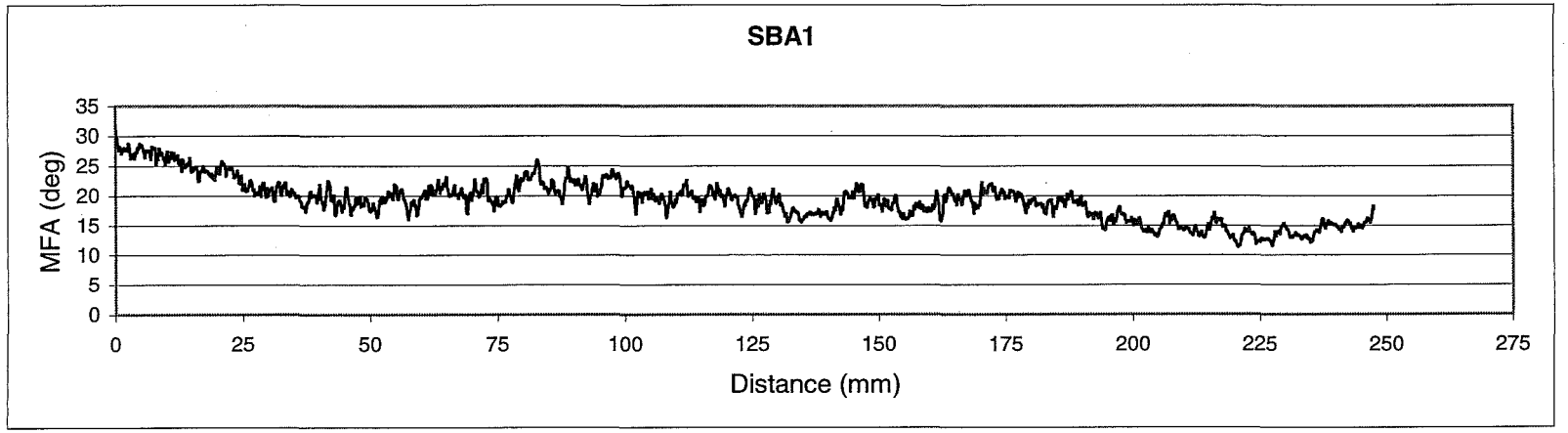

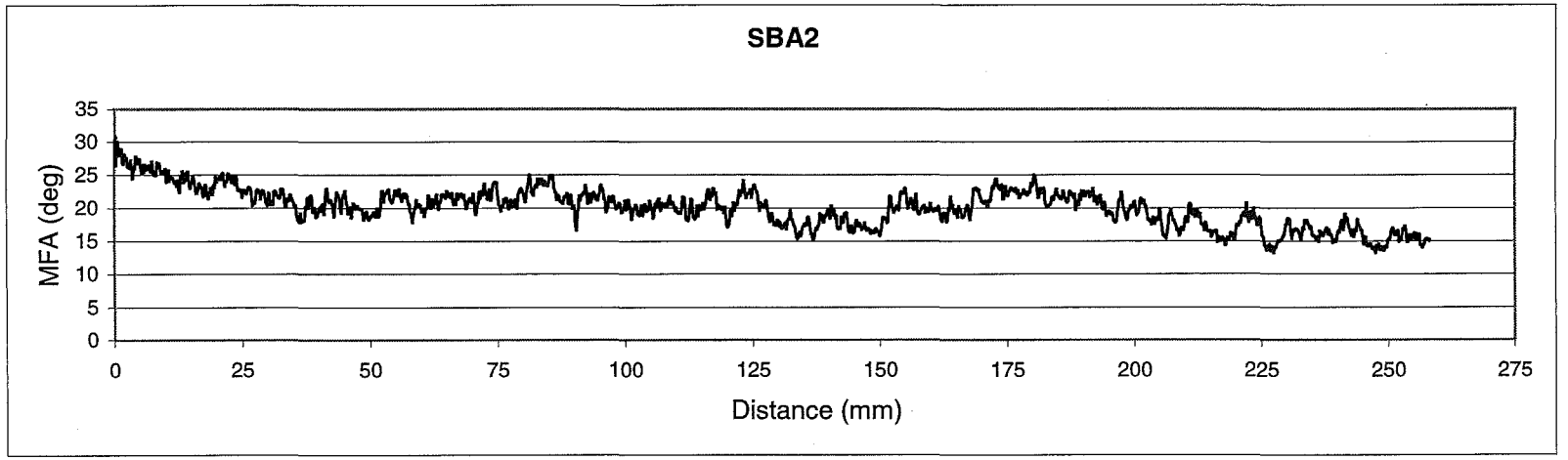

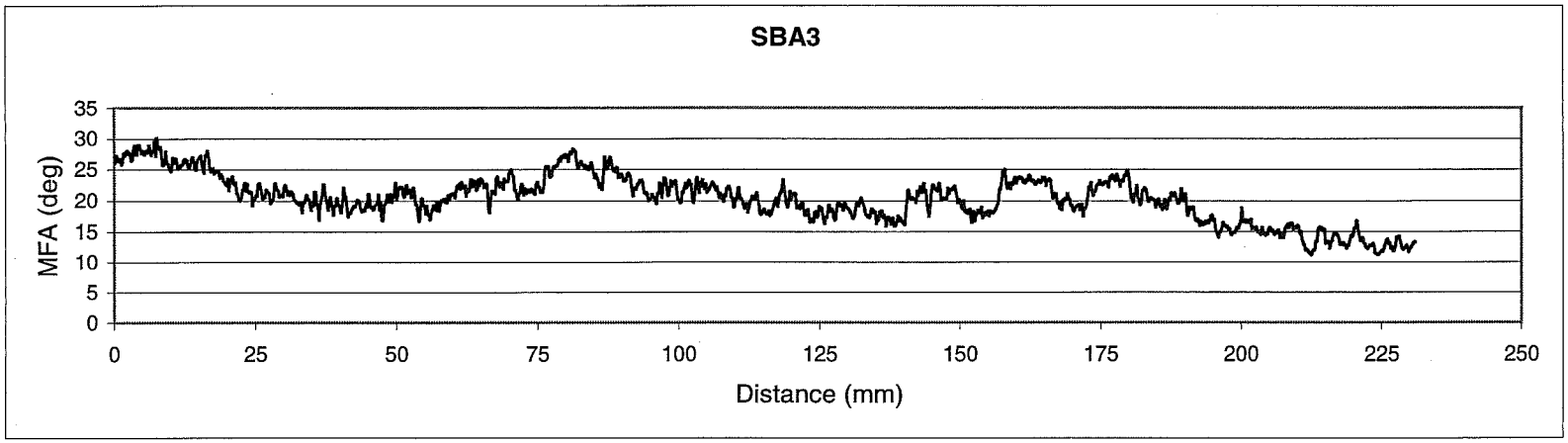
SBA3
MFA (deg)
35
30
25
20
15
10
5
0
0
25
50
75
100
125
150
175
200
225
250
Distance (mm)

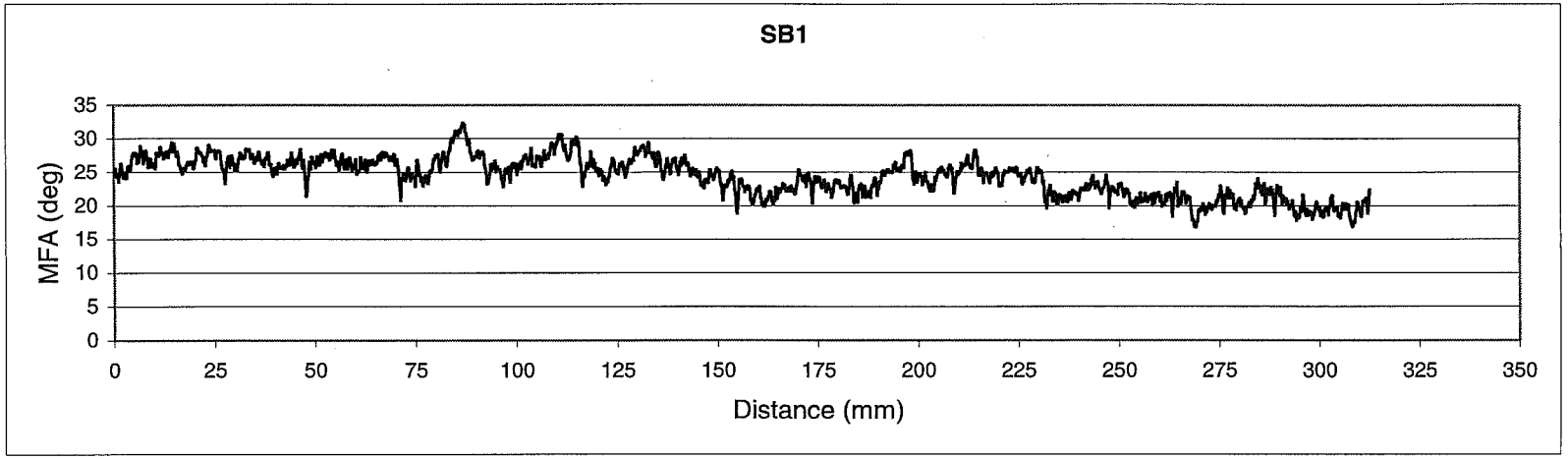
SB1
MFA (deg)
35
30
25
20
15
10
5
0
0
25
50
75
100
125
150
175
200
225
250
275
300
325
350
Distance (mm)

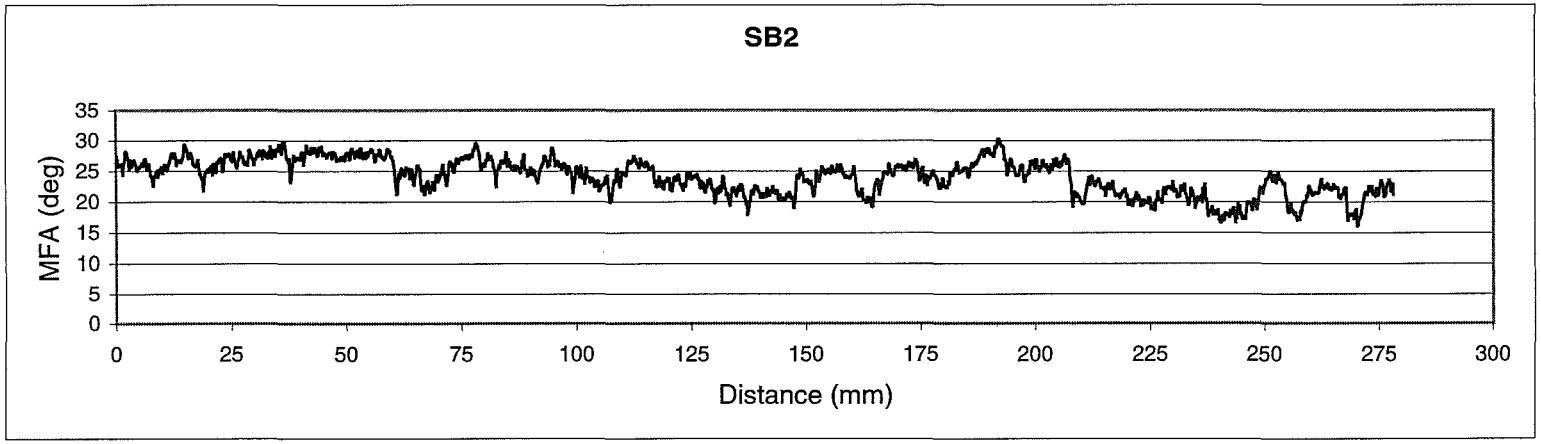
SB2
MFA (deg)
35
30
25
20
15
10
5
0
0
25
50
75
100
125
150
175
200
225
250
275
300
Distance (mm)

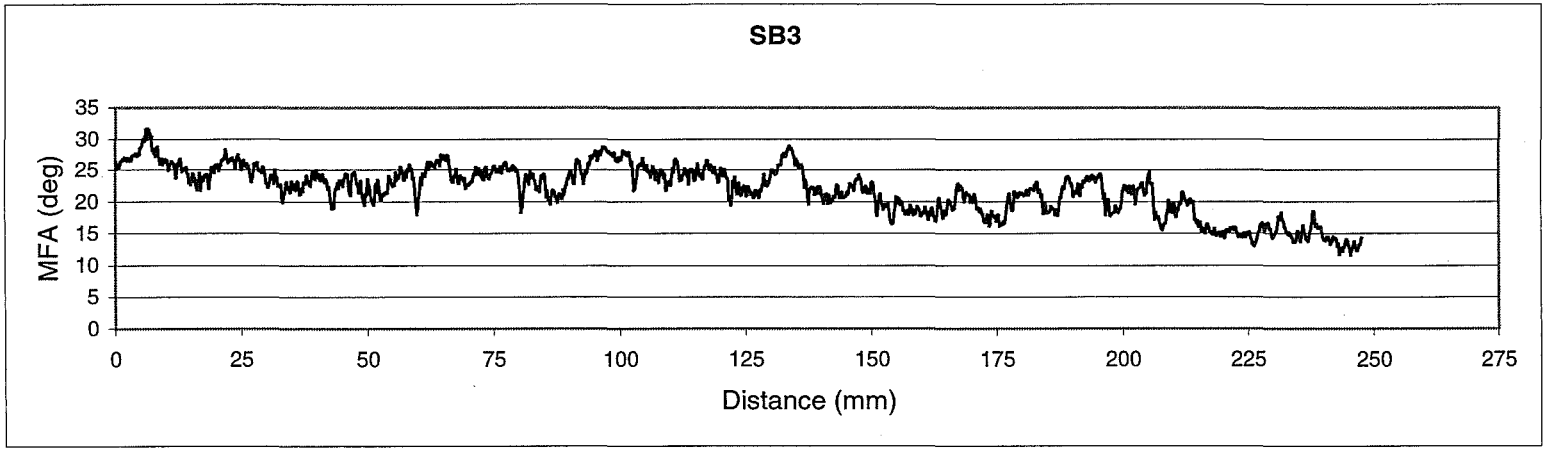
SB3
MFA (deg)
35
30
25
20
15
10
5
0
0
25
50
75
100
125
150
175
200
225
250
275
Distance (mm)

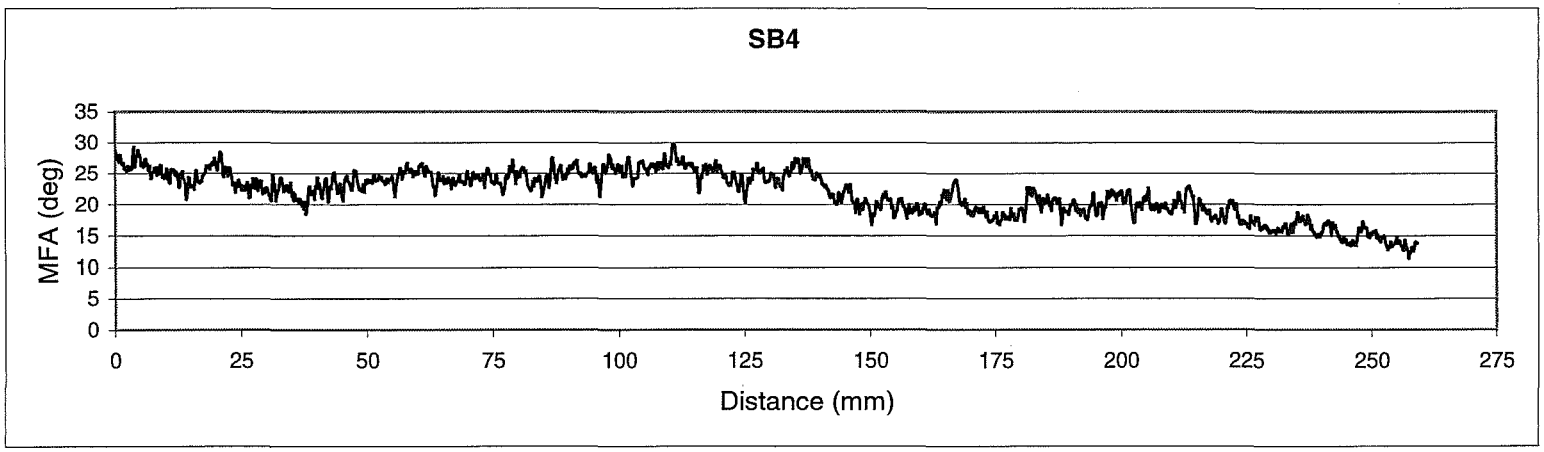
SB4
MFA (deg)
35
30
25
20
15
10
5
0
0
25
50
75
100
125
150
175
200
225
250
275
Distance (mm)

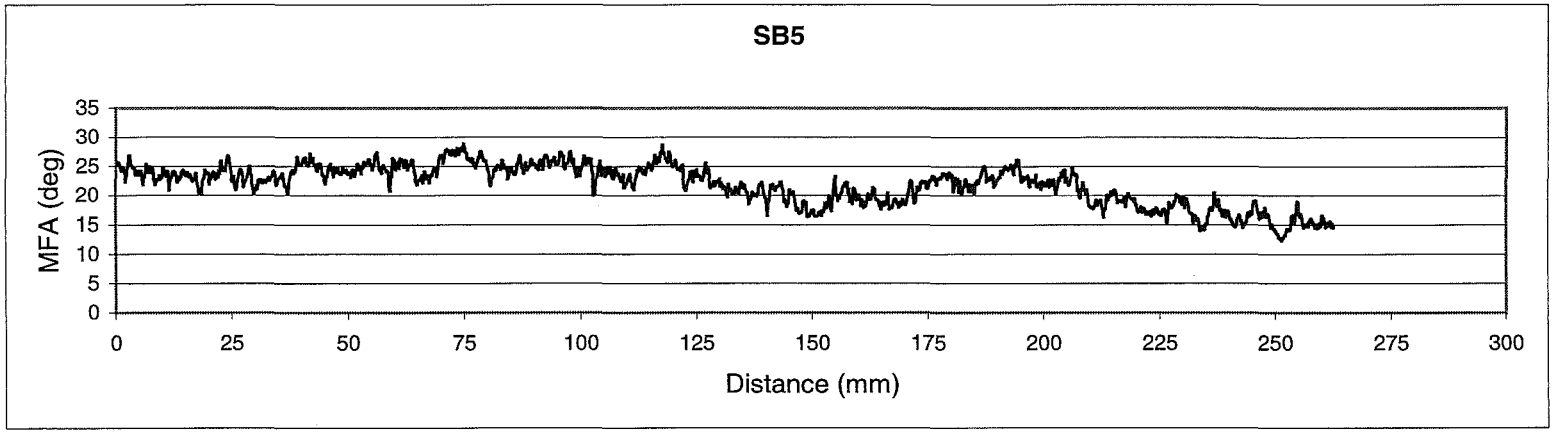
SB5
MFA (deg)
35
30
25
20
15
10
5
0
0
25
50
75
100
125
150
175
200
225
250
275
300
Distance (mm)

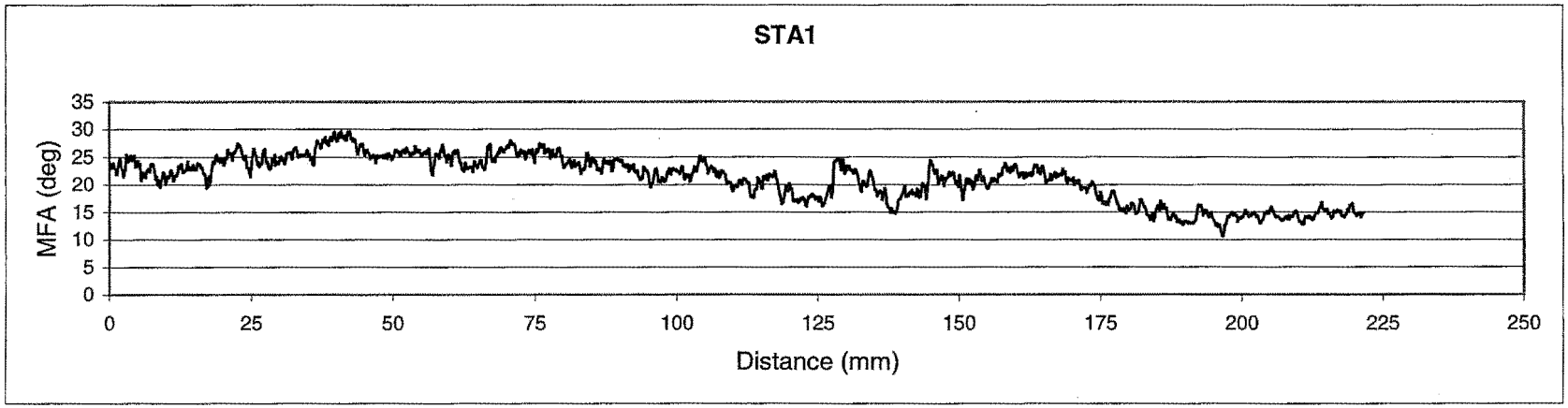
STA1
MFA (deg)
35
30
25
20
15
10
5
0
0
25
50
75
100
125
150
175
200
225
250
Distance (mm)

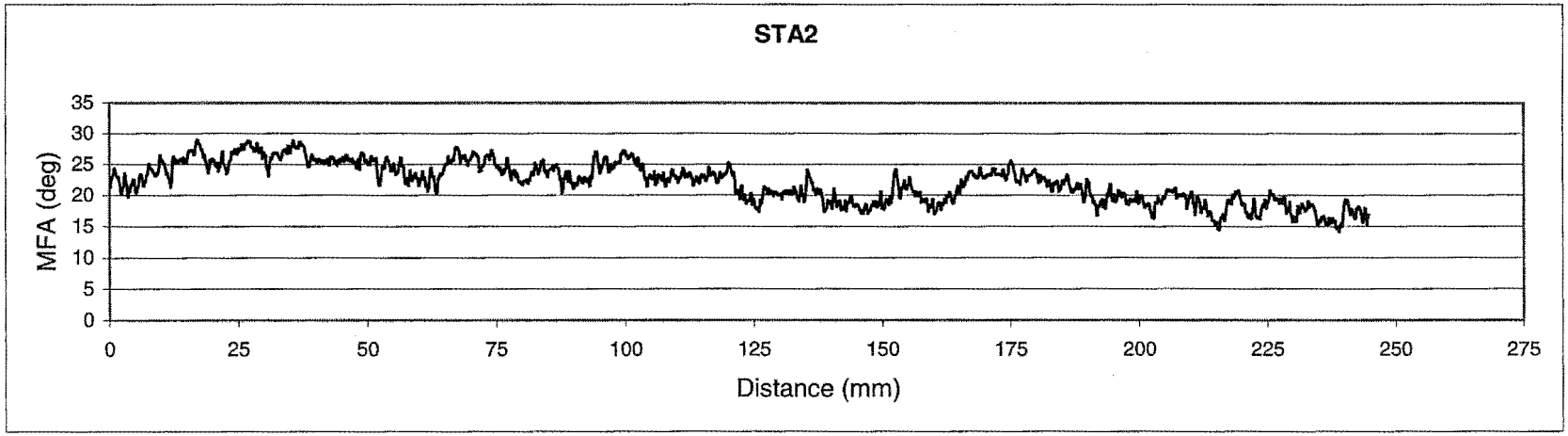
STA2
MFA (deg)
35
30
25
20
15
10
5
0
0
25
50
75
100
125
150
175
200
225
250
275
Distance (mm)

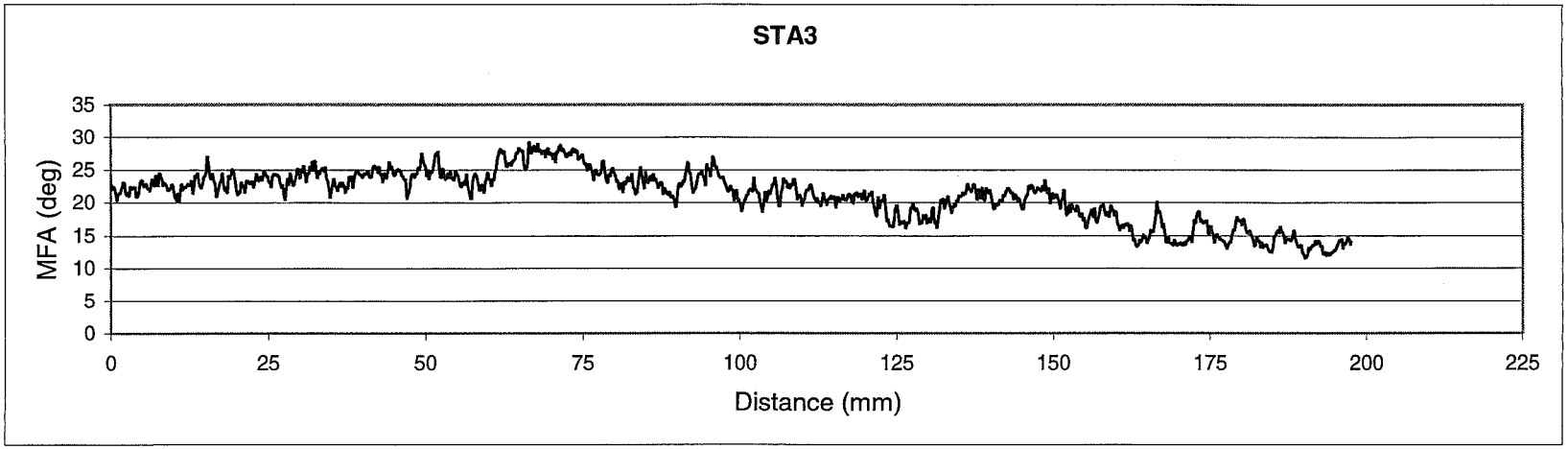
STA3
MFA (deg)
35
30
25
20
15
10
5
0
0
25
50
75
100
125
150
175
200
225
Distance (mm)

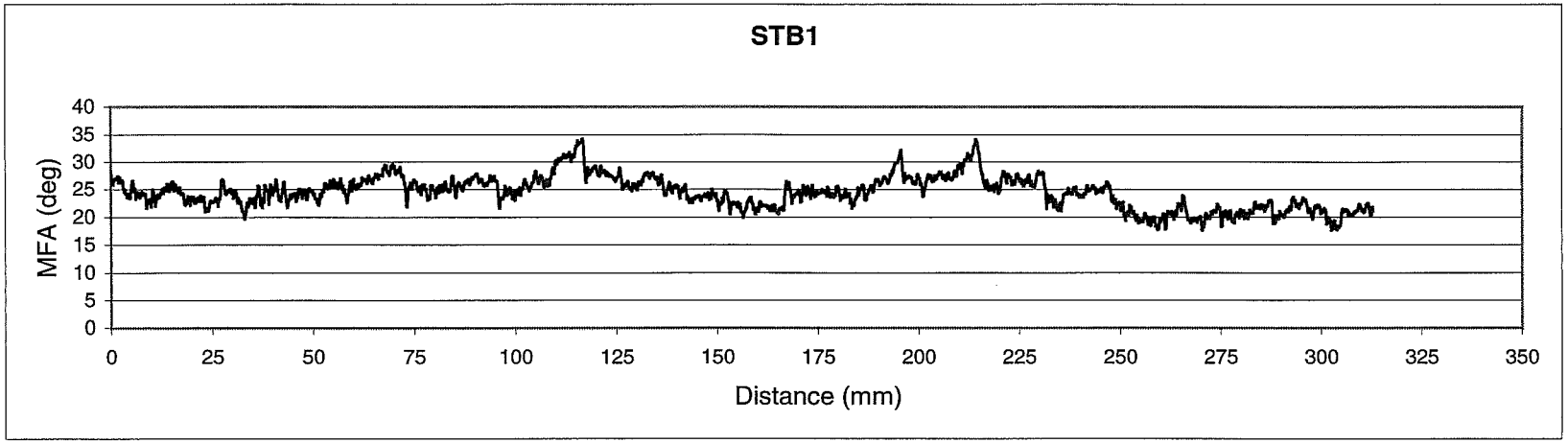
STB1
MFA (deg)
40
35
30
25
20
15
10
5
0
0
25
50
75
100
125
150
175
200
225
250
275
300
325
350
Distance (mm)

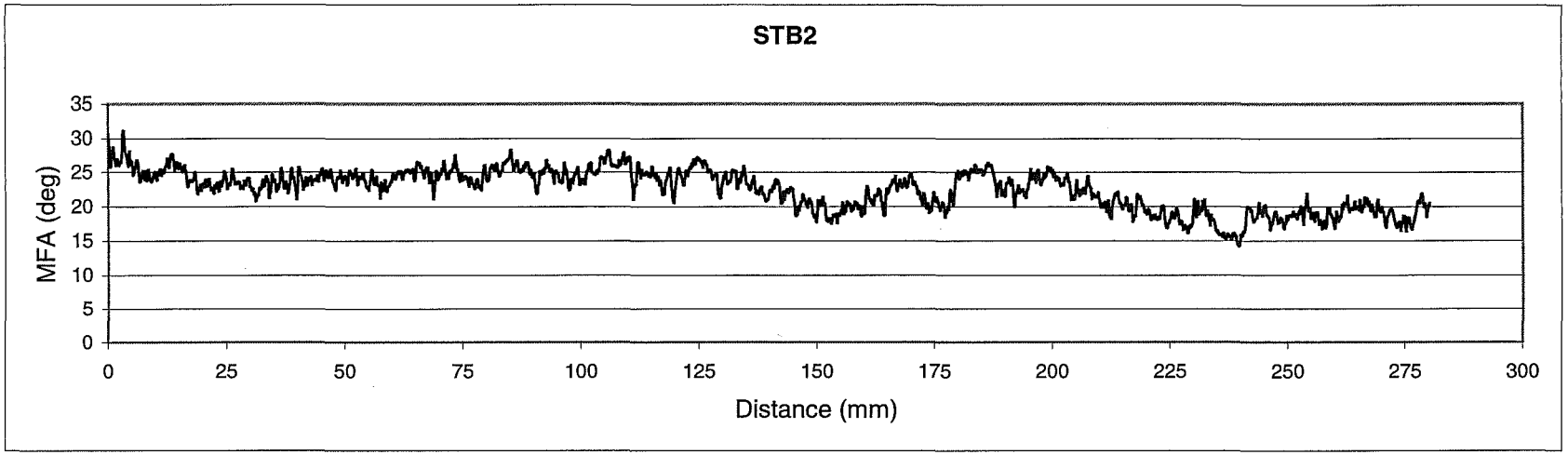
STB2
MFA (deg)
35
30
25
20
15
10
5
0
0
25
50
75
100
125
150
175
200
225
250
275
300
Distance (mm)

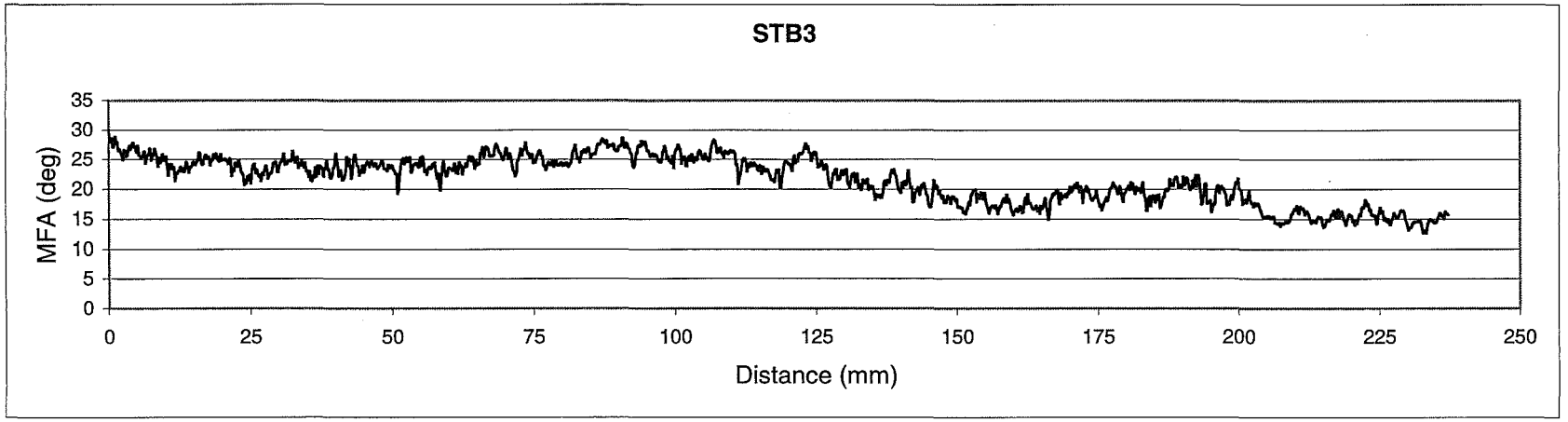
STB3
MFA (deg)
35
30
25
20
15
10
5
0
0
25
50
75
100
125
150
175
200
225
250
Distance (mm)

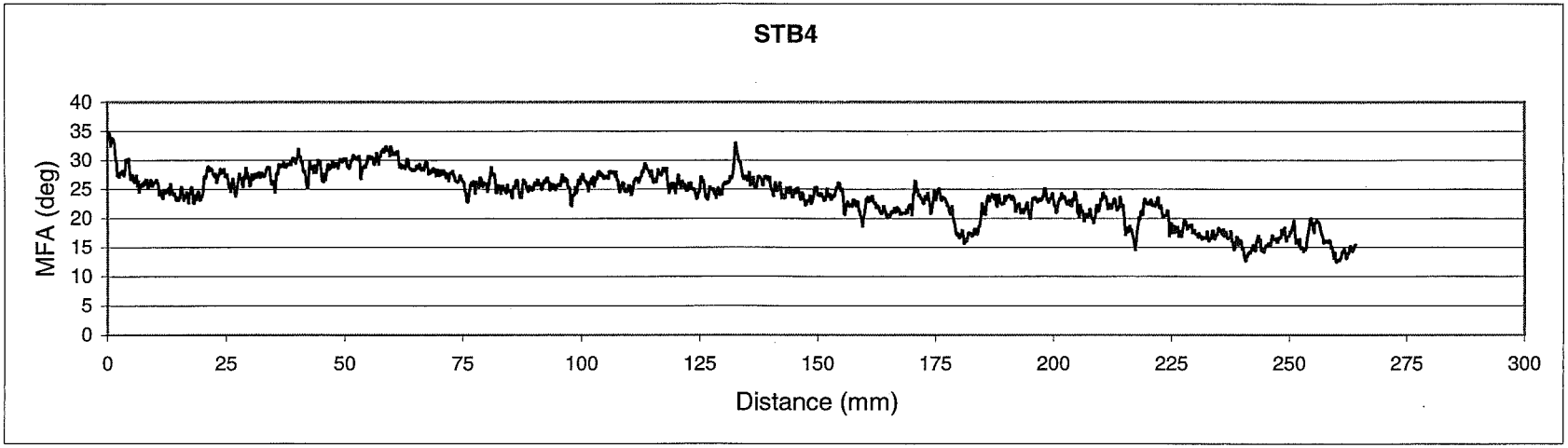
STB4
MFA (deg)
0
5
10
15
20
25
30
35
40
0
25
50
75
100
125
150
175
200
225
250
275
300
Distance (mm)

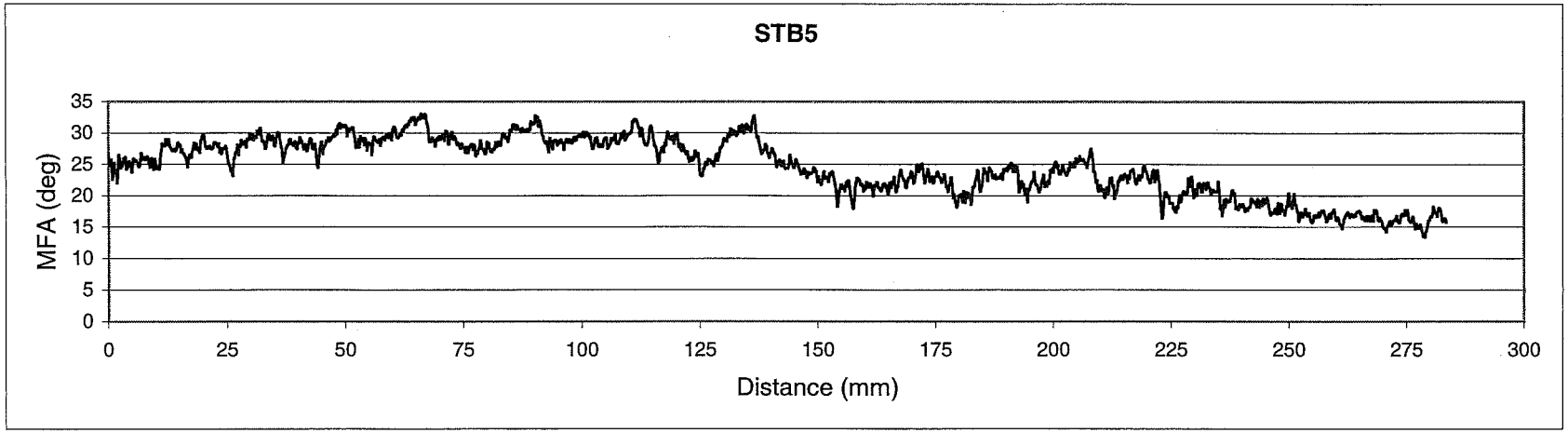
STB5
MFA (deg)
0
5
10
15
20
25
30
35
0
25
50
75
100
125
150
175
200
225
250
275
300
Distance (mm)

H. Spiral grain angle (SGA) vs. radial distance graphs of sixteen specimens

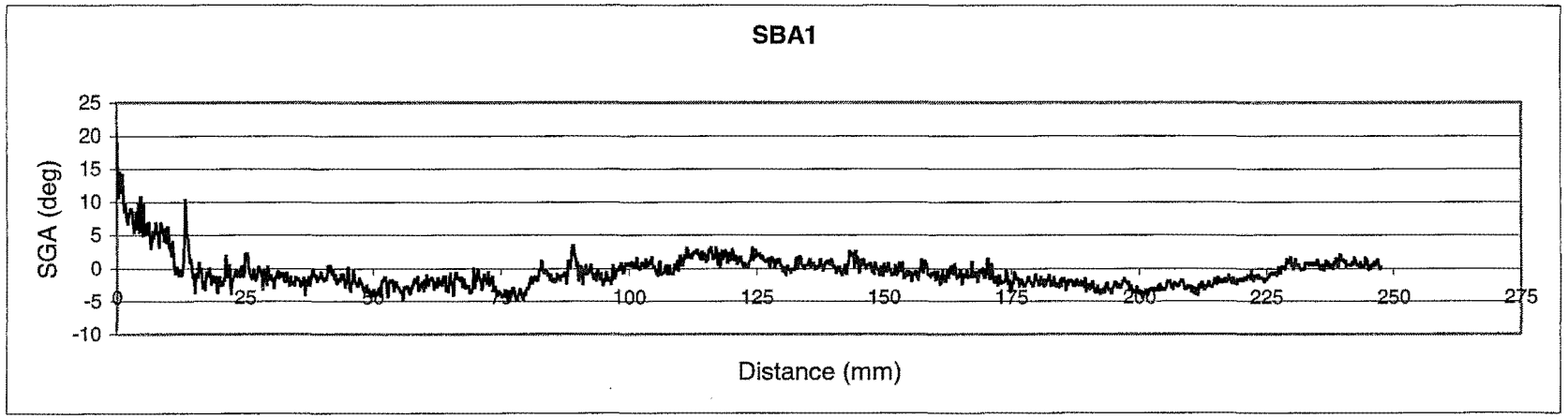

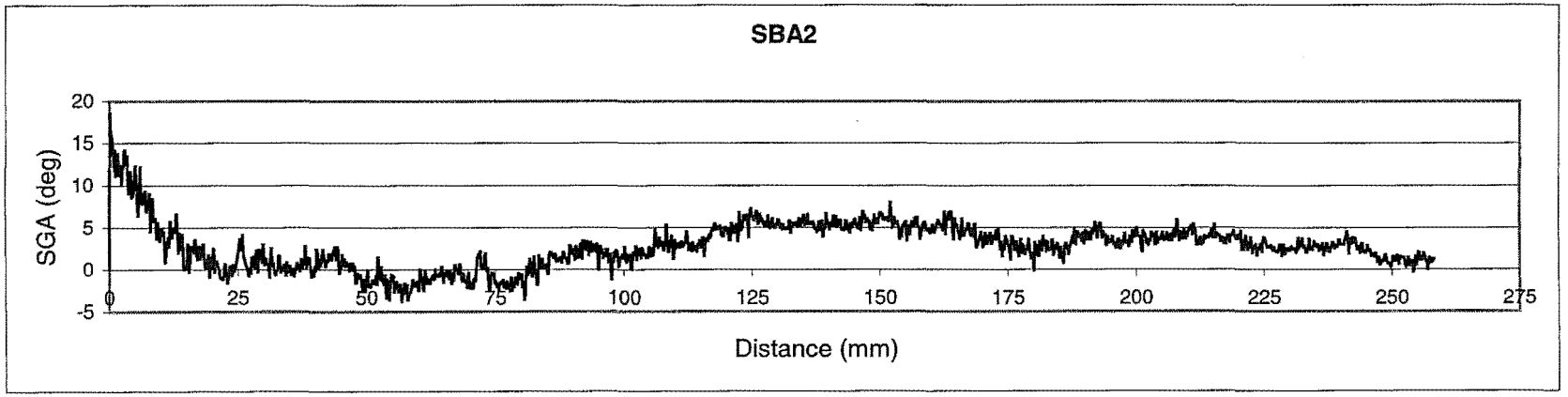

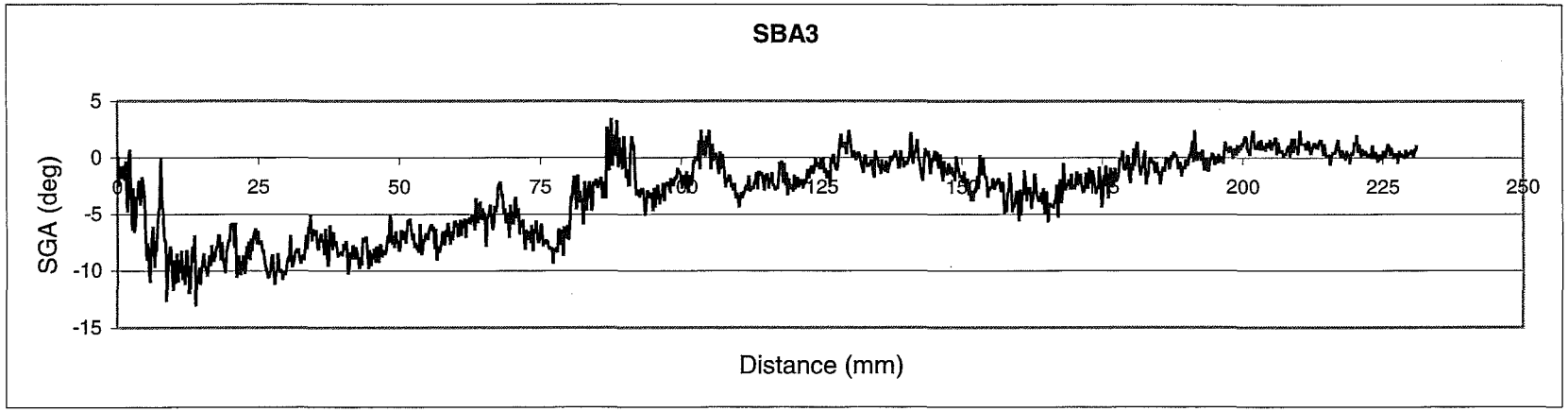
SBA3
SGA (deg)
5
0
-5
-10
-15
0
25
50
75
125
200
225
250
Distance (mm)

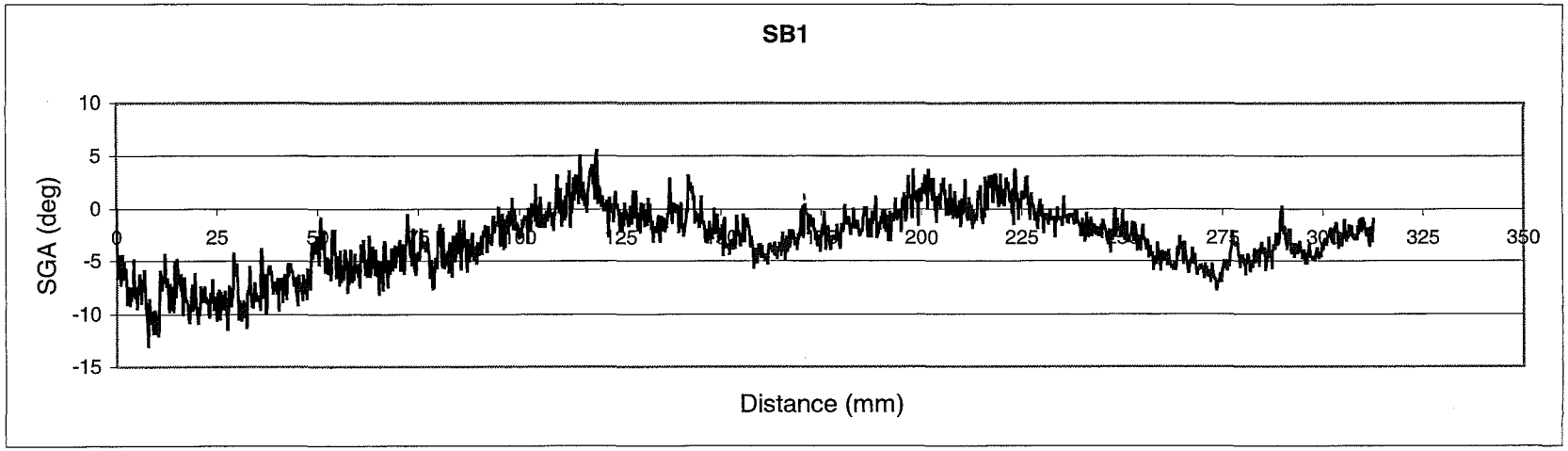
SB1
SGA (deg)
10
5
0
-5
-10
-15
0
25
200
225
325
350
Distance (mm)

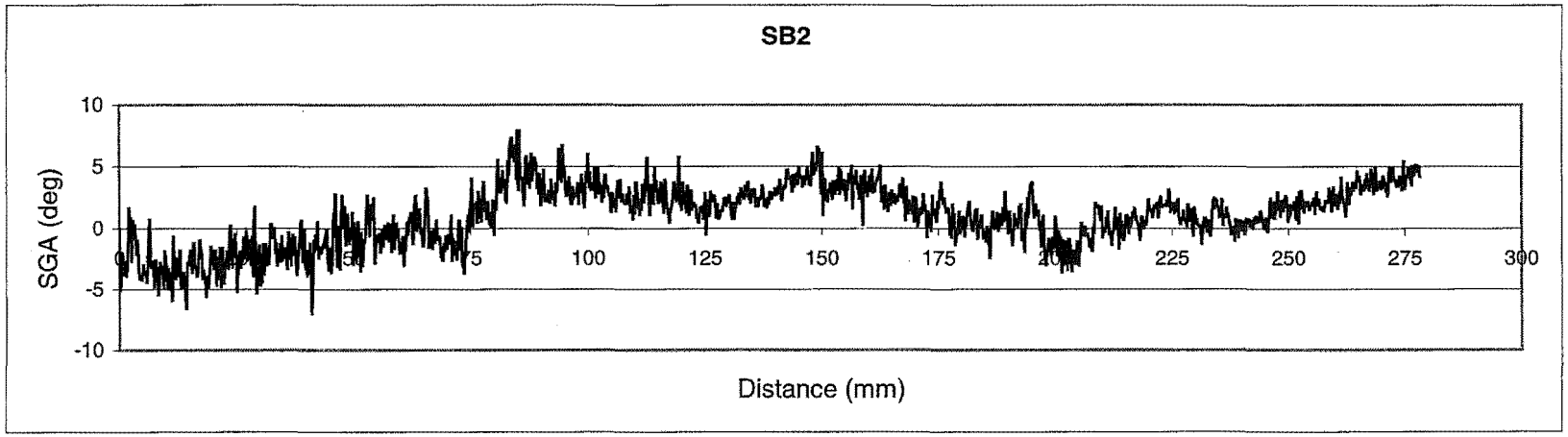
SB2
SGA (deg)
10
5
0
-5
-10
0
100
125
150
175
225
250
275
300
Distance (mm)

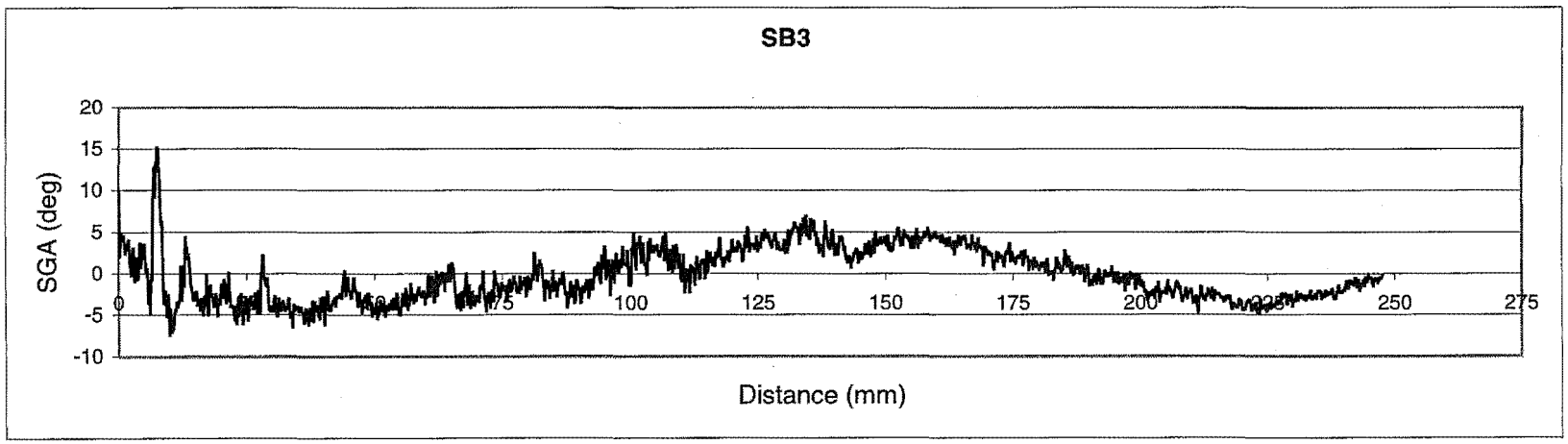
SB3
SGA (deg)
20
15
10
5
0
-5
-10
0
100
125
150
175
200
250
275
Distance (mm)

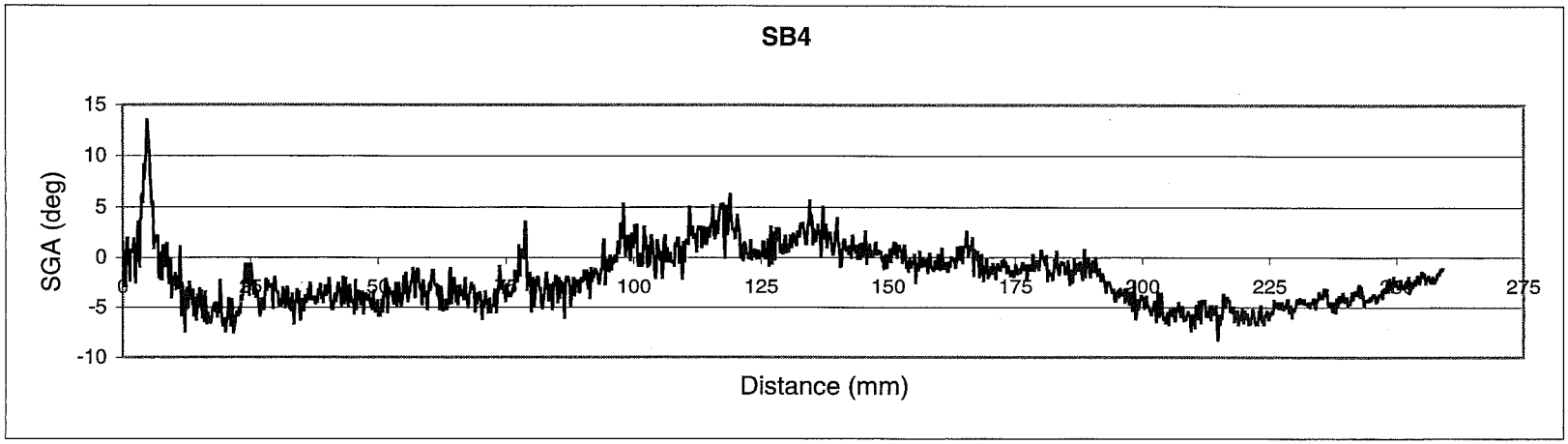
SB4
SGA (deg)
15
10
5
0
-5
-10
0
25
50
100
125
150
175
200
225
275
Distance (mm)

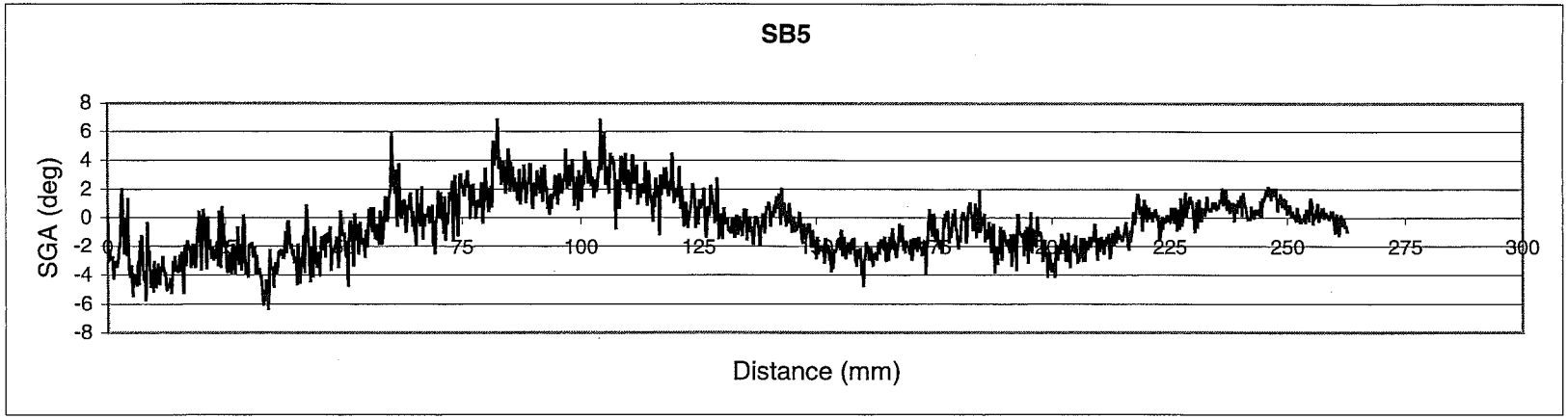
SB5
SGA (deg)
8
6
4
2
0
-2
-4
-6
-8
0
75
100
125
225
250
275
300
Distance (mm)

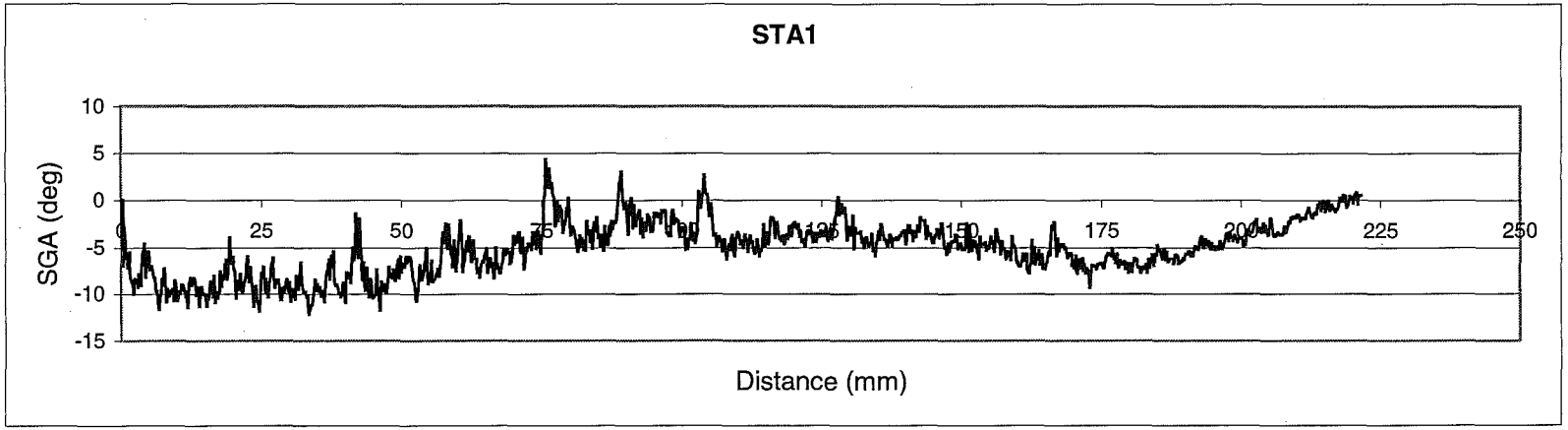
STA1
SGA (deg)
10
5
0
-5
-10
-15
25
50
175
225
250
Distance (mm)

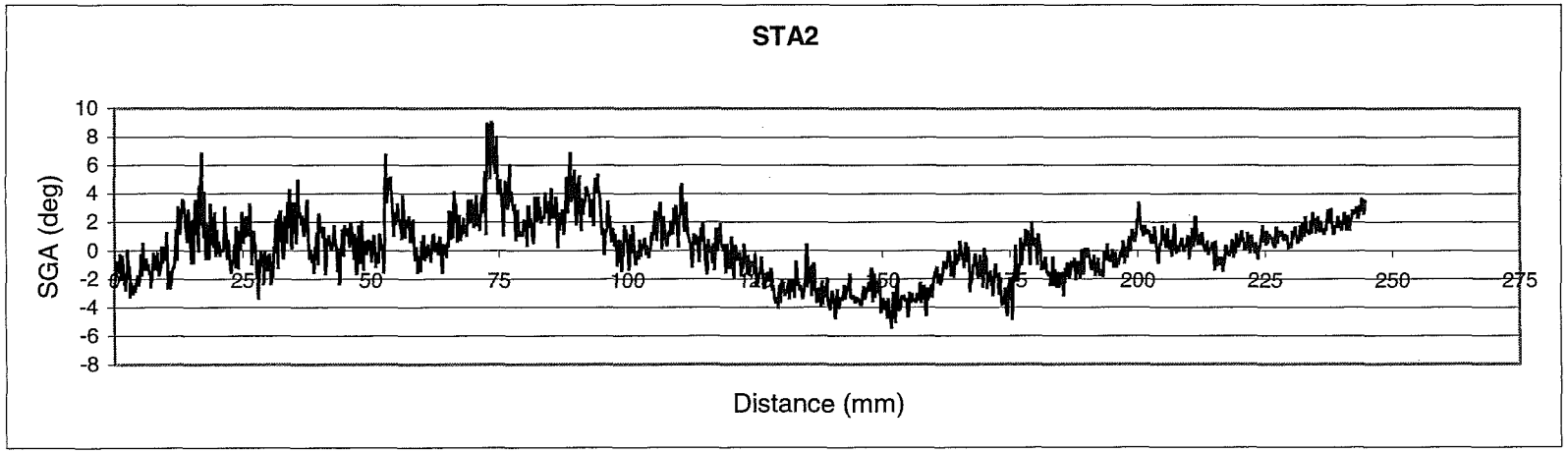
STA2
SGA (deg)
10
8
6
4
2
0
-2
-4
-6
-8
25
50
75
100
200
225
250
275
Distance (mm)

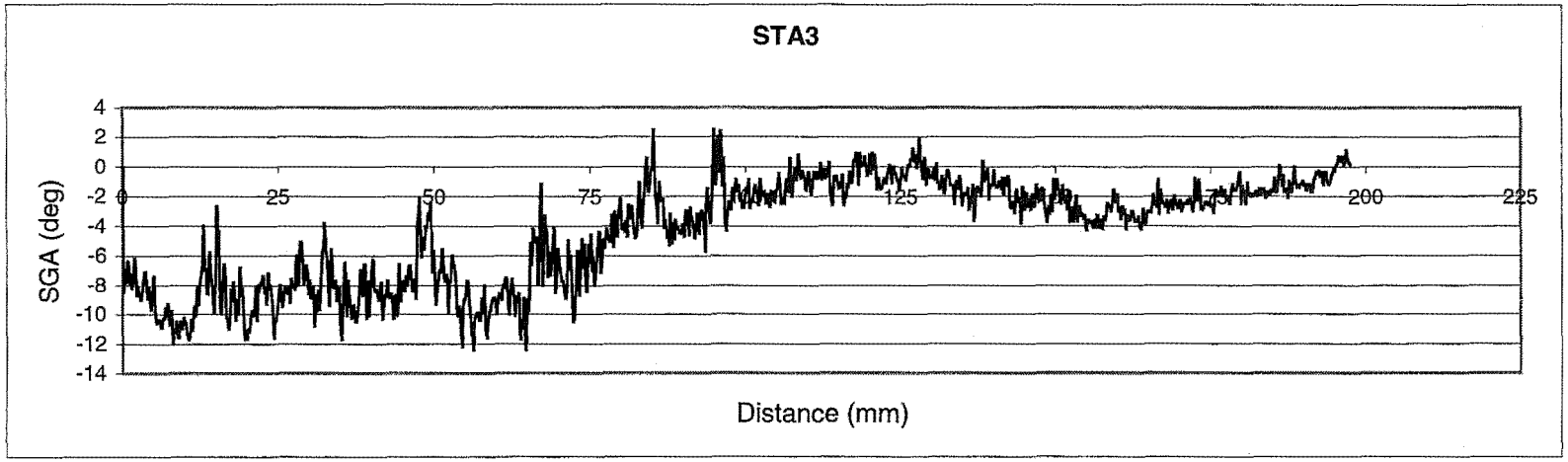
STA3
SGA (deg)
4
2
0
-2
-4
-6
-8
-10
-12
-14
0
25
50
75
125
200
225
Distance (mm)

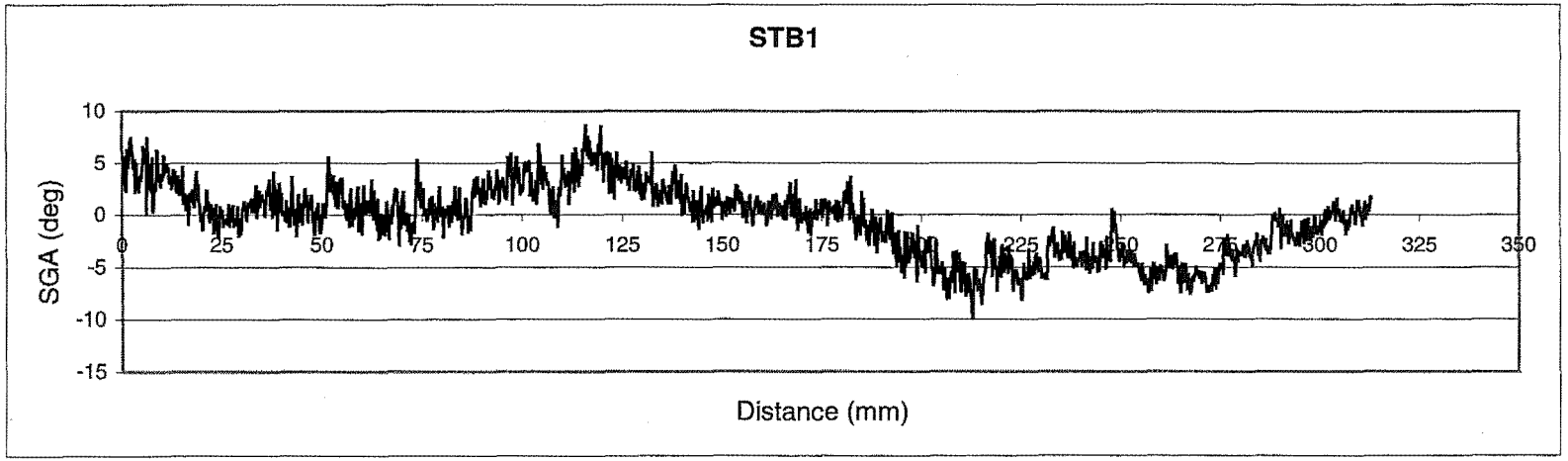
STB1
SGA (deg)
10
5
0
-5
-10
-15
0
25
50
75
100
125
150
175
225
300
325
350
Distance (mm)

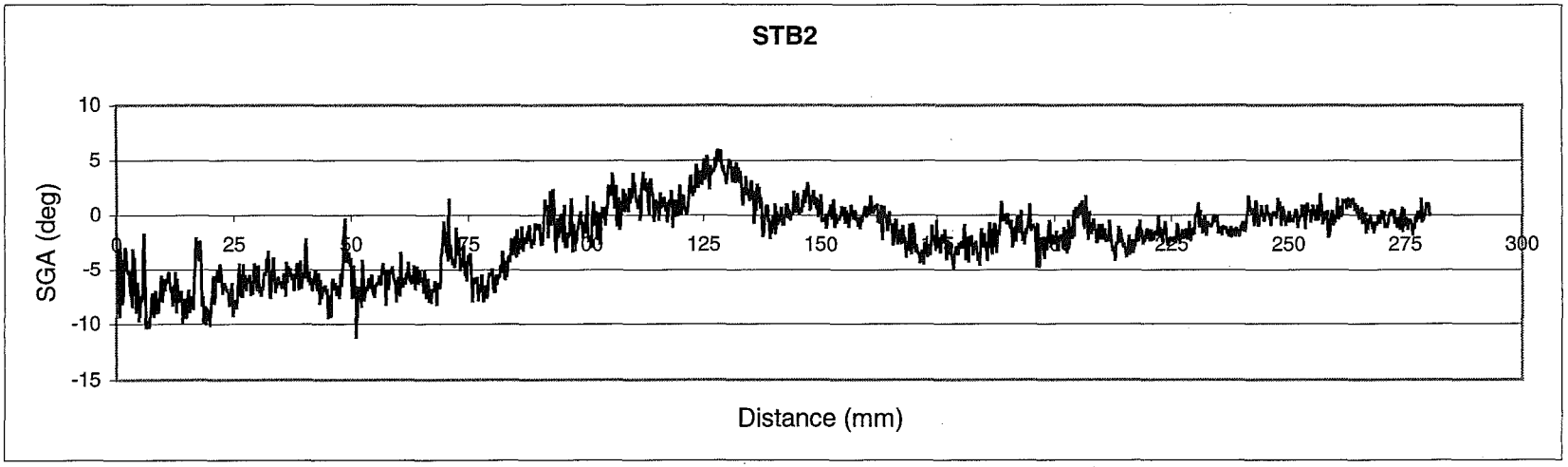
STB2
SGA (deg)
10
5
0
-5
-10
-15
0
25
50
75
100
125
150
225
250
275
300
Distance (mm)

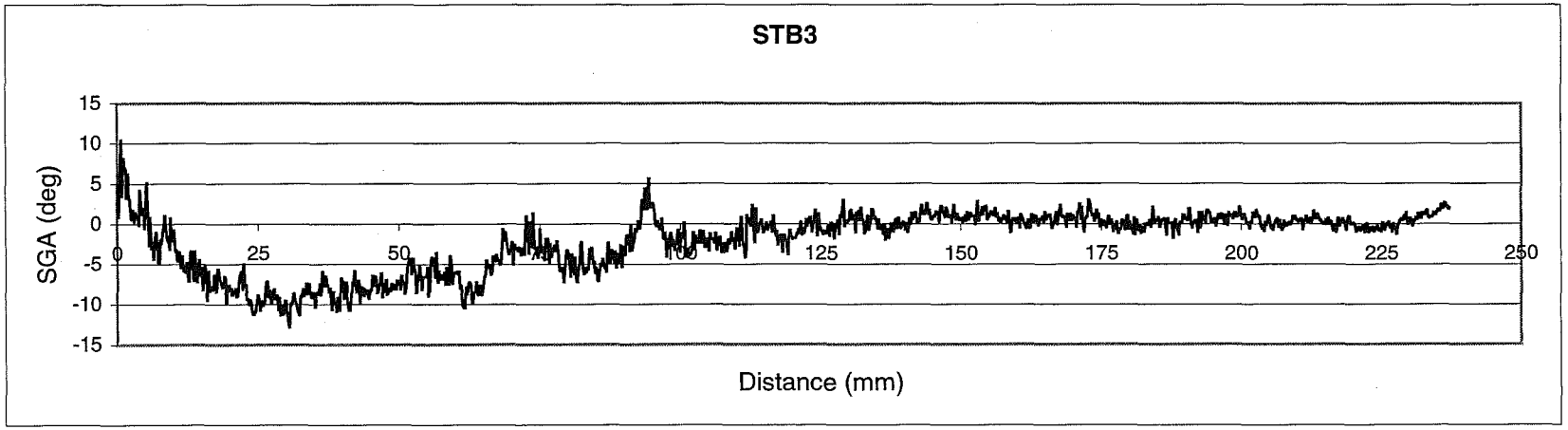
STB3
SGA (deg)
15
10
5
0
-5
-10
-15
0
25
50
125
150
175
200
225
250
Distance (mm)

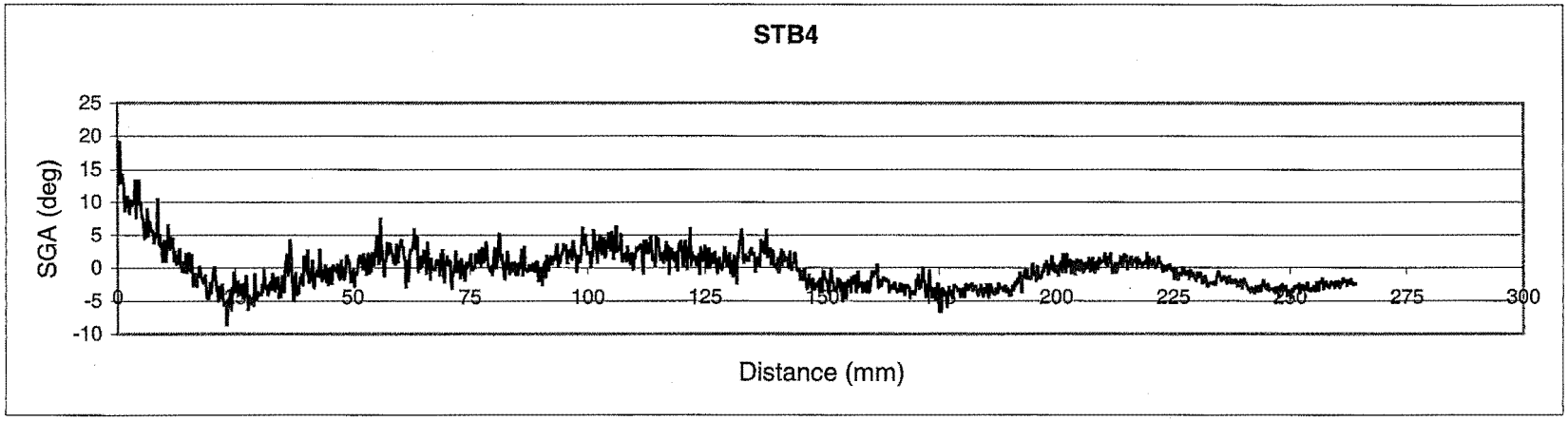
STB4
SGA (deg)
25
20
15
10
5
0
-5
-10
0
25
50
75
100
125
150
200
225
250
275
300
Distance (mm)

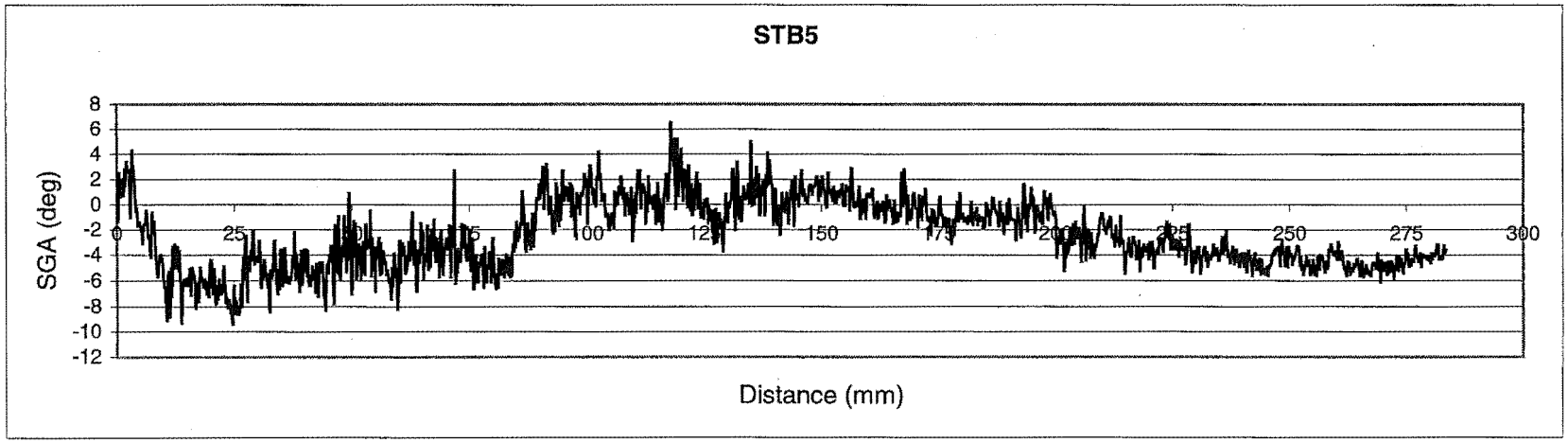
STB5
SGA (deg)
8
6
4
2
0
-2
-4
-6
-8
-10
-12
0
25
250
275
300
Distance (mm)

I. Deformed and undeformed FE meshes of twenty boards

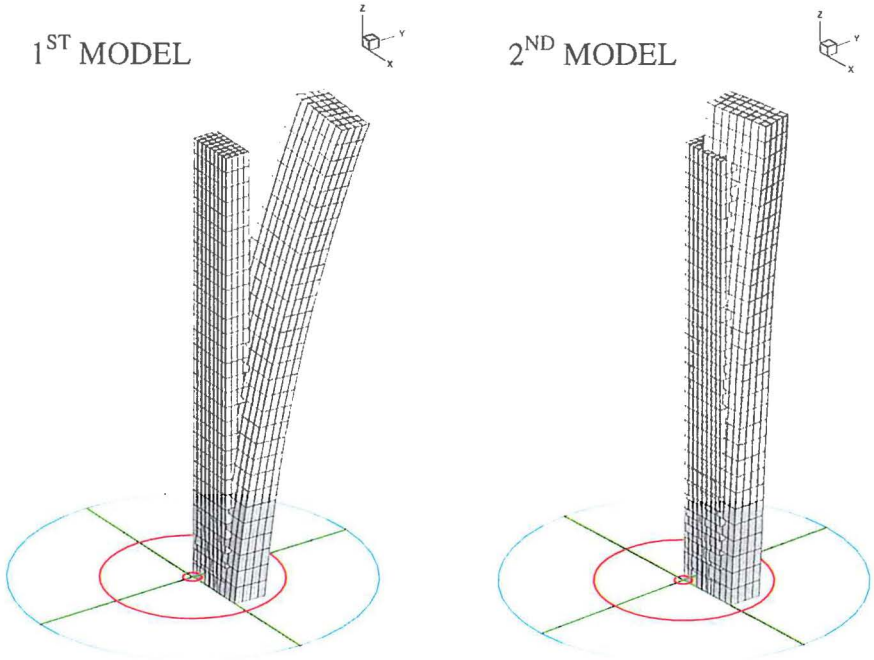

Figure I1. Deformed and undeformed FE meshes of board B1.

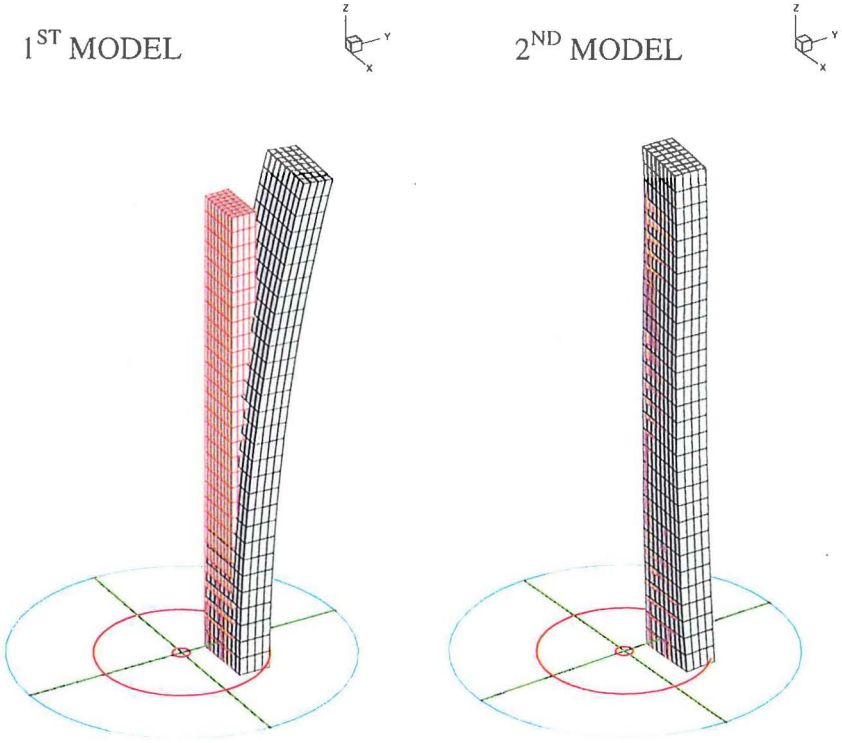

Figure I2. Deformed and undeformed FE meshes of board B2.

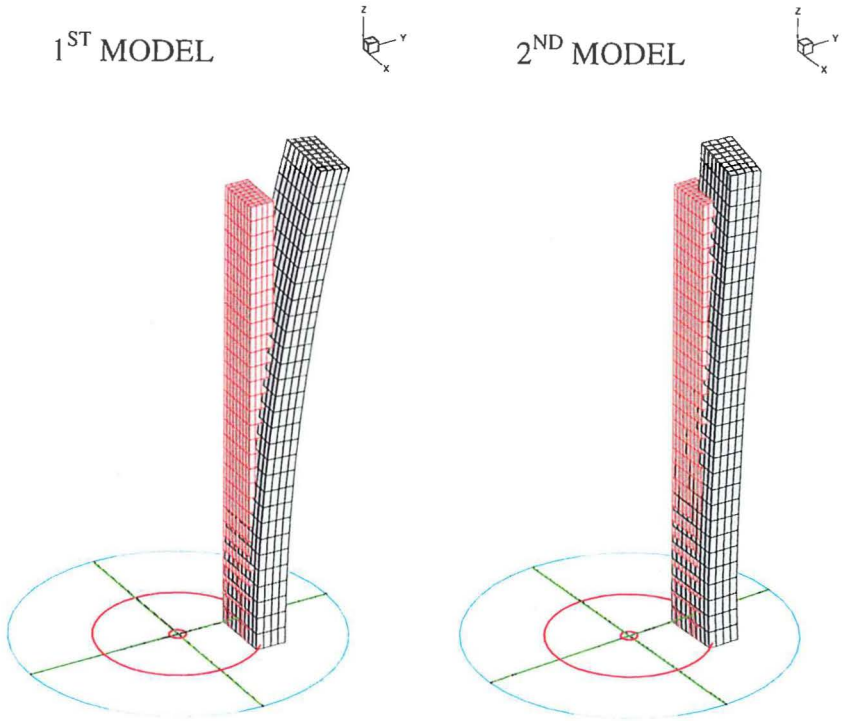

Figure I3. Deformed and undeformed FE meshes of board B3.

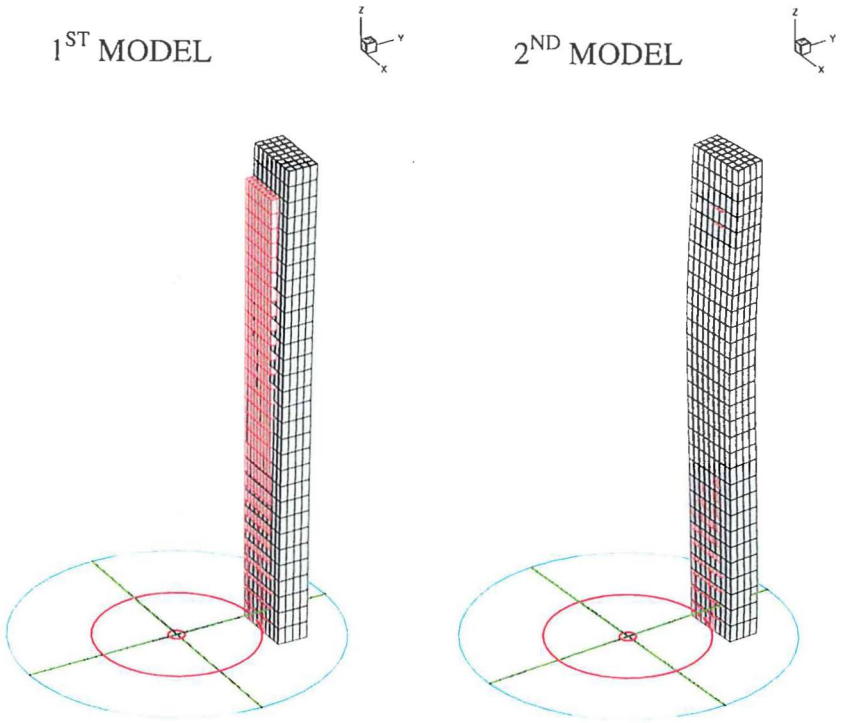

Figure I4. Deformed and undeformed FE meshes of board B4.

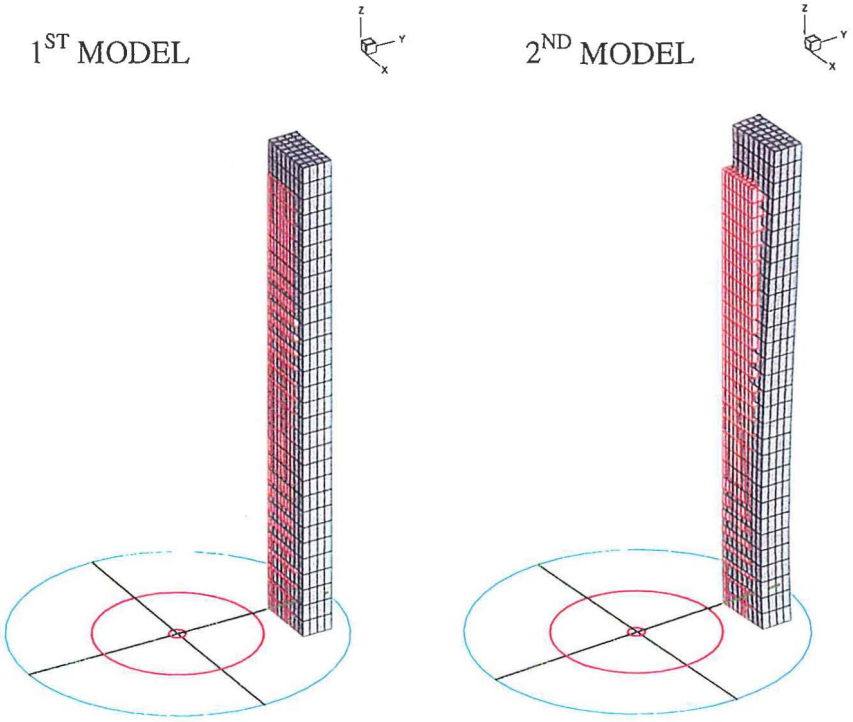

Figure I5. Deformed and undeformed FE meshes of board B5

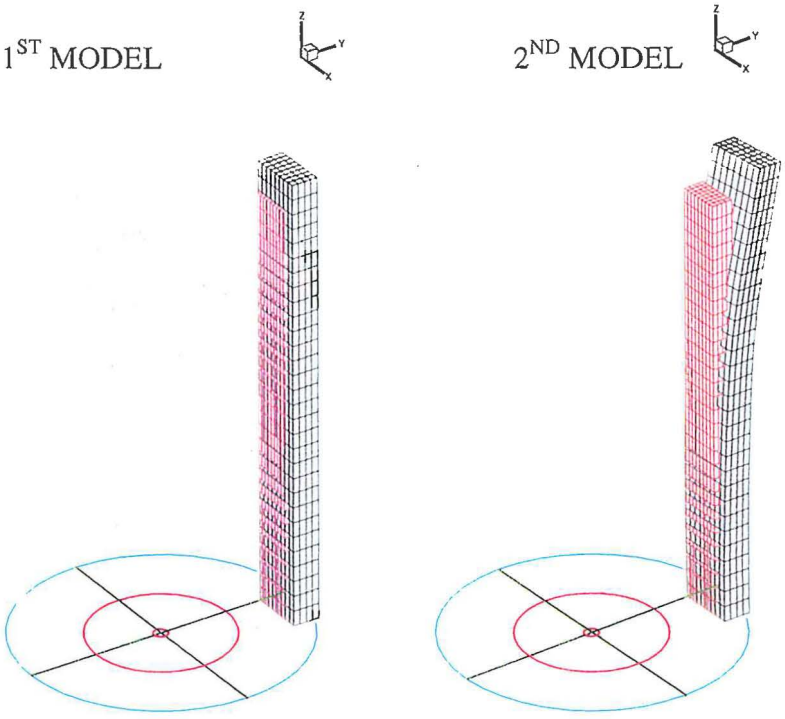

Figure I6. Deformed and undeformed FE meshes of board B6

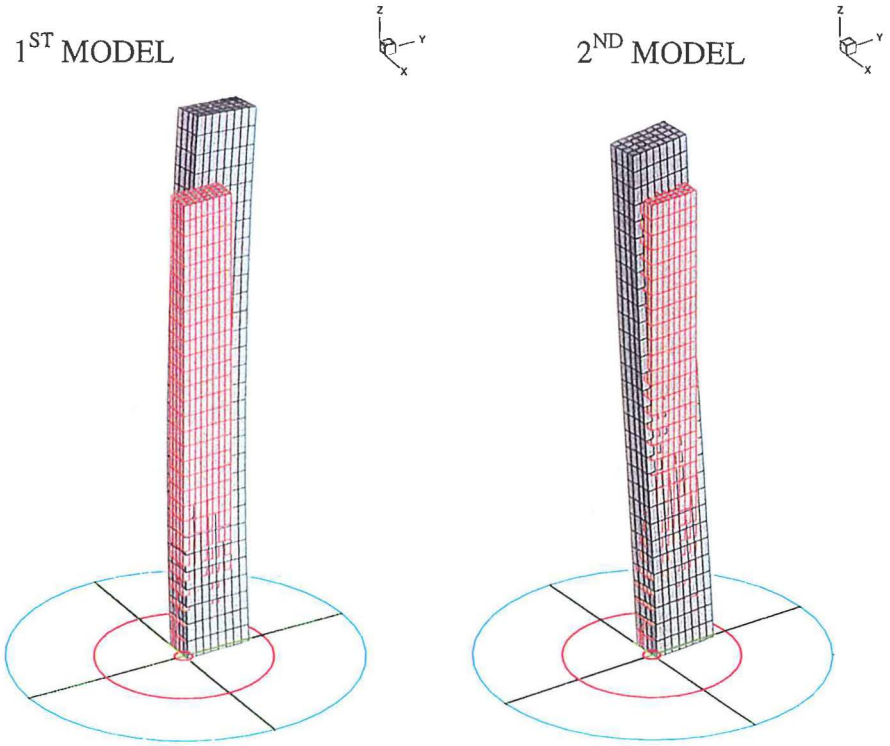

Figure I7. Deformed and undeformed FE meshes of board B7

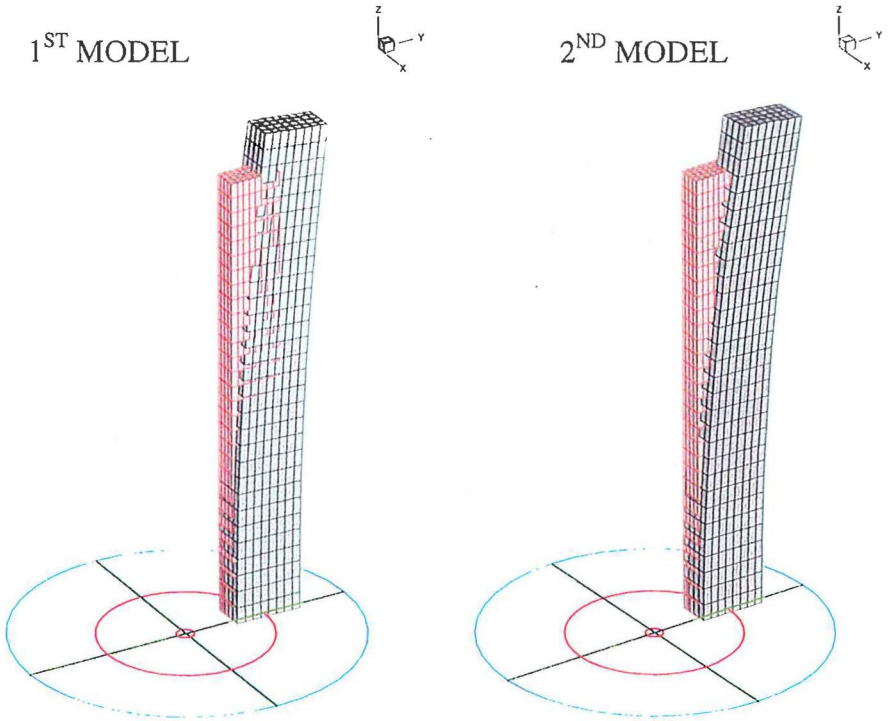

Figure I8. Deformed and undeformed FE meshes of board B8

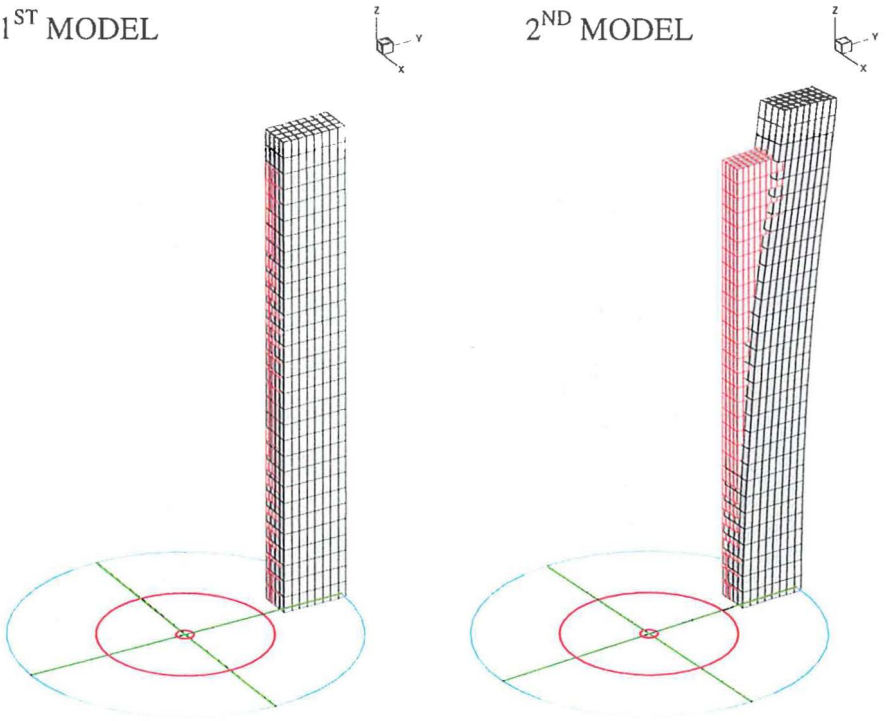

Figure I9. Deformed and undeformed FE meshes of board B9

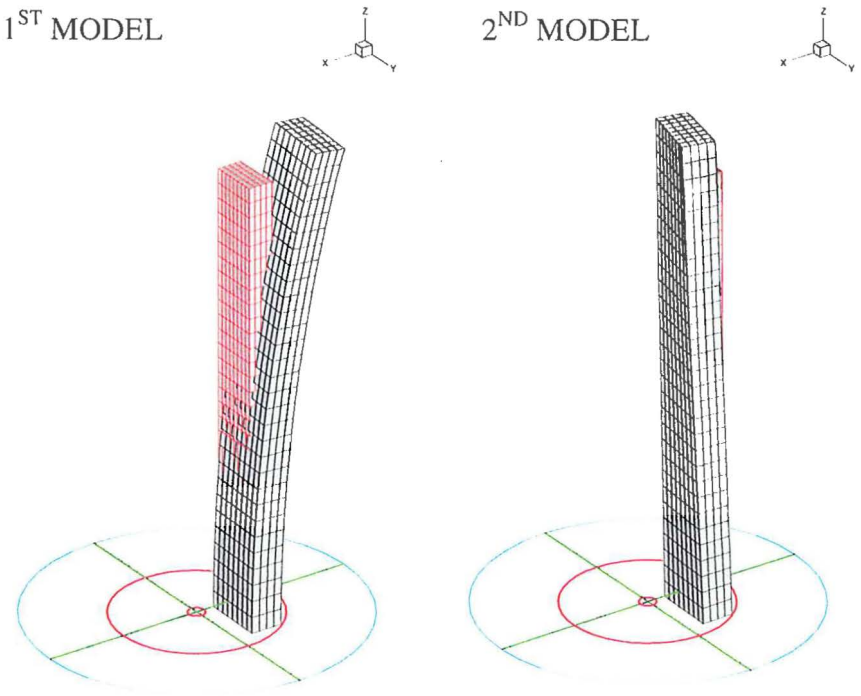

Figure I10. Deformed and undeformed FE meshes of board B10

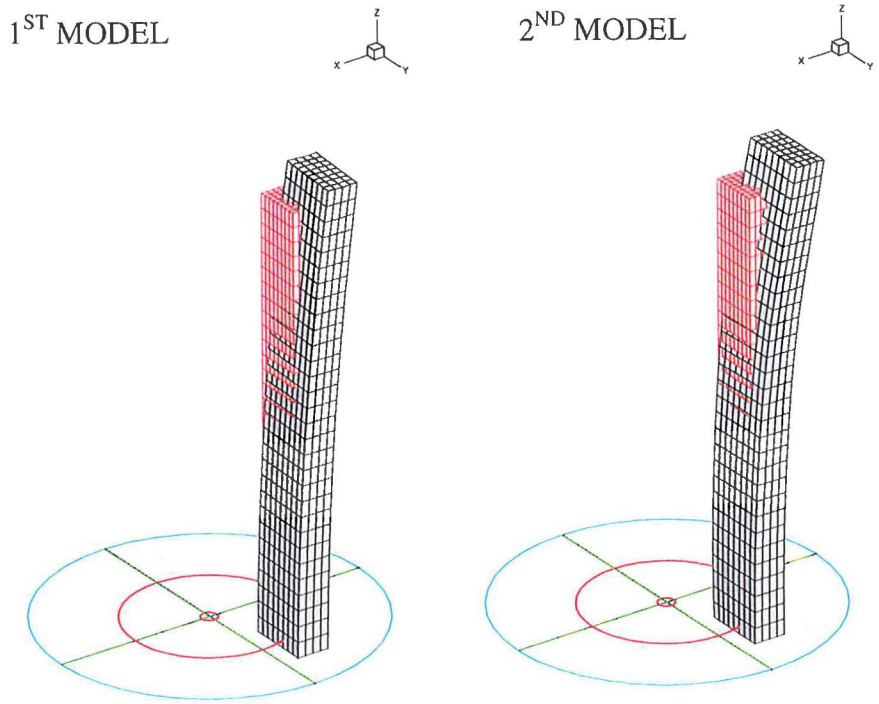

Figure I11. Deformed and undeformed FE meshes of board B11

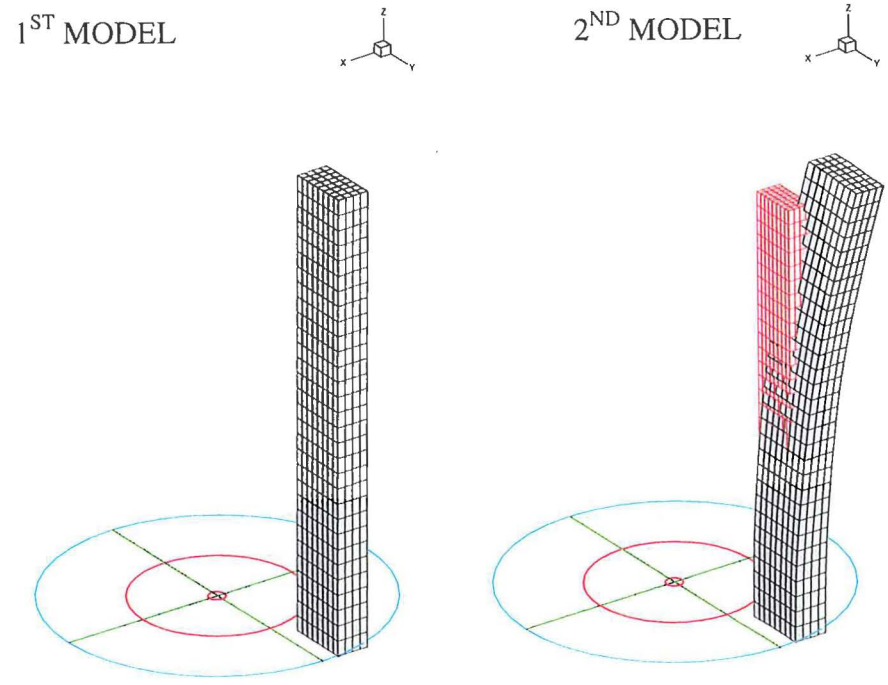

Figure I12. Deformed and undeformed FE meshes of board B12

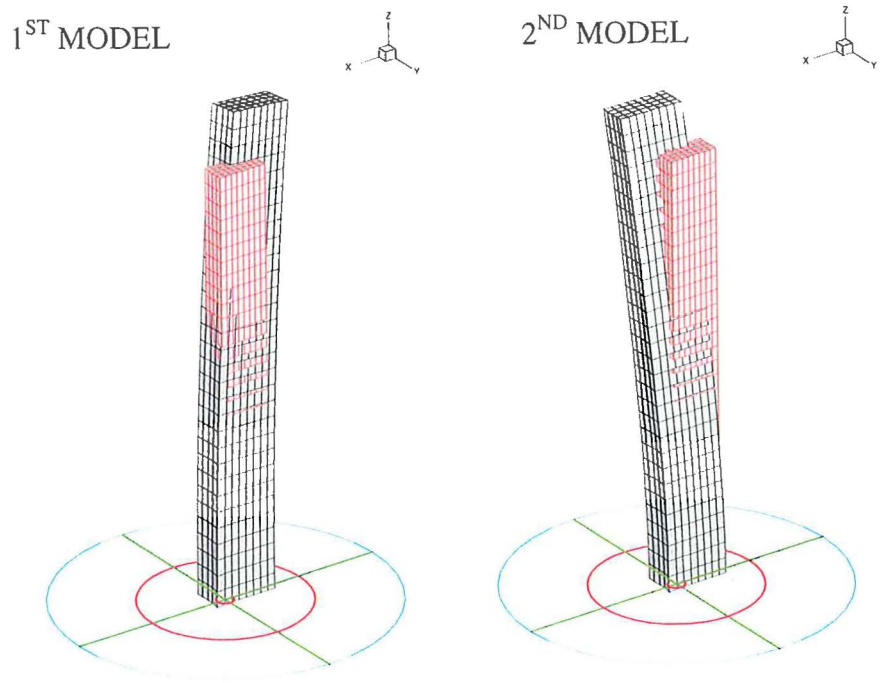

Figure I13. Deformed and undeformed FE meshes of board BA1

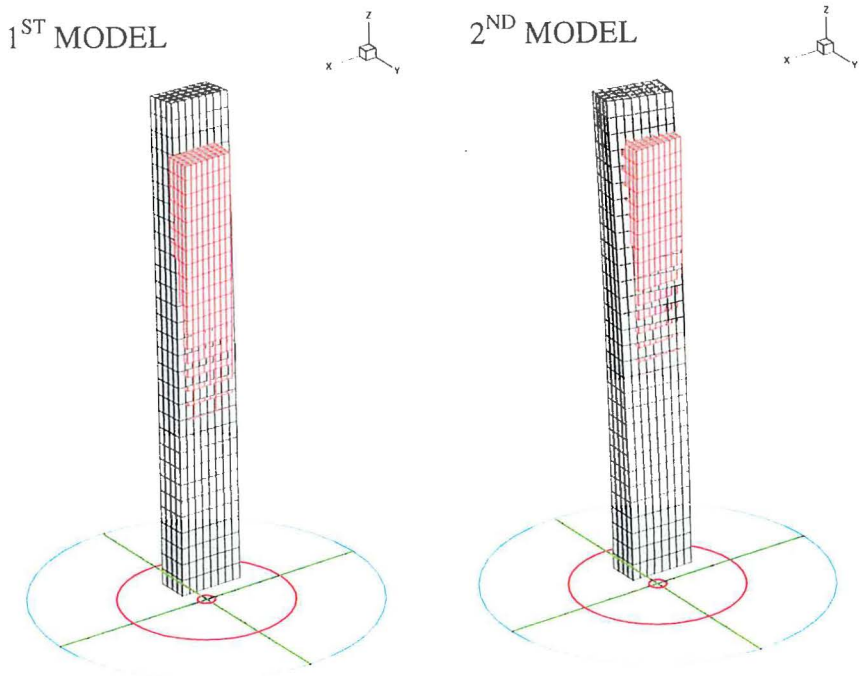

Figure I14. Deformed and undeformed FE meshes of board BA2

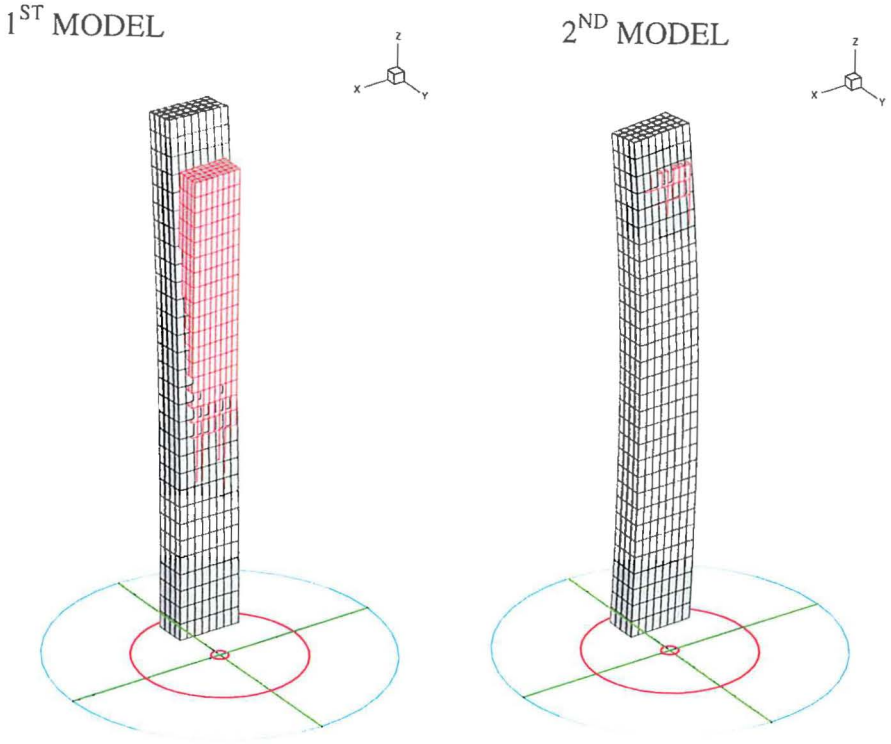

Figure I15. Deformed and undeformed FE meshes of board BA3

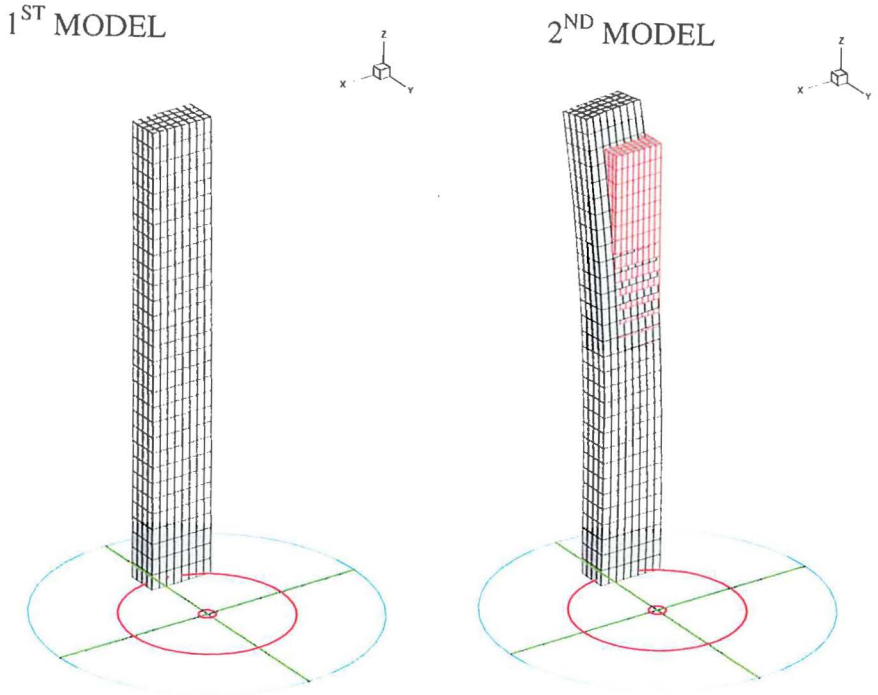

Figure I16. Deformed and undeformed FE meshes of board BA4

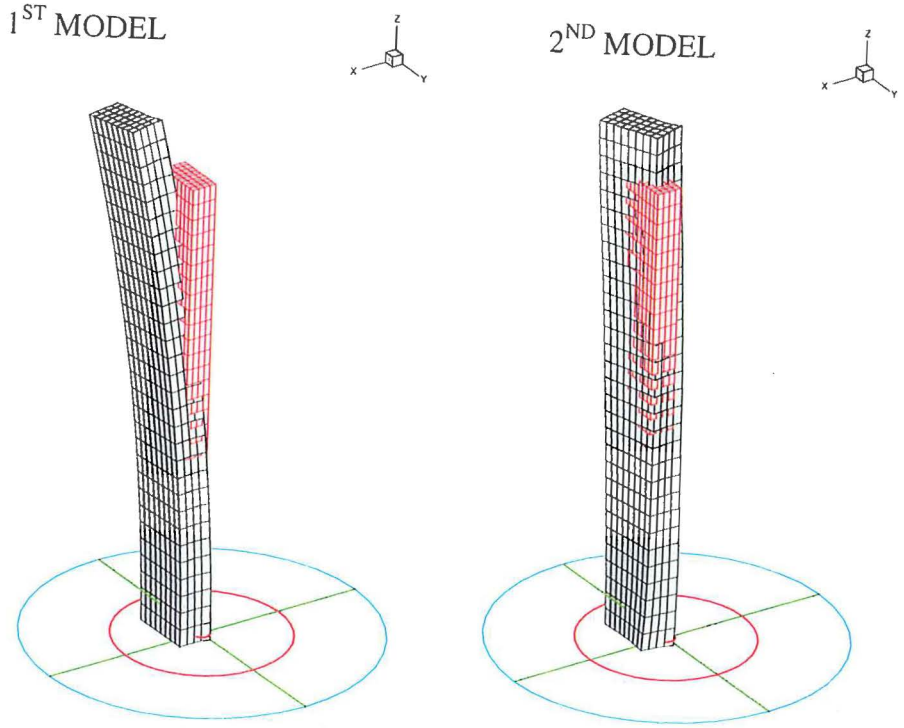

Figure I17. Deformed and undeformed FE meshes of board BA5

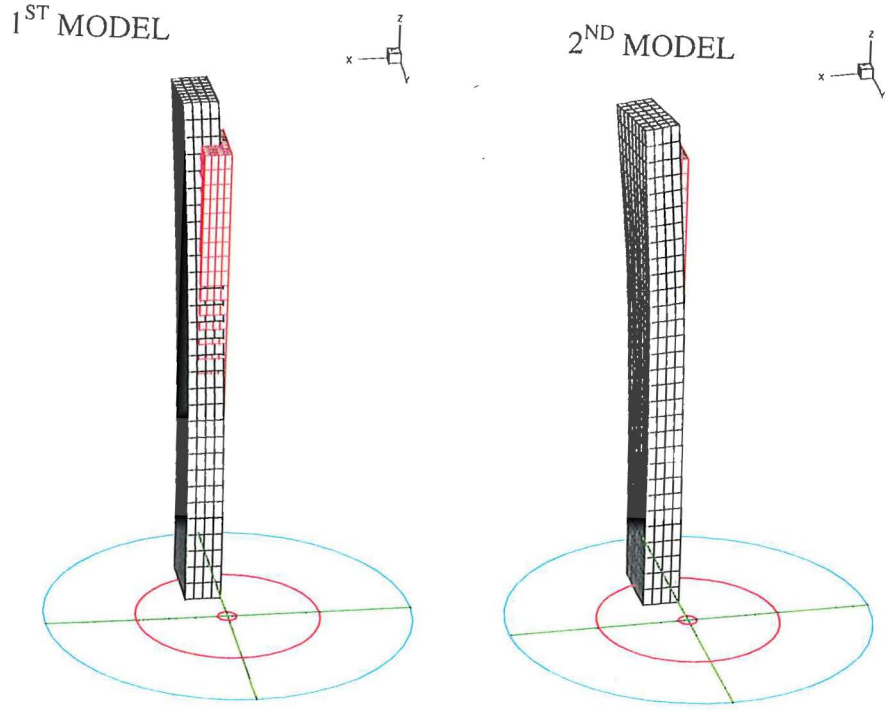

Figure I18. Deformed and undeformed FE meshes of board BA6

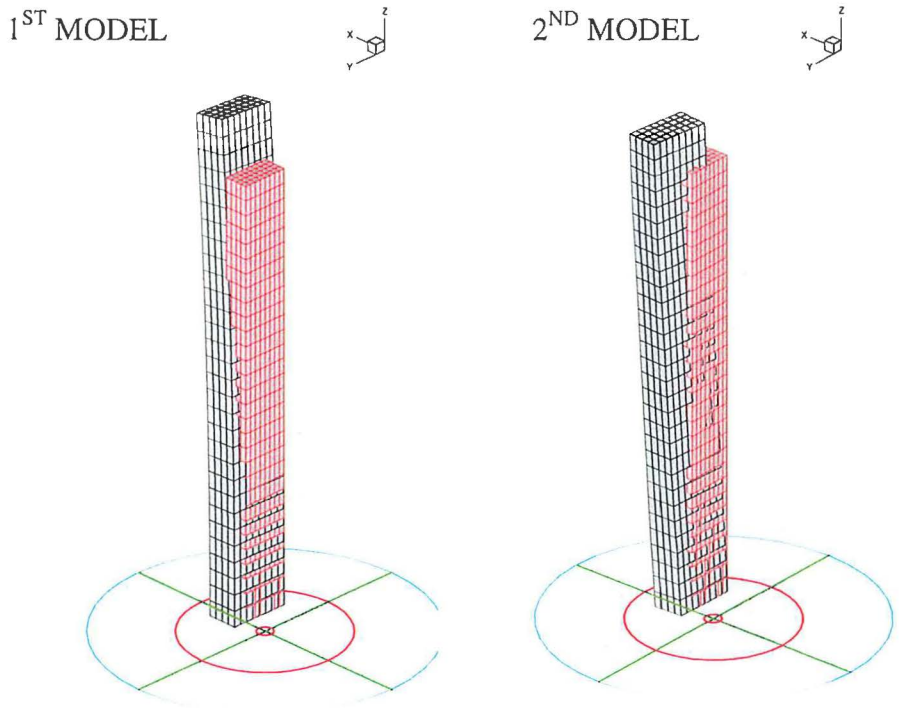

Figure I19. Deformed and undeformed FE meshes of board BA7

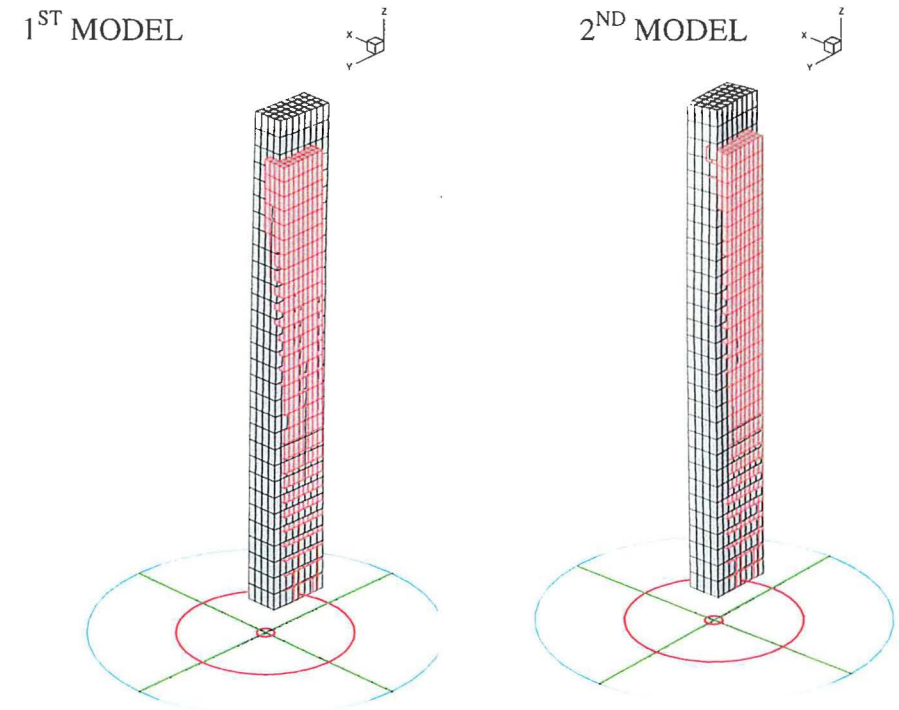

Figure I20. Deformed and undeformed FE meshes of board BA8

J. Contour plots of board B1

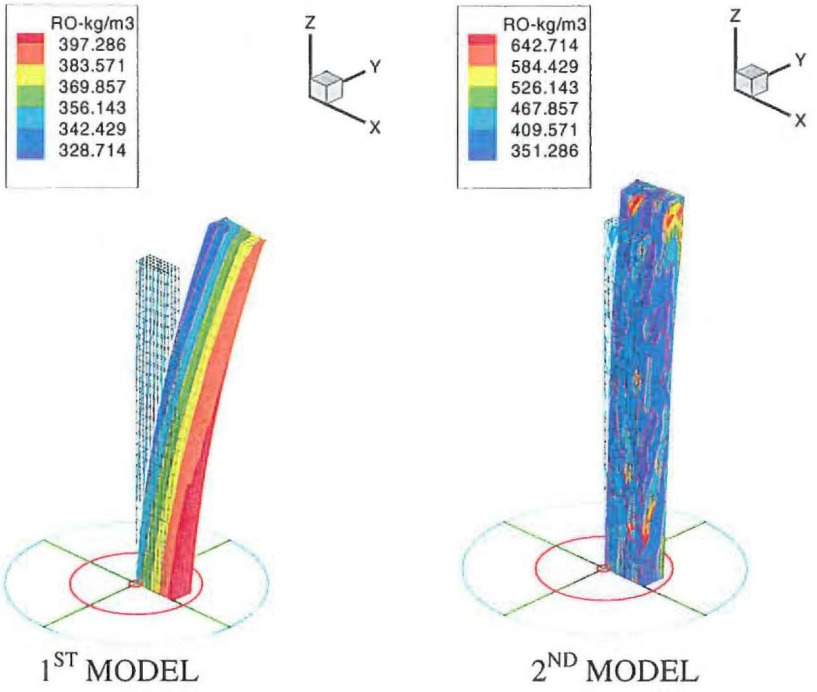

Figure J1. Distribution of density (RO) in board B1.

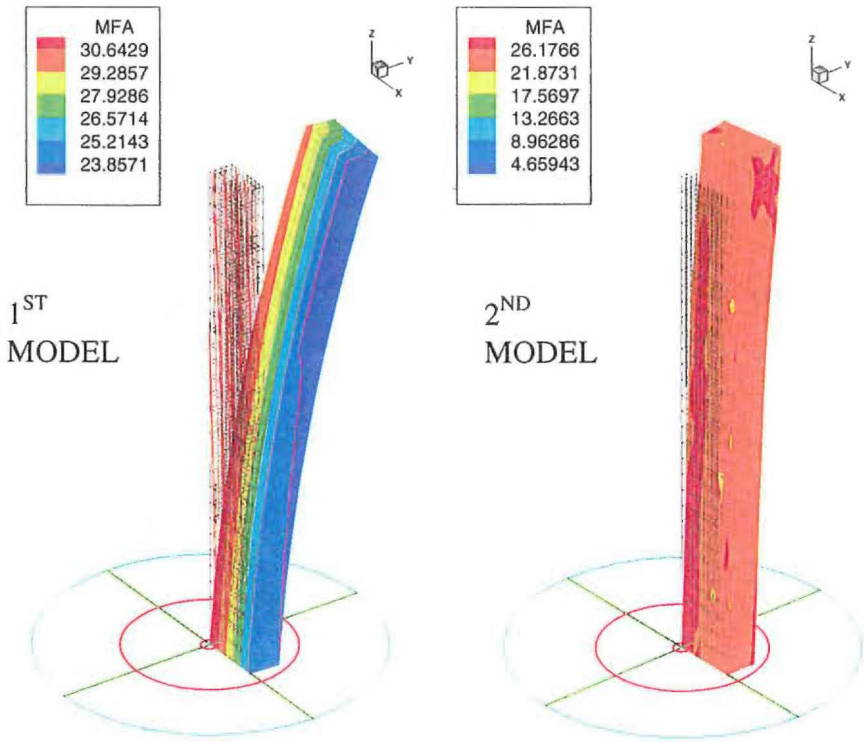

Figure J2. Distribution of microfibril angle (MFA) in board B1.

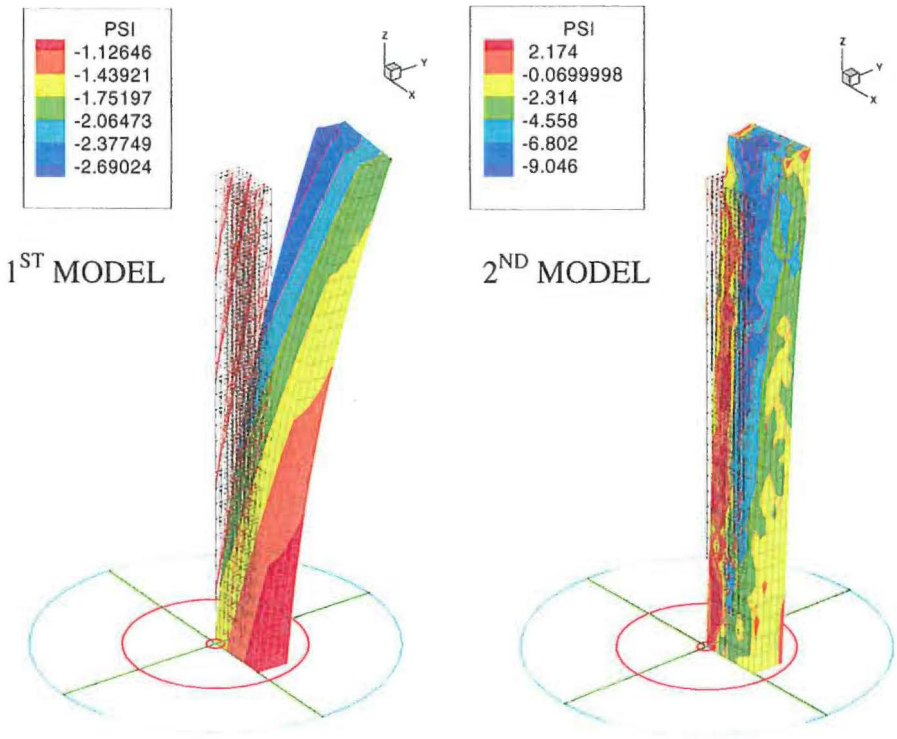

Figure J3. Distribution of spiral grain angle (PSI) in board B1.

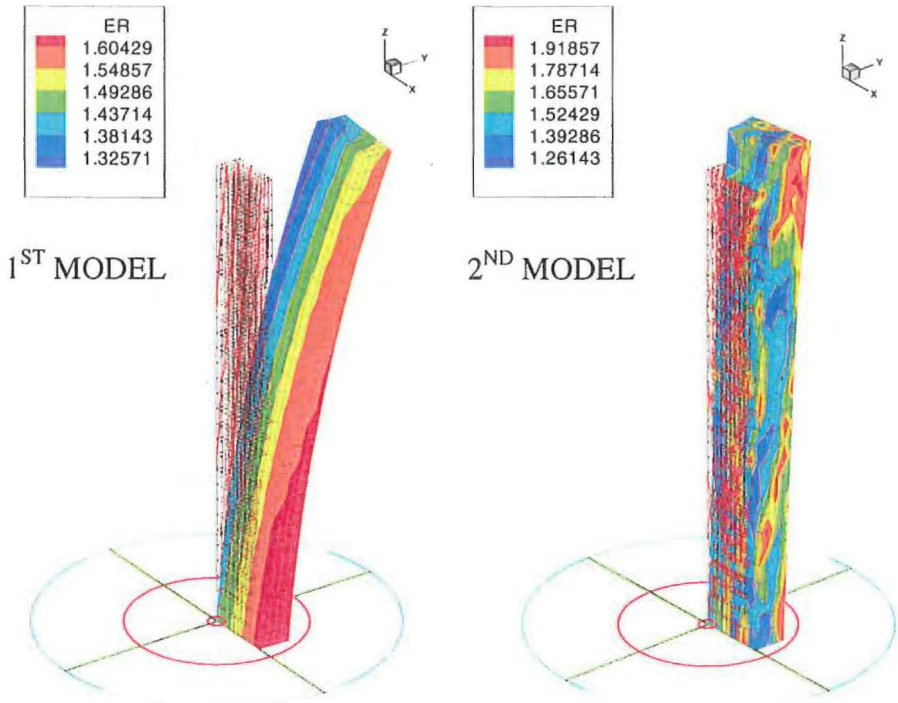

J4. Distribution of elastic modulus in the radial direction (ER) in board B1.

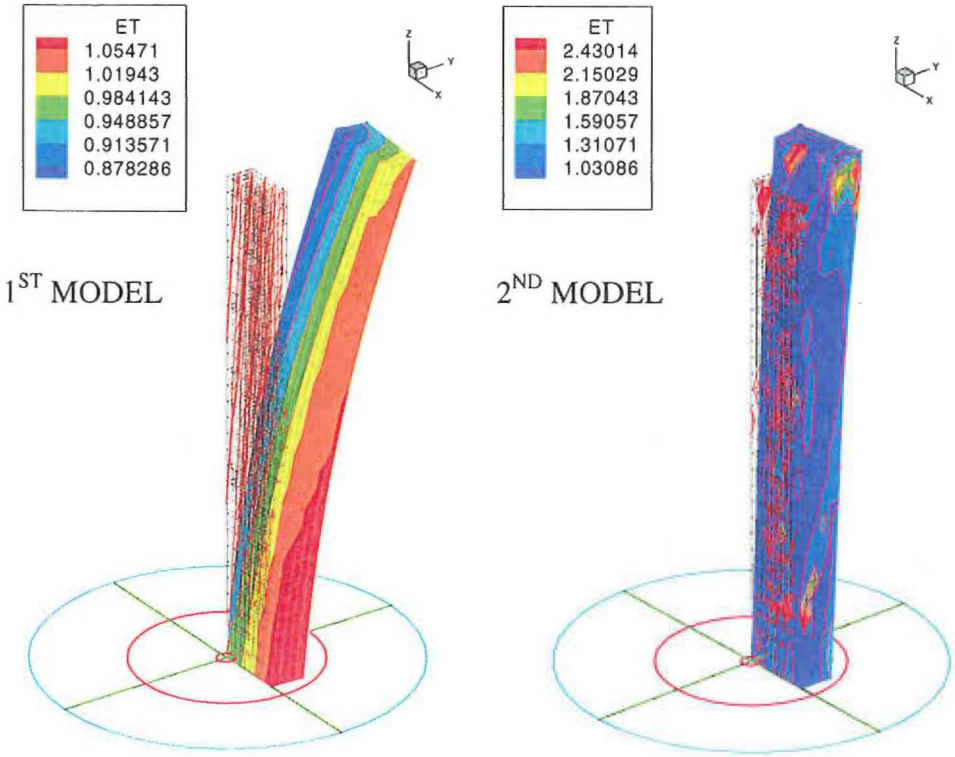

Figure J5. Distribution of elastic modulus in the tangential direction (ET) in board B1.

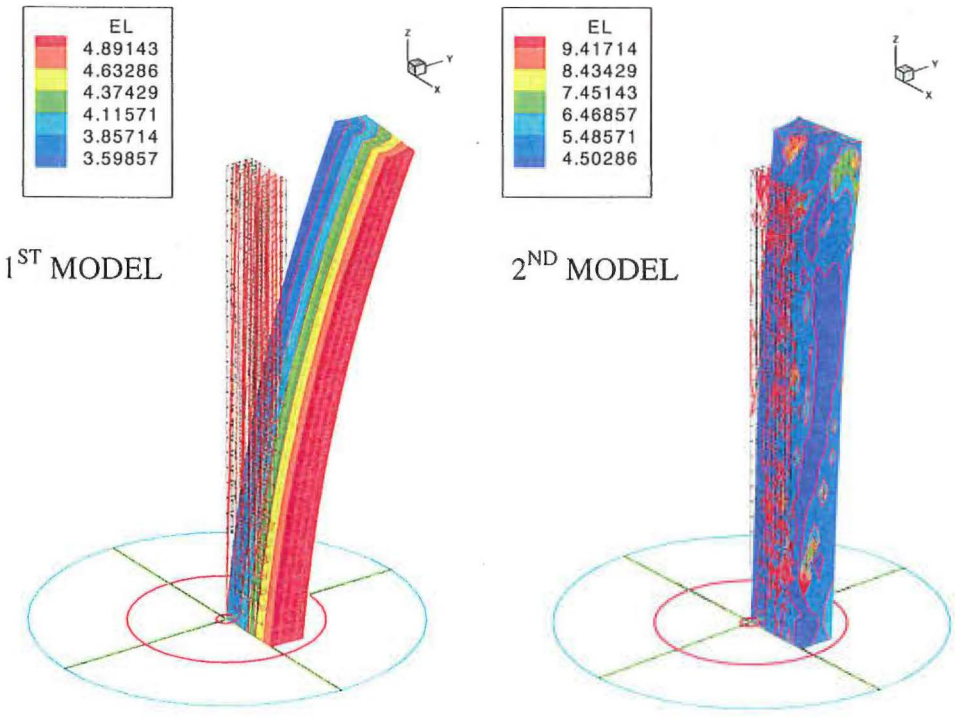

Figure J6. Distribution of elastic modulus in the longitudinal direction EL in board B1.

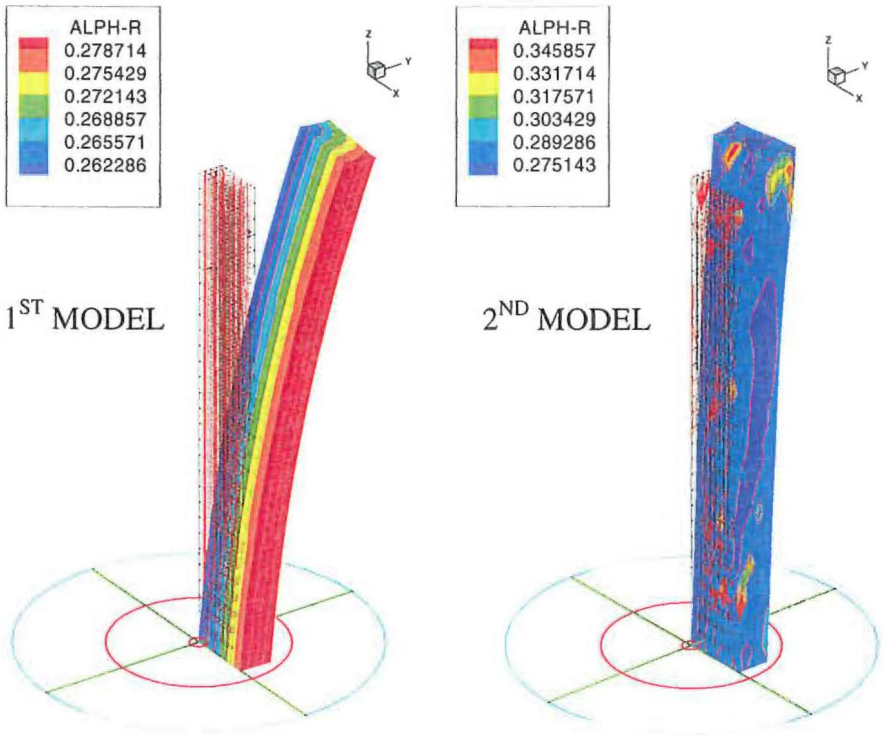

Figure J7. Variation of shrinkage in the radial direction in board B1.

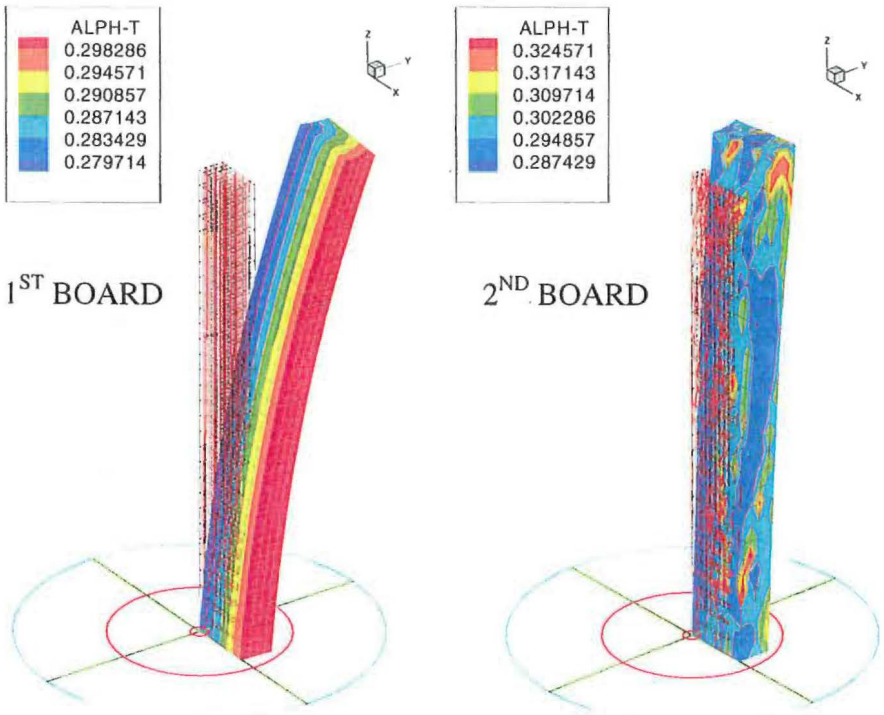

Figure J8. Variation of shrinkage in the tangential direction in board B1.

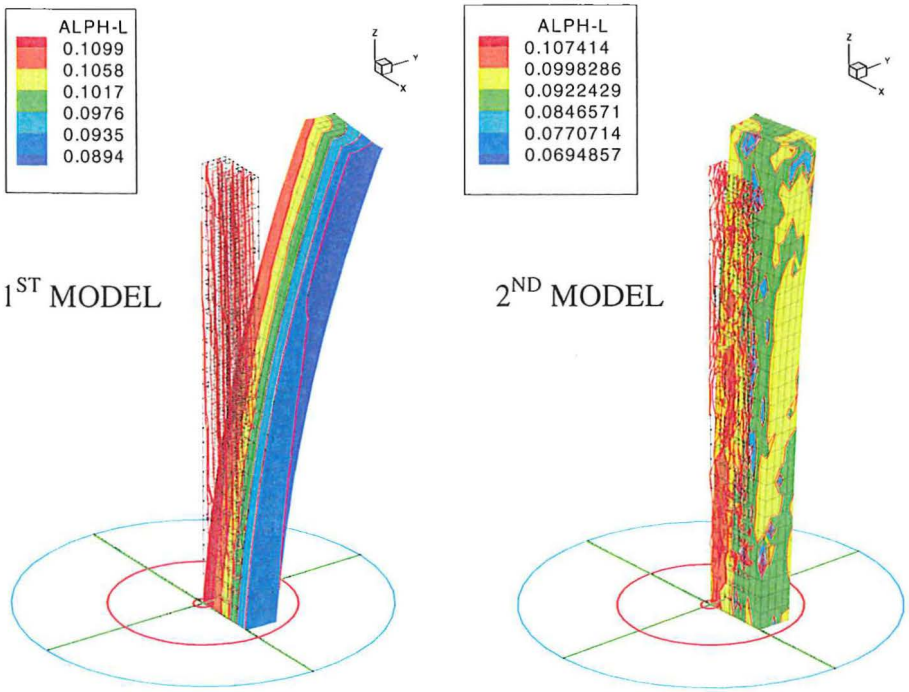

Figure J9. Variation of shrinkage in the longitudinal direction in board B1.

K. Measurement of dimensions for shrinkage/swelling and warp deformation

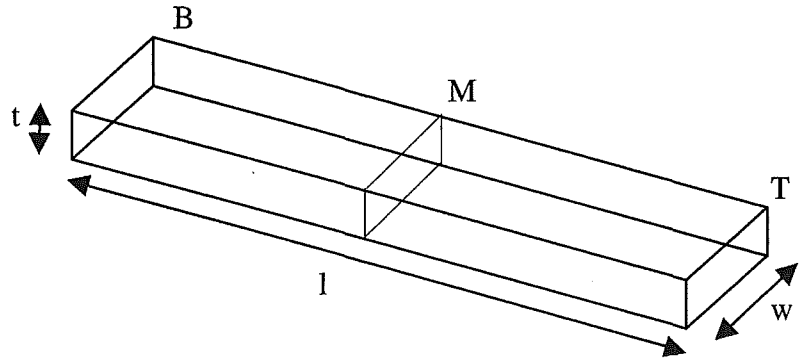

The length (*l*) is measured between the ends B and T of board on four sides using a metre scale. The width (*w*) and the thickness (*t*) are measured at the ends B and T, and at the mid point M for each side of the board using a vernier scale. The average changes of length, width and thickness are calculated from the measurements with moisture variations.

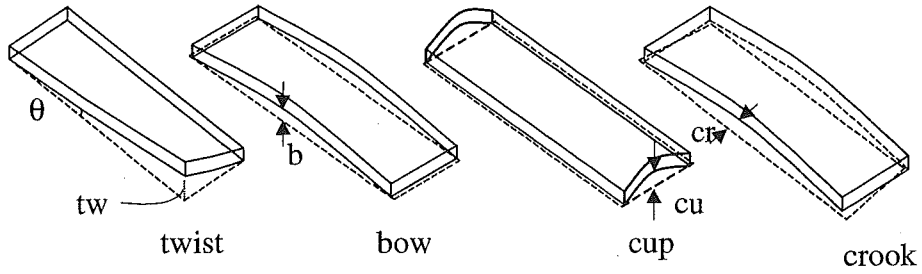

The board is placed on a flat surface and the maximum displacement of bow (*b*), cup (*cu*) and crook (*cr*) were measured with respect to the surface using a vernier scale. The twist angle (θ) is calculated by measuring the displacement (*tw*) and length (*l*). The changes of twist, bow, cup and crook are calculated from these measurements with moisture variations.

L. Graphs of measured shrinkage/ swelling and warp deformation

Keys for the graphs: DVS – volumetric shrinkage for desorption, DLS – longitudinal shrinkage for desorption, DWS – shrinkage along the width for desorption, DTS – shrinkage along the thickness for desorption, AVS – volumetric swelling for adsorption, ALS – longitudinal swelling for adsorption, AWS – swelling along the width for adsorption and ATS – swelling along the thickness for adsorption.

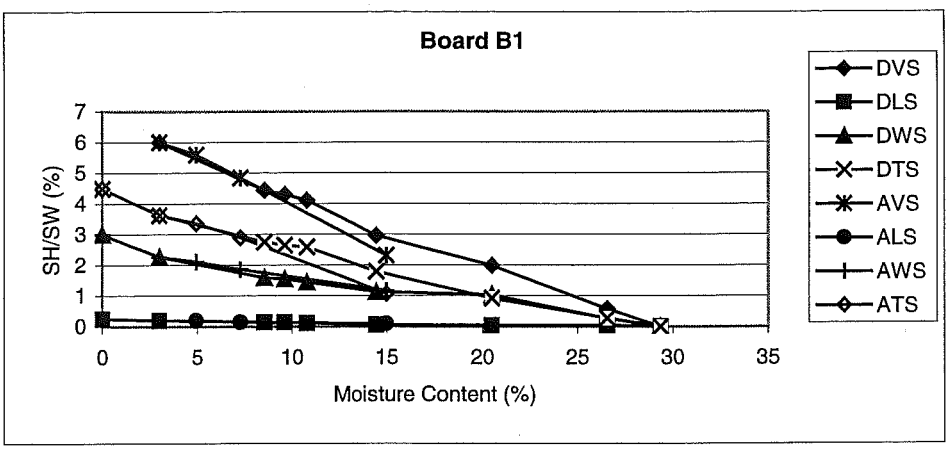

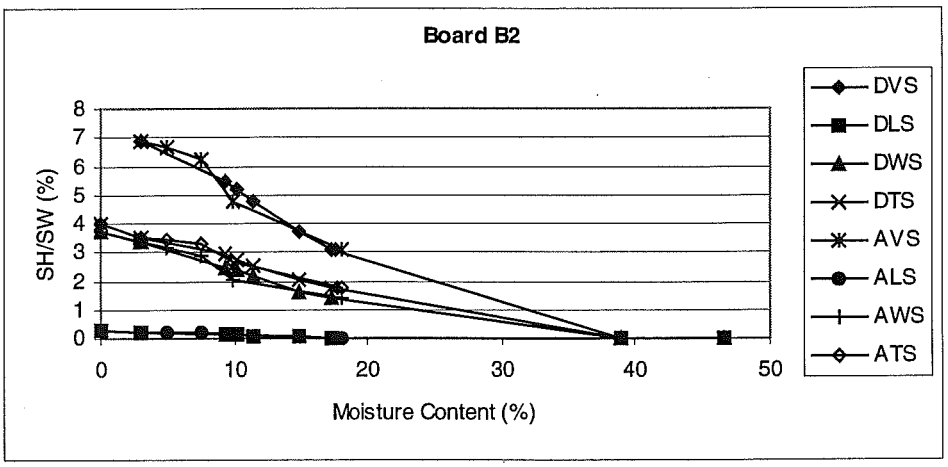

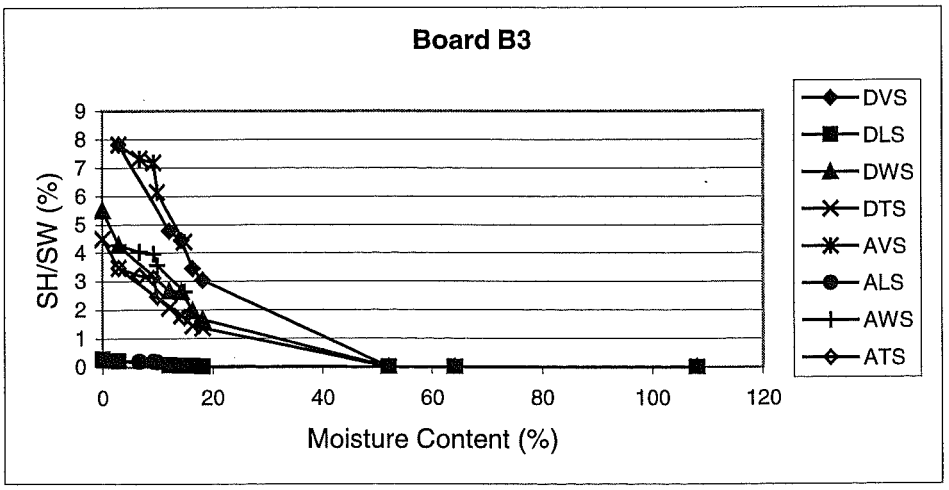

Figure L1. Shrinkage behaviours of boards B1, B2 and B3 from the measurements.

Keys for the graphs: DVS – volumetric shrinkage for desorption, DLS – longitudinal shrinkage for desorption, DWS – shrinkage along the width for desorption, DTS – shrinkage along the thickness for desorption, AVS – volumetric swelling for adsorption, ALS – longitudinal swelling for adsorption, AWS – swelling along the width for adsorption and ATS – swelling along the thickness for adsorption.

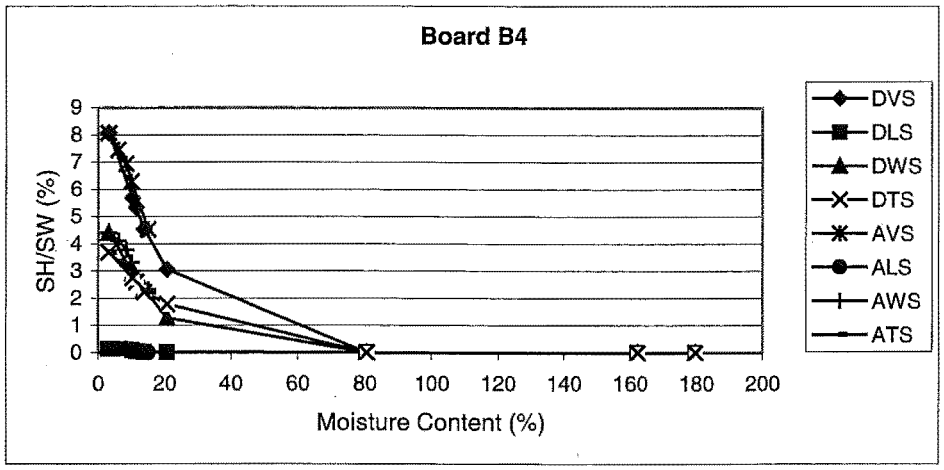

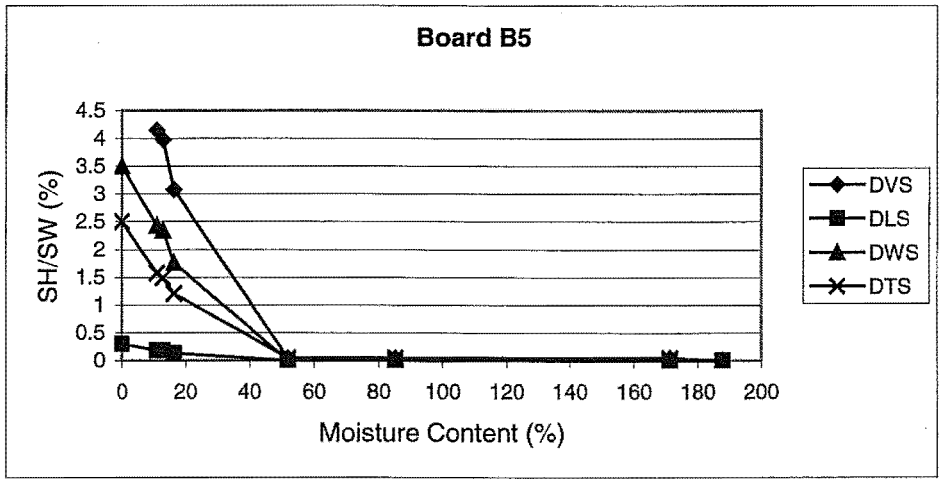

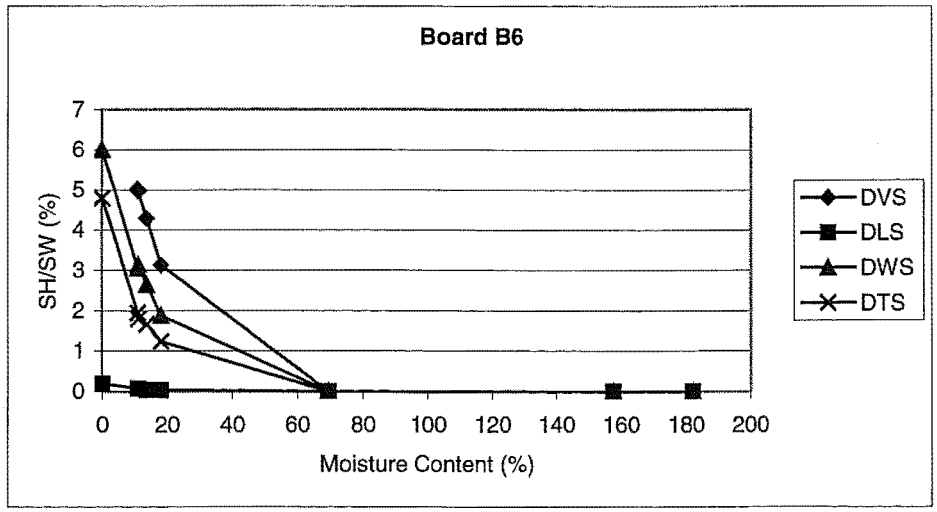

Figure L2. Shrinkage behaviours of boards B4, B5 and B6 from the measurements.

Keys for the graphs: DVS – volumetric shrinkage for desorption, DLS – longitudinal shrinkage for desorption, DWS – shrinkage along the width for desorption, DTS – shrinkage along the thickness for desorption, AVS – volumetric swelling for adsorption, ALS – longitudinal swelling for adsorption, AWS – swelling along the width for adsorption and ATS – swelling along the thickness for adsorption.

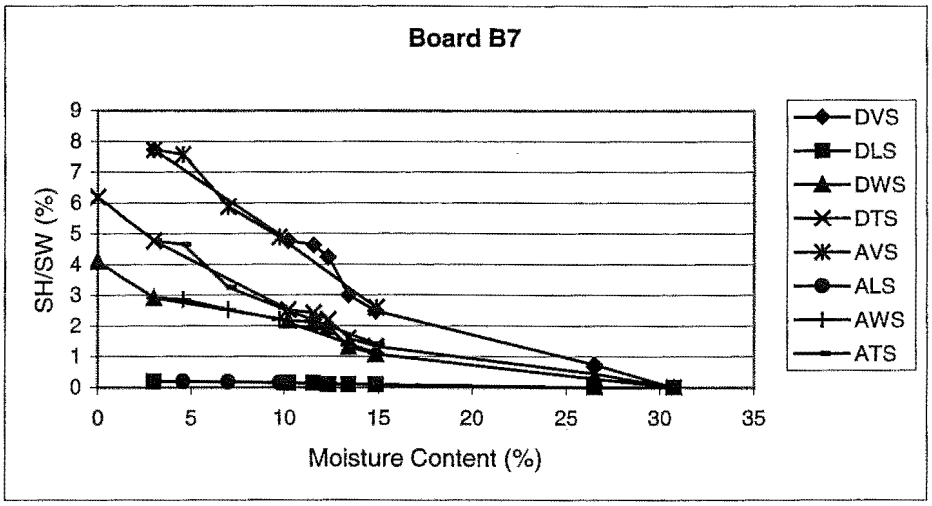

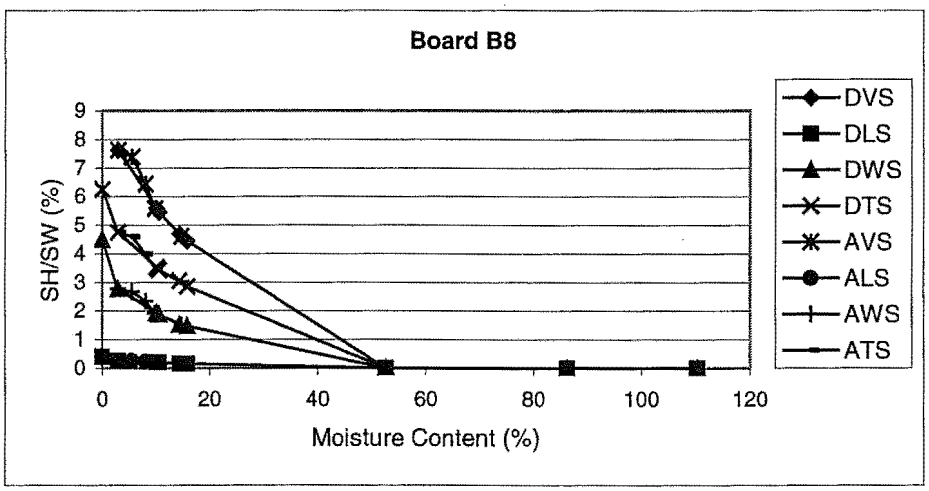

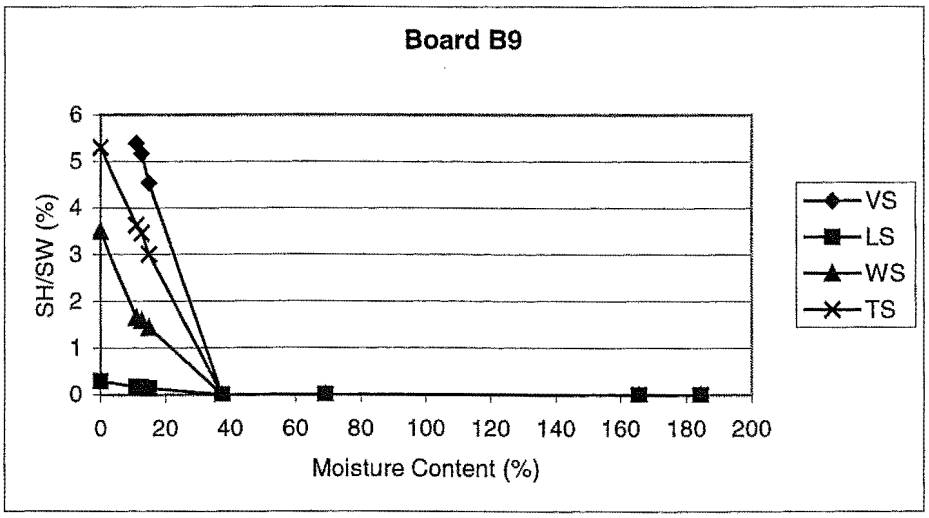

Figure L3. Shrinkage behaviours of boards B7, B8 and B9 from the measurements.

Keys for the graphs: DVS – volumetric shrinkage for desorption, DLS – longitudinal shrinkage for desorption, DWS – shrinkage along the width for desorption, DTS – shrinkage along the thickness for desorption, AVS – volumetric swelling for adsorption, ALS – longitudinal swelling for adsorption, AWS – swelling along the width for adsorption and ATS – swelling along the thickness for adsorption.

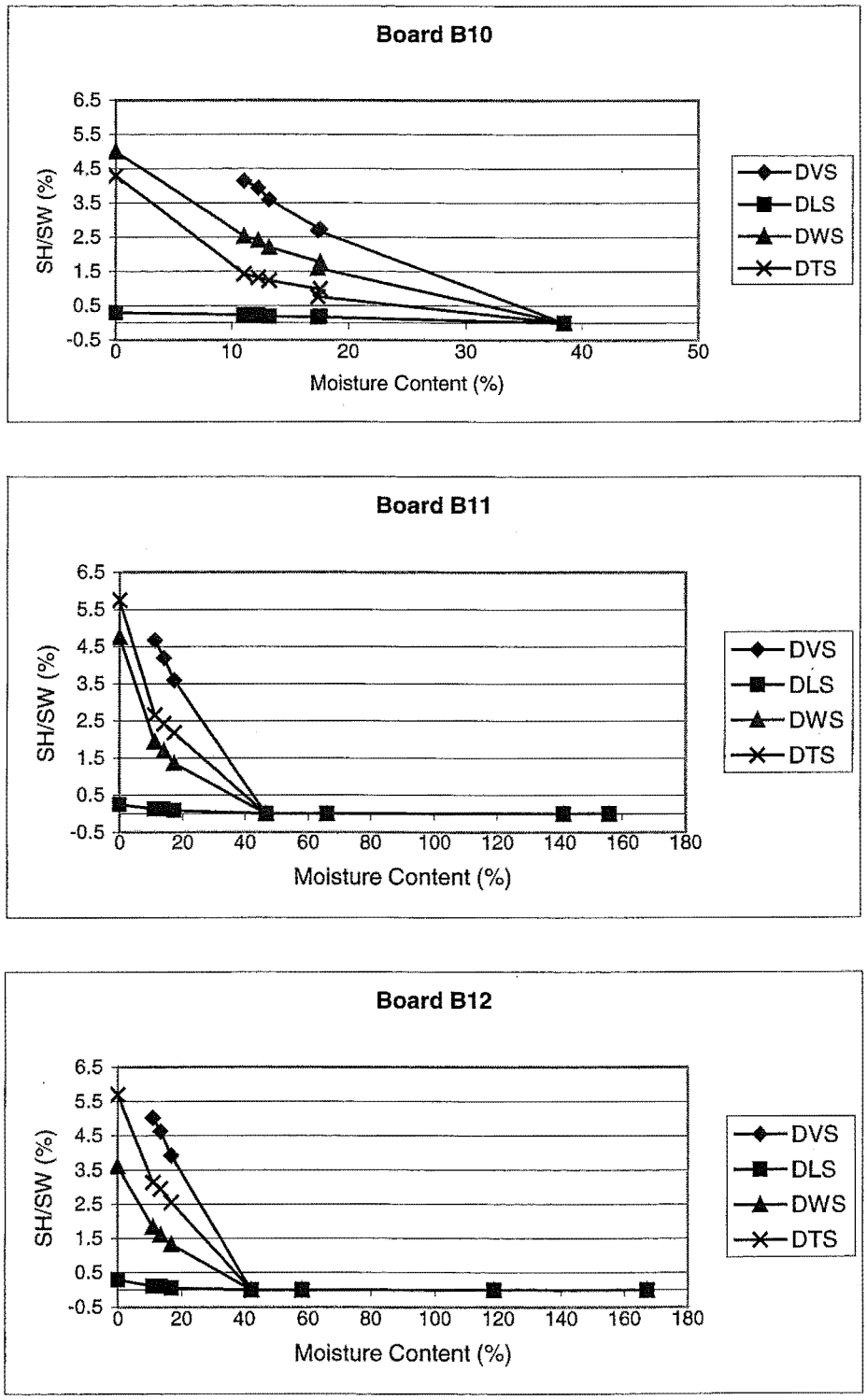

Figure L4. Shrinkage behaviours of boards B10, B11 and B12 from the measurements.

Keys for the graphs: DVS – volumetric shrinkage for desorption, DLS – longitudinal shrinkage for desorption, DWS – shrinkage along the width for desorption, DTS – shrinkage along the thickness for desorption, AVS – volumetric swelling for adsorption, ALS – longitudinal swelling for adsorption, AWS – swelling along the width for adsorption and ATS – swelling along the thickness for adsorption.

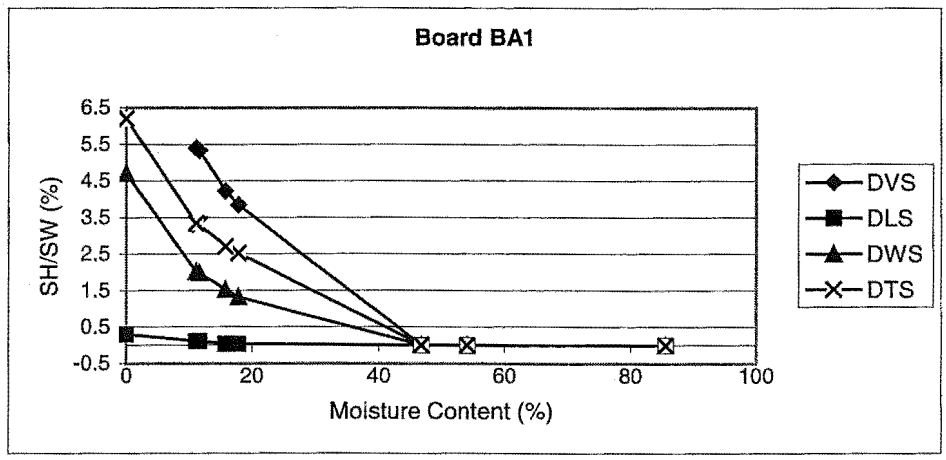

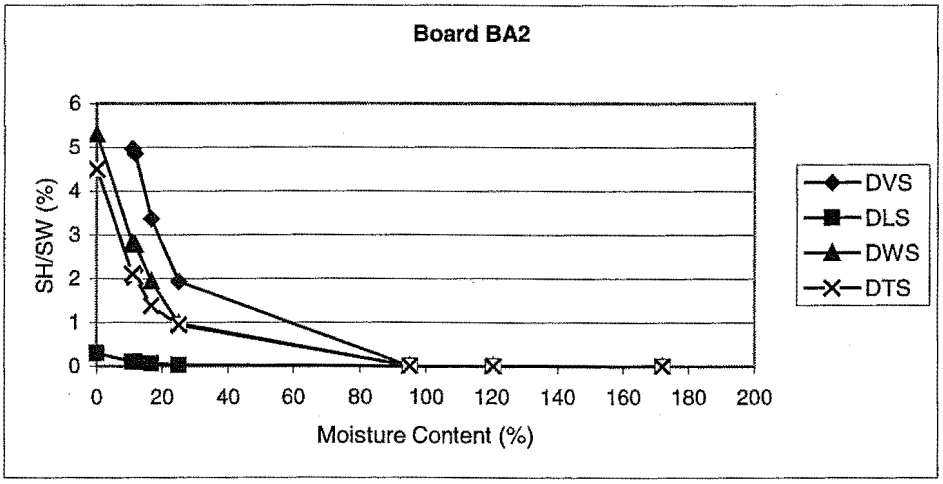

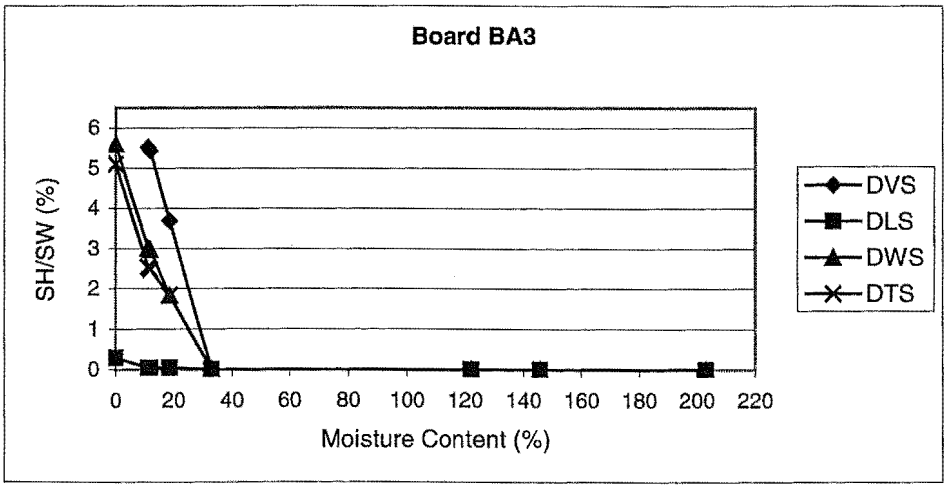

Figure L5. Shrinkage behaviours of boards BA1, BA2 and BA3 from the measurements.

Keys for the graphs: DVS – volumetric shrinkage for desorption, DLS – longitudinal shrinkage for desorption, DWS – shrinkage along the width for desorption, DTS – shrinkage along the thickness for desorption, AVS – volumetric swelling for adsorption, ALS – longitudinal swelling for adsorption, AWS – swelling along the width for adsorption and ATS – swelling along the thickness for adsorption.

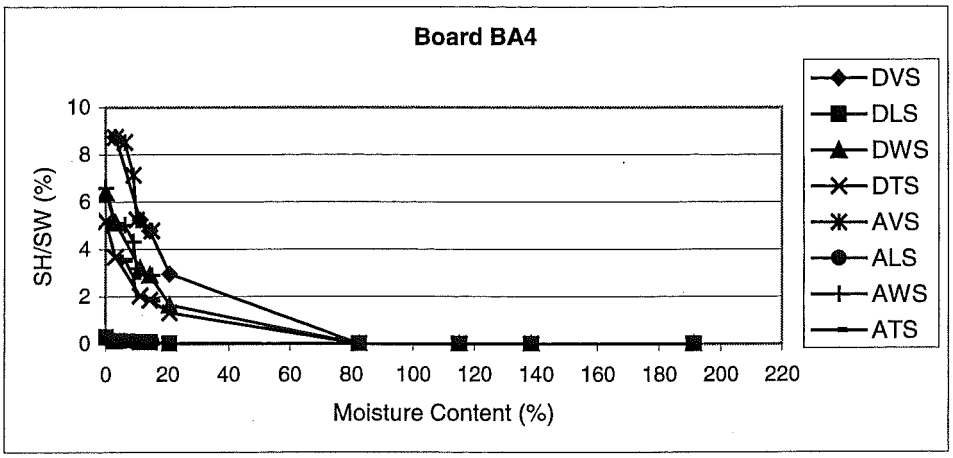

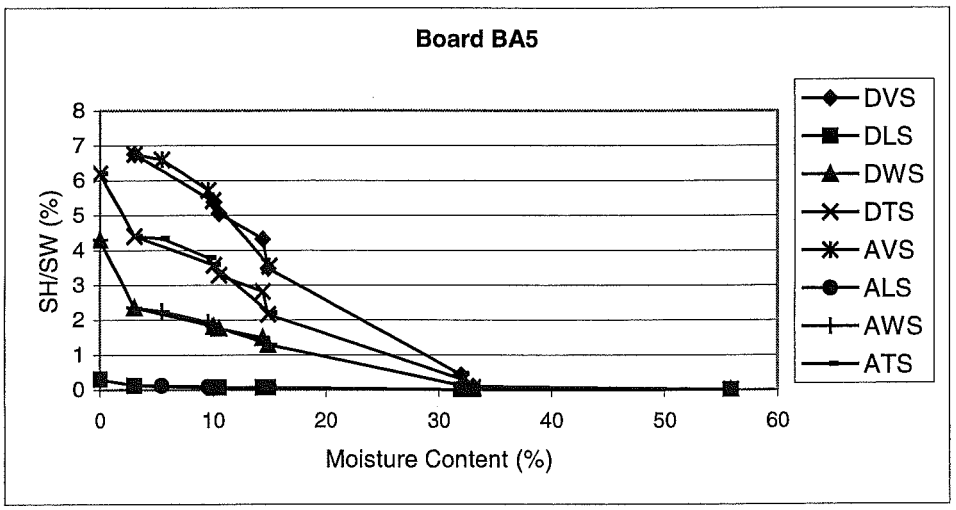

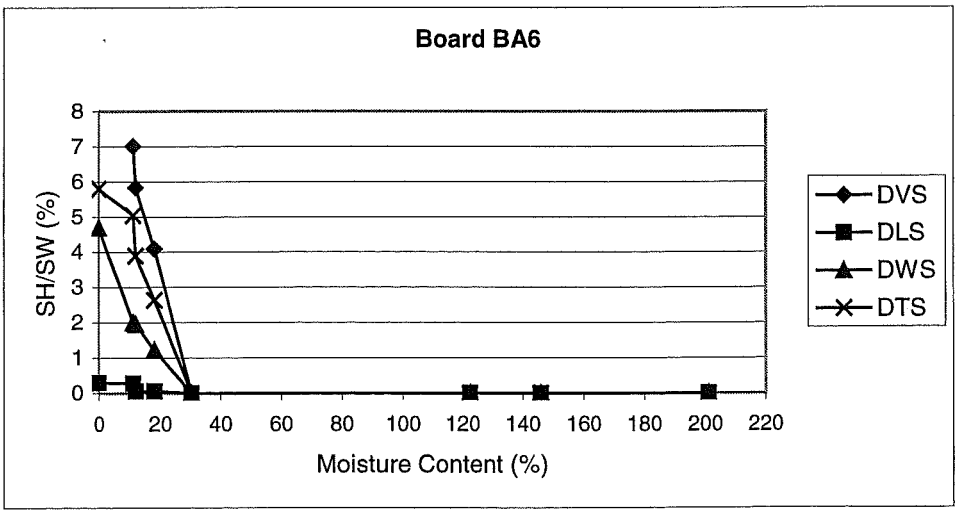

Figure L6. Shrinkage behaviours of boards BA4, BA5 and BA6 from the measurements.

Keys for the graphs: DVS – volumetric shrinkage for desorption, DLS – longitudinal shrinkage for desorption, DWS – shrinkage along the width for desorption, DTS – shrinkage along the thickness for desorption, AVS – volumetric swelling for adsorption, ALS – longitudinal swelling for adsorption, AWS – swelling along the width for adsorption and ATS – swelling along the thickness for adsorption.

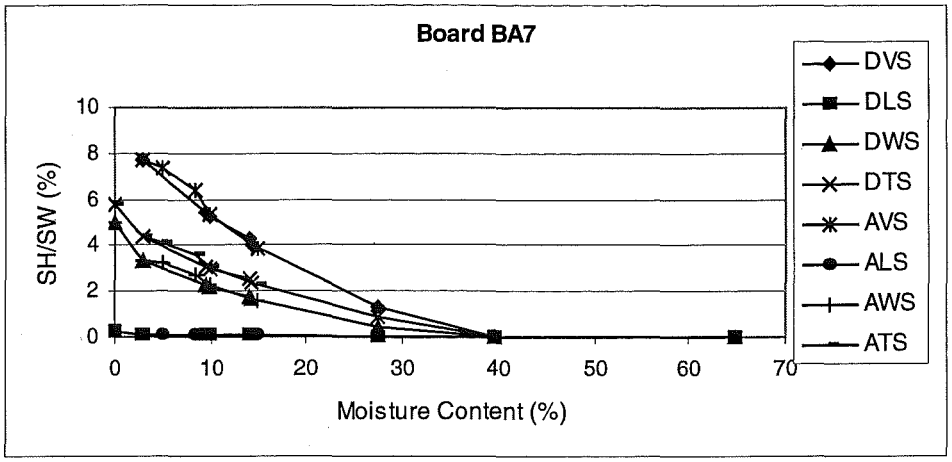

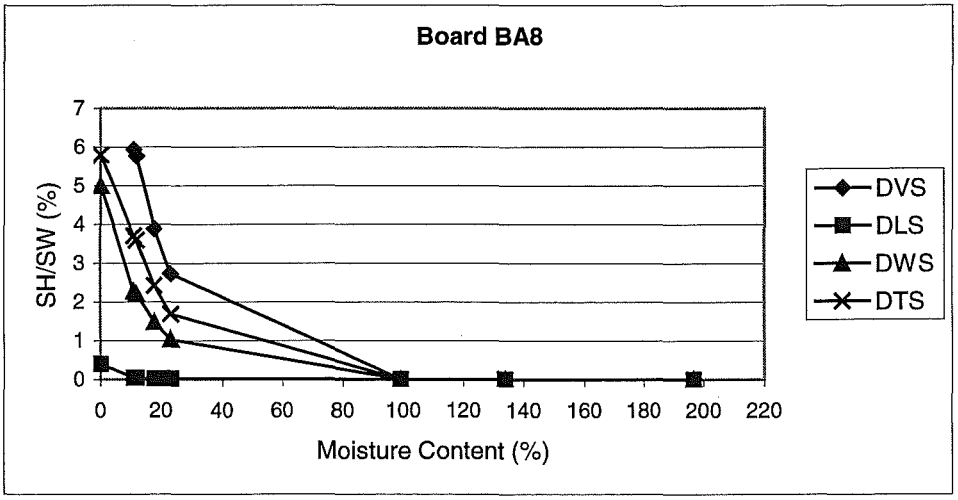

Figure L7. Shrinkage behaviours of boards BA7 and BA8 from the measurements.

Keys for the graphs: DCR – crooking for desorption, DBO – bowing for desorption, DCU – cuping for desorption, DTW – twisting the thickness for desorption, ACR – crooking for adsorption, ABO – bowing for adsorption, ACU – cuping for adsorption and ATW – twisting for adsorption.

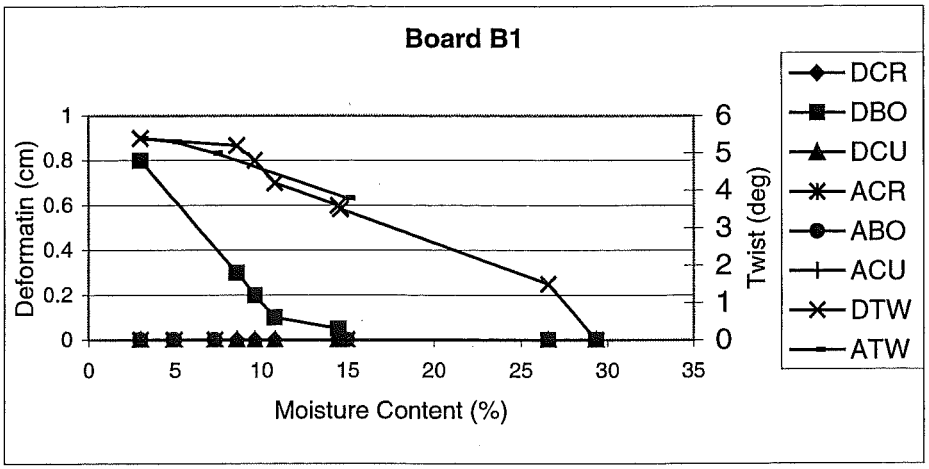

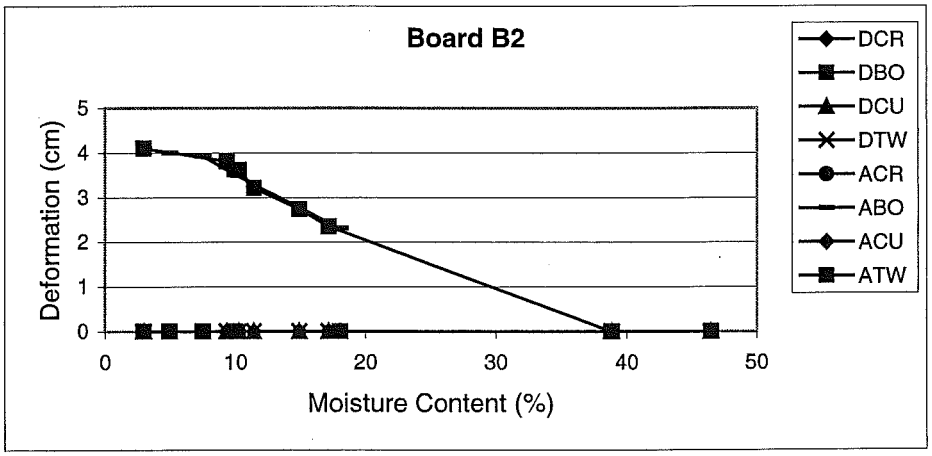

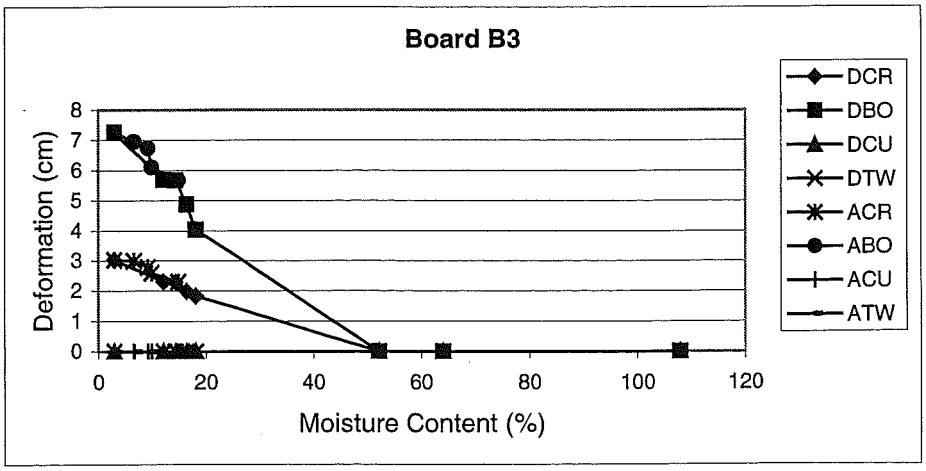

Figure L8. Deformation of boards B1, B2 and B3 from the measurements.

Keys for the graphs: DCR – crooking for desorption, DBO – bowing for desorption, DCU – cuping for desorption, DTW – twisting the thickness for desorption, ACR – crooking for adsorption, ABO – bowing for adsorption, ACU – cuping for adsorption and ATW – twisting for adsorption.

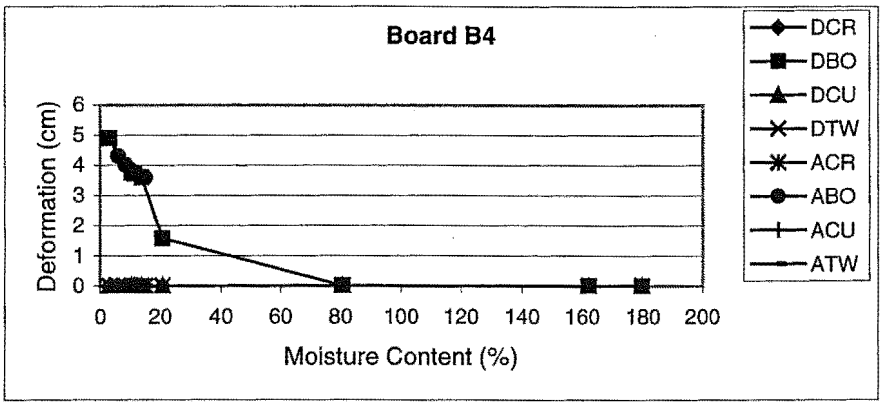

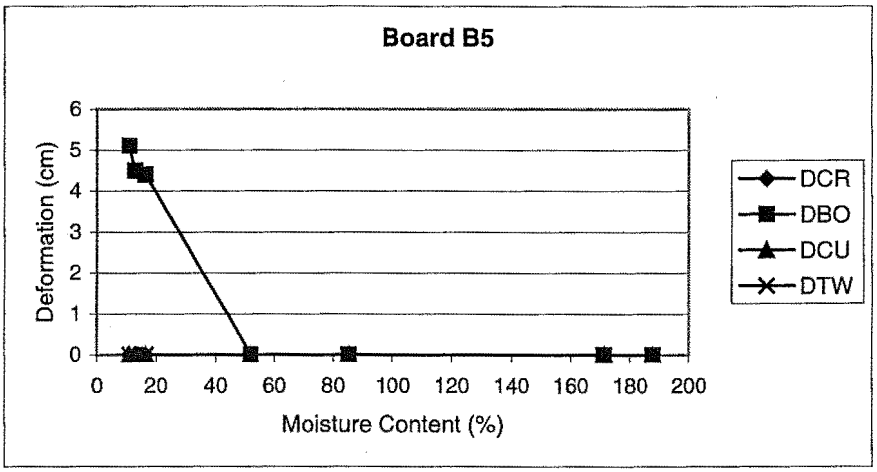

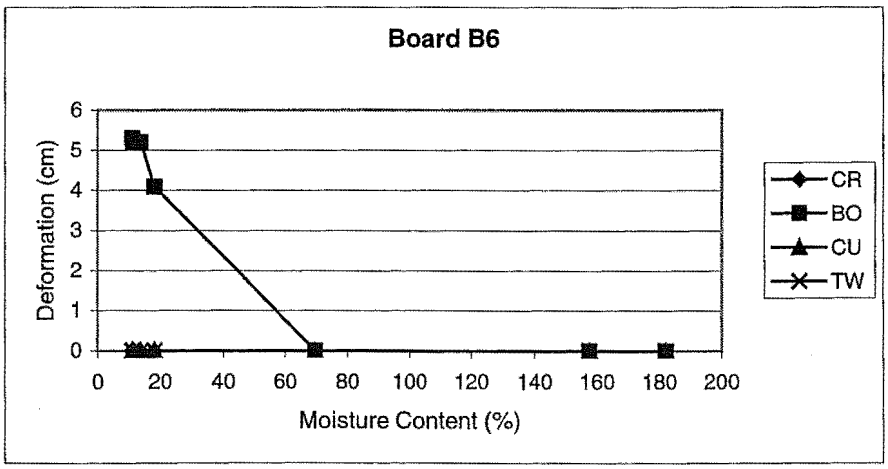

Figure L9. Deformation of boards B4, B5 and B6 from the measurements.

Keys for the graphs: DCR – crooking for desorption, DBO – bowing for desorption, DCU – cuping for desorption, DTW – twisting the thickness for desorption, ACR – crooking for adsorption, ABO – bowing for adsorption, ACU – cuping for adsorption and ATW – twisting for adsorption.

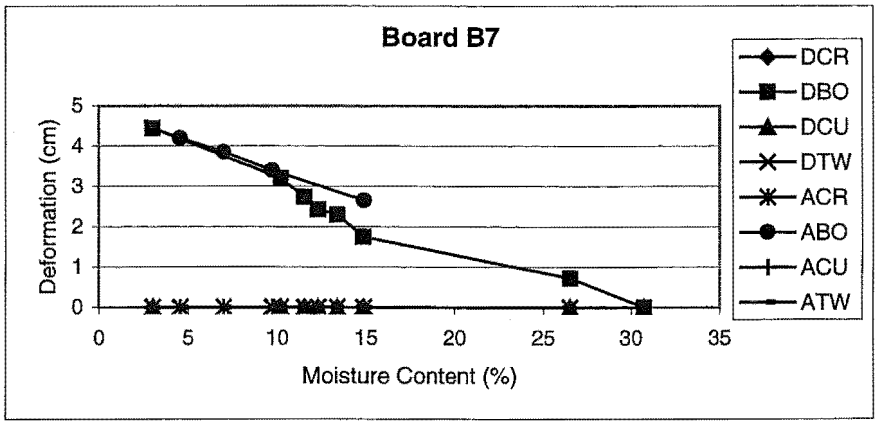

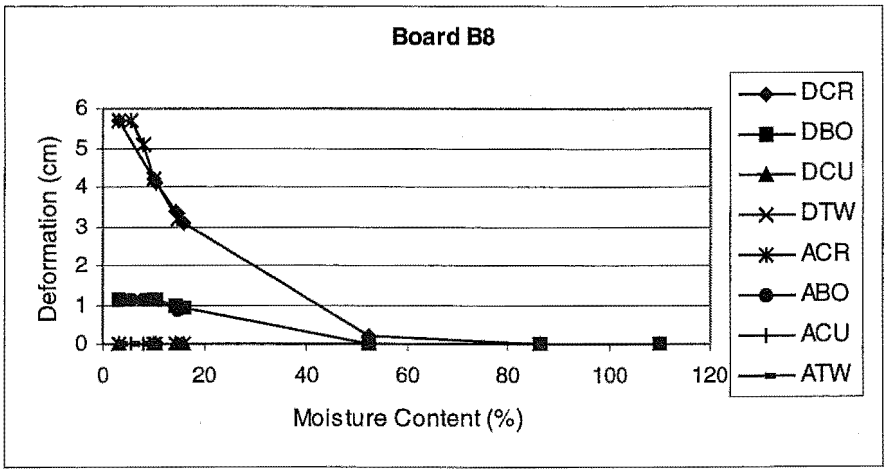

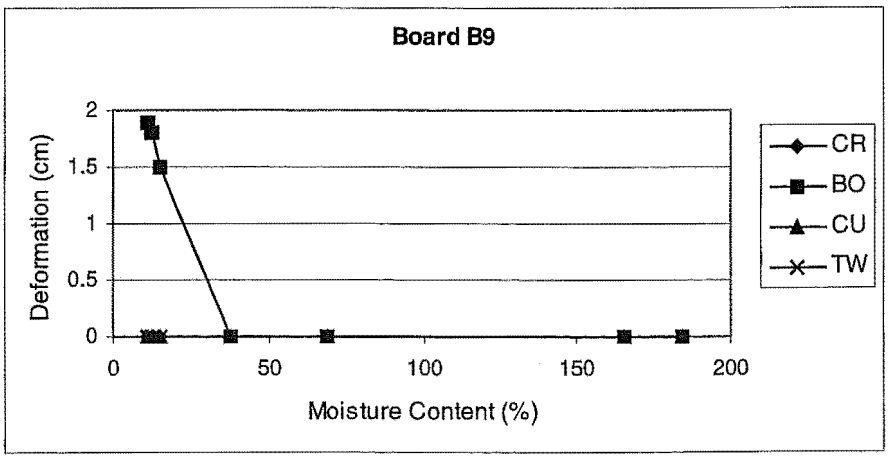

Figure L10. Deformation of boards B7, B8 and B9 from the measurements.

Keys for the graphs: DCR – crooking for desorption, DBO – bowing for desorption, DCU – cuping for desorption, DTW – twisting the thickness for desorption, ACR – crooking for adsorption, ABO – bowing for adsorption, ACU – cuping for adsorption and ATW – twisting for adsorption.

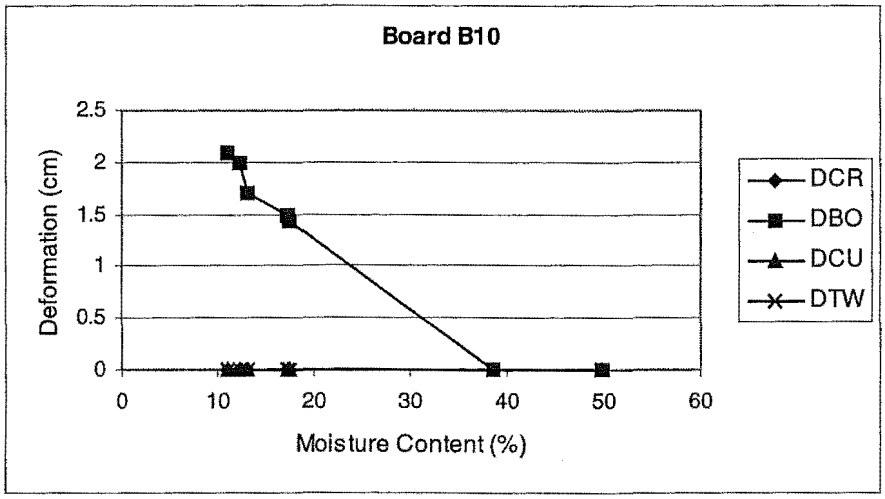

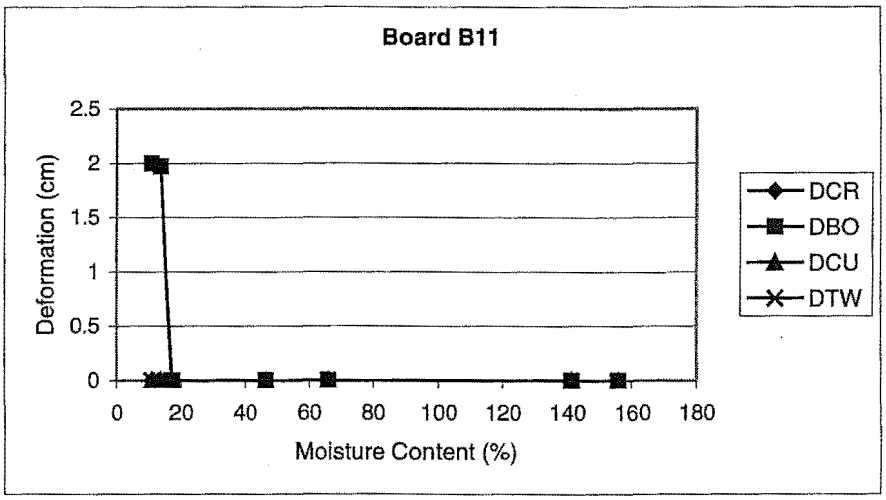

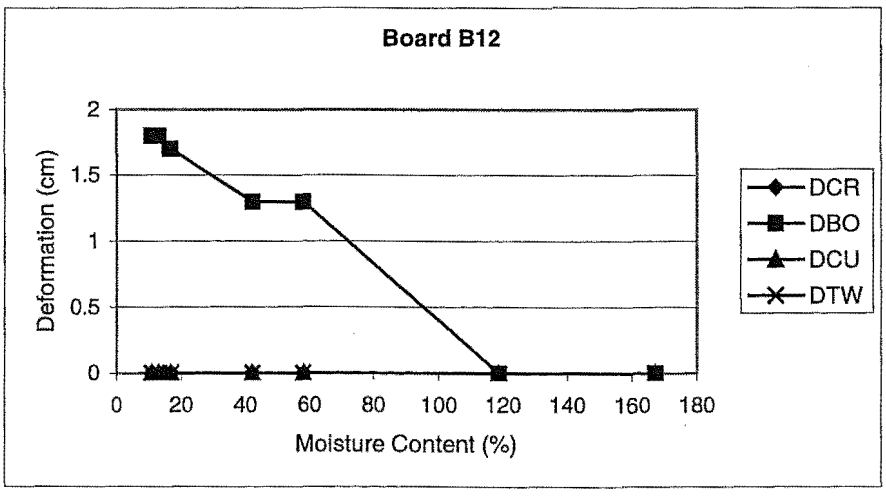

Figure L11. Deformation of boards B10, B11 and B12 from the measurements.

Keys for the graphs: DCR – crooking for desorption, DBO – bowing for desorption, DCU – cuping for desorption, DTW – twisting the thickness for desorption, ACR – crooking for adsorption, ABO – bowing for adsorption, ACU – cuping for adsorption and ATW – twisting for adsorption.

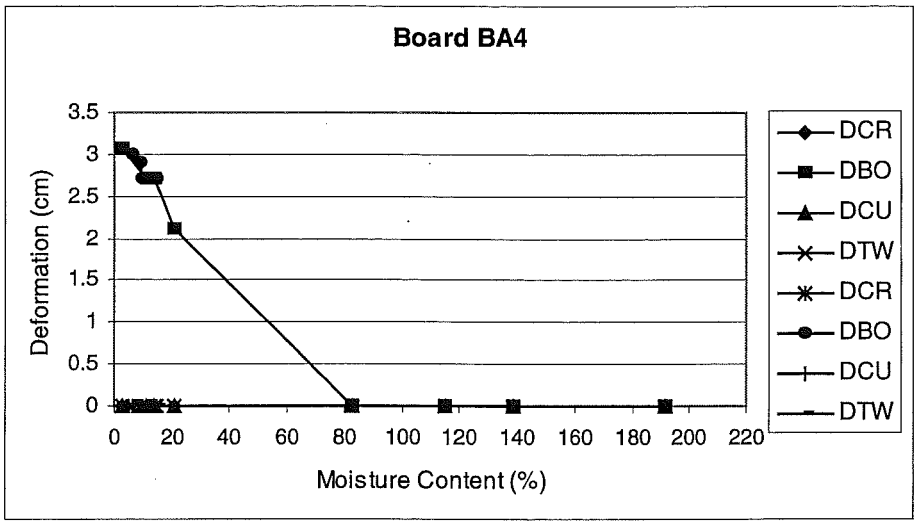

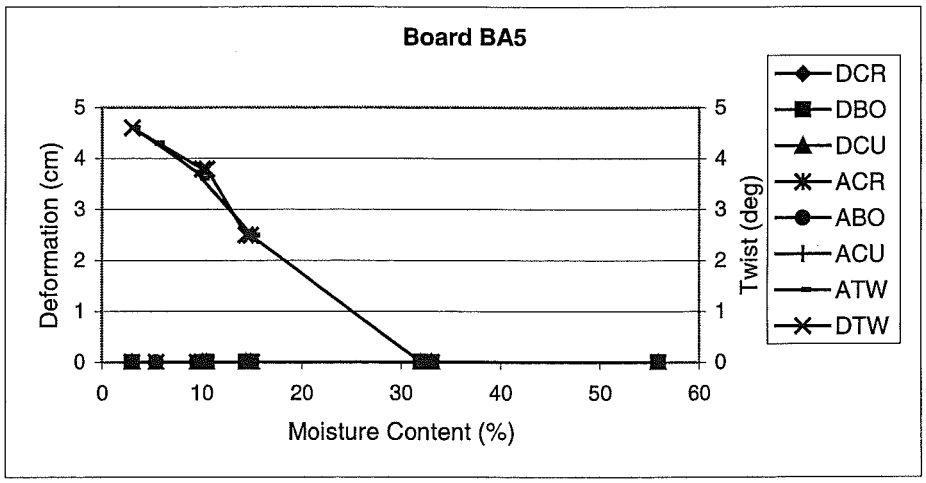

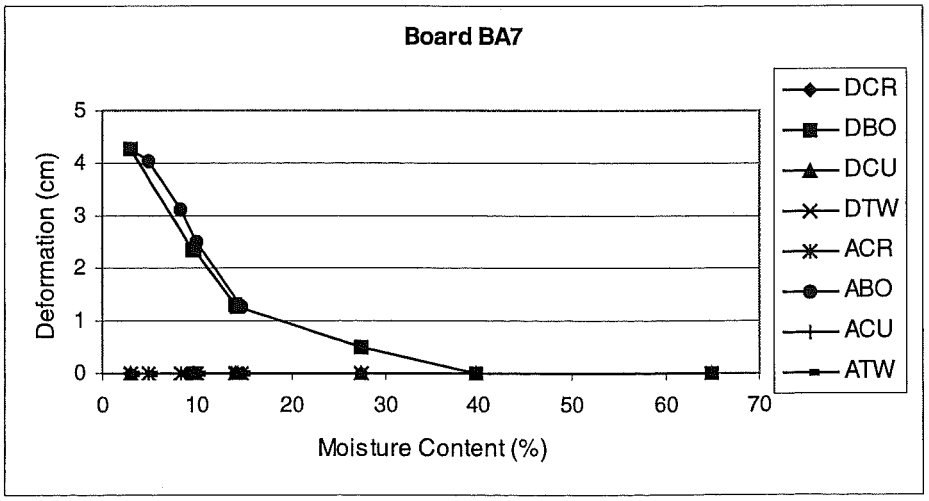

Figure L12. Deformation of boards BA4, BA5 and BA7 from the measurements.

Keys for the graphs: DCR – crooking for desorption, DBO – bowing for desorption, DCU – cuping for desorption, DTW – twisting the thickness for desorption, ACR – crooking for adsorption, ABO – bowing for adsorption, ACU – cuping for adsorption and ATW – twisting for adsorption.

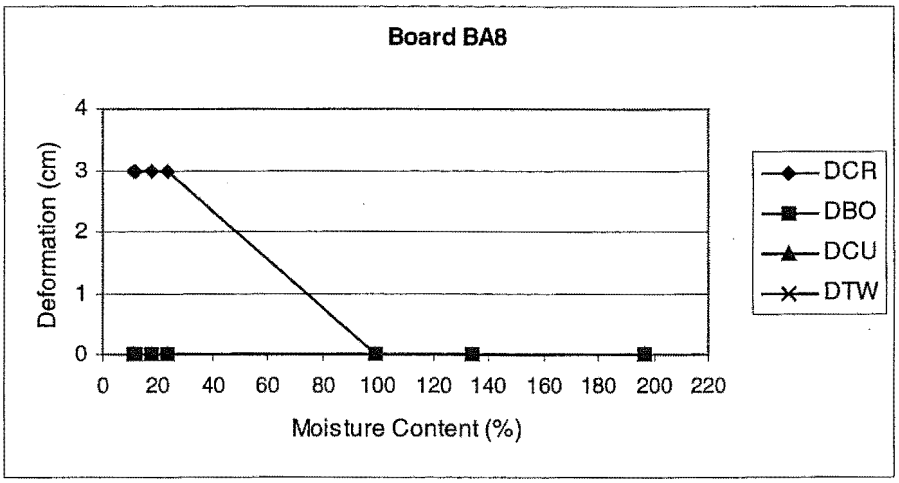

Figure L13. Deformation of board BA8 from the measurements.